

**Integrated analysis of anomalous microseismic behavior in a Montney  
treatment: Engineering parameters, locations, moment tensors, and  
geomechanics**

by

Thi Hanh Bui

A thesis submitted in partial fulfillment of the requirements for the degree of

Doctor of Philosophy

in

Geophysics

Department of Physics  
University of Alberta

© Thi Hanh Bui, 2024

# Abstract

Microseismic monitoring is crucial for evaluating hydraulic fracturing operations and understanding the subsurface. Processing and analyzing microseismic signals induced by fracturing fluid injection provides insights into pore pressure and in-situ stress changes. However, the large volume of recorded data and the variability in microseismic signals present significant challenges in the efficient and accurate processing and analysis of microseismic data. For example, an automated energy-based detector, the short-time average over the long-time average, can result in many false alarms, making event detection in large data sets time-consuming. Determining event locations also faces challenges due to velocity model errors, uncertainties in arrival time picking, or lack of geophone coverage. Large data sets demand location algorithms to provide hypocentral estimation with high accuracy and at a preferably low computational cost. Accelerating location algorithms to resolve the efficiency challenge is thus crucial. Furthermore, hydraulic fracture networks in the subsurface are complex, contributing to highly variable recorded microseismic waveforms. Understanding the geomechanical context is also essential for interpreting microseismic behavior.

This thesis studies an extensive microseismic data set induced from 78 hydraulic fracturing treatment stages across four horizontal wells in the Montney reservoir in northeastern British Columbia, Canada. The microseismic activity exhibits substantial variations between treatment stages, with most events concentrated near the heel of the wells. Different hypotheses have been proposed for the leading cause of anomalous microseismic behavior. It could be operational issues, changes in treatment parameters, errors in microseismic data processing, pre-existing faults, and changes

in the geological and geomechanical properties of the medium.

First, I examine operational problems by scrutinizing fracturing treatment records for each stage, studying issues like screen-out conditions that may cause cessation of the fracturing process, and determining their correlation with the microseismicity. Second, changes in treatment parameters are considered, specifically breakdown pressure, injection rate, and treatment duration, to understand their impact on microseismic activity. Third, I investigate whether anomalies result from inefficient detection algorithms, using different automated detection methods to determine any related processing errors. Fourth, I perform an integrated analysis to study the impacts of geological and geomechanical changes on microseismicity. The treatment wells could travel in and out of zones with lateral variation in lithology or pre-existing fractures/-faults in the medium can lead to the event anomaly.

Major findings indicate that operational issues, treatment parameter changes, and data processing are not the primary causes of the microseismic anomaly. Evidence from the evolution of the microseismic cloud distance over time, moment tensor characteristics, landing heights of the treatment wells, variations in lithology, and high shear-wave velocity anisotropy strongly suggest that geological and geomechanical changes are most likely linked with anomalous microseismic behavior. The integrated analysis of treatment parameters, event locations, moment tensor, and geomechanics provides a comprehensive understanding of microseismic behavior in the Montney reservoir, presenting an interesting case study for microseismic analysis.

Beyond investigating the cause of the event anomaly, this thesis contributes to the data processing field by improving automated processing algorithms for large, noisy microseismic data sets. The proposed fast matched filter workflow effectively detects potential microseismic events, outperforming traditional triggering-based detectors. Two time-frequency methods, the sparse Gabor transform and neighboring block thresholding, are investigated for signal enhancement and automated event detection. The sparse Gabor transform is more promising, effectively reducing noise

while preserving signal characteristics. Furthermore, a quadratic interpolation algorithm is introduced to accelerate grid searches for event localization, providing a more efficient alternative to estimate event hypocenters.

In conclusion, this thesis unravels the leading cause of abnormal microseismic behavior in the Montney treatment and contributes to the microseismic data processing field by improving automated event detection and location algorithms. The results have implications for optimizing hydraulic fracturing operations and enhancing the efficiency of automated processing algorithms for large data sets.

# Preface

This dissertation is submitted for the degree of Doctor of Philosophy in Geophysics at the University of Alberta. The research described herein is original, and neither this nor any substantially similar dissertation was or is being submitted for any other degree or other qualification at any other university.

A manuscript including a version of **chapter 4** of this thesis has been submitted to Geophysics. I am responsible for code development, data analysis, figure preparation, and manuscript writing.

An article including a version of **chapter 5** of this thesis has been published in Geophysics as Bui, H., van der Baan, M. and Sacchi, M., 2023, Comparison of sparse Gabor-based methods for detection of microseismic events, Geophysics, 88(2), L27-L35, doi: 10.1190/geo2022-0240.1. I am responsible for code development, data analysis, figure preparation, and manuscript writing.

A manuscript including a version of **chapter 6** of this thesis has been submitted to Geophysical Journal International. I am responsible for code development, data analysis, figure preparation, and manuscript writing.

*To my beloved parents, husband, daughter, sister, and brother*

# Acknowledgements

I would like to express my sincere gratitude to my supervisor, Dr. Mirko van der Baan, for his continued guidance and support throughout my Ph.D. study and research. His immense knowledge of Geophysics inspires me to explore and solve different geophysical problems. I am truly grateful for his patience in explaining difficult concepts to me. He always makes things easy to understand, and that helps me learn and build a solid understanding of Geophysics. Without his incredible support, I would not be who I am today.

I would like to thank the members of my supervisory and candidacy committee, Dr. David Potter, Dr. Vadim Kravchinsky, Dr. Juliana Leung, and Dr. John-Paul Zonneveld, for their insightful questions, comments, and feedback. I would like to thank Dr. Heather DeShon and Dr. Moritz Heimpel for agreeing to be a part of the final examination committee for my Ph.D. defense and their insightful questions and comments during the examination. Special thanks to Dr. Heather DeShon and Dr. David Potter for their insightful feedback on my thesis. I would also like to thank Dr. Gordon Rostoker for being the chair of my candidacy examination and Dr. Natalia Ivanova for being the chair of my final examination.

I would like to thank Dr. Mauricio Sacchi for his support on the sparse Gabor transform methods. I would also like to thank Dr. Thomas Eyre for his support on moment tensor inversion codes.

I would like to thank all my past and present colleagues and friends at the University of Alberta for their direct or indirect support, particularly all the students and staff of the Distributed and Passive Sensing (formerly the Microseismic Industry

Consortium).

I would like to thank an anonymous company for the permission to use and show the microseismic data acquired during hydraulic fracturing treatments. I am thankful to the sponsors of the Consortium for Distributed and Passive Sensing for the financial support. I would also like to thank scholarship providers who gave me extra financial support throughout my Ph.D.

I would also like to thank Mrs. Ruby Hunjan, Dr. Mirko's wife, for organizing wonderful parties at their home for our entire group and making us feel at home away from home.

I wholeheartedly thank my family for their unconditional love, numerous sacrifices, and support throughout my Ph.D. program. Thank you for constantly encouraging me to pursue my academic dream.

# Table of Contents

<b>1</b>	<b>Introduction</b>	<b>1</b>
1.1	Background . . . . .	1
1.1.1	Unconventional resources and hydraulic fracturing . . . . .	1
1.1.2	Microseismic data analysis . . . . .	2
1.1.3	Geomechanics and induced microseismicity . . . . .	5
1.2	Motivation and contribution . . . . .	6
1.2.1	Statement of problem . . . . .	6
1.2.2	Research questions . . . . .	8
1.2.3	Thesis objectives . . . . .	12
1.2.4	Main contribution . . . . .	13
1.3	Thesis overview . . . . .	14
<b>2</b>	<b>Geological setting of the study area and data background</b>	<b>18</b>
2.1	Introduction . . . . .	18
2.2	Geological setting of the study area . . . . .	20
2.2.1	Study area and tectonic setting . . . . .	20
2.2.2	Geology of Montney formation . . . . .	20
2.3	Hydraulic fracturing operations . . . . .	24
2.4	Microseismic data . . . . .	25
2.5	Miscellaneous data . . . . .	26
2.6	Objectives . . . . .	28
<b>3</b>	<b>Preprocessing microseismic data: Sensor orientation estimation, data rotation, signal preconditioning, and velocity model building</b>	<b>30</b>
3.1	Introduction . . . . .	31
3.2	Methodology . . . . .	31
3.2.1	Sensor orientation estimation . . . . .	31
3.2.2	Data rotation . . . . .	37
3.2.3	Signal preconditioning . . . . .	42

3.2.4	Velocity model building . . . . .	43
3.3	Implementation and results . . . . .	43
3.3.1	Sensor orientation estimation and data rotation . . . . .	43
3.3.2	Signal preconditioning . . . . .	50
3.3.3	Velocity model building . . . . .	52
3.4	Conclusions . . . . .	53
<b>4</b>	<b>Detecting events in big microseismic data sets using a fast matched filter algorithm</b>	<b>56</b>
4.1	Introduction . . . . .	57
4.2	Methodology . . . . .	59
4.2.1	Fast MF detection theory and workflow . . . . .	59
4.2.2	Detection performance statistics . . . . .	65
4.3	Implementation and Results . . . . .	66
4.3.1	Data overview . . . . .	66
4.3.2	Fast MF implementation . . . . .	66
4.3.3	Detection results . . . . .	75
4.4	Discussions . . . . .	81
4.4.1	Pros and cons of multiplexing . . . . .	81
4.4.2	Pros and cons of the MF versus STA/LTA . . . . .	82
4.4.3	Another cross-correlation-based detection alternative . . . . .	83
4.5	Conclusions . . . . .	84
<b>5</b>	<b>Comparison of sparse Gabor-based methods for detection of microseismic events</b>	<b>85</b>
5.1	Introduction . . . . .	86
5.2	Methodology . . . . .	88
5.2.1	Sparse Gabor transform . . . . .	88
5.2.2	Neighboring block thresholding . . . . .	89
5.2.3	Detecting events . . . . .	90
5.3	Implementation and Detection Results . . . . .	91
5.3.1	Synthetic Data Example . . . . .	91
5.3.2	Real Data Example . . . . .	94
5.3.3	Event detection . . . . .	98
5.3.4	Detection results . . . . .	98
5.3.5	Amplitude fidelity . . . . .	100
5.4	Conclusions . . . . .	104

<b>6</b>	<b>Locating microseismic events using S-P time difference and quadratic interpolation</b>	<b>107</b>
6.1	Introduction . . . . .	108
6.2	Methodology . . . . .	111
6.2.1	The location problem . . . . .	111
6.2.2	Grid search via lookup tables . . . . .	112
6.2.3	Quadratic interpolation between grid points . . . . .	114
6.2.4	NonLinLoc . . . . .	120
6.3	Implementation and Results . . . . .	121
6.3.1	Synthetic Data Examples . . . . .	121
6.3.2	Real Data Example . . . . .	138
6.4	Discussions . . . . .	142
6.4.1	Pros and cons of quadratic interpolation . . . . .	142
6.4.2	Alternative acceleration methods . . . . .	148
6.5	Conclusions . . . . .	150
<b>7</b>	<b>Moment-tensor inversion of hydraulic-fracturing-induced events in a Montney reservoir, northeastern British Columbia</b>	<b>151</b>
7.1	Introduction . . . . .	152
7.2	Methodology . . . . .	154
7.2.1	Source mechanisms of microseismic events . . . . .	154
7.2.2	Moment-tensor inversion using amplitude methods . . . . .	155
7.3	Forward modeling . . . . .	160
7.3.1	Model setup . . . . .	160
7.3.2	Effects of acquisition geometry . . . . .	162
7.3.3	Moment-tensor inversion results of synthetic amplitude data . . . . .	165
7.4	A Case Study . . . . .	171
7.4.1	Data overview . . . . .	171
7.4.2	A rough estimate from amplitude ratios . . . . .	171
7.4.3	Moment-tensor inversion results using amplitude-based method . . . . .	174
7.5	Discussions . . . . .	176
7.6	Conclusions . . . . .	179
<b>8</b>	<b>Integrated analysis of anomalous microseismic behavior in a Montney treatment: Engineering parameters, locations, moment tensors, and geomechanics</b>	<b>181</b>
8.1	Introduction . . . . .	182

8.2	Methods . . . . .	185
8.2.1	Investigate operational issues . . . . .	185
8.2.2	Investigate treatment parameters . . . . .	187
8.2.3	Investigate event detection . . . . .	188
8.2.4	Investigate locations, moment tensors, geomechanics . . . . .	188
8.3	Results . . . . .	193
8.3.1	Investigate operational issues . . . . .	193
8.3.2	Investigate treatment parameters . . . . .	195
8.3.3	Investigate event detection . . . . .	196
8.3.4	Investigate location, moment tensors, geomechanics . . . . .	197
8.4	Discussions . . . . .	208
8.5	Conclusions . . . . .	212
<b>9</b>	<b>Conclusions and suggested directions for future research</b>	<b>214</b>
9.1	Conclusions . . . . .	214
9.2	Suggested directions for future research . . . . .	216

# List of Tables

3.1	Orientation results obtained from different shot recordings for the first sensor in the vertical monitoring array. For the rotation angle, $\theta_{rot}$ , the results are converted into the same range of angle value $[0\ 2\pi]$ ; (SD: standard deviation). . . . .	46
3.2	Orientation results obtained from different shot recordings for the first sensor in tool string 2 in the horizontal array (SD: standard deviation).	49
4.1	Detection results of the fast MF when using different threshold values on a 2-hour microseismic data set. ( $\sigma$ : detection threshold). . . . .	75
5.1	Detection results of a 50-min microseismic data set. The computation time in the table only includes the time that the algorithms run and extract potential events and does not include the time for classifying events. . . . .	101
6.1	Resulting coefficients of the full 3D quadratic function (equation 6.9).	124
6.2	Interpolated locations and corresponding errors in each dimension when using a coarse grid spacing of 200 m and finer grid spacings of 30 and 10 m when using the full 3D quadratic function with 27 unknown coefficients. $x_{min}$ , $y_{min}$ , and $z_{min}$ are the coordinates of the initial location where I have the minimum value of the sum of all traveltime differences (estimated from the coarse grid search). $x_{int}$ , $y_{int}$ , and $z_{int}$ are the coordinates of the optimal location obtained from interpolation. $\Delta x$ , $\Delta y$ , and $\Delta z$ are the absolute differences between the interpolated and actual source location. $e_x$ , $e_y$ , and $e_z$ are the errors in percentage between the interpolated and actual source locations. The actual source location is at $x_S = 763$ m, $y_S = 402$ m, and $z_S = 2464$ m. . . .	126
6.3	Resulting coefficients of the simplified quadratic function (equation 6.15).	130

6.4	Interpolated locations and corresponding errors in each dimension when using a coarse grid spacing of 200 m and finer grid spacings of 30 and 10 m when using the simplified quadratic function with 10 unknown coefficients. $x_{min}$ , $y_{min}$ , and $z_{min}$ are the coordinates of the initial location where I have the minimum value of the sum of all traveltime differences (estimated from the coarse grid search). $x_{int}$ , $y_{int}$ , and $z_{int}$ are the coordinates of the optimal location obtained from interpolation. $\Delta x$ , $\Delta y$ , and $\Delta z$ are the absolute differences between the interpolated and actual source locations. $e_x$ , $e_y$ , and $e_z$ are the errors in percentage between the interpolated and actual source locations. The actual source location is at $x_S = 763$ m, $y_S = 402$ m, and $z_S = 2464$ m. . . .	130
6.5	Computation time of the grid search and the combination of grid search and quadratic interpolation (equation 6.15) when using a 3D search space 1000 m x 1000 m x 600 m with a coarse grid spacing of 200 m and finer grid spacings of 30 and 10 m. The actual source location is at $x_S = 763$ m, $y_S = 402$ m, and $z_S = 2464$ m. . . . .	132
6.6	NonLinLoc (NLL) locations and corresponding errors in each dimension when using a coarse grid spacing of 200 m and finer grid spacings of 30 and 10 m. $x_{NLL}$ , $y_{NLL}$ , and $z_{NLL}$ are the coordinates of the estimated location. $\Delta x$ , $\Delta y$ , and $\Delta z$ are the absolute differences between the NonLinLoc results and actual source locations. The actual source location is at $x_S = 763$ m, $y_S = 402$ m, and $z_S = 2464$ m. . . . .	133
6.7	Resulting coefficients of the simplified quadratic function (equation 6.15).	135
6.8	Interpolated locations and corresponding errors in each dimension when using a coarse grid spacing of 200 m and finer grid spacings of 30 and 10 m when using the simplified quadratic function with 10 unknown coefficients. $x_{min}$ , $y_{min}$ , and $z_{min}$ are the coordinates of the initial location where I have the minimum value of the sum of all traveltime differences (estimated from the coarse grid search). $x_{int}$ , $y_{int}$ , and $z_{int}$ are the coordinates of the optimal location obtained from interpolation. $\Delta x$ , $\Delta y$ , and $\Delta z$ are the absolute differences between the interpolated and actual source locations. $e_x$ , $e_y$ , and $e_z$ are the errors in percentage between the interpolated and actual source locations. The actual source location is at $x_S = 563$ m, $y_S = 352$ m, and $z_S = 2464$ m. . . .	135

6.9 NonLinLoc (NLL) locations and corresponding errors in each dimension when using a coarse grid spacing of 200 m and finer grid spacings of 30 and 10 m.  $x_{NLL}$ ,  $y_{NLL}$ , and  $z_{NLL}$  are the coordinates of the estimated location.  $\Delta x$ ,  $\Delta y$ , and  $\Delta z$  are the absolute differences between the NonLinLoc results and actual source locations. The actual source location is at  $x_S = 563$  m,  $y_S = 352$  m, and  $z_S = 2464$  m. . . . . 138

# List of Figures

1.1	The resource triangle. The top of the triangle represents medium- to high-quality reservoirs, which are conventional reservoirs (small volume, easy to develop but difficult to find). The bottom of the triangle shows the unconventional reservoirs (large volume, easy to find but more difficult to develop). (Holditch, 2003; Ma & Holditch, 2015). . . . .	2
1.2	(a) Map view and (b) profile view showing 4 horizontal treatment wells (namely, wells 1, 2, 3, and 4) with stages shown in different colors, vertical and horizontal monitoring arrays denoted by triangles, and treatment locations denoted by hexagrams. . . . .	7
1.3	Number of detected events in 20 treatment stages in the horizontal well 2, (a) recorded by sensors in the horizontal monitoring array, (b) recorded by sensors in the vertical monitoring array. The STA/LTA detection results are shown in blue, and results from the MF method are indicated in other colors representing the different template events. More details on the detection are discussed in Chapter 4. . . . .	8
1.4	A typical microseismic event recorded by sensors in the vertical monitoring array during treatment stage 18 in the horizontal well 2. There are 3 data components: 2 horizontal components shown in green and blue and one vertical component shown in red. . . . .	9
2.1	The study area highlighted by the red star and the tectonic map showing major structural elements that influence the Lower Triassic strata in the NE BC and Peace River Arch areas. Modified from BC Oil and Gas Commission (2021) and Berger et al. (2008). . . . .	21
2.2	Stratigraphic column of the Montney formation and surrounding formations in NE BC (Edwards et al., 1994; Furlong et al., 2018a, 2018b; González et al., 2022; Zonneveld & Moslow, 2018). Modified from González et al. (2022). . . . .	22

2.3	Examples of microseismic data segments (a) a good SNR segment and (b) a noisy data segment. The data have 3 components, with 2 horizontal components indicated in green and blue and a vertical component indicated in red. . . . .	27
2.4	Available well tops and log data measured from 2100 to 2600 m TVD at the vertical monitoring well. . . . .	28
2.5	Completion curves recorded during treatment stage 5 in the horizontal well 2. . . . .	29
3.1	A simple sketch showing a 3C sensor in the vertical borehole. $h_1$ , $h_2$ , and $z$ are three components of the sensor; $E$ , $N$ , and $Z$ denote three directions of the geographical frame corresponding to East, North and Vertical directions, respectively. . . . .	32
3.2	Sensor orientation estimation workflow for vertical-array data. . . . .	33
3.3	Illustration of a) Apparent azimuth $\theta_{app}$ , defined as the angle between the P-wave direction and the horizontal component $h_2$ , b) True azimuth $\theta_{true}$ , defined as the angle between the P-wave direction relative to the North direction, $N$ and $E$ denote the North and East directions of the geographical frame. . . . .	35
3.4	P-wave first motion in the vertical component; $Z_1$ denotes upward motion; $Z_2$ denotes downward motion; AZI denotes azimuth angle, BAZI denotes backazimuth angle; E, W, N, and S denote East, West, North, South directions (Havskov et al., 2009). . . . .	35
3.5	A simple sketch of a 3C sensor deployed in the horizontal borehole. $h_1$ , $h_2$ , and $z$ are 3 components of the sensor; $E$ , $N$ , and $Z$ denote the East, North and Vertical directions of the geographical frame, respectively. Due to the orientation of the well, $h_1$ and $h_2$ are in the (Z, N'S') plane and not in the (Z, North-South) plane. . . . .	37
3.6	Illustration of rotation using a rotation matrix (N and E denote the North and East directions, $h_1$ and $h_2$ , are the two horizontal components of the sensors). . . . .	38
3.7	A simple sketch depicting a sensor in the horizontal borehole. $h_1$ , $h_2$ , and $z$ are 3 sensor components; $E$ , $N$ , and $Z$ are 3 directions, East, North and Vertical, of the geographical frame. After compensating for the orientation of the well, $h_1$ and $h_2$ are positioned in the plane of (Z, North-South). . . . .	41
3.8	Locations of orientation shots and vertical monitoring array. . . . .	45

3.9	a) Unrotated seismic waveforms of one shot recording excited at the shot location 1 and recorded by the first sensor in the vertical array, and b) Hodogram of the two unrotated horizontal components, $h_1$ and $h_2$ , of the first sensor. The result is obtained from the segment containing the most P-wave energy in the unrotated shot recording excited at shot location 1. . . . .	45
3.10	a) Rotated seismic waveforms of the shot recording excited at shot location 1 and recorded by the first sensor in the vertical array and b) Hodogram of the two rotated horizontal components, East-West and North-South, of the first sensor. The result is obtained from the rotated recording excited at shot location 1. . . . .	46
3.11	Different positions of the tool string in the horizontal borehole (ts: tool string). . . . .	48
3.12	a) Unrotated seismic waveforms of a shot recording excited at shot location 1 and recorded by the first sensor in the tool string 2 in the horizontal array, b) Hodogram of the two unrotated horizontal components, $h_1$ and $h_2$ , of the first sensor. The result is obtained from the shot recording excited at shot location 1 and recorded by the first sensor in tool string 2 in the horizontal array. . . . .	48
3.13	a) Rotated seismic waveforms of the shot recording excited at shot location 1 and recorded by the first sensor in tool string 2 in the horizontal array, b) Hodogram of the two rotated horizontal components, East-West and North-South, of the first sensor. The result is obtained from a shot recording excited at shot location 1 and recorded by the first sensor in tool string 2 in the horizontal array. . . . .	50
3.14	a) Seismogram of a raw microseismic event, b) Seismogram of a raw noise, c) Amplitude spectrum magnitude of the event and noise in linear format, d) Amplitude spectrum magnitude of the event and noise in dB format. The black rectangles in c) and d) show the dominant signal frequency range of [60, 300] Hz. . . . .	51
3.15	a) Raw data and b) Filtered data. After filtering, significant enhancement is observed in the data, with a clear microseismic event containing both P- and S- phases in the red rectangle. The P-wave arrives first at about 7.27 s, followed by the S-wave at 7.38 s. . .	52

3.16	The 1D velocity model built from sonic logs. The first track shows the compressional sonic logs (blue curve), the initial Vp model (magenta stair plot), and the final Vp model (orange stair plot). The second track shows the shear sonic logs (grey curve), the initial Vs model (dark-red stair plot), and the final Vs model (green stair plot). The third track shows the number of layers defined from well tops. . . . .	54
4.1	(a) Raw data, (b) Filtered data. After filtering, I can observe significant data enhancement with more visible P- and S-phases (highlighted by the red rectangle). The P-wave onset is at about 7.27 s, followed by the S-wave at 7.38 s. . . . .	67
4.2	Performance of the conventional and recursive STA/LTA. (a) 3C input data (the blue and green represent the two horizontal components, and the red represents the vertical component). (b) STA/LTA ratios obtained from the conventional STA/LTA with a computation time of 1.85 s. (c) STA/LTA ratios obtained from the recursive STA/LTA with a computation time of 0.01 s. . . . .	68
4.3	A 3C template example with clear P- and S-wave onsets at around 0.4 s and 0.5 s, respectively (the blue and green represent the two horizontal components, and the red represents the vertical component). . . . .	69
4.4	Dendrogram illustrating the results of agglomerative hierarchical clustering with 3 main clusters for the potential templates extracted from stage 18, treatment well 2 (recorded by the horizontal array) using the recursive STA/LTA. . . . .	70
4.5	Example of a multiplexed template. After multiplexing, the 3C template (Figure 4.3 is reformatted to a single data stream. I window the template waveform (highlighted by the orange rectangle) to support a more efficient NCC computation. . . . .	71
4.6	(a) Excellent event example. This true event has both clear P- and S-phases. b) A zoom section showing the P- and S-phases (highlighted by the orange and blue rectangles). The data have 3 components, with 2 horizontal components indicated in green and blue and a vertical component indicated in red. . . . .	73

4.7	(a) Probable event example. This true event has unclear P- and clear S-phases. b) A zoom section showing the P- and S-phases (highlighted by the orange and blue rectangles). The data have 3 components, with 2 horizontal components indicated in green and blue and a vertical component indicated in red. . . . .	73
4.8	Example of a noise record picked up by the fast MF. The data have 3 components, with 2 horizontal components indicated in green and blue and a vertical component indicated in red. . . . .	74
4.9	(a) Histogram of the correlation values between potential template events extracted by the recursive STA/LTA and noise randomly selected from the pilot data set. (b) Histogram of the correlation values between pairs of potential template events extracted by the recursive STA/LTA from the pilot data set. . . . .	76
4.10	Examples of (a) a tube wave and (b) an electrical noise record incorrectly identified as true events by the STA/LTA. The data have 3 components, with 2 horizontal components indicated in green and blue and a vertical component indicated in red. . . . .	78
4.11	Detection results of the fast MF and the STA/LTA on the vertical-array data from 78 treatment stages in 4 treatment wells: (a) Well 1, (b) Well 2, (c) Well 3, and (d) Well 4. STA/LTA results are indicated in blue, while the fast MF results using different representative template events are displayed in other colors. Each treatment stage has its own representative template set, either 1, 2, or 3 templates, depending on the repetitiveness of the sources. MF detection results using templates numbered 1, 2, and 3 are shown in red, orange, and green, respectively.	80
4.12	Detection results of the fast MF and the STA/LTA on the horizontal-array data from 40 treatment stages in 2 treatment wells: (a) Well 2 and (b) Well 4. STA/LTA results are indicated in blue, while the fast MF results using different representative template events are displayed in other colors. Each treatment stage has its own representative template set, either 1, 2, or 3 templates, depending on the repetitiveness of the sources. MF detection results using templates numbered 1, 2, and 3 are shown in red, orange, and green, respectively. . . . .	81

5.1	(a) Synthetic data, (b) Synthetic data with bandpass-filtered noise, (c) Gabor spectrogram obtained from the Gabor transform, (d) Gabor spectrogram obtained from the sparse inversion, (e) Waveform reconstructed from the inverted Gabor coefficients. . . . .	93
5.2	(a) Synthetic data, (b) Synthetic data with bandpass-filtered noise, (c) Spectrogram normalized by the noise level, (d) Spectrogram after neighboring block thresholding, and (e) Waveform reconstructed using thresholded coefficients. . . . .	95
5.3	(a) Raw microseismic data with good signal-to-noise ratio, (b) Data with random noise added, (c) Gabor spectrogram from the Gabor transform, (d) Gabor spectrogram from the sparse inversion, (e) Waveform reconstructed from the inverted Gabor coefficients. . . . .	97
5.4	Estimating an appropriate trade-off parameter for the sparse inversion.	98
5.5	(a) Raw microseismic data, (b) Data with random noise, (c) Spectrogram normalized by the noise level, (d) Spectrogram after neighboring block thresholding, and (e) Waveform reconstructed using thresholded coefficients. . . . .	99
5.6	(a) Microseismic data with real noise and added random noise; (b), (c), and (d) Characteristic function computed from the sparse inversion, the neighboring block thresholding technique, and the STA/LTA method, respectively. . . . .	100
5.7	(a) Raw, noisy microseismic data with six events numbered from 1 to 6; (b), (c), (d), and (e) Characteristic function and data computed from the sparse Gabor transform and the neighboring block thresholding method, respectively. Note the changed amplitude range after the application of neighboring block thresholding. . . . .	102
5.8	(a) Original microseismic data, (b) Waveform reconstructed from the sparse inversion, (c) Waveform reconstructed from the neighboring block thresholding. While the sparse inversion preserves the P- and S-waves and the maximum amplitude, changes in P- and S-waves and maximum amplitude are observed in the neighboring block thresholding result. . . . .	103

5.9	Cross plots show the maximum absolute amplitude of the original data and the reconstructed data from (a) the sparse Gabor transform and (b) the neighboring thresholding method. Percent of changes in the maximum absolute amplitudes between the original and reconstructed data from (c) the sparse Gabor transform and (d) the neighboring thresholding method. Note the very different amplitude ranges between the left and right columns. . . . .	105
5.10	Cross plots show the S/P amplitude ratios of the original data and the reconstructed data from (a) the sparse Gabor transform and (b) the neighboring thresholding method. . . . .	106
6.1	A 3D gridded model with each node representing a possible location; $dx$ , $dy$ , and $dz$ are the grid spacings in the x, y, and z dimensions, respectively. . . . .	113
6.2	Illustrative source-receiver configuration with 3 vertical monitoring arrays depicted by open triangles and a true source indicated by the red star. . . . .	122
6.3	Open circles indicate data points computed using a coarse grid spacing of 200 m in each dimension. The filled red circle is where I have the minimum value, and the red star represents the actual source location. . . . .	123
6.4	Filled, blue circles represent the 26 data points neighboring the minimum value (filled, red circle). These 27 grid points are used to solve the unknown coefficients of the quadratic function. . . . .	124
6.5	Interpolation results when using the full 3D quadratic function (equation 6.9) with the illustrative source-receiver configuration on a coarse grid spacing of 200 m in each dimension. a) Interpolated and true data surfaces in the x-y plane. b) Interpolated and true data surfaces in the y-z plane. c) Interpolated and true data surfaces in the x-z plane. . . . .	128
6.6	Interpolation results when using the full 3D quadratic function (equation 6.9) with the illustrative source-receiver configuration on a fine grid spacing of 10 m in each dimension. a) Interpolated and true data surfaces in the x-y plane. b) Interpolated and true data surfaces in the y-z plane. c) Interpolated and true data surfaces in the x-z plane. . . . .	129
6.7	Field-based source-receiver configuration with vertical and horizontal monitoring arrays depicted by open triangles and a true source indicated by the red star. . . . .	134

6.8	Interpolation results when using the simplified quadratic function (equation 6.15) with the field-based source-receiver configuration on a coarse grid spacing of 200 m in each dimension. a) Interpolated and true data surfaces in the x-y plane. b) Interpolated and true data surfaces in the y-z plane. c) Interpolated and true data surfaces in the x-z plane. . .	136
6.9	Interpolation results when using the simplified quadratic function (equation 6.15) with the field-based source-receiver configuration on a fine grid spacing of 10 m in each dimension. a) Interpolated and true data surfaces in the x-y plane. b) Interpolated and true data surfaces in the y-z plane. c) Interpolated and true data surfaces in the x-z plane. . .	137
6.10	Locations of treatment wells and monitoring arrays. The black star symbol indicates the sleeve locations. The black triangle indicates the vertical monitoring array. The horizontal array was on a moving tool string with four positions indicated by blue, cyan, orange, and red triangles corresponding to tool strings 1, 2, 3, and 4, respectively. . .	139
6.11	Residuals of the predicted and observed S-P traveltimes. . . . .	141
6.12	Initial event locations obtained from the grid search method with a grid spacing of 20 m. a) Map view. b) and c) Profile views. . . . .	143
6.13	Interpolated results when applying the interpolation on the grid (grid spacing = 20 m) estimated locations. a) Map view. b) and c) Profile views. . . . .	144
6.14	Initial locations obtained from the grid search method with a grid spacing of 10 m. a) Map view. b) and c) Profile views. . . . .	145
6.15	Interpolated results when applying the interpolation on the grid (grid spacing = 10 m) estimated locations. a) Map view. b) and c) Profile views. . . . .	146
6.16	Location error ellipsoids computed for events obtained from interpolation on the grid (grid spacing = 10 m) estimated locations. a) Map view. b) and c) Profile views. . . . .	147
7.1	Tensile earthquake model, $\Sigma$ is the fault plane, $[\mathbf{u}]$ is the dislocation vector, $\mathbf{n}$ is the fault normal, and $\alpha$ is the slope. Angle $\beta$ is defined as $\beta = (90^\circ - \alpha)/2$ (Vavryčuk, 2011). . . . .	155

7.2	The normalized probability density for S/P amplitude ratios for shear and tensile events based on a uniform sampling of the focal sphere. For a random direction of propagation from the source, a 100% probability of $S/P < 4.617$ are tensile events while only 9.1% probability of $S/P < 4.617$ are shear events (Eaton et al., 2014). . . . .	156
7.3	A 3D view of the acquisition geometry shows two monitoring arrays: vertical and horizontal arrays and a microseismic source. Blue circles represent the sensors in each array, and the orange star indicates the source. . . . .	161
7.4	Upper hemisphere projection of the focal sphere showing the dimensionless normalized P-wave amplitudes and S/P amplitude ratios for a southwest-northeast strike-slip fracture plane for 4 different source mechanisms: $\alpha = 0^\circ$ - pure shear, $\alpha = 30^\circ$ and $45^\circ$ - a combined tensile and shear, and $\alpha = 90^\circ$ - pure tensile. The red stars indicate the sensor locations. . . . .	164
7.5	Hudson's source-type plots showing the inversion results from 50 synthetic amplitude data sets for different mechanisms, from pure shear (a and d), a combined tensile and shear (b and e) to pure tensile (c and f) using different inputs: only P-wave amplitudes in the 3C (green dots), only P-wave amplitudes in the Z component (black dots), both P- and S-wave amplitudes in the Z component (magenta dots), and both P- and S-wave amplitudes in the 3C (blue dots). The big red cross indicates the actual source location. Figure 7.5a, b, c shows the results for data computed using <b>two monitoring arrays</b> . Figure 7.5d, e, f display the results for data calculated using <b>only the horizontal array</b> . (The green points on Figure 7.5d, e, f are not observed as they are in the same places as the black points.) . . . . .	167
7.6	Stereonet plots showing nodal-plane orientation results from moment-tensor inversion of 50 synthetic data sets computed using <b>both vertical and horizontal monitoring arrays</b> for two mechanisms: (a-d) pure shear $\alpha = 0^\circ$ and (e-h) pure tensile $\alpha = 90^\circ$ using different inputs: (a and e) only P-wave amplitudes in the Z component, (b and f) only P-wave amplitudes in 3 data components, (c and g) using both P- and S-wave in the Z component, (d and h) using both P- and S-wave in 3 data components. The great circles correspond to the nodal planes and the shorter dashed lines correspond to rakes. The solid magenta line indicates the true fracture-plane orientation for comparison. . . .	169

7.7	Stereonet plots showing nodal-plane orientation results from moment-tensor inversion of 50 synthetic data sets computed using <b>only the horizontal array</b> for two mechanisms: (a-d) pure shear $\alpha = 0^\circ$ and (e-h) pure tensile $\alpha = 90^\circ$ using different inputs: (a and e) only P-wave amplitudes in the Z component, (b and f) only P-wave amplitudes in 3 data components, (c and g) using both P- and S-wave in the Z component, (d and h) using both P- and S-wave in 3 data components. The great circles correspond to the nodal planes and the shorter dashed lines correspond to rakes. The solid magenta line indicates the true fracture-plane orientation for comparison. . . . .	170
7.8	Source mechanism screening test results using S/P amplitude ratios calculated using data recorded by the (a) vertical and (b) horizontal monitoring q arrays. Tensile events are indicated by blue, and shear events are indicated by orange. The number on top of each bar displays tensile/shear events in each stage. . . . .	173
7.9	Histogram of S/P amplitude ratios computed from the (a) vertical-array and (b) horizontal-array data in stage 11. . . . .	174
7.10	Hudson's source-type plots for visualizing the moment-tensor inversion results of microseismic events in well 2. The inversion results are plotted for every 5 treatment stages: (a) stages 1-5, (b) stages 6-10, (c) stages 11-15, and (d) stages 16-20. . . . .	177
7.11	Examples of three-component waveforms (2 horizontal components shown in green and blue, and one vertical component displayed in red) showing the S-wave segment from treatment stages 1, 11, 18, and 20. For the events in stages 18 and 20, the onsets of the fast S-waves are indicated by pink, and the onsets of the slow S-wave are denoted by black. The S-waves are faster in the horizontal components of the events in stages toward the heel of the well. . . . .	179
8.1	(a) Map view and (b) profile view showing 4 horizontal treatment wells (namely, wells 1, 2, 3, and 4) with stages shown in different colors, vertical and horizontal monitoring arrays denoted by triangles, and treatment locations denoted by hexagrams. . . . .	183
8.2	Number of detected events from data recorded by the vertical monitoring array in 20 treatment stages in treatment well 2. The STA/LTA detection results are shown in blue, and results from the MF method are indicated in other colors, representing the different template events. . . . .	184

8.3	A typical microseismic event recorded by sensors in the vertical monitoring array during treatment stage 18 in the horizontal well 2. There are 3 data components: 2 horizontal components shown in green and blue and one vertical component shown in red. . . . .	185
8.4	Examples of r-t plots with (a) “normal”, (b) “fault reactivation”, and (c) “halted growth” patterns. Black stars denote microseismic events propagating towards the northeast (NE) and red towards the northwest (SW). Yellow, blue, and green lines indicate the start of injection, formation breakdown pressure, and frac hit time (Ortega Perez, 2022).	192
8.5	Time slices of shear wave splitting parameter through the well (a) without and (b) with microseismic events. There is a strong correlation between microseismic events (filled circles with colors representing the treatment stages) and regions with high shear velocity anisotropy (indicated by red) (MacFarlane & Davis, 2015). . . . .	193
8.6	Number of events detected in each treatment stage in well 2 and information on operational problems. The green check mark indicates stages with normal treatment. . . . .	194
8.7	(a) Surface pressure (MPa), (b) Injection rate ( $m^3/min$ ), (c) Treatment duration (min), and (d) Injection energy (KJ) calculated for each treatment stage in well 2. . . . .	195
8.8	Event detection results of (a) vertical-array and (b) horizontal-array data in well 2. STA/LTA results are indicated in blue, while the fast MF results using different representative template events are displayed in other colors. . . . .	197
8.9	Event locations with error ellipsoids computed for events obtained from interpolation on the grid (grid spacing = 10 m) estimated locations. (a) Map view. (b) and (c) Profile views. . . . .	198
8.10	Stress map of the study area. The orientations of the maximum horizontal stress are indicated by black lines with line length proportional to quality (Modified from (Reiter et al., 2014)). . . . .	199
8.11	(a) r-t plot showing the distance of events from the treatment location versus the origin time of the events. (b) A zoom section displaying the r-t plot of events during treatment stages 17-20. . . . .	200
8.12	S/P amplitude ratios result from the vertical-array and horizontal-array data. Tensile events are indicated by blue color; shear events are indicated by orange color. The numbers in the figures show the number of tensile/shear events in each stage. . . . .	201

8.13	Hudson’s source-type plot for visualizing the moment-tensor inversion results of microseismic events in well 2. . . . .	202
8.14	Montney depth trend using available well tops and regional depth trend from tops in nearby wells. All the dashed lines indicate the predicted depth trend obtained from the regional tops using geoSCOUT. All the dotted lines show the depth trend obtained using available well tops in treatment well 2 and the vertical monitoring well. Event locations are superimposed using filled circles with colors indicating different treatment stages. Black triangles indicate the vertical monitoring array and triangles with other colors indicate the horizontal array. . . . .	203
8.15	(a) Gamma ray log plotted along with the trajectory of well 2. The variations in the GR log between treatment stages are highlighted using different colors. (b) Number of detected events in well 2. . . . .	205
8.16	(a) Gamma ray log plotted along with the trajectory of well 1. The variations in the GR log between treatment stages are highlighted using different colors. (b) Number of detected events in well 1. . . . .	206
8.17	(a) Gamma ray log plotted along with the trajectory of well 3. The variations in the GR log between treatment stages are highlighted using different colors. (b) Number of detected events in well 3. . . . .	206
8.18	(a) Gamma ray log plotted along with the trajectory of well 4. The variations in the GR log between treatment stages are highlighted using different colors. (b) Number of detected events in well 4. . . . .	207
8.19	Three-component waveforms of the S-wave of microseismic events from treatment stages 1, 11, 18, and 20. For the events in stages 18 and 20, the onsets of the fast S-waves are indicated by pink and the onsets of the slow S-wave are denoted by black. . . . .	207
8.20	A cross-section of the shear wave splitting parameter through 2 wells (02/07-07 and 00/07-07) in the Montney (MacFarlane & Davis, 2015). . . . .	208

# Chapter 1

## Introduction

### 1.1 Background

#### 1.1.1 Unconventional resources and hydraulic fracturing

Unconventional resources are oil and gas resources trapped in reservoirs with low-to-ultralow permeability, making it difficult to extract the hydrocarbons using traditional methods as in conventional resources (Ma & Holditch, 2015). The unconventional resources typically include tight gas sands, gas shales, heavy oil sands, coalbed methanes, oil shales, and gas hydrates (Ma & Holditch, 2015). These resources are abundant, with approximately 70% of the world's oil and over 100 times more natural gas than conventional reservoirs (McKean, 2017; Smith & Montgomery, 2015). The resource triangle (Figure 1.1) (Holditch, 2003) depicts the abundance of unconventional resources effectively, with a significant portion of the bottom of the triangle considered unconventional reservoirs (Ma & Holditch, 2015).

Unconventional resources require specialized recovery techniques to extract the hydrocarbons (McKean, 2017). For shale plays, horizontal drilling and multistage hydraulic fracturing techniques have been widely applied to enhance oil and gas production (van der Baan et al., 2013). Horizontal drilling allows drainage over a larger well contact area and improves the fluid flow, which is inherently slow in tight reservoirs due to low porosity and permeability (van der Baan et al., 2013). Hydraulic fracturing involves injecting treatment fluids, which are mixtures of water, sand, and

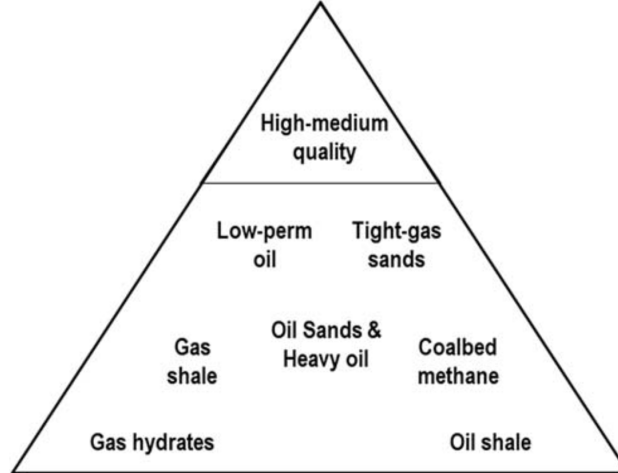


Figure 1.1: The resource triangle. The top of the triangle represents medium- to high-quality reservoirs, which are conventional reservoirs (small volume, easy to develop but difficult to find). The bottom of the triangle shows the unconventional reservoirs (large volume, easy to find but more difficult to develop). (Holditch, 2003; Ma & Holditch, 2015).

chemicals, into the wellbore at high pressure to create new fractures, reactivate existing zones of weakness in the reservoir, and create pathways for the trapped oil or gas to flow to the surface, enhancing the fluid flow rate (Eaton, 2018; van der Baan et al., 2013). The fracturing stimulation process causes changes in local pore pressure and in-situ stress in the rocks, resulting in brittle failures that are recorded as microseismicity (Eaton, 2018; van der Baan et al., 2013).

### 1.1.2 Microseismic data analysis

Microseismic monitoring is crucial in improving the understanding and remote assessment of microseismic activity induced by hydraulic fracturing treatments. It enables the evaluation of treatment efficiency, helps identify operational issues, and provides critical information for understanding fault activation and out-of-zone fracture growth (Eaton, 2018).

In microseismic data analysis, we examine the microseismic signals caused by changes in the local pore pressure and in-situ stress due to fluid injection. These signals are tiny induced earthquakes and often have negative magnitudes ranging

from -2 to 0 (Eaton, 2018), with magnitude detection limits depending on both sensor sensitivity and the hydraulic fracturing site (Maxwell et al., 2008). Microseismic signals are often recorded continuously at high sample rates (e.g., 0.25 ms) over hours, days, or longer by sensitive sensors deployed either downhole or on the surface (Akram & Eaton, 2012). Downhole microseismic recordings typically exhibit lower noise levels compared to surface microseismic recordings, with a difference of up to a factor of 10 (Eisner et al., 2011a). They also have a broader frequency bandwidth (ranging from 15 to over 200 Hz) with multiple modes, including P- and S-waves. Surface microseismic recordings have a more limited frequency bandwidth (ranging from 10 to 70 Hz) with a single mode (P wave only) (Eaton, 2018).

Noise in microseismic data can come from different sources. For example, the impacts of gas bubbles on tools within the wellbore and surrounding formation activities, such as nearby drilling, can contribute to noise (Warpinski, 2009). Noise from the surface, such as nearby seismic surveys and trains, can also affect microseismic recordings (Warpinski, 2009). Downhole microseismic recordings may be subject to tube waves, electrical noise, and random noise, while surface microseismic recordings may be affected by surface waves and random noise.

In this thesis, I analyze downhole microseismic data; thus, I focus on the types of noise prevalent in downhole recordings, such as tube waves and electrical noise. Tube waves are a type of acoustic wave that propagates along the steel-cased borehole (Gadallah & Fisher, 2008). St-Onge and Eaton (2011) demonstrate that on seismograms, they appear as high-amplitude linear events with an apparent velocity of around 1.5 km/s. The tube waves arise from the top of the geophone assembly and can obscure P- and S-wave arrivals (St-Onge & Eaton, 2011). Unlike tube waves, electrical noise is generated by the cabling from the sensors. Maxwell (2014) shows that it usually has a more limited frequency bandwidth than microseismic events. The common mode and harmonics of electrical noise are frequently around 50 or 60 Hz (Maxwell, 2014).

Event detection is one of the crucial aspects of microseismic data analysis. Since being continuously recorded, microseismic data often have noise prevalent in many parts; thus, identifying seismic events in large data sets is time-consuming. Different automated methods have been used for detecting microseismic events. However, many of them, such as the short-time average over the long-time average (STA/LTA) and power spectral density (PSD), are not convenient for big data sets due to the large number of false alarms (Bui & van der Baan, 2020; Bui et al., 2023; Trnkoczy, 2012; Vaezi & van der Baan, 2015). The demand for accelerated, automated detection and selection algorithms is increasing. Also, detection algorithms work more efficiently on data with a good signal-to-noise ratio (Maxwell, 2014); thus, combining signal enhancement with event identification is also essential. Frequency filtering techniques, such as bandpass or highpass filters, are widely used for simplicity, yet under caution of signal distortions (Maxwell, 2014). Algorithms with more complex noise filters that enhance data quality and preserve the microseismic signals are thus more promising (Bui et al., 2023).

Determination of the event hypocenter locations is the next essential step in microseismic data analysis. The event location is a nonlinear problem with four unknowns, including three spatial coordinates of the hypocenter and the event origin time, which is the occurrence time of the initial energy release of a seismic event (Lomax et al., 2009). This step can be challenging since many factors, such as velocity model errors, low data quality with unclear P-/S-phases, uncertainties in arrival time picking, lack of geophone coverage, and changes in anisotropic velocity of the medium, can lead to significant bias in the estimated location (Cipolla et al., 2011; Eisner et al., 2011b; Maxwell, 2014). Various location algorithms have been proposed to estimate event locations with higher accuracy, such as global grid searches, waveform stacking locations, and inversion methods (Bai et al., 2009; Castellanos & van der Baan, 2013; Eisner et al., 2009; Grigoli et al., 2016; Li & van der Baan, 2016; Lomax et al., 2009; Waldhauser, 2001; Zhang et al., 2019; Zhou et al., 2015).

Microseismic data are often large; location algorithms are not only required to estimate event hypocenters with high accuracy but at a preferably low computational cost. For instance, the grid search method can estimate the location using the traveltimes information of P- and S-waves in a straightforward way; however, it is computationally prohibitive when locating events over a large search space with small grid spacing (Bui & van der Baan, 2023; Pike, 2014). Accelerating location algorithms to resolve the efficiency challenge is thus crucial.

Hydraulic fracture networks are often complex in the subsurface, and the recorded microseismic waveforms are highly variable; case studies with integrated analysis of microseismicity, known geology, geomechanics, and treatment data are thus crucial. Numerous case studies on the analysis of microseismicity have been published, such as works by Abdulaziz (2013), De Meersman et al. (2009a), Duhault (2012), Ma and Zoback (2017), and Vermilyen and Zoback (2011). These studies provide practical knowledge for understanding microseismic behavior and hydraulic fracturing performance in the subsurface. With the growth of microseismic monitoring and analysis, new case studies continue to benefit the understanding and interpretation of microseismicity and the fracturing process in the reservoir and surrounding rocks.

### **1.1.3 Geomechanics and induced microseismicity**

Comprehending the geomechanical context in which microseismic events occur and the underlying physical processes is essential for properly interpreting microseismic behavior. Cipolla et al. (2011) shows that the reservoir fluids, the existing stress regime, natural fractures, matrix permeability, and rock properties greatly influence microseismic event patterns. A thorough understanding of the reservoir environment and the mechanism behind microseisms can help constrain the interpretation. According to Cipolla et al. (2011), the causes of microseismic events can be (1) changes in pore pressure, (2) deformation effects, (3) crack propagation or tip effects, and (4) fluid activation of natural fractures or planes of weakness. The leak-off of fractur-

ing fluids from fractures into rock pores and fissures, induced by localized pressure increases within the fracture, can result in pore pressure changes and lead to shear failures (Cipolla et al., 2011; Maxwell, 2014; Warpinski et al., 2004). In unconventional reservoirs with permeability less than 0.01 millidarcy, microseismicity induced by pore pressure changes will be proximal to the hydraulic fracture (Cipolla et al., 2011). The opening of hydraulic fractures can also cause rock deformation, altering stress around the fracture and inducing microseismicity (Cipolla et al., 2011). Tensile and shear stresses generated at the tip of the hydraulic fracture can also result in microseismic events (Cipolla et al., 2011; Shapiro & Dinske, 2009). The existence of natural fractures can also generate microseisms. When hydraulic fractures intersect with natural fractures, fluid entry can alter the effective stress and mechanical properties, resulting in shear failures (Cipolla et al., 2011).

## **1.2 Motivation and contribution**

### **1.2.1 Statement of problem**

This thesis examines an extensive 1.2 terabyte raw microseismic data set induced from 78 hydraulic fracturing treatment stages in 4 horizontal wells in a Montney reservoir in northeastern British Columbia (NE BC), Canada. The microseismic data set was recorded by 3-component (3C) sensors deployed in vertical and horizontal monitoring arrays. Figure 1.2 shows map and depth views of 4 horizontal treatment wells (wells 1, 2, 3, and 4), the two monitoring arrays, and sleeve locations where the hydraulic fracturing stimulation is performed. Each horizontal well has 18-20 treatment stages. The horizontal array moves every 5 treatment stages so it has 4 different locations (tool strings 1, 2, 3, and 4), indicated by 4 different colors. The microseismic activity in these wells behaves anomalously, exhibiting significant variations between treatment stages, with events concentrated near the heel of the treatment wells and hardly any events in the other areas. The underlying causes of

this unusual behavior remain unclear and require investigation.

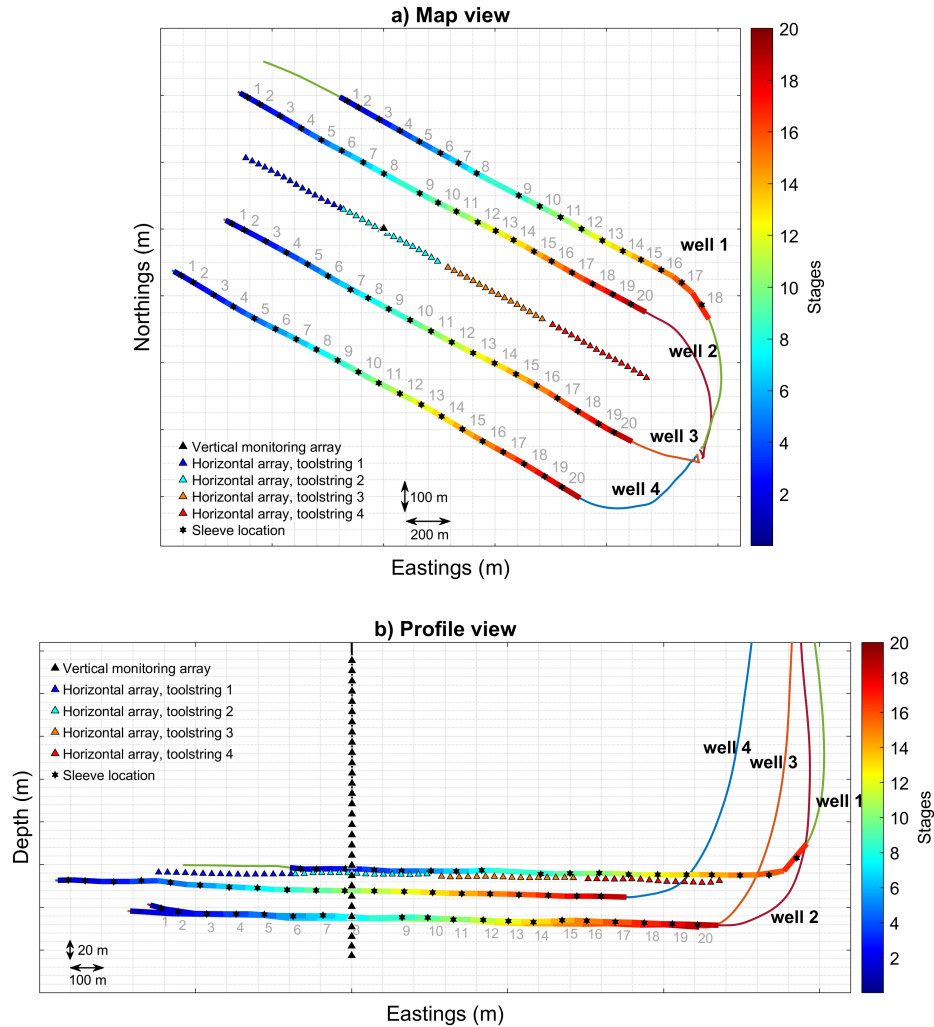


Figure 1.2: (a) Map view and (b) profile view showing 4 horizontal treatment wells (namely, wells 1, 2, 3, and 4) with stages shown in different colors, vertical and horizontal monitoring arrays denoted by triangles, and treatment locations denoted by hexagrams.

Figure 1.3 shows the number of detected events in 20 treatment stages in the horizontal well 2. For comparison, I plot the detection results obtained from 2 methods: the short-time average over the long-time average (STA/LTA), a traditional, incoherent energy detector, and the matched filter (MF), a cross-correlation-based detector. Both detection methods identify approximately 20,000 excellent microseismic events and have a similar event distribution, with stages near the heel of the well observing many events (e.g., up to 1,000 events in stages 18, 19, 20) and stages near the toe of

the well having a few events (e.g., fewer than 50 events in stages 5, 6). Figure 1.4 shows a typical 3C microseismic event recorded by sensors in the vertical monitoring array during treatment stage 18 in the horizontal well 2. Two horizontal data components are shown in green and blue; the vertical data component is displayed in red. Two seismic phases are observed, a P-phase at about 0.21 s and an S-phase at around 0.34 s. More details on the detection methods, implementations, and results are discussed in Chapter 4.

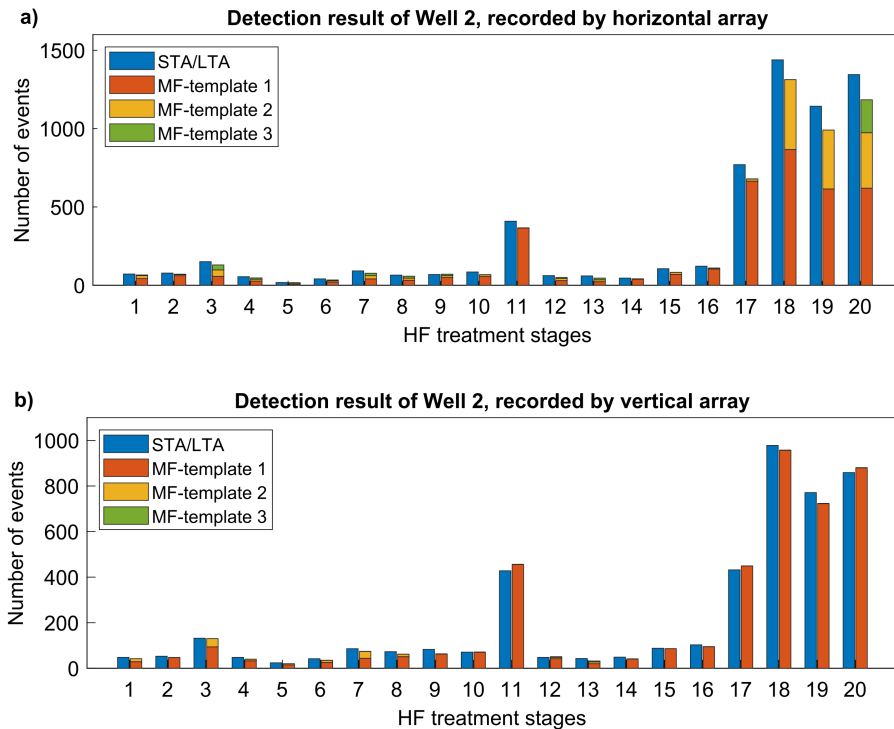


Figure 1.3: Number of detected events in 20 treatment stages in the horizontal well 2, (a) recorded by sensors in the horizontal monitoring array, (b) recorded by sensors in the vertical monitoring array. The STA/LTA detection results are shown in blue, and results from the MF method are indicated in other colors representing the different template events. More details on the detection are discussed in Chapter 4.

## 1.2.2 Research questions

Different hypotheses have been proposed for the leading cause of anomalous microseismic behavior. The event anomaly could be attributed to operational issues, changes in treatment parameters, errors in microseismic data processing, changes in the ge-

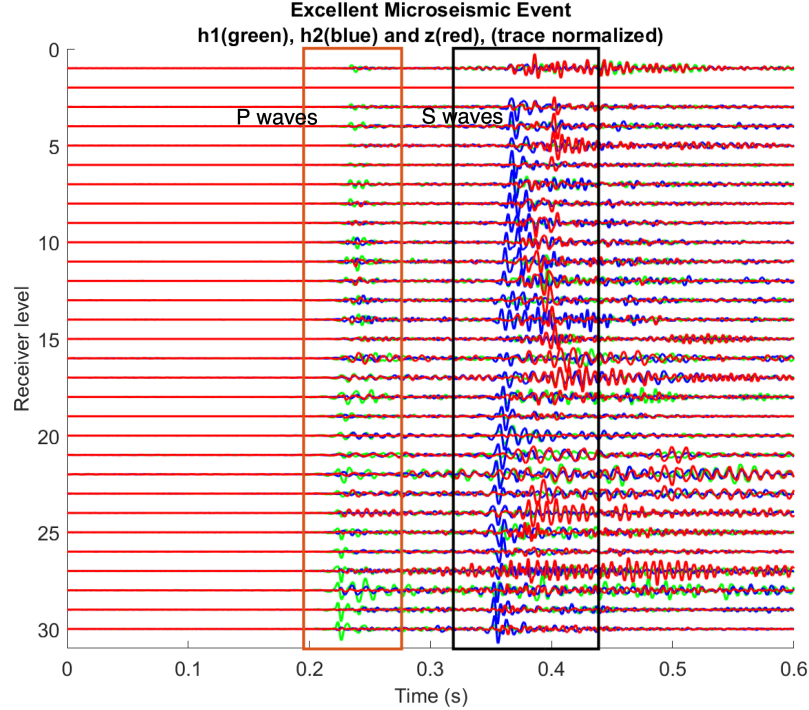


Figure 1.4: A typical microseismic event recorded by sensors in the vertical monitoring array during treatment stage 18 in the horizontal well 2. There are 3 data components: 2 horizontal components shown in green and blue and one vertical component shown in red.

omechanical properties of the medium or the existence of natural fractures/faults.

First, I investigate if any operational issues require the cessation of the fracturing treatments that link to the unusual microseismic behavior between stages. In hydraulic fracturing, the brittle failures induced by the stimulation are recorded as microseismicity by sensitive sensors in nearby monitoring arrays (Eaton, 2018). A typical fracturing treatment is aimed to create hydraulic fractures in the rocks and thus is expected to observe many microseismic events. Treatments with operational issues where fractures cannot get breakdown and monitoring arrays are shut down might correlate to less active microseismicity in some stages. To answer this question, I study the treatment records of every fracturing stage from available fracturing observer notes and completion reports and identify any issues that occurred during frac operations along with their impacts on microseismic activity.

For example, a screen-out condition can happen during the treatment and cause a rapid rise in the pump pressure, which exceeds the safe-operating parameters of the wellbore and wellhead equipment (Maxwell, 2014). When the screen-out condition occurs, the fracturing operation needs to be ceased, and monitoring arrays are shut down to have time for flow back to clean any obstructions. Screen-out conditions will lead to lost production time due to added steps and affect hydraulic fracturing creation/reactivation and microseismic recording. Supposing multiple operational issues happen during the treatment and impact the microseismicity, I further question if these problems are the leading cause of the event anomaly or just a contributing factor. In that case, I consider if the event anomaly strongly correlates with issues during operations, if any stages with normal treatment operation have few events, and whether any stages with a substantial number of events have operational issues or vice versa.

Second, I investigate if the anomalous behavior of microseismicity relates to changes in any treatment parameters, such as breakdown pressure (the pressure at which the rock formation breaks and creates fractures (Tariq et al., 2021; Warpinski et al., 2004), injection (slurry) rate, and treatment duration. I analyze the completion data to see if a poor injectivity rate could lead to fewer events and if stages having a lower treating pressure are easier for fractures to get breakdown and induce more events. To address these questions, I calculate the injection energy for every treatment stage and compare it with the number of events detected in each stage. The injection energy is the total energy put into the fracturing system, which is the product of the treatment duration, the average surface pressure, and the injection rate (Boroumand & Eaton, 2012). The injection energy will reflect if a low injection rate, a high surface pressure, or a longer treatment duration is associated with an event anomaly.

Third, I examine whether the abnormal microseismic behavior originated from inefficient detection algorithms that produce many false alarms (when noise is incorrectly detected as a potential event) and missed events (when the event occurs, but

the detector does not detect it) (Bui & van der Baan, 2020). Traditional automated triggering-based detectors such as the STA/LTA method have detection performance depending strongly on the setup parameters, including lengths of the short and long windows used for calculating the STA/LTA ratio and the detection threshold. The STA/LTA with a very low detection threshold can trigger many false alarms. Using only one detection algorithm may lead to biased results; for instance, a too-low detection threshold can lead to many false alarms or careless event classification can result in wrongly classified potential events. I thus investigate different detection methods, including the STA/LTA and the cross-correlation-based matched filter. Traditional detectors often filter noise using simple frequency filterings, such as bandpass or high-pass filters, which might be inefficient. I therefore study the detection performance statistics of algorithms that combine signal enhancement with automated event detection and selection.

Fourth, I investigate whether the event anomaly is associated with changes in the geomechanical properties of the medium or the presence of existing fractures/faults. The horizontal treatment wells could travel in and out of zones with lateral variation in lithology, which can influence the behavior of microseismicity. Also, if the rocks have natural fractures/faults or zones of weaknesses, in that case, hydraulic fractures can intersect with these pre-existing fractures, and fluid entry can alter effective stress and mechanical properties, leading to microseismicity (Cipolla et al., 2011; Maxwell, 2014). To address this question, I locate the event hypocenters, estimate their source mechanism, and perform an integrated analysis of locations, moment tensors, and known geomechanics of the study area from published resources. Uncertainties in input data arise from many sources (i.e., arrival time picking, choice of velocity model, and limited acquisition geometry) and have a combined effect on the hypocenter estimates; thus, careful data processing and exploration of parameter space can reduce hypocentral uncertainty. Here, the data set is extensive, and I need to optimize the algorithms to efficiently process and perform integrated analysis of event locations

and source mechanisms. The integration reveals unusual spatial patterns of microseismicity and provides more reliable interpretations when incorporated with known geomechanics.

### 1.2.3 Thesis objectives

First, this thesis aims to identify the primary causes of the anomalous behavior of microseismicity between treatment stages observed in the big data set from the Montney treatments in NE BC, Canada. Different hypotheses are considered, including operational issues such as poor stage isolation and screen-out condition, treatment parameters such as poor injectivity rate, data processing problems such as false triggers generated by detection algorithms, changes in the geomechanical properties of the medium such as the lateral-facies variability, and the presence of pre-existing faults. Knowing the reasons behind the substantial variations of microseismicity between stages can help optimize the hydraulic fracturing stimulation, enable the treatment effectiveness and efficiency, and further increase the oil and gas production.

Second, I focus on improving automated processing algorithms and workflows for big, noisy microseismic data sets. Microseismic signals, which are tiny earthquakes with negative magnitudes, are often embedded in noisy and continuous recordings. Traditional detection methods often require substantial manual labor in event identification and selection. I aim to build a fast matched filter algorithm to accelerate the detection process and generate a higher detection probability, resolving the efficiency challenges of generic detectors. Since microseismic signals are non-stationary, I also investigate time-frequency detection approaches, including the sparse Gabor transform and the neighboring block thresholding, which combine signal enhancement with automated event detection and selection. I also focus on enhancing the event location performance by combining the grid searches and a quadratic interpolation technique to resolve the computational challenge of the grid searches and speed up the event location refinement.

### 1.2.4 Main contribution

The advancements in microseismic monitoring provide insightful understandings of the subsurface as well as the performance and effects of hydraulic fracturing operations. However, the large volume of recorded data and the variability of microseismic signals continue to pose significant challenges in efficiently and accurately processing and analyzing microseismic data. In addressing these challenges, this thesis contributes to improving automated processing algorithms and workflows for big microseismic data sets and performing an integrated analysis of microseismic processing results, treatment data, and geomechanics in understanding the underlying causes of the event anomaly in the extensive microseismic data set. The main contributions are listed below.

The first contribution is the development of a fast and efficient matched filter algorithm for detecting microseismic events in large data sets. The algorithm accelerates the detection process by using a fast normalized cross-correlation computation technique and yields a higher precision rate with fewer false alarms than the commonly used STA/LTA method. I implement this algorithm on a raw microseismic data set with nearly 20,000 events detected on two monitoring wells, demonstrating its usefulness and suitability in detecting events in big data sets (Bui & van der Baan, 2020).

Second, I investigate two time-frequency methods that combine signal enhancement with automated event detection and selection: the sparse Gabor transform and the neighboring block thresholding (Bui et al., 2023). The analysis shows that the sparse Gabor transform is more promising than the neighboring block threshold technique, with enhanced detection capability, improved data quality, and preserved absolute and relative amplitudes of the P- and S-phases of the signals.

Third, I build a quadratic interpolation technique to accelerate the grid searches over large search spaces and refine the event locations (Bui & van der Baan, 2023).

The quadratic interpolation technique performs well on both synthetic and real microseismic data examples, typically leading to similar event locations as those obtained from the grid search using 10 times smaller grid spacings in all three directions, at a minor additional computational expense, and without the need to generate travel-times at new spatial positions.

The fourth contribution is the presentation of a complete processing workflow implemented on an extensive, raw, downhole microseismic data set, from sensor orientation and data rotation to moment tensor inversion. Details of algorithms and implementations provide a comprehensive example for microseismic analysts in processing and analyzing raw microseismic data.

Finally, I present an integrated analysis of a Montney treatment, incorporating microseismic processing results, analysis of treatment data, and geomechanics. The integrated approach provides an insightful understanding of the leading causes behind the abnormal behavior of microseismicity between treatment stages. The analyses show that operational issues, changes in treatment parameters, and data processing are not the primary causes of the event anomaly. Geological and geomechanical changes are most likely linked with anomalous microseismic behavior.

### **1.3 Thesis overview**

**Chapter 2** shows the geological setting of the Montney reservoir in NE BC in the study area and the data background. Details of different geological units, lithological properties, thickness trend of the Montney in the study area along with a summary of hydraulic fracturing operations are presented. This chapter describes different types of data, including microseismic data, geophone geometry, well logs and treatment data, used in the following chapters on event detection, location, and source mechanism estimation and integrated analysis of the Montney treatment to understand the leading causes of the event anomaly.

**Chapter 3** describes preprocessing steps for the raw, extensive 1.2 tetrabytes,

downhole microseismic data, including sensor orientation estimation and data rotation in the vertical and horizontal boreholes, noise attenuation, and velocity model building. The horizontal boreholes impose more challenges in sensor orientation estimation than the vertical boreholes; however, the combined use of horizontal and vertical observation wells leads to better ray coverage, translating into generally better-resolved locations. The signal preconditioning step reduces the unwanted noise and enhances the data quality, facilitating detection algorithms to work more efficiently. The velocity model derived from well logs and available well tops is indispensable for the event location step, which is used to calculate the predicted traveltimes of the P- and S-waves and estimate the most likely hypocentral locations.

**Chapter 4** presents a fast matched filter (MF) implementation that can solve the efficiency challenge for traditional automated triggering-based detectors. In this implementation, I combine a recursive STA/LTA for the extraction and selection of representative template events, a multiplexing technique for reformatting the data and utilizing parallel computation, and a fast normalized cross-correlation (NCC) technique to accelerate the event detection process. The fast NCC technique employs summed-area tables to calculate the NCC coefficients between the template events and the data which is about 450 times faster than the normal NCC computation while generating the same results. The fast MF workflow identifies about 20,000 excellent microseismic events in both vertical and horizontal monitoring arrays from the entire data set of 4 treatment wells. It works well with the large data set, showing a higher detection probability and fewer false alarms, and does not require substantial manual selection of desired events as in the STA/LTA. The detection results reveal similar characteristics between treatment wells, with the majority of events concentrated towards the well's heel.

**Chapter 5** examines two time-frequency methods which combine signal enhancement with automated event detection and selection, including the sparse Gabor transform and the neighboring block thresholding. Although automated triggering-based

algorithms can detect many potential events in the data, their precision rates are often low and they require substantial manual labor to select desired events of interest. The time-frequency methods use thresholding in the time-frequency domain to increase signal enhancement, then use an energy detection criterion which improves event detection with higher precision rates. The analyses indicate that the sparse Gabor transform is more promising in enhancing event detection since this method attenuates the noise significantly while preserving the signals.

**Chapter 6** presents a quadratic interpolation technique that speeds up the event location of the grid searches over large search spaces, resolving the computational challenge of the grid search method. Synthetic examples show that this method performs well, leading to similar event locations as those obtained using 10 times smaller grid spacings in all three directions, at a minor additional computational expense, and without the need to generate traveltimes at new spatial positions. I then employ the quadratic interpolation on the coarse-grid-estimated location of over 1000 microseismic events in 20 stages in a treatment well to speed up the location refinements.

**Chapter 7** focuses on moment tensor inversion analysis of over 1000 microseismic events in 20 stages in a treatment well using amplitude-based methods. First, synthetic amplitudes are used to examine the acquisition geometry effects on the inversion and test different input parameters to find the best inversion scheme. Then, a source mechanism screening test using S/P amplitude ratios is applied to quickly allow the first classification of shear and tensile events. After that, the screening test results are compared with the full moment tensor inversion of the microseismic events using P- and S-wave amplitudes in all three data components from both monitoring arrays. The analysis reveals different moment tensor characteristics depending on the stages, indicating that event anomaly might be related to a geological/geomechanical role.

**Chapter 8** presents an integrated analysis of over 1000 microseismic events in 20

stages in a treatment well to understand the underlying causes of the substantial variations in microseismicity between stages. Operational issues, changes in treatment parameters, event locations, distance-time (r-t) plots, source mechanisms, variations in lithology are incorporated. The analyses show that operational issues, changes in treatment parameters, and data processing are not the leading causes of the event anomaly. Geological and geomechanical changes are most likely linked with anomalous microseismic behavior.

**Chapter 9** concludes the thesis with key findings and provides suggestions for future research.

# Chapter 2

## Geological setting of the study area and data background

### Summary

The microseismic data used in this thesis are recorded during hydraulic fracturing treatments in 4 horizontal wells targeted at the Lower and Middle Montney formation in northeastern British Columbia (NE BC), Canada. This chapter gives an overview of the geological setting of the study area, microseismic data, supplementary data used for the implementations of processing algorithms and an integrated analysis presented in chapters 3 through 8. This chapter also highlights the objectives of data processing and analysis.

### 2.1 Introduction

This chapter presents the geological framework of the study area, which is located in the Montney formation in NE BC, Canada. The Montney formation, an early Triassic-aged formation, extends over a large continuous area of approximately 130,000  $km^2$  of NE BC and west-central Alberta (AB) in the Western Canada Sedimentary Basin (WCSB) (BC Oil and Gas Commission, 2021; Playter et al., 2018; Zonneveld & Moslow, 2018). Since the 1950s, exploration activities for oil and gas in the Montney were restricted to vertical drilling for conventional resources such as shoreface clastic/bioclastic units and turbidite sandstone/siltstone deposits (Davies et al., 2018;

González et al., 2022; Moslow, 2000). It was later discovered that the unconventional resources hosted in bituminous siltstone, fine to very fine-grained sandstone and bioclastic packstone/grainstone hold greater potential (Zonneveld & Moslow, 2018). Recent exploration efforts have targeted these fine-grained intervals in the Montney, particularly in NE BC and westernmost AB (Zonneveld et al., 2011). With advancements in horizontal drilling and multistage hydraulic fracturing, the Montney formation has evolved from a conventional oil and gas play to one of North America's leading unconventional plays, with expected 449 trillion cubic feet of marketable natural gas, 14,521 million barrels of marketable natural gas liquids, and 1,125 million barrels of marketable oil (BC Oil and Gas Commission, 2012; González et al., 2022; National Energy Board, BC Oil and Gas Commission, Alberta Energy Regulator and BC Ministry of Natural Gas development, 2013; Zonneveld & Moslow, 2018).

This chapter also provides an overview of the data used in processing case studies and analyses in the following chapters. Hydraulic fracturing operations, microseismic and miscellaneous data, and data analysis objectives are described. I first summarize the hydraulic fracturing operations, with 78 treatment stages carried out in 4 horizontal treatment wells in the Montney formation in NE BC, and the microseismic data induced by the hydraulic fracturing activities. Over 300 hours of microseismic data continuously recorded by 3-component (3C) sensors in vertical and horizontal monitoring arrays were provided. Then, I describe various treatment and completion data types, such as breakdown pressure, injection rate, treatment duration, proppant concentration, completion curves, and fracturing observer notes. Well data, including well tops and logs, are also presented. Finally, I outline the objectives of the data usage in the processing case studies and analysis in the following chapters.

## 2.2 Geological setting of the study area

### 2.2.1 Study area and tectonic setting

The study area is in the Montney formation in NE BC, located south of the Fort Saint (St.) John Graben and northeast of the Canadian fold and thrust belt (Berger et al., 2008). Figure 2.1 shows the location of the study area (highlighted by the red star) and major structural elements that influence the Lower Triassic strata in the NE BC and Peace River Arch areas. Berger et al. (2008) generates the map by integrating high-resolution aeromagnetic data with seismic and well data. According to Berger et al. (2008), faults within the NE BC and Peace River Arch areas can be categorized into three types: (1) deep-seated basement faults (in red) that may follow significant terrain boundaries (e.g., the Hay River Shear Zone) or develop along major basement features within the same basement terrain (e.g., the Rycroft and Dunvegan faults); (2) a series of faults exhibiting the structural style of divergent wrench fault systems (in blue), consisting of “pull-apart” basins, asymmetrical grabens, and weakly developed “failed arm” features that may be related to a Proterozoic rift system reactivated during the Palaeozoic time which culminated during the Mississippian collapse of the Peace River Arch and the formation of the Fort St. John Graben; and (3) younger and shallower faults (in green) that formed during the development of the thrust belt and the adjacent foreland basin.

### 2.2.2 Geology of Montney formation

The Triassic-aged Montney formation, a significant stratigraphic unit in the WCSB, covers approximately 130,000  $km^2$ , extends through a vast area of NE BC and west-central Alberta (BC Oil and Gas Commission, 2021; Golding et al., 2014; Playter et al., 2018; Zonneveld & Moslow, 2018). Although the Montney primarily represents a Lower Triassic stratigraphic unit, it records deposition from the (latest) Permian to just before the Middle Triassic, with an interval spanning approximately 5 million

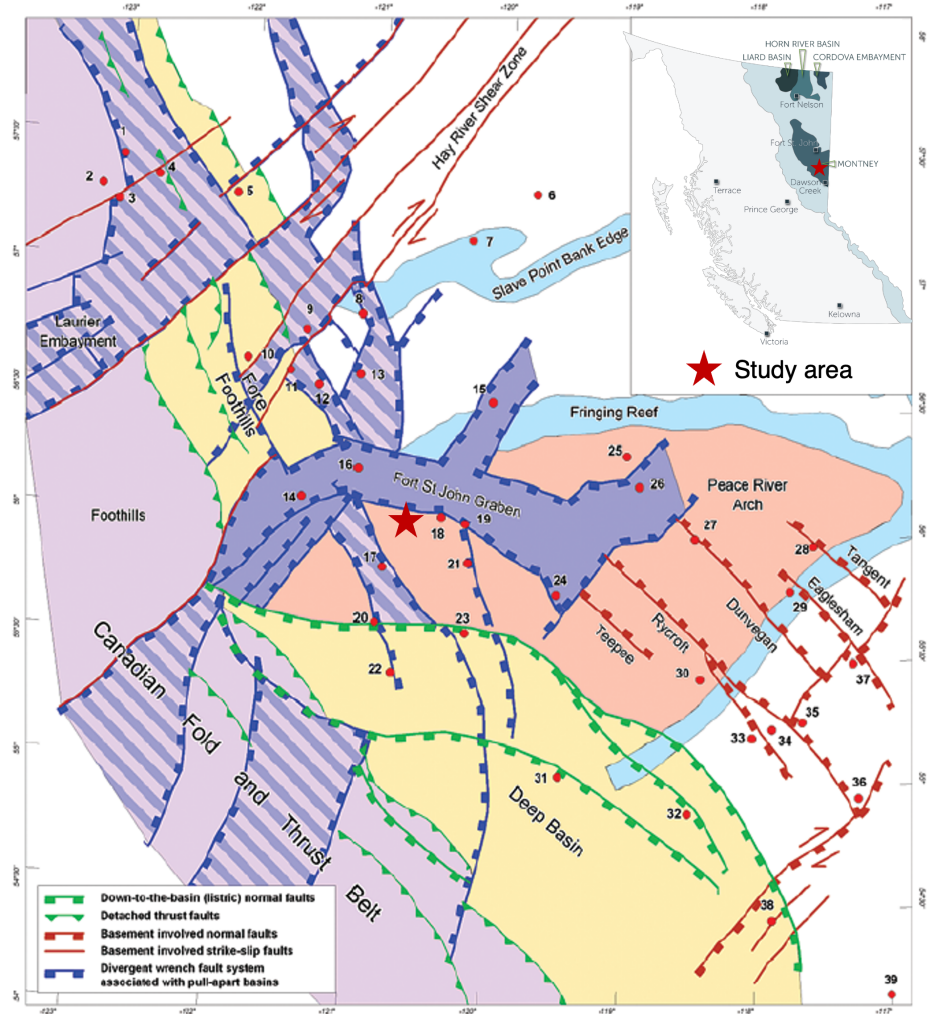


Figure 2.1: The study area highlighted by the red star and the tectonic map showing major structural elements that influence the Lower Triassic strata in the NE BC and Peace River Arch areas. Modified from BC Oil and Gas Commission (2021) and Berger et al. (2008).

years (Davies et al., 2018; Henderson, 1997; Moslow et al., 2018). Figure 2.2 shows the stratigraphic column of the Montney formation and surrounding formations in NE BC (Edwards et al., 1994; Furlong et al., 2018a, 2018b; González et al., 2022; Zonneveld & Moslow, 2018). The base of the Montney formation is placed at the top of the Paleozoic Era, overlying an erosional unconformity on Permian Belloy formation (González et al., 2022; Zonneveld & Moslow, 2018). The top of the Montney formation is typically characterized by an erosional boundary, characterized by the *Glossifungites* Ichnofacies and/or a phosphatic conglomerate lag overlain by the Sun-

set Prairie formation or Triassic Doig formation (Davies et al., 1997; Furlong et al., 2018a, 2018b).

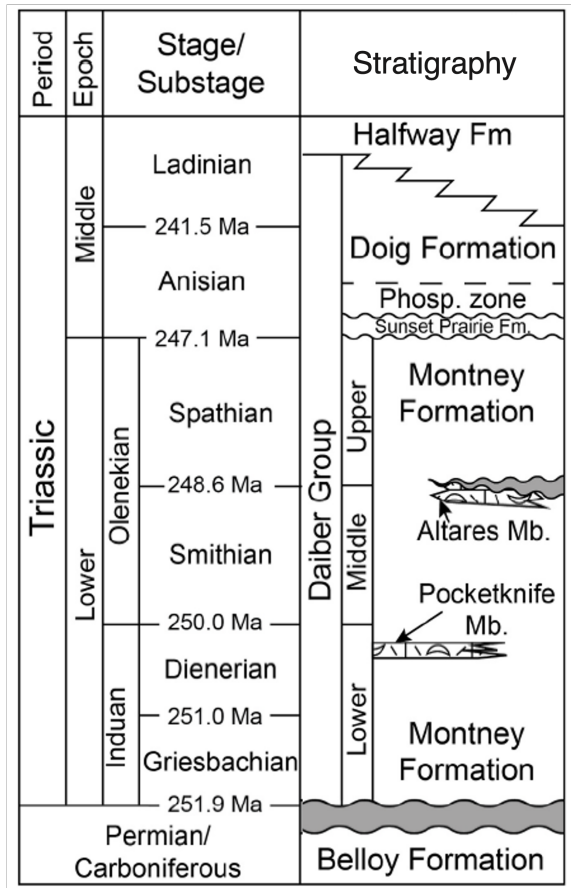


Figure 2.2: Stratigraphic column of the Montney formation and surrounding formations in NE BC (Edwards et al., 1994; Furlong et al., 2018a, 2018b; González et al., 2022; Zonneveld & Moslow, 2018). Modified from González et al. (2022).

According to Zonneveld et al. (2011), the Montney formation is a complex sequence dominated by siltstone and sandstone, although shale and bioclastic packstone/grainstone are also present in some areas and intervals. The Montney records deposition on a shallow clastic ramp setting, with the thickest accumulation occurring in the vicinity of the collapsed Peace River Arch (Crombez et al., 2016; Zonneveld et al., 2010b, 2011). Various depositional environments characterized deposition within the Montney formation, including distal offshore successions, such as turbidite channel and fan complexes, and lower to upper shoreface deltaic intervals and estuarine suc-

cessions (Davies et al., 1997; Moslow, 2000; Zonneveld et al., 2010b, 2010a, 2011). According to Zonneveld et al. (2011), most Montney successions are dominantly fine-grained clastic deposition, including siltstone or very fine-grained sandstone (e.g., very little sand coarser than 125  $\mu\text{m}$ ). Diagenetic clay mineral deposition was not favored in Montney successions due to environmental conditions, including the aridity of the depositional region and long transport distances from sediment source areas (Zonneveld et al., 2011).

The Montney formation can be divided into Lower, Middle, and Upper units based on basin-wide unconformities that coincide with major stratigraphic boundaries (Dienerian-Smithian and Smithian-Spathian) (Zonneveld & Moslow, 2018). The Lower Montney, which is of Griesbachian-Dienerian age, is widespread in the WCSB (Golding et al., 2014; Moslow et al., 2018; Zonneveld & Moslow, 2018). The type core in BC mainly comprises fine to medium-grained laminated bituminous dolomitic siltstone and calcispheric dolosiltstone, along with thin (2.5 to 20 cm) very fine-grained sandstone interbeds (Zonneveld & Moslow, 2018). The Middle Montney is Smithian age and comprises a thick sequence of bituminous dolomitic siltstone, with interbeds of very fine-grained sandstone (Golding et al., 2014; Moslow et al., 2018; Zonneveld & Moslow, 2018). The Upper Montney is Spathian age and consists of a thick succession of fine- to coarse-grained, sandy, bituminous, dolomitic siltstone with subordinate very fine-grained sandstone, which locally becomes dominant towards the top (Golding et al., 2014; Zonneveld & Moslow, 2018). In some parts of BC, a bioclastic carbonate interval exists, known as the Altares Member; it occurs laterally to and interfingers with the Middle Montney (Zonneveld & Moslow, 2018). The Upper Montney is Spathian age and consists of a thick succession of fine- to coarse-grained, sandy, bituminous, dolomitic siltstone interbedded with subordinate very fine-grained sandstone, which locally becomes dominant towards the top (Golding et al., 2014; Zonneveld & Moslow, 2018). Throughout much of NE BC, the Upper Montney overlies the Altares Member at the Smithian/Spathian boundary and is un-

conformably overlain by the Sunset Prairie formation (Zonneveld & Moslow, 2018).

The Montney formation is westward-thickening, thinning to 0 m at its eastern and northeastern edges while increasing to over 300 m on its western side (Chalmers et al., 2011; Golding et al., 2014; González et al., 2022; Zonneveld & Moslow, 2018). In NE BC, the Montney formation consists of interbedded successions of fine- and coarse-grained siltstone, very fine-grained sandstone, and bioclastic siltstone intervals (González et al., 2022). Unconventional plays within the fine-to-coarse-grained siltstone beds in NE BC have become critical components of Canada’s hydrocarbon inventory (González et al., 2022). However, it is essential to note that the lithostratigraphy of the Montney in this area has many complexities associated with the subtle grain-size variation, diminutive biogenic structures, lateral-facies variability, and distribution of local discontinuities (González et al., 2022). Heterogeneities related to grain size, physical sedimentary structures, and biogenic structures impact the reservoir quality (Gegolick, 2017; Ghanizadeh et al., 2018; González et al., 2022). González et al. (2022) also stresses that these rocks exhibit small-to-large-scale heterogeneities and, in some intervals, are characterized by thin interbeds of rheologically anisotropic properties that can potentially affect the drilling and completion of such targets. Understanding the lateral-facies variability and overall stratigraphic architecture of the Montney formation in NE BC is crucial for delineating its variable characteristics vertically and laterally (González et al., 2022) and, in turn, aiding in the interpretation of microseismic activity emitted from hydraulic fracturing treatments.

## **2.3 Hydraulic fracturing operations**

Hydraulic fracturing (HF) stimulation was performed from 15<sup>th</sup> July to 04<sup>th</sup> August 2015 in 4 horizontal treatment wells (Figure 1.2, Chapter 1). The targeted formations are the Lower and Middle Montney in an oil and gas field in NE BC. The open-hole completion technique with sliding sleeves was used for all treatment wells, where the injection was performed with no isolation between the borehole and the formation.

Hydraulic fractures in this type of completion tend to initiate along preexisting fractures, and the injection is designed to distribute fractures along the open-hole length (Maxwell, 2014). In this study, the HF was performed in 18-20 stages along the open-hole section of 4 horizontal wells. The HF treatments in these wells were carried out using a slickwater stimulation fluid plus sand proppant. For each fracturing stage, the peak treatment pressure is approximately 63 MPa.

## 2.4 Microseismic data

A total of 78 hydraulic fracturing treatments were performed in 4 horizontal wells. Microseismic data emitted from the treatments were recorded continuously at a high sampling rate of 0.25 ms over 326 hours from 15<sup>th</sup> July to 04<sup>th</sup> August 2015 by 3C sensors deployed in two monitoring wells (Figure 1.2), with the vertical monitoring array having 30 sensors and the horizontal monitoring having 16 sensors. Sensors in the vertical monitoring array were deployed on a fixed-position tool string with an equal spacing of 10 m. In contrast, sensors in the horizontal monitoring array were deployed 30 m equally spacing on a moving toolstring which moved every 5 treatment stages.

Figure 1.2 also depicts 4 different locations of the horizontal array, named by toolstrings 1, 2, 3, and 4. The vertical array was deployed between 1361.7 and 1706.8 m true vertical depth sub-sea (TVDSS, defined as the depth measured vertically from the sea level to a certain target downhole). The horizontal array was deployed at approximately 1645 m TVDSS. The true vertical depth (TVD, defined as the depth measured vertically from a point in the well, often the kelly bushing elevation, to a certain target downhole) is the sum of TVDSS and kelly bushing elevation. The vertical monitoring well has a kelly bushing elevation of 846.3 m; thus, the TVD of the vertical monitoring array ranges from 2208 to 2553 m. The horizontal treatment and monitoring wells belong to the same well pad with a kelly bushing elevation of 819.6 m; thus, the TVD of the horizontal monitoring array is at about 2464.6

m. The targeted Lower and Middle Montney units in the study area have TVD at approximately 2460-2485 m (Middle Montney) and 2500-2520 m (Lower Montney). Wells 1 and 4 targetted the Middle Montney, and wells 2 and 3 targetted the Lower Montney. The microseismic data induced by treatments in wells 2 and 4 were recorded by both monitoring arrays, while the data from wells 1 and 3 were recorded by the vertical monitoring array only.

The given microseismic data set is raw in SEG-2 format and about 1.2 terabytes. Figure 2.3 shows examples of raw microseismic data segments, one with a good signal-to-noise ratio (SNR) (Figure 2.3a) and another exhibiting more noise (Figure 2.3b), recorded by 30 sensors in the vertical monitoring array. There are 3C data with two horizontal components shown in green and blue and a vertical component shown in red. Overall, the recordings have good data quality, with 29 of 30 sensors recording the waveforms, although many parts of the data contain noise due to being continuously recorded.

## 2.5 Miscellaneous data

In addition to the microseismic data field files, supplementary information regarding geophone geometry is available, including the geophone positions and surface dynamite shots used for estimating geophone orientations. There are 4 dynamite shot locations with corresponding trace data in the SEG-2 format. The trajectory of treatment and monitoring wells are also available. Well tops and log data, including caliper, density, P-sonic, S-sonic, and Gamma-ray logs measured at the vertical monitoring well, are also provided (Figure 1.2). Figure 2.4 shows a portion of log data measured at the vertical monitoring well from 2100 to 2600 m TVD. The well tops are shown on the fifth column from left to right, with the Upper Montney at 2289.8 m TVD, the Middle Montney at 2469.6 m TVD, and the Lower Montney at 2552.7 m TVD. The top of the Montney in the study area is overlain by the Doig phosphate zone and the Triassic Doig formation. The base of the Montney is at 2593.7 m TVD.

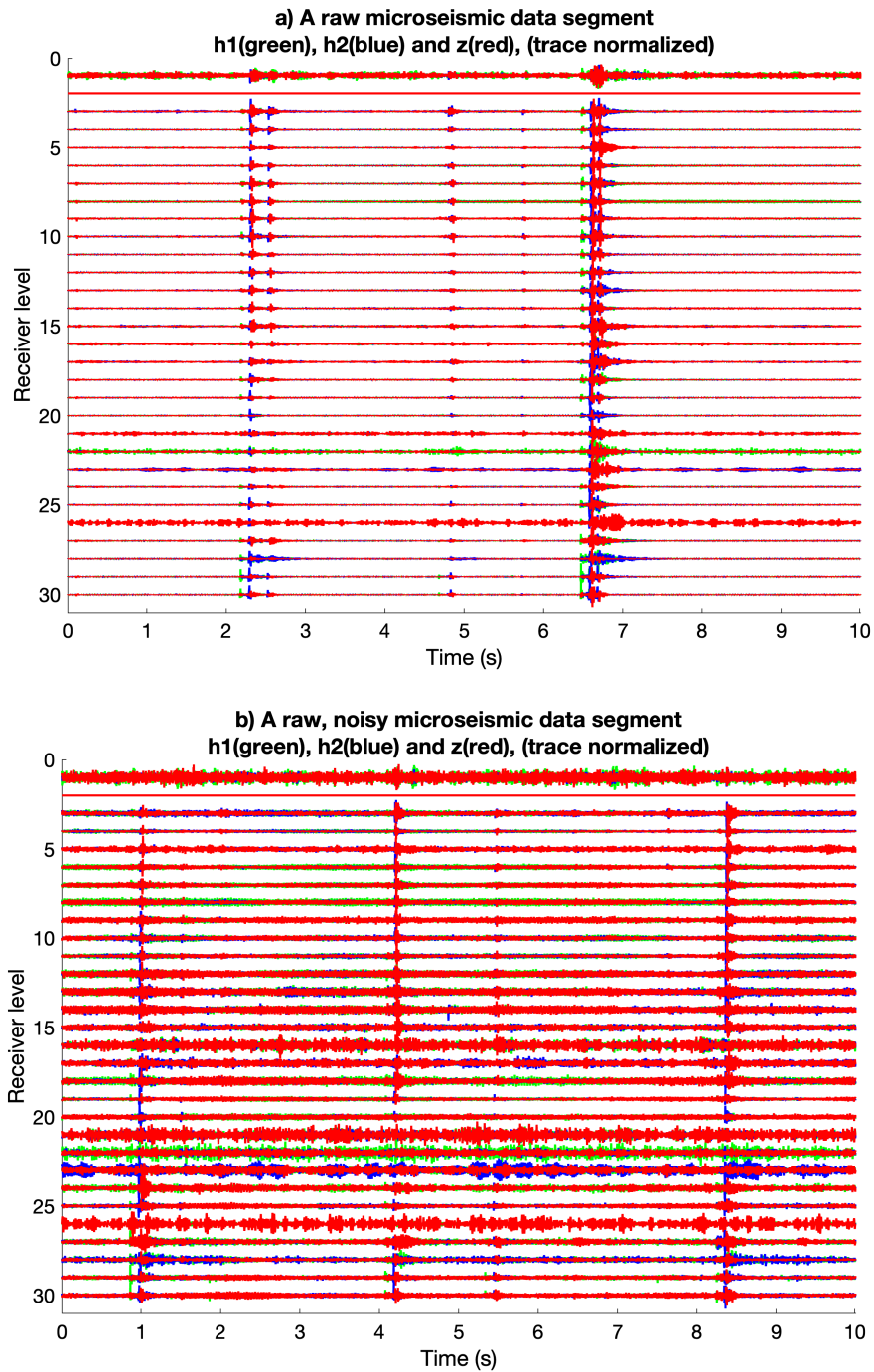


Figure 2.3: Examples of microseismic data segments (a) a good SNR segment and (b) a noisy data segment. The data have 3 components, with 2 horizontal components indicated in green and blue and a vertical component indicated in red.

Furthermore, I have treatment data, including completion curves and fracturing reports. Figure 2.5 shows the completion curves, showing information on pressure, proppant concentration, and injection rate, recorded during treatment stage 5 in the

horizontal well 2 (Figure 1.2).

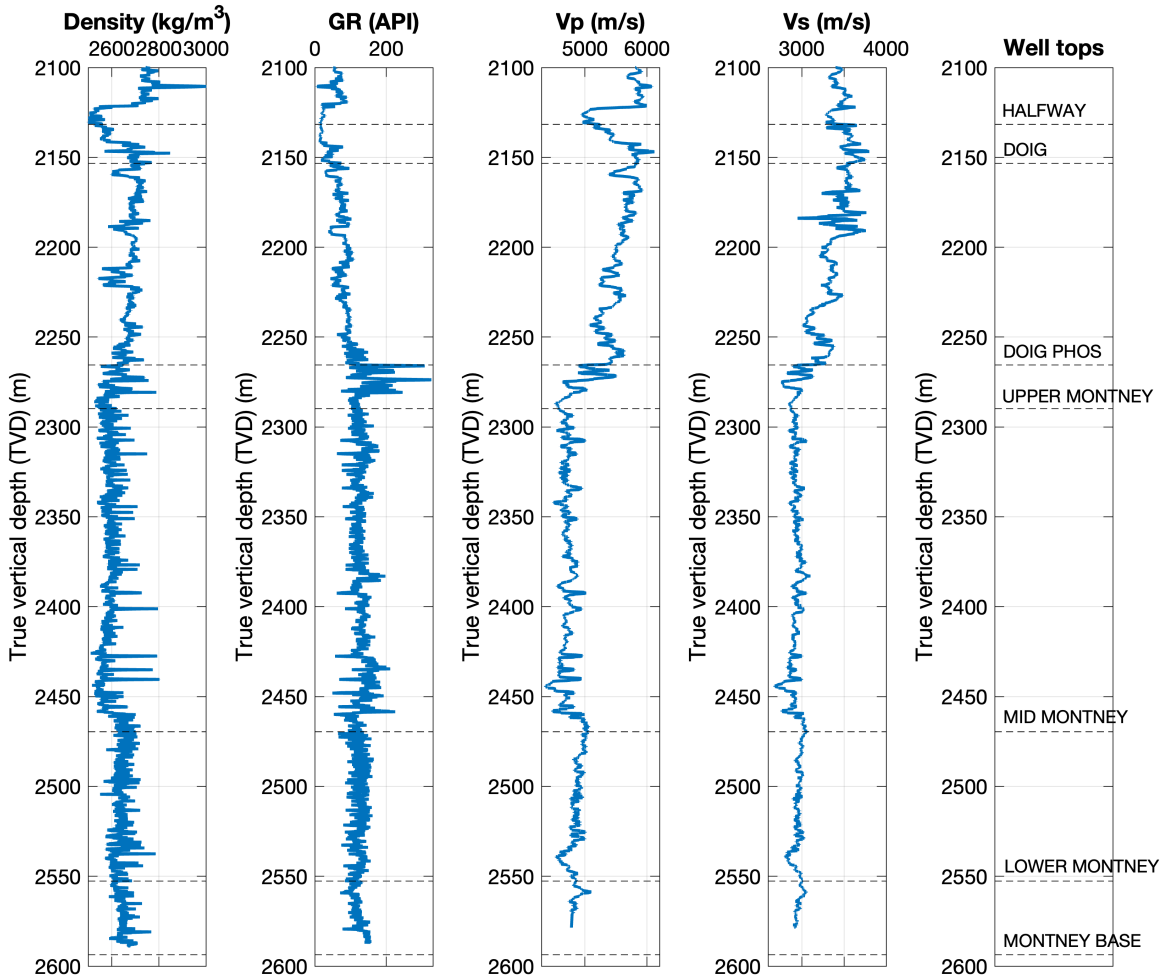


Figure 2.4: Available well tops and log data measured from 2100 to 2600 m TVD at the vertical monitoring well.

## 2.6 Objectives

As mentioned in Chapter 1, the primary objective of this thesis is to investigate the leading causes of the event anomaly through comprehensive processing and analysis of microseismic data, treatment data, well data, and geomechanics and improve the accuracy and efficiency of automated event detection and location algorithms for large microseismic data sets. The 1.2 terabyte raw microseismic data set offers an opportunity to perform a complete processing workflow, from basic steps, such as

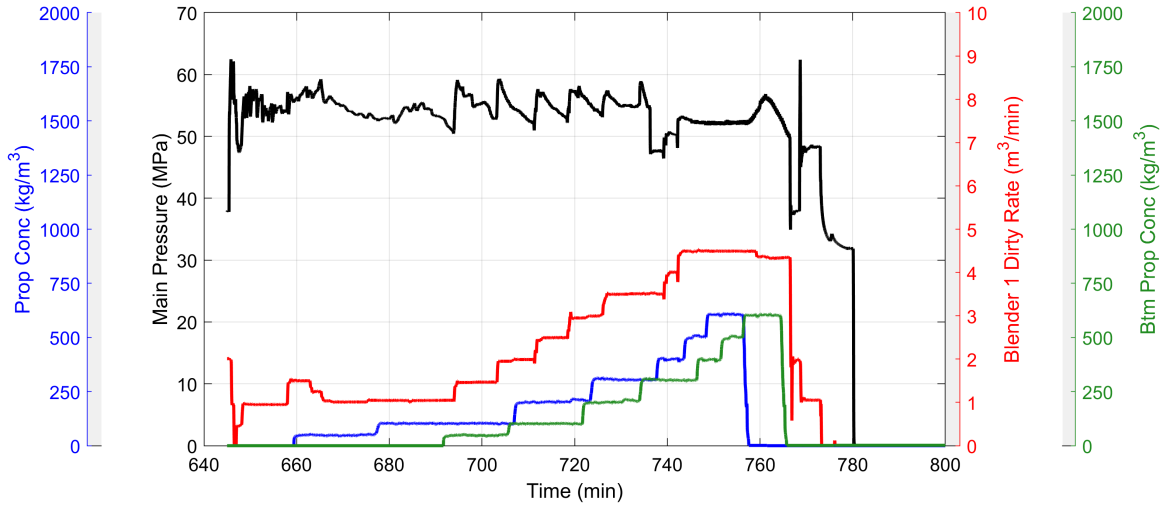


Figure 2.5: Completion curves recorded during treatment stage 5 in the horizontal well 2.

header creation and sensor orientation estimation, to more advanced processing, such as source mechanism estimation. The extensive data set enables the evaluation of the feasibility, efficiency, and reliability of automated event detection and location algorithms, which are discussed in Chapters 4, 5, and 6. Although the acquisition geometry with vertical and horizontal monitoring arrays is not ideal for event location due to lack of coverage in certain directions, it provides an insightful example of how the horizontal monitoring array poses more challenges in sensor orientation estimation than the vertical array (discussed more in Chapter 3) and reveals the impact of limited acquisition geometry on the interpolation results of the grid-estimated event locations and the estimated source mechanisms (discussed in Chapters 6 and 7). Results from microseismic data processing are then integrated with treatment data analysis and known geological and geomechanical information to make interpretations of the causes behind the event anomaly (discussed in Chapter 8).

# Chapter 3

## Preprocessing microseismic data: Sensor orientation estimation, data rotation, signal preconditioning, and velocity model building

### Summary

This chapter details the preprocessing steps for microseismic data, including sensor orientation estimation, data rotation, signal preconditioning, and velocity model construction. Sensor orientation estimation and data rotation are necessary for downhole microseismic data to correct the amplitude and polarity of the recorded microseismic data since the 3-component (3C) sensors deployed in the borehole tend to have different orientations. These steps are performed differently for data in vertical and horizontal boreholes, with the horizontal-array data posing more computational challenges than vertical-array data, requiring compensation for the wellbore direction before rotating the 3C data. Then, frequency filtering is applied to reduce unwanted noise in the data and improve the signal-to-noise (SNR) ratio. I describe the filter design using amplitude spectral analysis and include examples highlighting the waveforms before and after filtering. After that, I show how a 1-dimensional (1D) velocity model, one of the critical inputs for estimating hypocentral locations of microseismic events, is built using compressional and shear sonic logs and available well tops.

## 3.1 Introduction

Microseismic monitoring involves different tasks, including passive seismic recording, data processing, collecting geological background information, building geomechanical models and making interpretations. Among them, microseismic data processing is one of the most important and time-consuming parts. It helps extract insightful information on microseismic sources from the recorded waveforms (Maxwell, 2014). Microseismic data can be recorded by surface or downhole monitoring arrays. This thesis focuses on data recorded by sensors deployed in the borehole. A standard processing workflow for downhole microseismic data often includes sensor orientation, data rotation, signal conditioning, velocity model building, event detection, event localization, and source characterization (Maxwell, 2014). This chapter presents the first four preprocessing steps, from estimating the orientation of the sensors to building the velocity model. The following sections explain each step with detailed workflows and example results from the raw data.

## 3.2 Methodology

### 3.2.1 Sensor orientation estimation

For downhole microseismic acquisition, when deployed in the borehole, the 3C sensors tend to rotate due to their weight and the wireline design (Grechka & Heigl, 2017). As a result, the sensors in the monitoring array have different orientations. Usually, only the axial component (often the vertical component  $z$ ) of the sensors can be predetermined. In contrast, the other two horizontal components,  $h_1$  and  $h_2$ , of the sensors could be pointed in any direction (Maxwell & Le Calvez, 2010). Therefore, it is required to estimate the true orientation of the sensors and rotate the 3C data to obtain waveforms with true amplitude and polarity before further processing, such as event detection and location. Since the provided microseismic data are recorded by sensors in vertical and horizontal monitoring arrays, this section elaborates on the

steps for estimating the orientation of sensors in both arrays.

### Vertical-array data

Figure 3.1 shows a simple sketch of a 3C sensor deployed in a vertical borehole. The vertical component,  $z$ , can be predetermined as the wellbore is vertical. Sensor orientation estimation aims to obtain the true directions of the two horizontal components,  $h_1$  and  $h_2$ , of each sensor in the two directions, East-West and North-South, of the geographical frame.

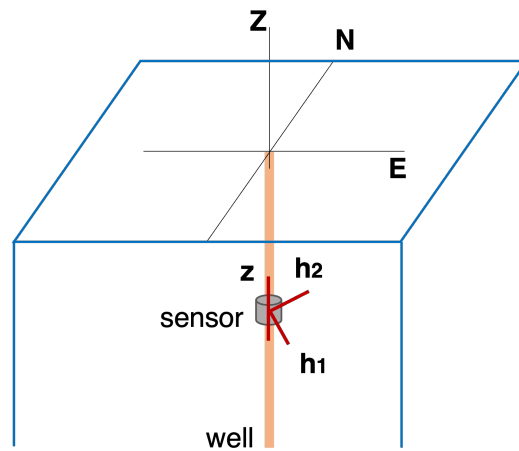


Figure 3.1: A simple sketch showing a 3C sensor in the vertical borehole.  $h_1$ ,  $h_2$ , and  $z$  are three components of the sensor;  $E$ ,  $N$ , and  $Z$  denote three directions of the geographical frame corresponding to East, North and Vertical directions, respectively.

Figure 3.2 shows a typical workflow for estimating sensor orientation in the vertical boreholes. First, the monitoring geometry of the data is defined. Wellhead positions for each well, directional survey, and locations of the sensor arrays in the borehole are defined in a common coordinate system (Maxwell, 2014; Pike, 2014). The coordinate reference system should be checked to avoid errors in the geometry (Maxwell, 2014). Then, orientation shots with known locations are used to determine the orientation of the two horizontal components,  $h_1$  and  $h_2$ , of the sensors using polarization analysis. The orientation shots (known as controlled sources or calibration shots) can be perforation shots, ball drop events, string shots in the boreholes, explosives on the surface

or other check shots (Maxwell, 2014; Pike, 2014). Recordings of these calibration shots often have a good signal-to-noise ratio, so it is easy to pick the onset of the seismic phases. If calibration shots are unavailable or unusable due to operational difficulties, early microseismic events recorded during a treatment can be used to estimate sensor orientations (Maxwell, 2014; Pike, 2014). By doing so, the assumption is made that early events are most likely to occur near the wellbore at the breakdown pressure and that there is no variation due to azimuthal velocity anisotropy from stage to stage (Maxwell, 2014; Pike, 2014).

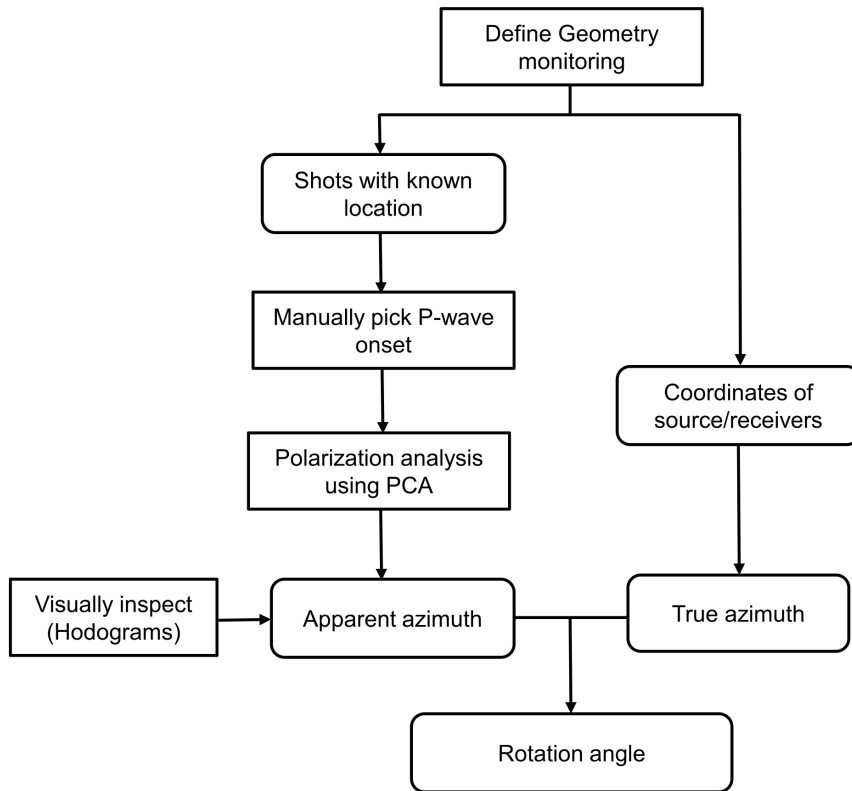


Figure 3.2: Sensor orientation estimation workflow for vertical-array data.

The next step is to determine and pick the onset of a seismic phase, either a P-wave or an S-wave, on the shot recordings. Normally, the P-phase is used as its onset is more visible to pick than the S-wave. Data segments containing most of the first-arrival P-wave energy are then selected as input for polarization analysis. Usually, these segments should have a length within one pulse width to capture mostly the

direct arrival and minimize uncertainties in polarization analysis. Then, polarization analysis can be performed on the selected data segments to estimate the direction of the first-arrival P-wave motion. Polarization analysis is done using the Principal Component Analysis (PCA) method, which derives the eigenvectors corresponding to the highest eigenvalues of the covariance matrix of the data segments. These eigenvectors are used to compute the apparent azimuth,  $\theta_{app}$ , which is the azimuth angle between the P-wave direction and the horizontal component  $h_2$  of the sensor (Figure 3.3a).

When estimating the apparent azimuth angle, it should be noted that there is an ambiguity of  $180^\circ$  in the computation since the polarity of the first-arrival P wave in the vertical direction can be up or down. The polarity of the first motion can be manually checked and considered in the calculation to obtain the correct apparent azimuth. Figure 3.4 shows an example of P-wave first motion with two possible polarities, downward motion ( $Z_1$ ) and upward motion ( $Z_2$ ) (Havskov et al., 2009). The polarization analysis gives the backazimuth angle; if the first-arrival P wave is upward, I add  $180^\circ$  to obtain the correct backazimuth angle; if the first motion is downward, I keep the estimated result from polarization analysis. The resulting apparent angles can be visually inspected using hodogram analysis. A hodogram is a graphical depiction of the seismic wave motions (Maxwell, 2014). By cross-plotting the relative signal amplitude of two unrotated horizontal components,  $h_1$  and  $h_2$ , of the data segments containing most of the P-wave energy, the arrival direction of the P-wave and its corresponding apparent azimuth angle for each sensor can be quickly estimated (Maxwell, 2014).

The true azimuth,  $\theta_{true}$ , which is the angle between the P-wave direction relative to the North direction (Figure 3.3b), can be computed using coordinates of the orientation shots and sensors in the monitoring array. Denote  $x_1, y_1$  the coordinates of a shot in the 2-dimensional (2D) plane (North, East) and  $x_2, y_2$  the coordinates of a

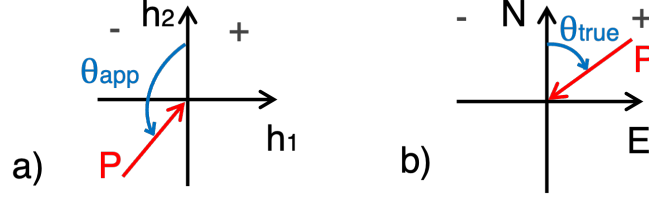


Figure 3.3: Illustration of a) Apparent azimuth  $\theta_{app}$ , defined as the angle between the P-wave direction and the horizontal component  $h_2$ , b) True azimuth  $\theta_{true}$ , defined as the angle between the P-wave direction relative to the North direction,  $N$  and  $E$  denote the North and East directions of the geographical frame.

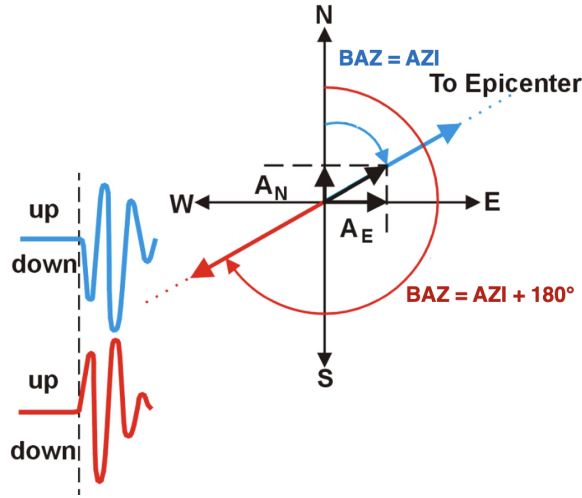


Figure 3.4: P-wave first motion in the vertical component;  $Z_1$  denotes upward motion;  $Z_2$  denotes downward motion; AZI denotes azimuth angle, BAZI denotes backazimuth angle; E, W, N, and S denote East, West, North, South directions (Havskov et al., 2009).

sensor in this plane,  $\theta_{true}$  is computed using

$$\theta_{true} = \text{atan2}(x_1 - x_2, y_1 - y_2) \frac{180}{\pi}. \quad (3.1)$$

After obtaining the apparent and true azimuth angles for all sensors in the array, the rotation angle  $\theta_{rot}$  for each sensor is computed, which is the angle between the horizontal component  $h_2$  and the North direction and is derived using

$$\theta_{rot} = -\theta_{app} + \theta_{true}. \quad (3.2)$$

where  $\theta_{rot}$  is the rotation angle,  $\theta_{app}$  is the apparent azimuth angle, and  $\theta_{true}$  is the true azimuth angle. All angles are in degree units.

Usually, multiple shots from different locations are used to obtain the mean rotation angle,  $\theta_{mean}$ , for each sensor in the monitoring array to improve the statistical reliability (Maxwell, 2014; Pike, 2014). Uncertainties in the resulting mean rotation angles are then evaluated by standard deviations  $\sigma$ , which is given as

$$\sigma = \sqrt{\frac{\sum_{i=1}^N (\theta_i - \theta_{mean})^2}{N}}. \quad (3.3)$$

where  $\sigma$  is the standard deviation (in degrees),  $\theta_i$  is the rotation angle (in degrees) obtained from the shot recording  $i$ , and  $N$  is the number of shot recordings used for calculation. If there is a difference of  $360^\circ$  between  $\theta_i$  and  $\theta_{i+1}$ , the angles are converted into a common range of value by adding or subtracting  $\theta_i$  or  $\theta_{i+1}$  with  $360^\circ$ . Using shots from different locations also helps verify the orientation estimation by comparing the amplitude and polarity of the first motion between the unrotated and rotated shot recordings at different locations.

### Horizontal-array data

Estimating the orientation of sensors in the horizontal monitoring array is more complicated and uncertain than for the vertical array. While orientation shots with known locations are sufficient to estimate the sensor orientation for vertical-array data, the procedure involves more computation for horizontal-array data due to the difference in geometry. Figure 3.5 shows a simple sketch illustrating sensors in the horizontal boreholes.

The same workflow (as shown in Figure 3.2) is applied to obtain the rotation angles. However, in this case, the horizontal components,  $h_1$  and  $h_2$ , are in the plane orthogonal to the wellbore axis (Figure 3.5); thus, the ray angle of incidence,  $i$ , which is the acute angle between the P-wave direction and the line perpendicular to a horizontal interface, needs to be estimated. The incidence angle for each sensor can be obtained using different ways. A quick way is from coordinates of shots and

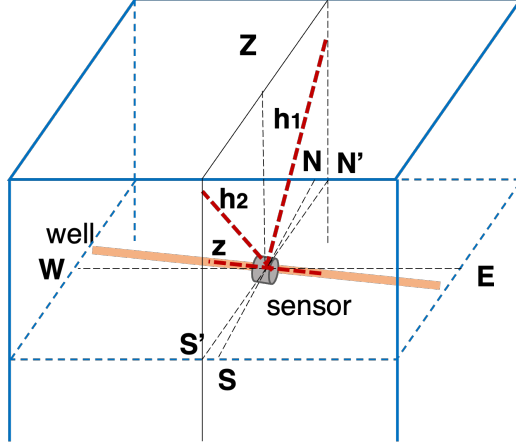


Figure 3.5: A simple sketch of a 3C sensor deployed in the horizontal borehole.  $h_1$ ,  $h_2$ , and  $z$  are 3 components of the sensor;  $E$ ,  $N$ , and  $Z$  denote the East, North and Vertical directions of the geographical frame, respectively. Due to the orientation of the well,  $h_1$  and  $h_2$  are in the  $(Z, N'S')$  plane and not in the  $(Z, \text{North-South})$  plane.

receivers using

$$i = \text{atan2}(x_1 - x_2, y_1 - y_2) \frac{180}{\pi}. \quad (3.4)$$

in which  $i$  is the incidence angle (in degrees),  $x_1, y_1$  are coordinates of the shot, and  $x_2, y_2$  are coordinates of the sensor. The incidence angles are often noisy since they are less well-polarized than in the azimuthal direction in the vertical array. Various seismic phases, including reflection, refraction, and direct waves, come from different directions and interfere with each other, affecting the inclination of hodograms (Maxwell & Le Calvez, 2010). A more precise approach to determining the incidence angle involves using the 1D ray bending algorithm; however, this method requires a velocity model and it can introduce uncertainties in the sensor orientation results.

### 3.2.2 Data rotation

The 3 orthogonal components  $(h_1, h_2, z)$  of the data can be rotated into 3 components (North-South, East-West and Vertical) of the geographical frame or 3 components (radial, transverse and pseudo vertical) of the wave frame depending on processing purposes. Generally, the data are rotated into the geographical frame and then rotated into the wave frame if analysts want to separate the S-wave phase more clearly.

## Rotating data into the geographical frame

The estimated sensor orientation results from the previous section are used to rotate the 3 orthogonal components of seismic waveforms,  $h_1$ ,  $h_2$  and  $z$ , into the 3 components of the geographical frame of reference, North-South, East-West and Vertical directions. The rotation procedure is performed differently for vertical-array and horizontal-array data. To rotate vertical-array data, a rotation matrix constructed from the estimated sensor orientation is used, whereas, for horizontal-array data, a rotation that first considers the wellbore orientation needs to be performed before the rotation based on the sensor orientation. Figure 3.6 illustrates how to rotate the vertical-array data into the geographical frame.

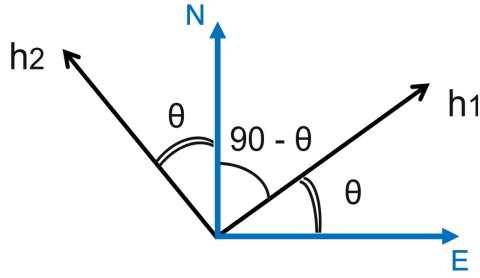


Figure 3.6: Illustration of rotation using a rotation matrix (N and E denote the North and East directions,  $h_1$  and  $h_2$ , are the two horizontal components of the sensors).

Denote  $\theta$  the rotation angle, which is the angle between the positive  $h_2$  component and the North direction. A standard 2D rotation matrix,  $\mathbf{R}_{2D}(\theta)$ , constructed from angle  $\theta$  is given as

$$\mathbf{R}_{2D}(\theta) = \begin{pmatrix} \cos \theta & \sin \theta \\ -\sin \theta & \cos \theta \end{pmatrix}. \quad (3.5)$$

A clockwise rotation is done through matrix multiplication. Thus,

$$\begin{pmatrix} E \\ N \end{pmatrix} = \begin{pmatrix} \cos \theta & \sin \theta \\ -\sin \theta & \cos \theta \end{pmatrix} \begin{pmatrix} h_1 \\ h_2 \end{pmatrix}. \quad (3.6)$$

The two horizontal components,  $h_1$  and  $h_2$ , of the data are rotated into two compo-

nents, East-West and North-South, of the geographical frame using

$$\begin{cases} E = h_1 \cos \theta + h_2 \sin \theta \\ N = -h_1 \sin \theta + h_2 \cos \theta \end{cases} . \quad (3.7)$$

where E and N denote the East-West and North-South components.

In general, for the data recorded by sensors in horizontal boreholes or deviated wells, a rotation using the well azimuth and inclination needs to be performed before rotating the data into the geographical frame of reference using the rotation matrix  $\mathbf{R}_{2D}(\theta)$  (equation 3.5). The azimuth of the well,  $\alpha$ , which is the angle between the North direction and the wellbore axis in the horizontal plane, can be computed using the coordinates of the receivers in the monitoring array or taken from well data. The well inclination,  $\phi$ , is the angle of the deviation of a wellbore from the vertical path. An inclination of  $0^\circ$  would be truly vertical, and an inclination of  $90^\circ$  would be horizontal. The horizontal well is a particular case of a deviated well that inclines at an angle of  $90^\circ$ . Using well azimuth and inclination, the unit vector of the well direction  $\vec{\mathbf{w}} = [X; Y; Z]$  is constructed using

$$\begin{cases} X = -\sin \phi \sin \alpha \\ Y = -\sin \phi \cos \alpha \\ Z = \cos \phi \end{cases} . \quad (3.8)$$

Denote  $\vec{\mathbf{u}}$  the unit vector around which the initial coordinates are rotated. It is defined by the cross product of two units vectors, the well direction  $\vec{\mathbf{w}}$ , and the vertical direction  $\vec{\mathbf{j}} = [0; 0; 1]$  using

$$\vec{\mathbf{u}} = \frac{\vec{\mathbf{w}} \times \vec{\mathbf{j}}}{\|\vec{\mathbf{w}} \times \vec{\mathbf{j}}\|} . \quad (3.9)$$

Three elements,  $u_1, u_2, u_3$  of the unit vector and the well inclination  $\phi$ , are then used to construct a 3-dimensional (3D) rotation matrix,  $\mathbf{R}_{3D}(\phi)$ , using

$$\mathbf{R}_{3D}(\phi) = \begin{pmatrix} R_{11}(\phi) & R_{12}(\phi) & R_{13}(\phi) \\ R_{21}(\phi) & R_{22}(\phi) & R_{23}(\phi) \\ R_{31}(\phi) & R_{32}(\phi) & R_{33}(\phi) \end{pmatrix} . \quad (3.10)$$

where

$$\left\{ \begin{array}{l} R_{11}(\phi) = \cos \phi + u_1^2(1 - \cos \phi) \\ R_{12}(\phi) = u_1 u_2(1 - \cos \phi) - u_3 \sin \phi \\ R_{13}(\phi) = u_1 u_3(1 - \cos \phi) + u_2 \sin \phi \\ R_{21}(\phi) = u_2 u_1(1 - \cos \phi) + u_3 \sin \phi \\ R_{22}(\phi) = \cos \phi + u_2^2(1 - \cos \phi) \\ R_{23}(\phi) = u_2 u_3(1 - \cos \phi) - u_1 \sin \phi \\ R_{31}(\phi) = u_3 u_1(1 - \cos \phi) - u_2 \sin \phi \\ R_{32}(\phi) = u_3 u_2(1 - \cos \phi) + u_1 \sin \phi \\ R_{33}(\phi) = \cos \phi + u_3^2(1 - \cos \phi) \end{array} \right. . \quad (3.11)$$

in which  $u_1, u_2, u_3$  are elements of the unit vector  $\vec{\mathbf{u}}$  (equation 3.9), and  $\phi$  is the well inclination angle (in degrees).

The rotation matrix,  $\mathbf{R}_{3D}(\phi)$ , is used to rotate the 3 data components to compensate for the well orientation through matrix multiplication. Figure 3.7 illustrates the directions of a 3C sensor in the horizontal borehole after a rotation to compensate for the well orientation. The two horizontal components,  $h_1$  and  $h_2$ , are positioned in the vertical plane of (Z, North-South). Then, the 2D rotation matrix built from the mean rotation angle (equation 3.5) is used to rotate  $h_1$  and  $h_2$  and obtain the true directions using equations 3.6 and 3.7. In this case, the orientation is in the (Z, North) plane instead of the (North, East) plane as in the vertical boreholes. The matrix multiplication is used to rotate the horizontal component  $h_1$  into North (N) to have the true East component and the horizontal component  $h_2$  into Z to have the true North component.

### **Rotating data into the wave frame**

Rotating the data into the wave frame is usually done after the rotation into the geographical frame to observe a more visible separation between P- and S-phases. The rotation does not require any information on the source location. Data segments that contain most of the energy of the seismic phases are used to run the PCA

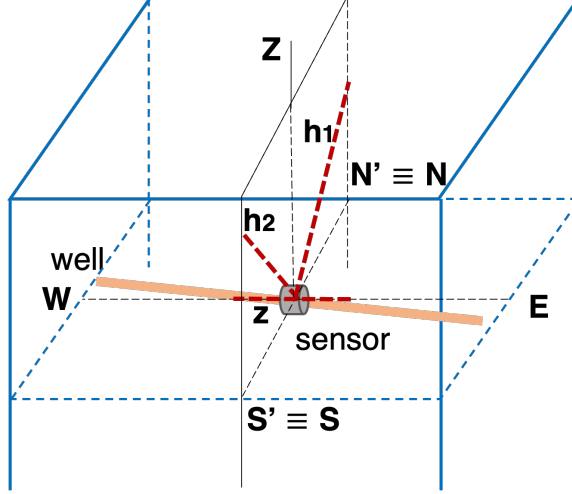


Figure 3.7: A simple sketch depicting a sensor in the horizontal borehole.  $h_1$ ,  $h_2$ , and  $z$  are 3 sensor components;  $E$ ,  $N$ , and  $Z$  are 3 directions, East, North and Vertical, of the geographical frame. After compensating for the orientation of the well,  $h_1$  and  $h_2$  are positioned in the plane of  $(Z, \text{North-South})$ .

method to find the main eigenvalue representativeness of the covariance matrix of the data. The unit vectors are constructed to rotate the 3 data components into the 3 components, radial, transverse and pseudo vertical, of the wave frame. The unit vector in the radial direction,  $\vec{r}$ , is defined using the main eigenvalues. The unit vector in the horizontal plane,  $\vec{h}$ , is defined using

$$\vec{h} = \frac{\vec{r} \times \vec{j}}{\|\vec{r} \times \vec{j}\|}. \quad (3.12)$$

where  $\vec{r}$  is the unit vector in the radial direction;  $\vec{j}$  is the unit vector in the true vertical direction,  $\vec{j} = [0; 0; 1]$ .

Similarly, the unit vector in the vertical plane (pointing upward),  $\vec{v}$ , is given as

$$\vec{v} = \frac{\vec{r} \times \vec{h}}{\|\vec{r} \times \vec{h}\|}. \quad (3.13)$$

A 3x3 rotation matrix is then built based on the unit vectors of the radial, vertical and horizontal planes using

$$\mathbf{R}_{3D} = \begin{pmatrix} r_1 & r_2 & r_3 \\ h_1 & h_2 & h_3 \\ v_1 & v_2 & v_3 \end{pmatrix}. \quad (3.14)$$

where  $r_1$ ,  $r_2$  and  $r_3$  are elements of the unit vector  $\vec{r}$  in the radial direction;  $h_1$ ,  $h_2$  and  $h_3$  are elements of the unit vector  $\vec{h}$  in the horizontal direction;  $v_1$ ,  $v_2$  and  $v_3$  are elements of the unit vector  $\vec{v}$  in the vertical direction. After that, the rotation matrix obtained from equation 3.14 can be multiplied with the three components,  $h_1$ ,  $h_2$  and  $z$ , of the data to rotate data into three components radial, transverse and pseudo vertical, of the wave frame.

### 3.2.3 Signal preconditioning

Generally, event detection algorithms work more efficiently on the preconditioned data as the signal conditioning and enhancement filters can reduce the unwanted noise in the data and improve the SNR of the data (Maxwell, 2014). The simplest form of conditioning is using frequency filters such as highpass, bandpass, or lowpass filtering (Maxwell, 2014). However, the preferred option is to minimize the involvement of filters as much as possible and preserve the signals (Maxwell, 2014). Microseismic data usually have both low-frequency and high-frequency noise in the signals; therefore, a bandpass filter is the preferred approach to reduce the noise outside the frequency bandwidth of the signals. I thus use the bandpass filter to enhance the quality of the data.

A quick way to obtain the optimal corner frequencies for the bandpass filter is by performing an amplitude spectrum analysis on the raw microseismic signals and noise. Microseismic events and background noise often differ in character and frequency content so that I determine the dominant frequency range of the microseismic event and obtain appropriate cutoff frequencies from the amplitude spectrum plots. When the corner frequencies are obtained, the bandpass filter is applied on each receiver level of the data to enhance the data quality, and the resulting data will then be ready for event detection.

### 3.2.4 Velocity model building

The velocity model is one of the critical aspects for estimating accurate hypocenter locations of microseismicity (Eisner et al., 2009; Maxwell et al., 2010; Warpinski et al., 2005). Usually, a laterally homogeneous or 1D velocity model is used in the location algorithm for computational convenience or due to unavailable information (Lomax et al., 2009). First, initial 1D P-wave velocity ( $V_p$ ) and S-wave velocity ( $V_s$ ) models are constructed using compressional and shear sonic logs and available well tops. Well tops help define the number of layers in the velocity models. A blocking technique is used to segment the well logs into different intervals (layers). The velocity value of each interval is obtained by taking the mean value of the log data.

The sonic tool measures propagation velocity along the axial direction of the logged well, whereas downhole microseismic data generally involve predominantly horizontal propagation and the most applicable velocity is the horizontal velocity across the formation (Maxwell, 2014). Van Dok et al. (2011) show that the seismic velocity is faster in the horizontal direction than in the vertical direction due to seismic anisotropy. Therefore, the initial velocity models must be calibrated to scale the vertical log-derived velocities and obtain horizontal formation velocities. Usually, the velocity calibration can be done using available seismic sources with known positions, such as perforation shots, string shots, or ball drop events. When these sources are unavailable, the velocity models can be calibrated using the assumption that microseismic events often fall into the proximity of the treatment location (Maxwell, 2014; Pike, 2014).

## 3.3 Implementation and results

### 3.3.1 Sensor orientation estimation and data rotation

First, I define the monitoring geometry of the dataset. The datum used in this dataset is the North American Datum of 1927 (NAD27). All the coordinates are converted

into a common geographical reference datum, UTM NAD27 zone 10N.

### Vertical-array data

I estimate the orientation of sensors in the vertical array using provided surface dynamite shots at 4 locations. Figure 3.8 shows the locations of orientation shots and the vertical monitoring array. Since orientation shots are explosives, I observe a strong P-phase on the seismograms. I manually pick the start and end of P-waves and use the data within this window for polarization analysis to obtain the apparent azimuth angle for each sensor. The window length is within one pulse width to ensure the data segments capture most P-wave energy. Figure 3.9a shows unrotated 3-component data recorded by sensor 1 in the vertical array with the P-wave window highlighted by the black rectangle. With the selected P-wave data segment, I obtain an apparent azimuth angle,  $\theta_{app} = -137.43^\circ$ , for sensor 1. The polarity of the first-arrival P-wave is also determined manually from the recordings. Figure 3.9a shows that the vertical first motion is upward, so I add an amount of  $180^\circ$  into the apparent azimuth angle. The resulting apparent azimuth angle,  $\theta_{app}$ , obtained from this shot recording is  $42.57^\circ$ . To visually inspect the estimated result, I use hodogram analysis. Figure 3.9b depicts the resulting hodogram of the 2 unrotated horizontal components,  $h_1$  and  $h_2$ , of sensor 1. The hodogram is generated using the same data segment used in the polarization analysis step, which contains most P-wave energy. I observe a linear direction of the P-wave motion, with the angle between  $h_2$  component and the P-wave direction around  $42^\circ$ , which is consistent with the resulting apparent angle obtained from polarization analysis.

After verifying the apparent azimuth angle, I compute the true azimuth angle,  $\theta_{true}$ , for sensor 1 using equation 3.1, coordinates of shot location 1 and sensor 1. The resulting  $\theta_{true}$  is about  $83.79^\circ$ . Then, I calculate the rotation angle,  $\theta_{rot}$ , for sensor 1 using equation 3.2 and obtain  $\theta_{rot} = 41.23^\circ$ . I use 7 shot recordings from different shot locations to compute the mean rotation angle,  $\theta_{mean}$ , for each sensor. Table

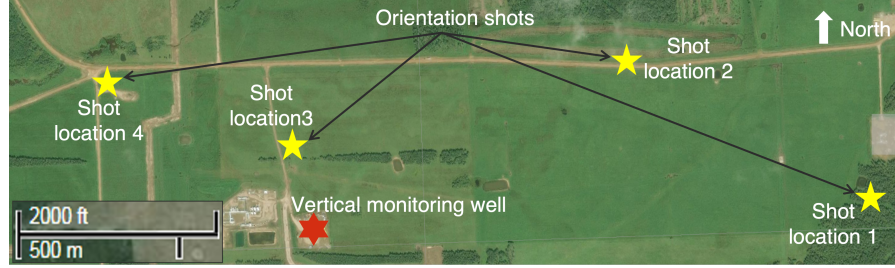


Figure 3.8: Locations of orientation shots and vertical monitoring array.

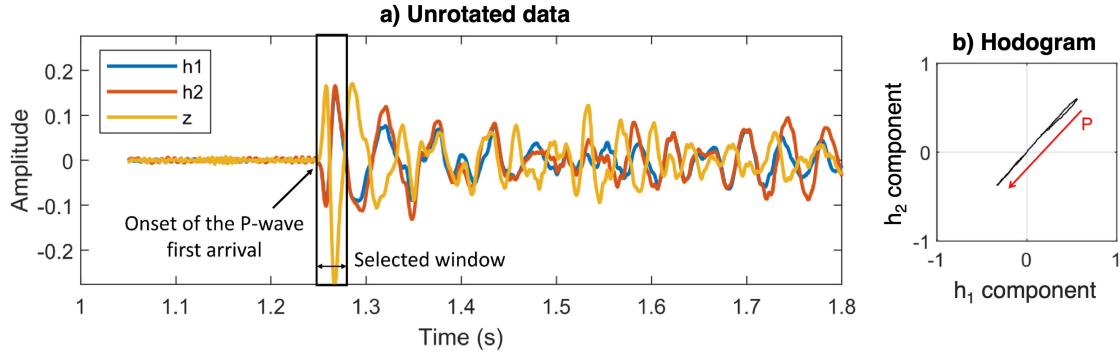


Figure 3.9: a) Unrotated seismic waveforms of one shot recording excited at the shot location 1 and recorded by the first sensor in the vertical array, and b) Hodogram of the two unrotated horizontal components,  $h_1$  and  $h_2$ , of the first sensor. The result is obtained from the segment containing the most P-wave energy in the unrotated shot recording excited at shot location 1.

3.1 shows the orientation results obtained from 7 shot recordings for the first sensor in the array. The resulting mean rotation angle for the first sensor is  $35.96^\circ$  with a standard deviation of  $5.80^\circ$ . Table 3.1 shows that the rotation angle from different shot recordings only has small variations, which is reliable.

Using the resulting mean rotation angle, I construct a 2D rotation matrix using equation 3.5 and perform a clockwise rotation using equations 3.6 and 3.7 to rotate the 2 horizontal components,  $h_1$  and  $h_2$ , into the East-West and North-South components of the geographical frame. Figure 3.10a shows the rotated seismic waveforms in the geographical frame with three components: East-West, North-South, and Vertical. Figure 3.10b shows the hodogram of the 2 rotated horizontal components, East-West and North-South, of sensor 1. After rotation, the true direction of the P-wave motion is obtained, with a true azimuth angle,  $\theta_{true}$ , of approximately  $83^\circ$  and the amplitude

Table 3.1: Orientation results obtained from different shot recordings for the first sensor in the vertical monitoring array. For the rotation angle,  $\theta_{rot}$ , the results are converted into the same range of angle value  $[0 2\pi]$ ; (SD: standard deviation).

Shot recording	$\theta_{true}$	$\theta_{app}$	$\theta_{rot}$		$\theta_{mean}$	SD
			Obtained	Converted		
1	83.79°	42.57°	41.23°	41.23°	35.96°	5.80°
2	83.81°	42.16°	41.65°	41.65°		
3	83.82°	41.96°	41.86°	41.86°		
4	55.41°	16.48°	38.93°	38.93°		
5	-46.64°	284.51°	-331.15°	28.85°		
6	-46.25°	284.63°	-330.88°	29.12°		
7	-46.93°	282.98°	-329.91°	30.09°		

and polarity of seismic waveforms are corrected.

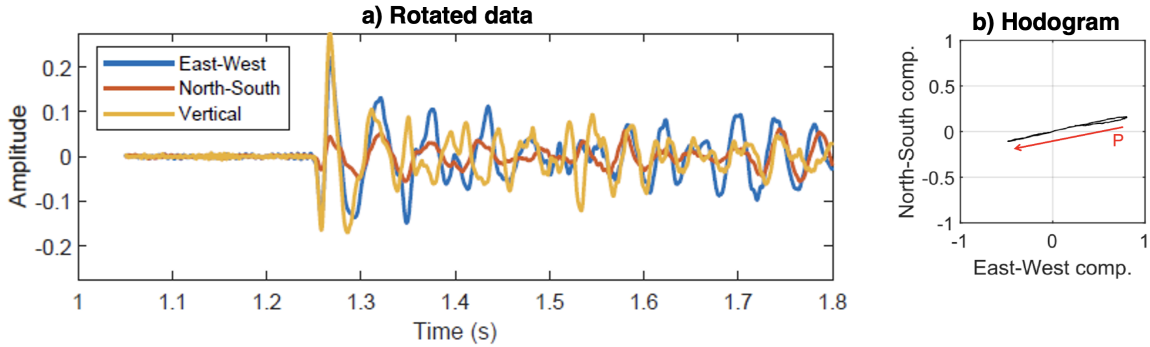


Figure 3.10: a) Rotated seismic waveforms of the shot recording excited at shot location 1 and recorded by the first sensor in the vertical array and b) Hodogram of the two rotated horizontal components, East-West and North-South, of the first sensor. The result is obtained from the rotated recording excited at shot location 1.

The last step is to verify the rotation result. This step is recommended because of a  $180^\circ$  ambiguity in defining the azimuth angles. To check the results, I consider the relative position of shot location 1 with the position of the monitoring array in the vertical well (Figure 3.8). The orientation shots are explosive, so the waves propagate in all directions with the East first motion. Shot 1 is in the East direction compared with the location of the sensors. Therefore, a stronger amplitude P-wave

moving from the East-West direction than the wave in the North-South direction will be observed. Figure 3.10a shows that I can retrieve this feature after the rotation. The amplitude of the East-West component of shot recording 1 is greater than that of the North-South component. Also, after rotation, the polarity of the waveforms is corrected, with the vertical first motion being negative (downward motion) (since I use the right-handed coordinates with the z-axis in the positive direction) and the first motion of the West and South directions being negative (downward motion).

### **Horizontal-array data**

The sensors in the horizontal monitoring array deployed on a moving tool string with 4 different positions. Figure 3.11 shows the positions of the tool string. I compute the orientations of all 16 sensors in the horizontal monitoring array for each tool string position using 2 shot recordings from different locations. The shot recordings are explosives; I use P-wave data to compute the apparent azimuth angles for the sensors through polarization analysis. This section shows example results from a shot recording excited at location 1 and recorded by tool string 2. Figure 3.12 shows the unrotated waveforms of the shot recording with a clear P-wave phase and the selected P-wave window within one pulse width to capture most P-wave energy.

I run polarization analysis using P-wave data within the selected window to estimate the apparent azimuth angle and obtain an  $\theta_{app}$  approximately of  $-117.82^\circ$ . The polarity of the P-wave first arrival is also determined. Figure 3.12a shows that the vertical first motion is downward (negative). Thus, the resulting apparent azimuth,  $\theta_{app}$ , computed from the shot recording at location 1 for the first sensor in the tool string 2, remains  $-117.82^\circ$ . To visually check the resulting apparent azimuth angle, I use hodogram analysis. Figure 3.12b displays the hodogram of the two unrotated horizontal components,  $h_1$  and  $h_2$ , of the first sensor. I observe a linear direction of the P-wave motion, with the angle between the  $h_2$  component and the P-wave direction around  $-117^\circ$ , which is consistent with the resulting angle obtained from

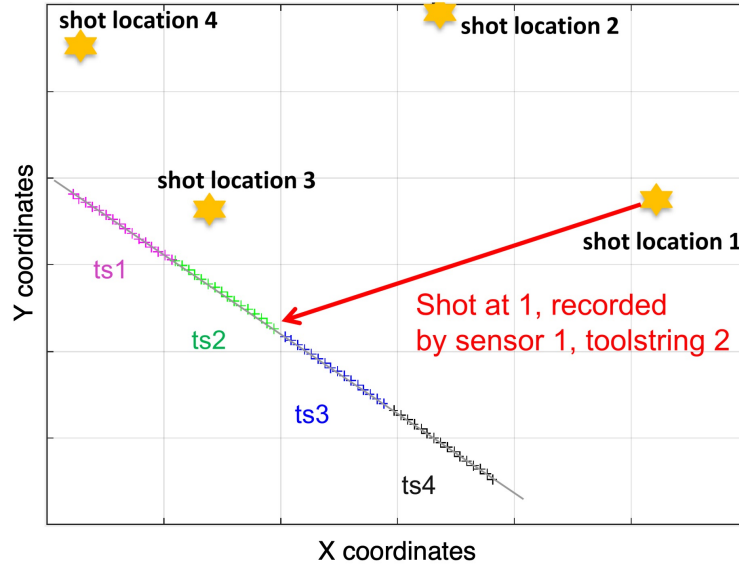


Figure 3.11: Different positions of the tool string in the horizontal borehole (ts: tool string).

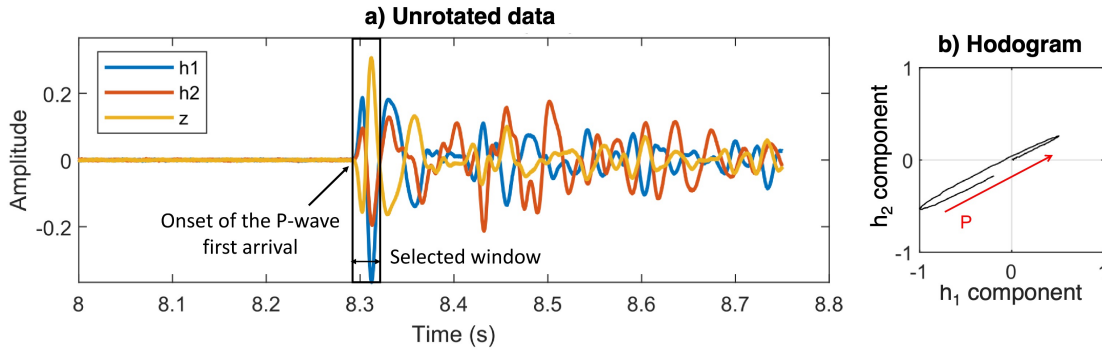


Figure 3.12: a) Unrotated seismic waveforms of a shot recording excited at shot location 1 and recorded by the first sensor in the tool string 2 in the horizontal array, b) Hodogram of the two unrotated horizontal components,  $h_1$  and  $h_2$ , of the first sensor. The result is obtained from the shot recording excited at shot location 1 and recorded by the first sensor in tool string 2 in the horizontal array.

polarization analysis.

After that, I estimate the incidence angle for the first sensor. To simplify, I utilize the coordinates of shot 1 and the first receiver to obtain the incidence angle,  $i$ , using equation 3.4. The resulting incidence angle is approximately  $79.53^\circ$ . Then, I compute the rotation angle,  $\theta_{rot}$ , for the first sensor using equation 3.2. I obtain  $\theta_{rot}$  being about  $197.35^\circ$ . I use 2 shot recordings from different shot locations to obtain the

mean rotation angle,  $\theta_{mean}$ , for each sensor. Table 3.2 shows the orientation results obtained from these shot recordings for the first sensor in tool string 2. The resulting mean rotation angle for the first sensor is  $193.28^\circ$  with a standard deviation of  $4.08^\circ$ . The rotation angle computed from different shots has only small variations and, thus, is reliable.

Table 3.2: Orientation results obtained from different shot recordings for the first sensor in tool string 2 in the horizontal array (SD: standard deviation).

Shot recording	$i$	$\theta_{app}$	$\theta_{rot}$	$\theta_{mean}$	SD
1	$79.53^\circ$	$-117.82^\circ$	$197.35^\circ$	$193.28^\circ$	$4.08^\circ$
2	$43.13^\circ$	$-146.07^\circ$	$189.20^\circ$		

After obtaining the estimated orientation of all 16 sensors in each tool string, I rotate the data into the geographical frame. In this case, the well is horizontal, so I first rotate the data according to the well orientation and then rotate to the geographical frame. The well orientation is obtained from the well data, with the well azimuth being about  $70^\circ$  and the well inclination being  $90^\circ$ . I construct the unit vector of the well direction,  $\vec{\mathbf{w}}$ , using equation 3.8 and then using equation 3.9 to obtain the unit vector  $\vec{\mathbf{u}}$ . The 3D rotation matrix,  $\mathbf{R}_{3D}(\phi)$ , is then derived using equations 3.10 and 3.11. The rotation according to the well orientation is done by performing matrix multiplication between the 3C data and the rotation matrix  $\mathbf{R}_{3D}(\phi)$ .

Next, I use the estimated orientations of the sensors in the horizontal array to construct a 2D matrix using equations 3.5, 3.6 and 3.7. Then, I rotate the 2 horizontal components,  $h_1$  and  $h_2$ , which are in the (Z, North) plane (Figure 3.7), to obtain East-West and North-South components in the geographical frame. Figure 3.13a shows the waveforms of the shot recording excited at location 1 and recorded by the first sensor in the tool string 2 after rotating into the geographical frame. Figure 3.13b shows

the hodogram of the 2 rotated horizontal components, East-West and North-South, of the first sensor in the tool string 2 after two rotations. The hodogram is generated using the data segment containing P-wave energy in the shot recording excited at shot location 1. After rotations, I obtain the true direction of the P-wave motion with the angle being about  $79^\circ$ , and the amplitude and polarity of the waveforms are corrected.

The last step is to verify the rotation result. Based on the relative position of the shot and receiver (Figure 3.11), a higher amplitude on the East-West component should be observed compared to the North-South component after rotation. Figure 3.13a clearly shows that the amplitude of the East-West is higher than the North-South. The polarity is also corrected with the vertical first motion being negative (the right-handed coordinates are used with the z-axis in the positive direction) and the first motion of the West and South directions being negative. Thus, the rotated results are ready to use as inputs for further processing steps.

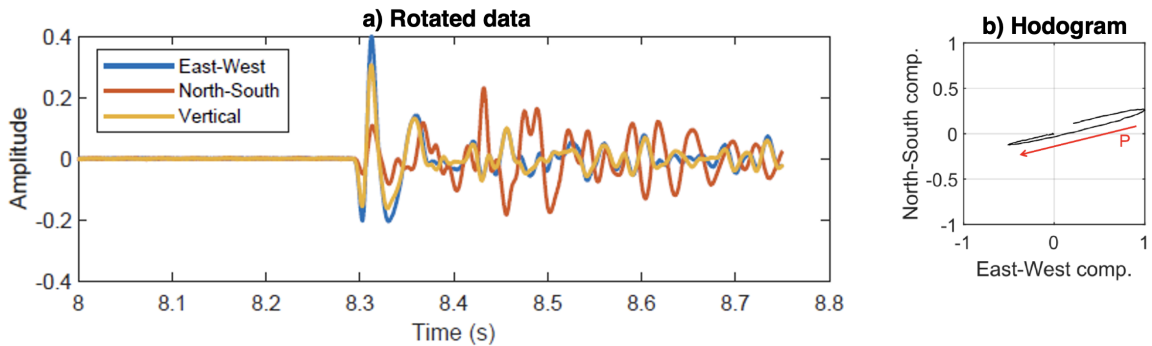


Figure 3.13: a) Rotated seismic waveforms of the shot recording excited at shot location 1 and recorded by the first sensor in tool string 2 in the horizontal array, b) Hodogram of the two rotated horizontal components, East-West and North-South, of the first sensor. The result is obtained from a shot recording excited at shot location 1 and recorded by the first sensor in tool string 2 in the horizontal array.

### 3.3.2 Signal preconditioning

I use a bandpass filter to reduce the noise in the data. The optimal cutoff frequencies for the bandpass filter are obtained by using spectral analysis. Figure 3.14 shows the

seismograms of a raw microseismic event and noise with their corresponding amplitude spectrum magnitude plots in both linear and dB formats. The amplitude spectrum plots (Figures 3.14c and 3.14d) show that the dominant frequency (highlighted by the black rectangles) of the microseismic signal ranging from 60 to 300 Hz with a peak frequency of around 150 Hz. Based on the spectral analysis result, I design a bandpass filter with two corner frequencies [60, 300] Hz to filter the data.

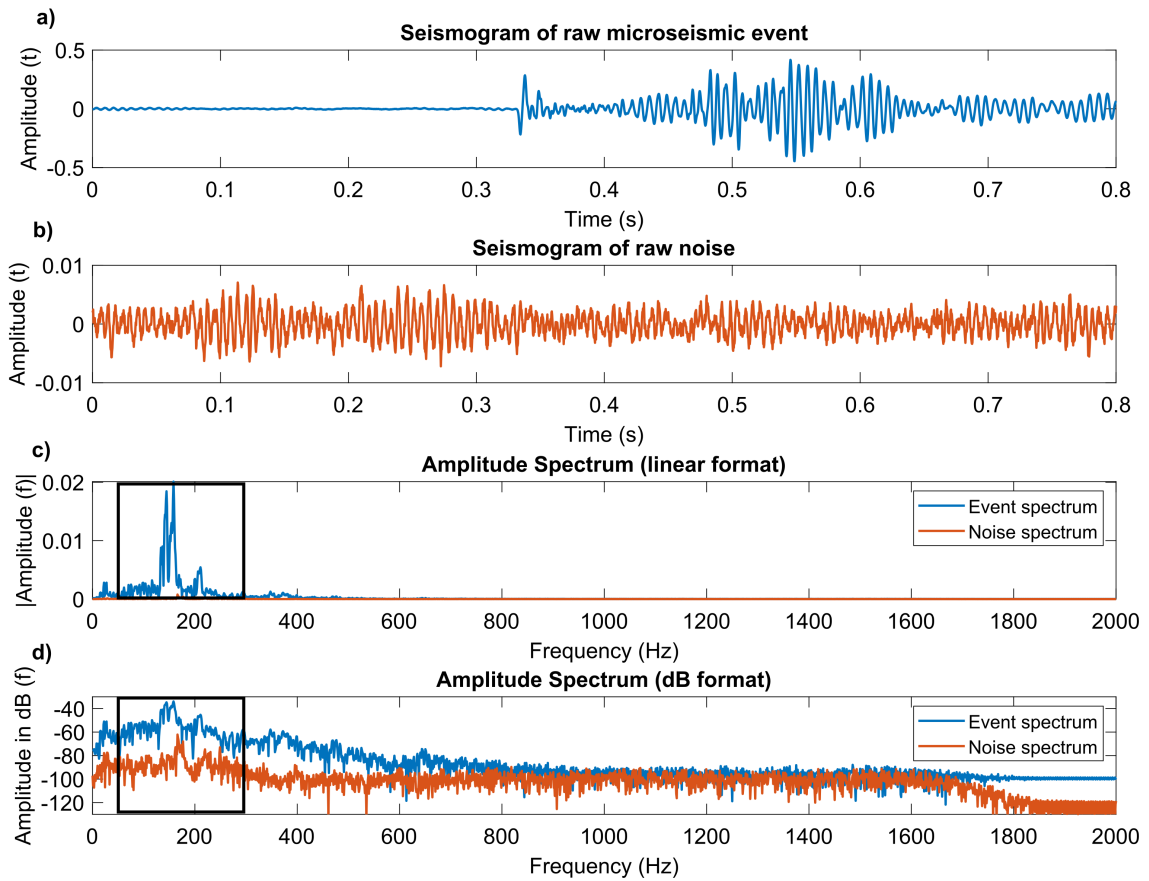


Figure 3.14: a) Seismogram of a raw microseismic event, b) Seismogram of a raw noise, c) Amplitude spectrum magnitude of the event and noise in linear format, d) Amplitude spectrum magnitude of the event and noise in dB format. The black rectangles in c) and d) show the dominant signal frequency range of [60, 300] Hz.

Figure 3.15 shows the data before and after applying the bandpass filter with the chosen cutoff frequencies. The data quality is enhanced significantly after filtering. In Figure 3.15a, the microseismic event could not be observed since it is masked by the high amplitude background noise. After filtering, the microseismic event becomes

apparent, with a clear P-phase at around 7.27 s and an S-phase at around 7.38 s (Figure 3.15b).

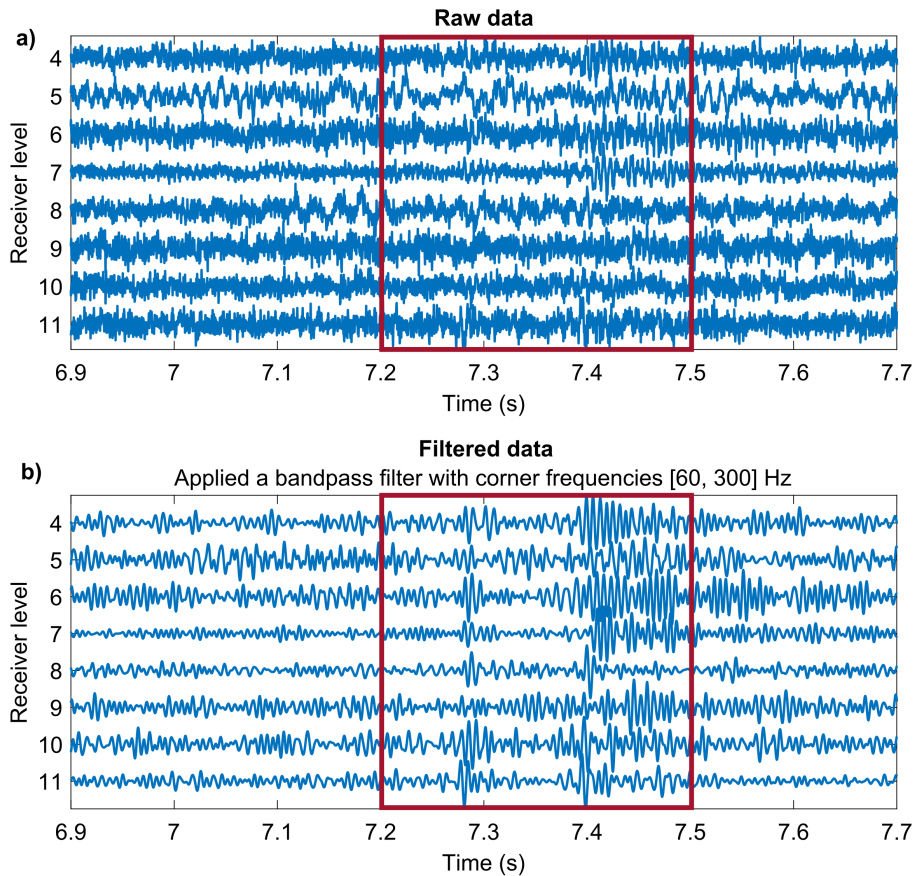


Figure 3.15: a) Raw data and b) Filtered data. After filtering, significant enhancement is observed in the data, with a clear microseismic event containing both P- and S- phases in the red rectangle. The P-wave arrives first at about 7.27 s, followed by the S-wave at 7.38 s.

### 3.3.3 Velocity model building

First, I construct an initial velocity model using the compressional and shear sonic logs from the monitoring well. The initial  $V_p$  and  $V_s$  models can be quickly obtained from the available sonic logs using the blocking technique. Using the well tops information in the vertical monitoring well, I define 12 layers, namely F, E, D, C, B, A, AA, Mid-B, Mid-A, Lower-B, Lower-A, and BSL. The blocking technique is then applied by taking the mean value of velocities within a layer. I later obtain the initial  $V_p$  and

Vs models shown as stairs plots in Figure 3.16 with the magenta stairs plot indicating the initial Vp model and the dark-red stairs plot indicating the initial Vs model.

In this study, seismic sources with known positions are unavailable; I thus calibrate the initial velocity models to scale the vertical log-derived velocities to horizontal formation velocities using a pragmatic way - testing. I examine different velocity models built from the initial models by adding from 5% to 50% of the velocity values into the initial models. As the microseismic events often fall into the proximity of the treatment location, I can define which velocity models perform best to run for the entire data. A too-low/high-velocity model will result in microseismic events away from the treatment positions. I chose the final velocities model to be 10-15% of the initial velocities models. In Figure 3.16, the final Vp model is indicated by the orange stair plot and the green stair plot indicates the final Vs model (the average Vp/Vs ratio is 1.63).

### 3.4 Conclusions

Sensor orientation estimation, data rotation, signal preconditioning, and velocity model construction are four crucial preprocessing steps to process the raw downhole microseismic data.

The first two steps are performed differently for data in vertical and horizontal boreholes. Sensor orientation estimation for horizontal boreholes is more complicated than for vertical boreholes. For vertical boreholes, the vertical direction of the sensors can be predetermined; I only need to estimate the unknown direction of the two horizontal components, and the computation is relatively straightforward. Providing the orientation shots with known locations is enough to obtain the true orientation of the horizontal components through polarization analysis of seismic phases. In contrast, sensor orientation for horizontal boreholes requires an estimation of the incidence angles, which can lead to some uncertainties due to not being well polarized by the seismic phases. These uncertainties can lead to errors in the event location. Similarly,

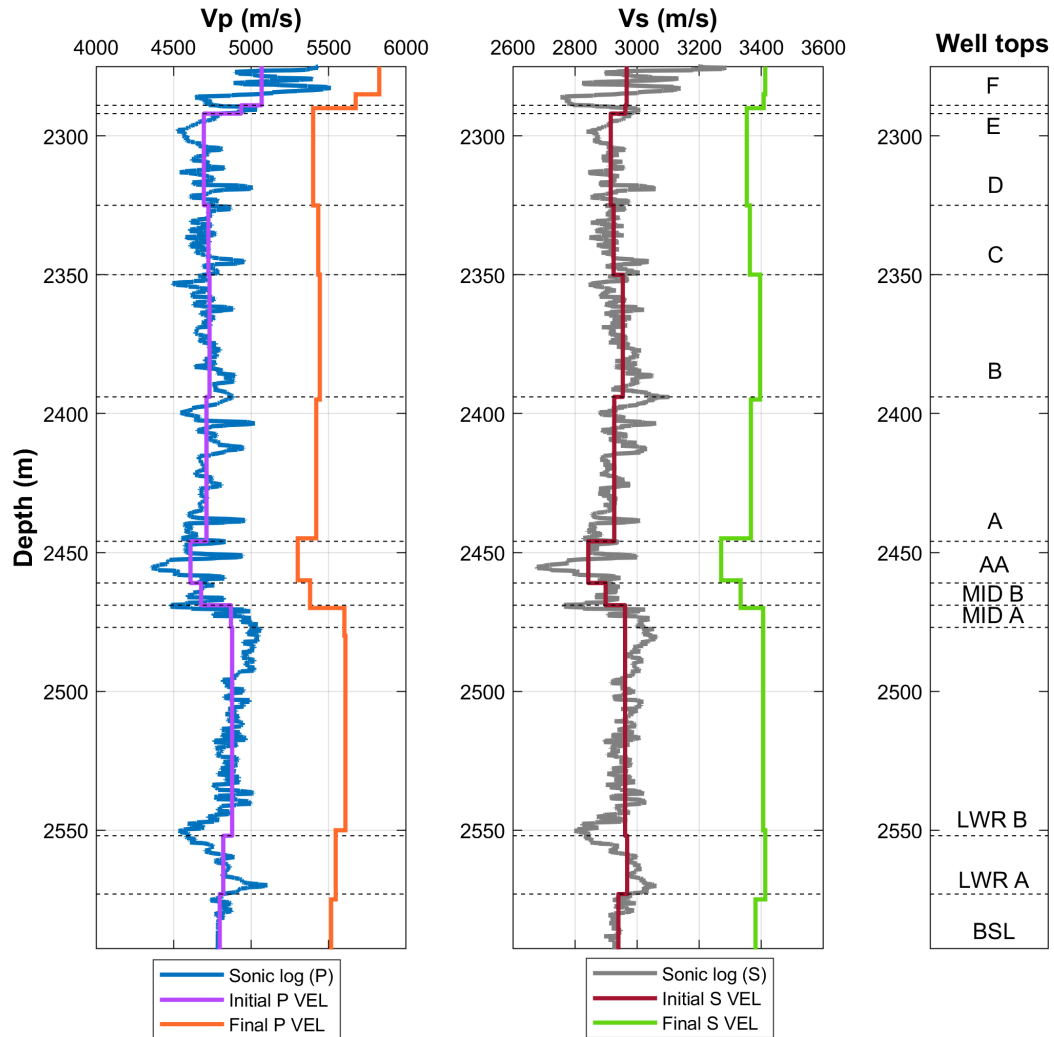


Figure 3.16: The 1D velocity model built from sonic logs. The first track shows the compressional sonic logs (blue curve), the initial  $V_p$  model (magenta stair plot), and the final  $V_p$  model (orange stair plot). The second track shows the shear sonic logs (grey curve), the initial  $V_s$  model (dark-red stair plot), and the final  $V_s$  model (green stair plot). The third track shows the number of layers defined from well tops.

rotating the data in the horizontal boreholes also requires more computations than data in the vertical boreholes. There are more sub-processing steps involved. I need to construct the 3D rotation matrix and perform a rotation to compensate for the wellbore direction before rotating the data into the geographical frame. The horizontal boreholes impose more challenges in processing than the vertical boreholes. The combined use of horizontal and vertical observation wells leads, however, to better ray coverage, translating into generally better-resolved locations.

After correcting the amplitudes and polarities of the waveforms, I apply a bandpass filter to attenuate the noise and improve the data quality. Microseismic events are more visible after filtering, which makes the detection algorithms more efficient with more events detected and fewer noise records (more details in Chapters 4 and 5). I generate a 1D P- and S-wave velocity model using available well logs and tops from the blocking technique. The velocity model is an indispensable input for event localization (more details in Chapter 6), which is used to calculate the predicted traveltimes of the P- and S-waves and estimate the most likely hypocentral locations.

# Chapter 4

## Detecting events in big microseismic data sets using a fast matched filter algorithm <sup>1</sup>

### Summary

Detection of microseismic events is a crucial yet demanding aspect of microseismic processing, as the events are tiny earthquakes embedded within continuously recorded data that often contain noise from various sources. Traditional automated triggering-based detectors, such as the short-time average over the long-time average (STA/LTA), are not convenient for big data sets due to low precision rates (many false alarms) and subsequent time-consuming event classification. Many studies use template matching and subspace detection, which detect events based on the level of similarity (indicated by normalized cross-correlation coefficients) between the continuous data and the template events to improve detection performance.

However, cross-correlation is often slow when applied to large time-series data sets with multiple receivers due to the computationally intensive process of calculating the normalization coefficients in each time window for each receiver. This study shows a fast matched filter (MF) implementation that can solve the efficiency challenge. The fast MF uses a fast normalized cross-correlation (NCC) technique that employs summed-area tables to calculate the NCC coefficients between the template events

---

<sup>1</sup>A manuscript including a version of this chapter has been submitted to *Geophysics*.

and the data. The implementation on real data shows that the fast NCC is about 450 times faster than the normal NCC computation while generating the same NCC coefficient results.

The fast MF detection process is also speeded up using a recursive STA/LTA formula to extract high-quality, distinctive template events and a multiplexing technique to reformat the 3-component data into a single stream for efficient cross-correlation calculation. I implement the fast MF workflow on a 1.2 terabyte microseismic data set and detect nearly 20,000 events in both vertical and horizontal monitoring wells. An STA/LTA detection with a low threshold is also used to capture most potential events from the entire data and provide an event reference list. I then compare the fast MF detection results with those from the generic STA/LTA and evaluate the detection performance statistics of the proposed fast MF implementation. The fast MF algorithm performs well with the large data set, with higher precision and accuracy rates, and does not require substantial manual selection of desired events as in the STA/LTA.

## 4.1 Introduction

In microseismic monitoring, microseismic signals are often tiny induced earthquakes with weak amplitudes and negative magnitudes, which humans can not feel (Eaton, 2018). These events are captured by highly sensitive sensors. During hydraulic fracturing treatments, the sensors often record the microseismic data continuously at a high sample rate over days or weeks; thus, validating the microseismic events is time-consuming. Different automated approaches have been proposed to accelerate event detection. The short-term average over long-term average (STA/LTA) is a traditional triggering-based method that considers potential events as sudden increases in amplitude or energy (Allen, 1978; Trnkoczy, 2012). The STA/LTA is insensitive to weak events and tends to incorrectly detect high-amplitude noise such as tube waves and electrical noise; thus, it often has a low precision rate (Akram & Eaton, 2016;

Trnkoczy, 2012; Vaezi & van der Baan, 2015). Another triggering-based method is the power spectral density (PSD), which works better with weak events than the STA/LTA. However, the PSD method cannot handle transient or time-varying noise, including noise originating from ambient or anthropogenic sources, as it assumes the background noise is stationary (Vaezi & van der Baan, 2015). Cross-correlation-based detectors, including matched filter and subspace detectors, are pattern-recognition methods. These methods detect events based on the similarities in waveforms with the template events, often have a higher precision rate, with fewer false triggers, and work better with noisy data (Bui & van der Baan, 2020; Gibbons & Ringdal, 2006; Gibbons, 2022). Machine learning-based approaches such as Akram et al. (2017), Perol et al. (2018), Chen et al. (2019), Dokht et al. (2019), Mousavi et al. (2019), Qu et al. (2020), Othman et al. (2021), Zhang et al. (2021), Birnie and Hansteen (2022), are also emerging in event detection with promising performances. However, these methods often require upfront efforts for preparing large training data sets. Also, there are not many microseismic training data sets. Without the training data that are complete and fully representative of the task, the ability to adapt properly to new data sets is not guaranteed (Zhang & van der Baan, 2021, 2022).

Because of its simplicity and high detection capacity, this study focuses on the matched filter method. The normal cross-correlation (a measure of the similarity of two signals) computation is often slow due to the computationally intensive process of calculating the normalization coefficients per time window. I thus build a fast matched filter (MF) algorithm using a fast normalized cross-correlation (NCC) technique proposed by Lewis (1995) in which the template events are cross-correlated with the continuous data to generate an NCC coefficient matrix for the detection. I also use a recursive STA/LTA formula and a multiplexing technique to accelerate the detection process and obtain an efficient NCC calculation. The recursive STA/LTA speeds up the template extraction, while the multiplexing technique reformats the data and simplifies mathematical expressions in the NCC computation. The multi-

plexing technique turns the 3-component (3C) data/templates into single continuous data streams, which enables parallel computing of the NCC calculation in the MATLAB environment.

The proposed fast MF algorithm works well with big, noisy microseismic data sets. In the following, I fully describe how the fast MF algorithm works and compare its detection performance on a 1.2 terabyte microseismic data set with the generic STA/LTA method.

## 4.2 Methodology

### 4.2.1 Fast MF detection theory and workflow

The matched filter (MF) is a cross-correlation-based detection method (Gibbons & Ringdal, 2006). Unlike the generic STA/LTA (Allen, 1978; Trnkoczy, 2012), which requires no information on the signals to be detected, the MF method searches for known signals (also known as template events/master events/parent events) (Gibbons & Ringdal, 2006). This method identifies potential events based on their similarity with the template events (Gibbons & Ringdal, 2006). The continuous data are cross-correlated with the template events, and the resulting absolute NCC coefficients are used to detect events. The absolute NCC coefficients range from 0 to 1. A high absolute NCC coefficient means a high waveform similarity, and a low absolute NCC coefficient indicates little similarity between the two waveforms (Gibbons & Ringdal, 2006).

The fast MF detection algorithm has 5 steps, including signal preconditioning, template extraction and selection, data multiplexing, fast NCC computation, potential event detection and quality control (QC) of the detection results.

#### **Step 1: Data preconditioning**

Like other detectors, the MF method works more efficiently on preconditioned data since this step reduces the unwanted noise and improves data quality (Maxwell et al.,

2008; Song et al., 2014). Frequency filters are the simplest methods for noise attenuation (Maxwell, 2014). However, the preferred option is to minimize the involvement of filters as much as possible and preserve the signals (Maxwell, 2014). Microseismic data often contain both low- and high-frequency noise; thus, the amplitude spectrum is carefully analyzed to design a suitable bandpass filter to attenuate the noise outside the signal’s frequency bandwidth.

## **Step 2: Choosing template events**

After denoising, a representative set of template events is required to capture all significant microseismic sources in the data and avoid duplicate detections. Template events should have a high signal-to-noise ratio (SNR) (e.g., clear P- and S-phases). The STA/LTA method is used to extract the template events since this method does not require any knowledge of the signals to be detected. The traditional STA/LTA often computes the ratio between the signal’s absolute average amplitude or energy in the short-time and long-time windows, with the short-time window (STA) being sensitive to a sudden increase in amplitude/energy and the long-time window (LTA) representing the background noise level (Akram & Eaton, 2016; Eaton, 2018; Trnkoczy, 2012). The STA and LTA window lengths are selected based on the dominant period of the signals (Akram & Eaton, 2012; Trnkoczy, 2012). This study speeds up the STA/LTA ratio calculation using a recursive formula (Allen, 1978; Bui & van der Baan, 2020; Withers et al., 1998). The recursive STA/LTA helps to avoid repeat summations of long data vectors in the memory, effectively reducing the computation time of the STA/LTA ratios. A high trigger detection threshold is also used for template detection to ensure template events of superior quality are used.

The chosen template events must also be distinctive to prevent duplicated events. For this reason, hierarchical clustering is used to group the potential template events extracted from the recursive STA/LTA into different groups. Then, one representative template event is selected from each group for the matching purpose. The hierarchical agglomerative clustering helps to visualize the clustering results represented by a

dendrogram to guide our cluster selection (Everitt et al., 2011). The clustering step starts with each microseismic event as a single cluster, merging clusters in successive steps until all form a single cluster (Everitt et al., 2011). The input for clustering is a dissimilarity or distance matrix  $D$ , which is given as

$$D_{\mathcal{T}_1, \mathcal{T}_2} = 1 - C_{\mathcal{T}_1, \mathcal{T}_2}, \quad (4.1)$$

where  $D_{\mathcal{T}_1, \mathcal{T}_2}$  may be viewed as a measure of inter-event distance in waveform similarity space for template events  $\mathcal{T}_1$  and  $\mathcal{T}_2$ ;  $C_{\mathcal{T}_1, \mathcal{T}_2}$  represents the maximum waveform correlation between template events  $\mathcal{T}_1$  and  $\mathcal{T}_2$  (Arrowsmith & Eisner, 2006).

The dendrogram resulting from clustering has dissimilarity on the vertical axis and hierarchical relationships on the horizontal axis. The dendrogram guides the selection of an appropriate number of clusters. The dissimilarity threshold used to cut the hierarchical tree in the dendrogram is context-dependent. It should not be too low or too high. A low threshold value can not preserve waveform variations, while a high threshold value will lose waveform sensitivity (Song et al., 2014). The threshold should be the value that best detects any large gap between two successive hierarchy levels (Song et al., 2014).

### **Step 3: Multiplexing**

After obtaining a good set of representative template events, a multiplexing technique introduced by Harris and Paik (2006) is used to reformat the 3-component (3C) data and templates. This multiplexing step turns the 3C data/templates into single continuous data streams, simplifying the mathematical expressions and supporting an efficient cross-correlation computation between the template and data. Instead of computing the cross-correlation function on the 3C data streams, I only need to calculate the function on a single data stream. Multiplexing simplifies the cross-correlation computation since only a single correlation coefficient is involved instead of combining correlation coefficients, possibly at different time lags, for all three components (Arrowsmith & Eisner, 2006).

#### Step 4: Fast NCC coefficient computation

After multiplexing, the continuous multiplexed data are cross-correlated with the multiplexed templates using a fast NCC technique proposed by Lewis (1995) to obtain the NCC coefficient matrix. Let  $f(t, r)$  denote the multichannel time series data of the size  $M \times R$  (where  $M$  is the number of time samples,  $R$  is the number of channels (receivers);  $t, r$  are the time sample and receiver indexes with  $1 \leq t \leq M$  and  $1 \leq r \leq R$ ). The template waveform  $\mathcal{T}$  has the size  $N \times R$  (where  $N$  is the number of time samples,  $N < M$ ). The NCC value  $C_{nor}$  at each data point  $(u, v)$  ( $u, v$  are time sample and receiver indexes) for the data  $f$  and the template  $\mathcal{T}$  is given as (Briechele & Hanebeck, 2001; Lewis, 1995)

$$C_{nor}(u, v) = \frac{\sum_{t,r} [f(t, r) - \bar{f}_{u,v}] [\mathcal{T}(t - u, r - v) - \bar{\mathcal{T}}]}{\sqrt{\sum_{t,r} [f(t, r) - \bar{f}_{u,v}]^2 \sum_{t,r} [\mathcal{T}(t - u, r - v) - \bar{\mathcal{T}}]^2}}, \quad (4.2)$$

where  $\bar{f}_{u,v}$  is the mean value of  $f(t, r)$  within the region of the template and  $\bar{\mathcal{T}}$  is the mean value of the template  $\mathcal{T}$ .

A MATLAB built-in function *normcorr2* is used to calculate NCC coefficient  $C_{nor}(u, v)$  in equation 4.2. This 2D normalized cross-correlation function is built based on Lewis's technique. It computes the normalized cross-correlation of template and data matrices, resulting in a matrix containing the correlation coefficients. To enable parallel computing in the MATLAB environment through *par-for* in for-loop iterations and speed up the calculation, the cross-correlation function is performed on each receiver separately along with the time series of the multiplexed data, which turns the correlation calculation from 2D to 1D. Thus the dependence on the receiver index  $v$  can be dropped; that is, equation 4.2 is simplified as

$$C_{nor}(u) = \frac{\sum_t [f(t) - \bar{f}_u] [\mathcal{T}(t - u) - \bar{\mathcal{T}}]}{\sqrt{\sum_t [f(t) - \bar{f}_u]^2 \sum_t [\mathcal{T}(t - u) - \bar{\mathcal{T}}]^2}}. \quad (4.3)$$

The numerator and denominator of equation 4.3 are calculated separately. The numerator can be rewritten as

$$N(u) = \sum_t f(t) (\mathcal{T}(t - u) - \bar{\mathcal{T}}) - \bar{f}_u \sum_t (\mathcal{T}(t - u) - \bar{\mathcal{T}}). \quad (4.4)$$

Substituting  $\mathcal{T}'(t - u) = \mathcal{T}(t - u) - \bar{\mathcal{T}}$ , equation 4.4 becomes

$$N(u) = \sum_t f(t)\mathcal{T}'(t - u) - \bar{f}_u \sum_t \mathcal{T}'(t - u). \quad (4.5)$$

Since  $\mathcal{T}'(t - u)$  has a zero mean and thus also a zero-sum, the term  $\bar{f}_u \sum_t \mathcal{T}'(t - u)$  is zero. Equation 4.5 can be rewritten as (Lewis, 1995)

$$N(u) = \sum_t f(t)\mathcal{T}'(t - u). \quad (4.6)$$

Equation 4.6 is a convolution of the data  $f(t)$  with the reversed template  $\mathcal{T}'(-t)$  and can be computed by the fast Fourier Transform (Briechle & Hanebeck, 2001; Lewis, 1995).

The bottleneck of equation 4.3 is the denominator since this cannot be computed using fast Fourier transforms. For the denominator, the term  $\sum_t [f(t) - \bar{f}_u]^2$  has to be recalculated at each time index  $u \in [1, M - N + 1]$ , whereas the term  $\sum_t [\mathcal{T}(t - u) - \bar{\mathcal{T}}]^2$  has to be calculated only once. Unfortunately, the denominator is needed to obtain a normalized correlation coefficient such that both strong and weak events can be detected. The issue is compounded if many different templates are used since each detection is based on the normalized correlation coefficient exceeding some threshold.

The term  $\sum_t [f(t) - \bar{f}_u]^2$  in the the denominator can be rewritten as follows (Briechle & Hanebeck, 2001; Lewis, 1995)

$$\sum_t [f(t) - \bar{f}_u]^2 = \sum_t f^2(t) - 2\bar{f}_u \sum_t f(t) + \sum_t \bar{f}_u^2. \quad (4.7)$$

The sum  $\sum_t$  is evaluated over the region of the template; thus, I have  $u \leq t \leq u + N - 1$ . With (Briechle & Hanebeck, 2001)

$$\sum_t (\bar{f}_u)^2 = N \left( \frac{1}{N} \sum_t f(t) \right)^2, \quad (4.8)$$

and

$$\bar{f}_u = \frac{1}{N} \sum_t f(t), \quad (4.9)$$

equation 4.9 is rewritten as (Briechle & Hanebeck, 2001)

$$\sum_t [f(t) - \bar{f}_u]^2 = \sum_t f^2(t) - 2\frac{1}{N}(\sum_t f(t))^2 + \frac{1}{N}(\sum_t f(t))^2 = \sum_t f^2(t) - \frac{1}{N}(\sum_t f(t))^2. \quad (4.10)$$

Lewis (1995) proposes an efficient way to calculate the denominator, which uses the summed-area table introduced by Crow (1984) in computer graphics and popularized by Lewis (1995) in computer vision. A summed-area table is an algorithm for quickly and efficiently generating the sum of values in a rectangular subset of the grid (Crow, 1984). The main idea of Lewis’s technique is to precalculate sum tables containing the integral over the waveform data  $f(t)$  and the squared waveform data  $f^2(t)$  (running sum) once for each receiver signal  $f$  in equation 4.9 (Briechle & Hanebeck, 2001; Lewis, 1995). These tables are used for efficient calculation of the term  $\sum_t [f(t) - \bar{f}_u]^2$  at each point ( $u$ ). The sum tables of the waveform data  $f(t)$  and the squared waveform data  $f^2(t)$  can then be obtained by calculating the column-wise prefix-sums (cumulative sums) and then the row-wise prefix-sums of the input data (represented in a matrix form with rows and columns) (Crow, 1984; Emoto et al., 2018).

### **Step 5: Event detection and QC of the detection results**

A potential event is identified when the NCC coefficient is higher than a user-defined trigger threshold, which strongly depends on the data quality and permitted variation in waveforms. An appropriate threshold (that gives a suitable trade-off between the number of true events, false alarms, and missed events) can be estimated pragmatically via testing pilot data using different threshold values between 0 and 1 or analytically through histograms of the cross-correlation values between pairs of template events and between the template events and randomly generated noise samples in the pilot data (Harris & Paik, 2006). Testing can quickly provide a good initial estimate of the trigger threshold since the data often have varying background noise. The analytical way ensures that the chosen threshold captures most of the true events in the data and does not generate many false alarms.

The last step is to inspect the detection results and classify the detected event, which is often subjective, depending on the processing purposes. Generally, for an event, the detection process can result in one of four possible outcomes: true positive, false positive, true negative, and false negative. A true positive (true event) occurs when an event is correctly identified, while a false positive (false trigger/false alarm) is when noise is incorrectly detected as a potential event. A true negative is when an event does not happen, and it is correctly detected as it does not occur. A false negative (missed event) is when an event occurs, but the detector fails to recognize it as a potential event.

### 4.2.2 Detection performance statistics

To assess the detection performance of the algorithm, I use the true positives (TP), true negatives (TN), false positives (FP), and false negatives (FN) to compute precision, recall, and accuracy rates. The precision is defined as the ratio between the number of TP and the total number of TP and FP, which is given by

$$Precision(\sigma) = \frac{TP(\sigma)}{TP(\sigma) + FP(\sigma)}, \quad (4.11)$$

where  $TP(\sigma)$  and  $FP(\sigma)$  are the number of true positives and false positives when using a detection threshold  $\sigma$ . The precision rate represents how useful the detection results are. The recall rate is the ratio between the TP and the total of TP and FN, which is given by

$$Recall(\sigma) = \frac{TP(\sigma)}{TP(\sigma) + FN(\sigma)}, \quad (4.12)$$

where  $TP(\sigma)$  and  $FN(\sigma)$  are the number of true positives and false negatives when using a detection threshold  $\sigma$ . The accuracy rate is the ratio between the sum of TP and TN versus the sum of TP, TN, FP, and FN, which is given by

$$Accuracy(\sigma) = \frac{TP(\sigma) + TN(\sigma)}{TP(\sigma) + TN(\sigma) + FP(\sigma) + FN(\sigma)}, \quad (4.13)$$

where  $TP(\sigma)$ ,  $FP(\sigma)$ ,  $TN(\sigma)$ , and  $FN(\sigma)$  are the number of true positives, false positives, true negatives, and false negatives when using a detection threshold  $\sigma$ ,

respectively.

## 4.3 Implementation and Results

### 4.3.1 Data overview

I implement the fast MF algorithm on 1.2 terabytes of downhole microseismic data emitted from 78 hydraulic fracturing treatment stages in 4 horizontal wells (Bui & van der Baan, 2020). The data are continuously recorded at a high sampling rate of 0.25 ms over about 326 hours by 30 3C receivers in the vertical monitoring array and 16 3C receivers in the horizontal monitoring array. The following subsections explain each implementation step using example data sets and then show the detection results of the full data set.

### 4.3.2 Fast MF implementation

#### Step 1: Data preconditioning

I use a bandpass filter to reduce the noise in the full data set before cross-correlation. Spectral analysis shows that the dominant frequency of the microseismic signal ranges from 60 to 300 Hz with a peak frequency of around 150 Hz. I thus design the bandpass filter with two corner frequencies [60, 300] Hz to filter the data. Figure 4.1 shows waveform data examples before and after filtering. The onsets of P- and S-phases are invisible before filtering due to noise (Figure 4.1a). After filtering, the noise has been significantly attenuated; I observe the P-phase at around 7.27 s and the S-phase at around 7.38 s (Figure 4.1b).

#### Step 2: Choosing template events

Next, I extract a set of potential template events for each treatment stage using the recursive STA/LTA. The recursive STA/LTA helps speed up the template detection and selection. Figure 4.2 illustrates the fast performance of the recursive STA/LTA compared with the conventional STA/LTA, which directly sums the signal's energy in the short and long windows, averages by the number of data samples, and computes

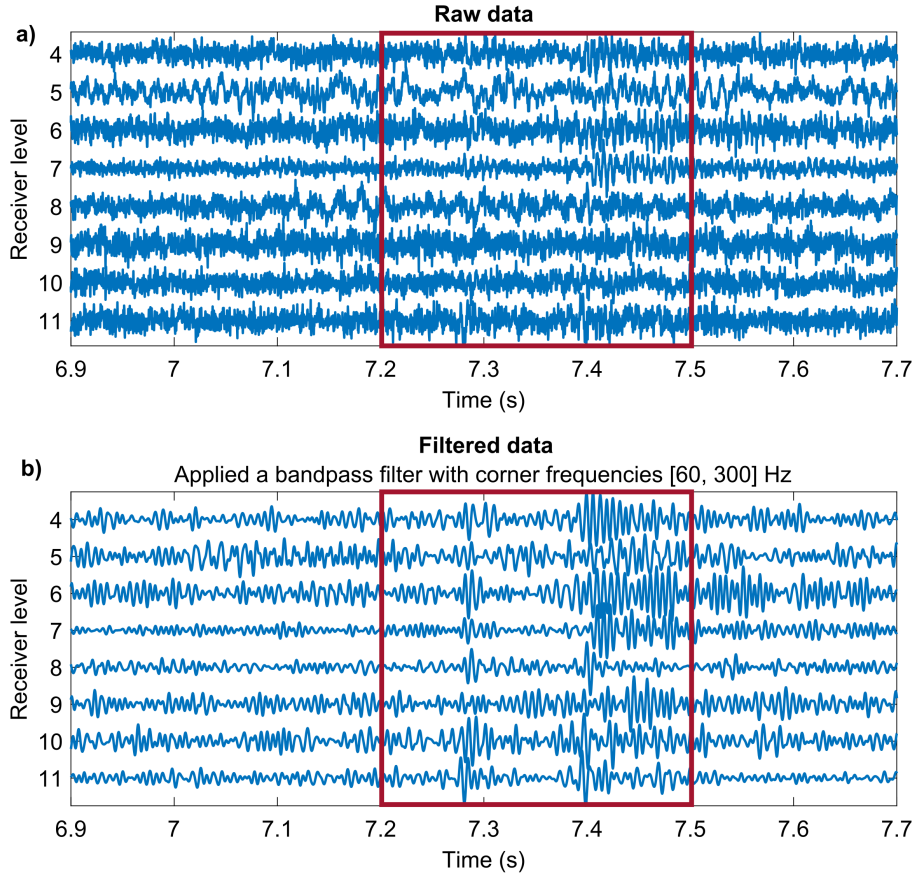


Figure 4.1: (a) Raw data, (b) Filtered data. After filtering, I can observe significant data enhancement with more visible P- and S-phases (highlighted by the red rectangle). The P-wave onset is at about 7.27 s, followed by the S-wave at 7.38 s.

the STA/LTA ratios. With the same data input (Figure 4.2a) and parameter setting, the recursive method only takes 0.01 s to compute the STA/LTA ratios, which is 185 times faster than the conventional STA/LTA. Figure 4.2b and 4.2c shows that the recursive STA/LTA yields a better response with clear peaks and a broader range of the STA/LTA ratio values than the conventional STA/LTA, and thus supports a more accurate trigger threshold to separate microseismic events and noise.

For the parameter setting, I set the STA window length 3 times the event's dominant period and the LTA window length 5 times longer than the STA window. Since the microseismic signal has a dominant period of about 0.0065 s, the STA window is 0.02 s, and the LTA window is 0.1 s. To obtain high SNR template events, I use a

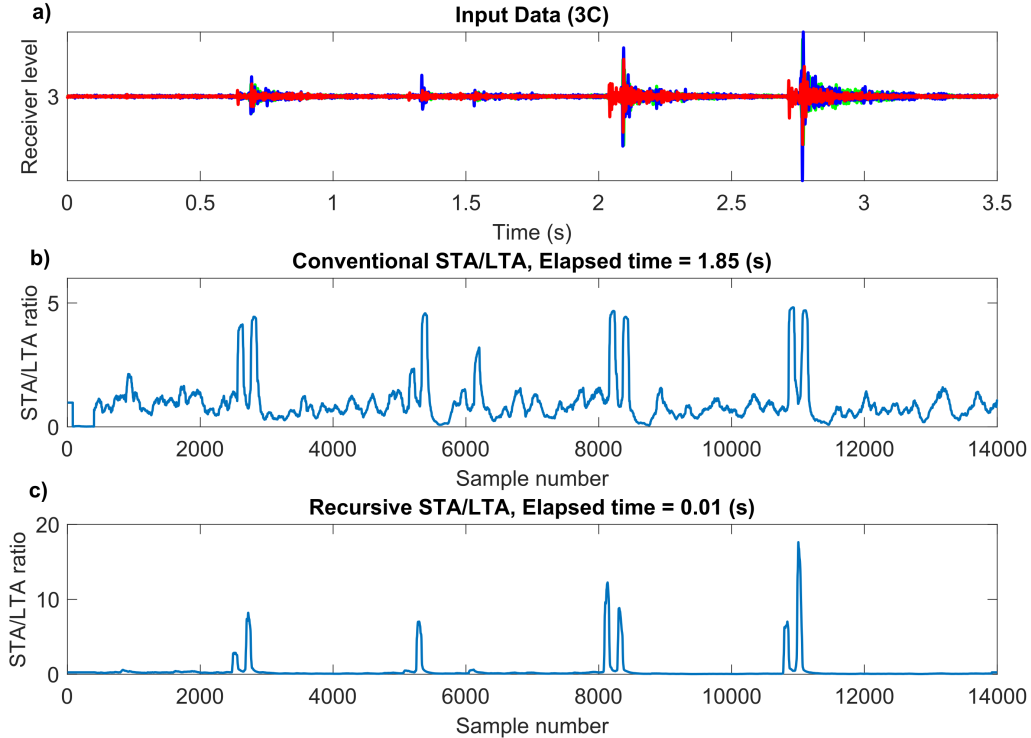


Figure 4.2: Performance of the conventional and recursive STA/LTA. (a) 3C input data (the blue and green represent the two horizontal components, and the red represents the vertical component). (b) STA/LTA ratios obtained from the conventional STA/LTA with a computation time of 1.85 s. (c) STA/LTA ratios obtained from the recursive STA/LTA with a computation time of 0.01 s.

high detection threshold of 8, and at least two-thirds of the receivers (20 receivers for the vertical monitoring array and 10 receivers for the horizontal monitoring array) must observe the signal. Figure 4.3 displays a chosen template example extracted using the recursive STA/LTA with a clear P-phase at about 0.4 s and an S-phase at around 0.5 s.

The potential template events extracted for each treatment stage are clustered into groups of distinctive events using the agglomerative hierarchical clustering method. Then, a representative template event is selected for each group to use for MF detection. This template selection step is performed for microseismicity in all 78 treatment stages recorded by the vertical monitoring array and 40 out of 78 stages recorded by the horizontal monitoring array. Since it is done repeatedly, this subsection only il-

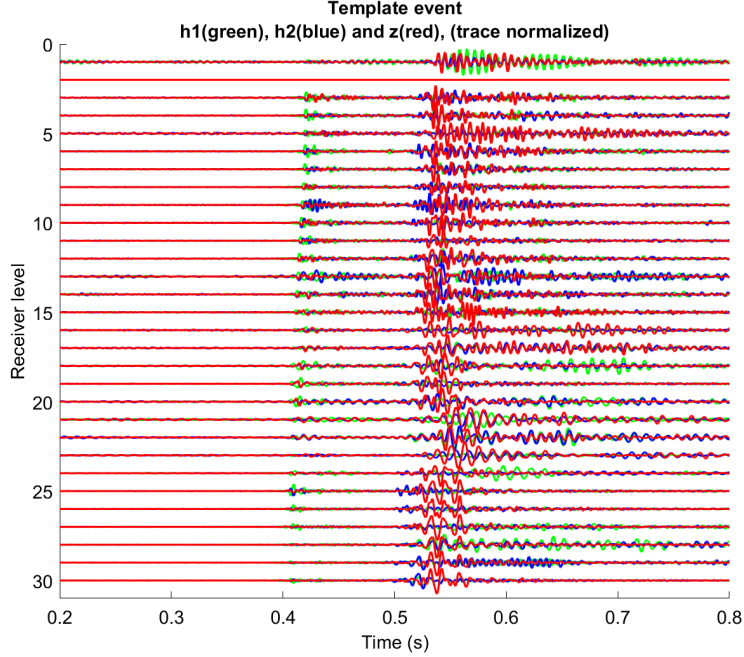


Figure 4.3: A 3C template example with clear P- and S-wave onsets at around 0.4 s and 0.5 s, respectively (the blue and green represent the two horizontal components, and the red represents the vertical component).

illustrates how the potential templates are grouped and representative templates are selected for a sample stage. Figure 4.4 shows the clustering result for stage 18 in treatment well 2 with data recorded by the horizontal array. The recursive STA/LTA with a threshold of 8 extracts 52 potential templates, all having an SNR larger than 20 dB. The dendrogram in Figure 4.4 shows the hierarchical clustering process of 52 potential template events. Events 39 and 45, having the smallest dissimilarity distance (largest correlation value), are initially clustered to form one group. Next, the clustering process continues, forming larger clusters based on dissimilarity distances. For example, the second group (36, 37), the third group (36, 37, 52), and the fourth group (39, 45, 36, 37, 52) are formed consecutively. The clustering continues until all 52 potential templates have been clustered into a single group. To ensure distinctive templates, I choose a threshold of 0.15 to cut the hierarchical tree, resulting in 10 clusters. Among them, 3 main clusters have more than one event and 7 different clusters have only one event. I only consider the 3 main clusters for detection pur-

poses (Figure 4.4). In each cluster, I pick one representative template event. Thus, this treatment stage has 3 representative template events. The template selection process remains consistent across all treatment stages, with each stage having a few representative template events (e.g., 1, 2, or 3, depending on the repetitiveness of the seismic sources).

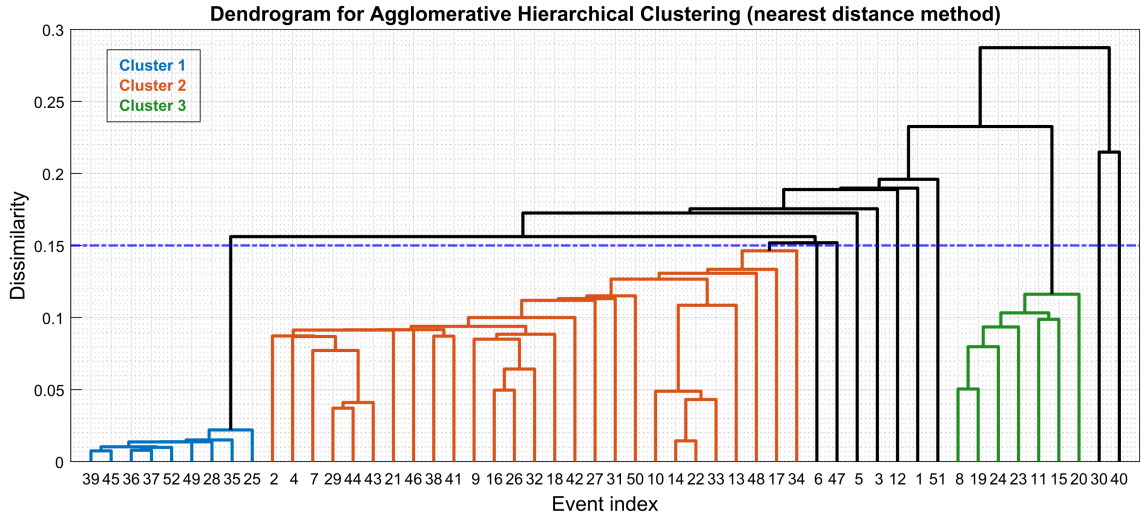


Figure 4.4: Dendrogram illustrating the results of agglomerative hierarchical clustering with 3 main clusters for the potential templates extracted from stage 18, treatment well 2 (recorded by the horizontal array) using the recursive STA/LTA.

### Step 3: Multiplexing

Then, I multiplex the 3C selected template events and data to reformat them into single data streams. Figure 4.5 shows the multiplexed template resulting from the 3C template event shown in Figure 4.3. The 3C template has a length of 0.8 s, and its multiplexed version has a length of 2.4 s. To facilitate an efficient NCC computation in the next step, I window the multiplexed template from 1.1 s to 1.9 s (highlighted by the orange rectangle in Figure 4.5) to only include the P- and S-phases and discard the noise outside this window. Trimming the template data segment speeds up the NCC computation and generates higher NCC values that enhance the detection process.

### Step 4: Fast NCC coefficients

After multiplexing, I cross-correlate the multiplexed template with the multiplexed

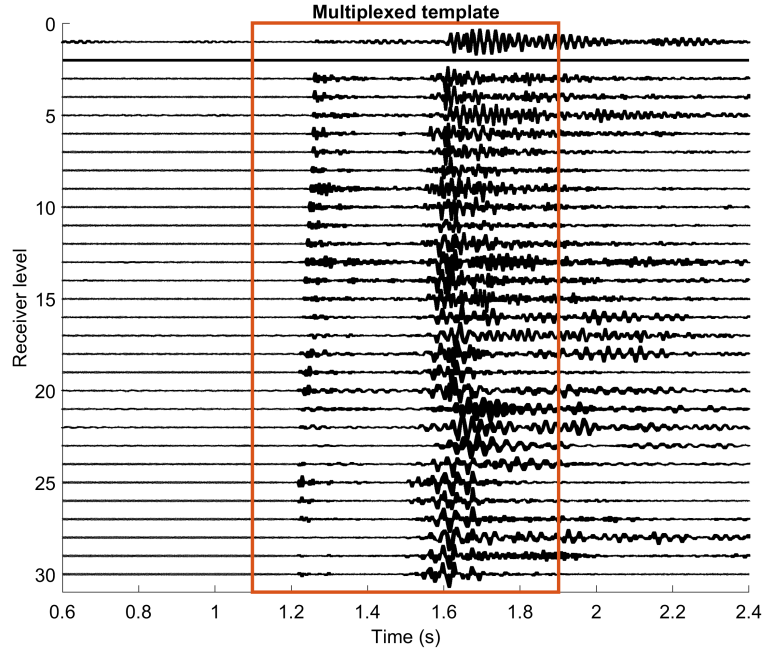


Figure 4.5: Example of a multiplexed template. After multiplexing, the 3C template (Figure 4.3 is reformatted to a single data stream. I window the template waveform (highlighted by the orange rectangle) to support a more efficient NCC computation.

continuous data using Lewis’s fast NCC computation technique to obtain the NCC coefficients matrix. The cross-correlation function is performed on each receiver level along with the time series of the multiplexed data to utilize parallel computing in the MATLAB environment. To assess how the fast NCC technique accelerates the computation, I first implement equation 4.3 to cross-correlate a template event of size  $3201 \times 30$  (time samples  $\times$  receivers) and a short data segment of size  $12,000 \times 30$  (time samples  $\times$  receivers). Then, I compare the computation time with the normal NCC computation (equation 3 in Gibbons and Ringdal (2006)), which computes the inner product of the time-series inputs (template and data) for each receiver and normalizes it using the square root of the product of the sum of squares of both inputs.

The test is performed on a computer having a CPU with a clock speed of 3.20 Gigahertz. The normal NCC formula (Gibbons & Ringdal, 2006) takes 79.755 s to compute the NCC coefficients, whereas the fast NCC technique (Lewis, 1995) takes only 0.178 s, approximately 450 times faster. Similarly, I test the cross-correlation

computation on a data segment 5 times longer (with a size of 60,000 time samples x 30 receivers). With the same template data (with a size of 3201 time samples x 30 receivers), the normal NCC formula (Gibbons & Ringdal, 2006) takes 546 s to complete the computation, while Lewis’s fast NCC technique takes only 1.2 s to generate the NCC coefficients matrix, which is about 455 times faster. Thus, the fast NCC technique is significantly more efficient than the normal NCC computation.

### **Step 5: Event detection and QC of the detection results**

To determine an appropriate detection threshold applicable to the full data set, I test different threshold values, including 0.4, 0.35, 0.3, 0.25, 0.2, and 0.15, on a 2-hour pilot data set from a random treatment stage in well 2, recorded by 30 3C sensors in the vertical monitoring array. To assess the detection performance statistics using precision, recall and accuracy rates (equations 4.11, 4.12, and 4.13), I classify the detection results of the pilot data set into true events (true positives), false alarms (false positives), true negatives (noise records), and missed events (false negatives). True events (true positives) include those with clear P- and S-phases (excellent events) and those with clear P- or S-phases (probable events). Figure 4.6 shows an excellent event example with both P- and S-phases visible. Figure 4.7 displays a probable event example with only the S-phase visible. False alarms (false positives/triggers) are noise records without clear P- and S-phases. Figure 4.8 shows a noise record example. To estimate the number of events missed by the fast MF, I detect the potential events in the pilot data using an STA/LTA with a threshold of 2. Using the STA/LTA with such a low threshold helps capture “all” 114 potential events and reveal the differences (the number of missed events) in the number of events detected by MF.

Table 4.1 shows the testing results of the fast MF with different detection thresholds. The fast MF has a 100% precision rate when using threshold values not smaller than 0.2 since there are no noise records incorrectly identified as true events by the fast MF when using these detection thresholds. When the threshold is lowered to 0.15, the precision rate of the fast MF drops significantly to 61.41% since it has 71

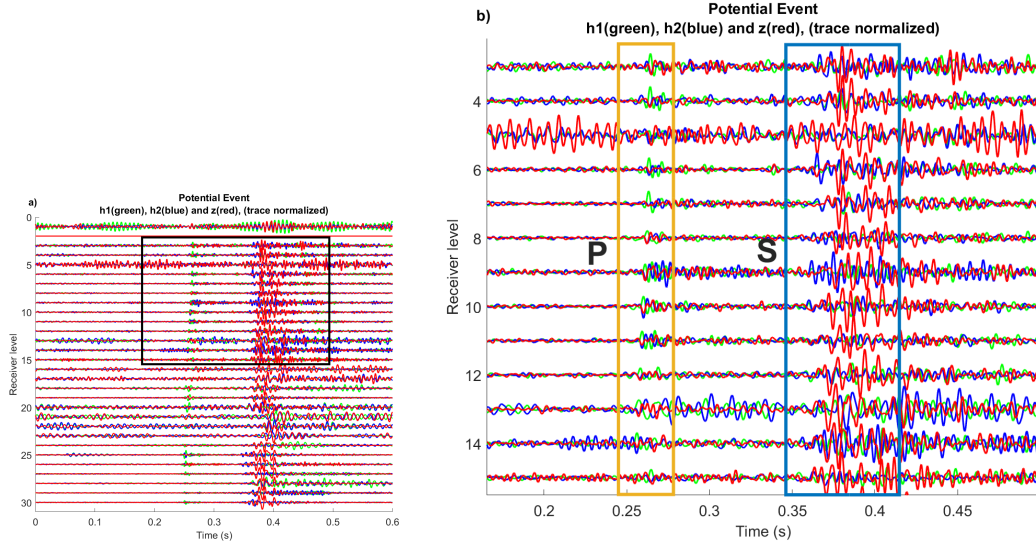


Figure 4.6: (a) Excellent event example. This true event has both clear P- and S-phases. b) A zoom section showing the P- and S-phases (highlighted by the orange and blue rectangles). The data have 3 components, with 2 horizontal components indicated in green and blue and a vertical component indicated in red.

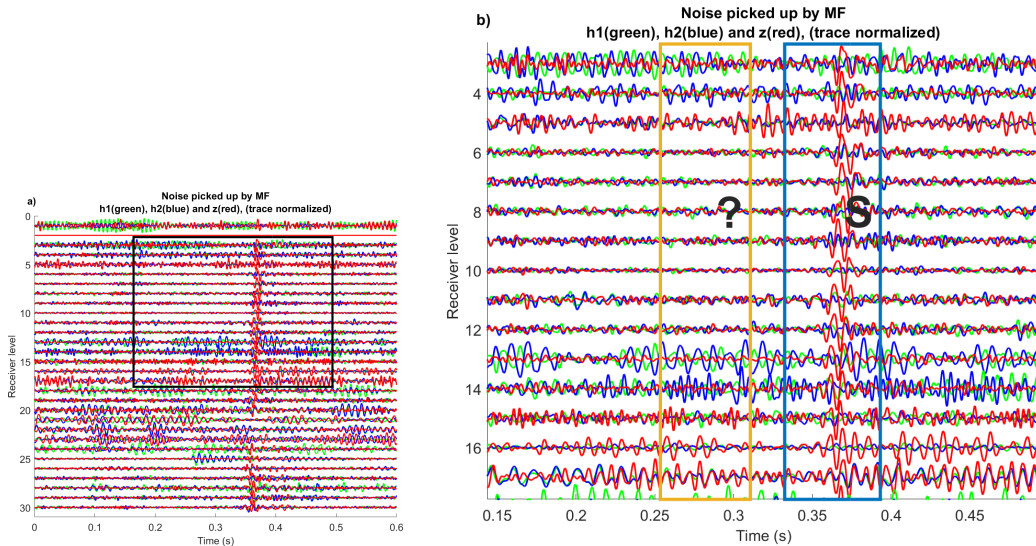


Figure 4.7: (a) Probable event example. This true event has unclear P- and clear S-phases. b) A zoom section showing the P- and S-phases (highlighted by the orange and blue rectangles). The data have 3 components, with 2 horizontal components indicated in green and blue and a vertical component indicated in red.

false alarms. When lowering the detection threshold from 0.4 to 0.2, the fast MF captures more true events and reduces missed events; thus, an increase in the recall and accuracy rates is observed. Compared with the results from a threshold of 0.20, the

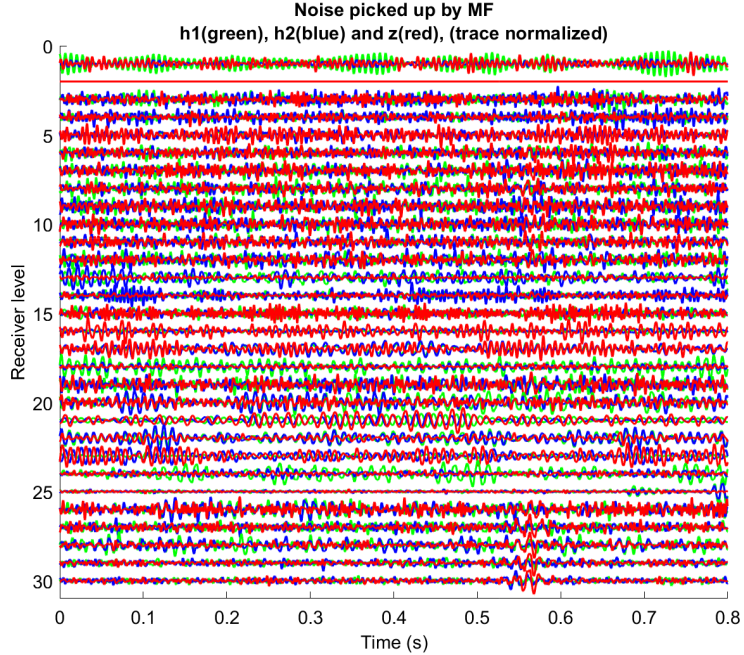


Figure 4.8: Example of a noise record picked up by the fast MF. The data have 3 components, with 2 horizontal components indicated in green and blue and a vertical component indicated in red.

fast MF with a threshold of 0.15 extracts many false triggers; therefore, its accuracy rate decreases from 71.43% to 61.08%, whereas the recall rate increases from 71.43% to 99.12% due to fewer missed events. Manually checking the 29 missed events by the fast MF with a threshold of 0.2 reveals these events are true events but with only one S-phase visible and unclear P-phase. These events are not useful for event locations since both P- and S-picks are used. Thus, a threshold of 0.2 is reasonable because it generates a high precision rate and acceptable recall and accuracy rates. Thus, this pragmatic testing approach provides a quick and effective initial selection of the detection threshold.

To ensure the chosen trigger threshold from testing is appropriate, I also calculate the correlation values between each pair of the potential template events extracted by the recursive STA/LTA from this pilot data set and the correlation values between these template events and noise randomly selected from this test data set. Figure 4.9a shows the histogram of the correlation between template events and noise ran-

Table 4.1: Detection results of the fast MF when using different threshold values on a 2-hour microseismic data set. ( $\sigma$ : detection threshold).

Detector	TPs	FPs	FNs	TNs	Precision (%)	Recall (%)	Accuracy (%)
MF ( $\sigma = 0.40$ )	33	0	81	0	100	28.95	28.95
MF ( $\sigma = 0.35$ )	43	0	71	0	100	37.72	37.72
MF ( $\sigma = 0.30$ )	57	0	57	0	100	50.00	50.00
MF ( $\sigma = 0.25$ )	69	0	45	0	100	60.53	60.53
<b>MF (<math>\sigma = 0.20</math>)</b>	<b>85</b>	<b>0</b>	<b>29</b>	<b>0</b>	<b>100</b>	<b>71.43</b>	<b>71.43</b>
MF ( $\sigma = 0.15$ )	113	71	1	0	61.41	99.12	61.08

domly selected from the pilot data set. Figure 4.9b represents the histogram of the correlation values between pairs of the potential template events. The histograms show that a correlation value of 0.2 is good enough as it produces a few false triggers out of all the correlation samples.

### 4.3.3 Detection results

The proposed fast MF detection is performed separately on each of the 78 treatment stages of the full microseismic data set from 4 treatment wells. Each treatment stage has its own template set, which has either 1, 2, or 3 representative template events depending on the repetitiveness of the seismic sources. These representative templates are extracted, grouped, and selected through the recursive STA/LTA and hierarchical clustering. The multiplexed data is then cross-correlated with the multiplexed templates using the fast NCC technique. A potential microseismic event is detected if the NCC coefficient exceeds the selected detection threshold of 0.2 and at least half of the receivers observe the events. Each event is extracted with a length of 0.8 s to include both P- and S-phases.

To assess the detection performance of the fast MF on this extensive data set, I use the STA/LTA method as a reference. The STA/LTA employs an STA window length of 0.02 s, an LTA window length of 0.1 s, a low threshold of 2, and at least half of

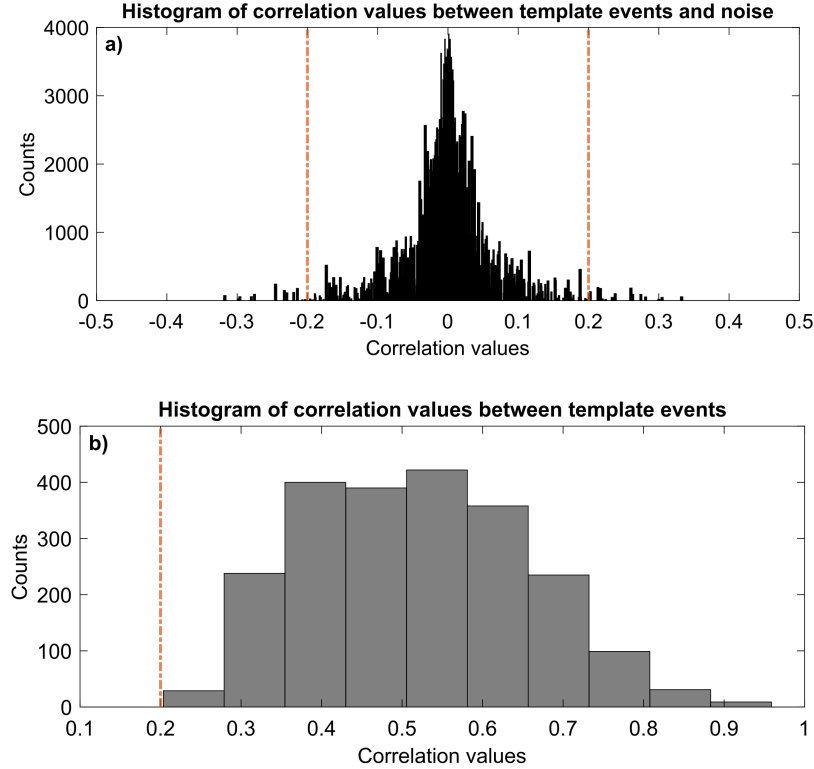


Figure 4.9: (a) Histogram of the correlation values between potential template events extracted by the recursive STA/LTA and noise randomly selected from the pilot data set. (b) Histogram of the correlation values between pairs of potential template events extracted by the recursive STA/LTA from the pilot data set.

the receivers observe the events. The STA/LTA with such a low detection threshold helps to detect “all” potential events from the full data set and reveal the number of events missed by the fast MF. The STA/LTA detection is also applied to each of the 78 treatment stages in the data. A potential event is extracted if the STA/LTA ratio is higher than the defined threshold, with a length of 0.8 s to include both P- and S-phases.

After the detection is completed, I classify the detection results from both MF and STA/LTA and compare their detection performance. In order to use the detected events in subsequent event location and moment tensor inversion, I categorize the detection results into only 2 groups, namely excellent and undesirable events, instead of 4 groups (true positives, false positives, true negatives, and false negatives) as shown in subsection 1.3.2. As mentioned, true events include excellent events (those

with clear P- and S-phases) and probable events (those with clear P- or S-phases). The probable events are true events; however, these events are not useful for further processing in this thesis (e.g., event location in Chapter 6 and moment tensor inversion in Chapter 7) since both P- and S-picks are needed. Probable events and noise records (false alarms) are undesirable events and will be discarded. Due to this classification, it is expected that many true events detected from the full data set will not be used since they are probable events.

The reference STA/LTA detects approximately 55,000 potential events, with many false alarms in the detection results, including tube waves (Figure 4.10a), electrical noise (Figure 4.10b), and high-amplitude random noise. Due to these incoherent noises, manually classifying the STA/LTA detection results is time-consuming. After manual inspection and classification, 21,766 excellent events are obtained from the full data set. Unlike the STA/LTA, the fast MF algorithm extracts nearly 30,000 potential events from this data set. After classification, 19,913 same excellent events are obtained. The classification method leads to approximately one-third of the MF detection results being categorized as undesirable events. However, it should be noted that more than 90% of these detections are probable events. The number of excellent events detected by the fast MF is comparable with the results from the STA/LTA but with approximately 30,000 (MF) instead of 50,000 (STA/LTA) potential events. The MF detection performs fast and generates much fewer false triggers, which significantly reduces the time required for classification. Thus, when considering the computation and manual classification times of both methods, the fast MF is more efficient than the generic STA/LTA when dealing with large microseismic data sets.

Figure 4.11a-d shows the fast MF and STA/LTA detection results of the vertical-array data for all treatment stages in 4 treatment wells. Similarly, Figure 4.12a and 4.12b shows the MF and STA/LTA detection results for horizontal-array data. The results from both vertical and horizontal arrays show that the MF algorithm detects

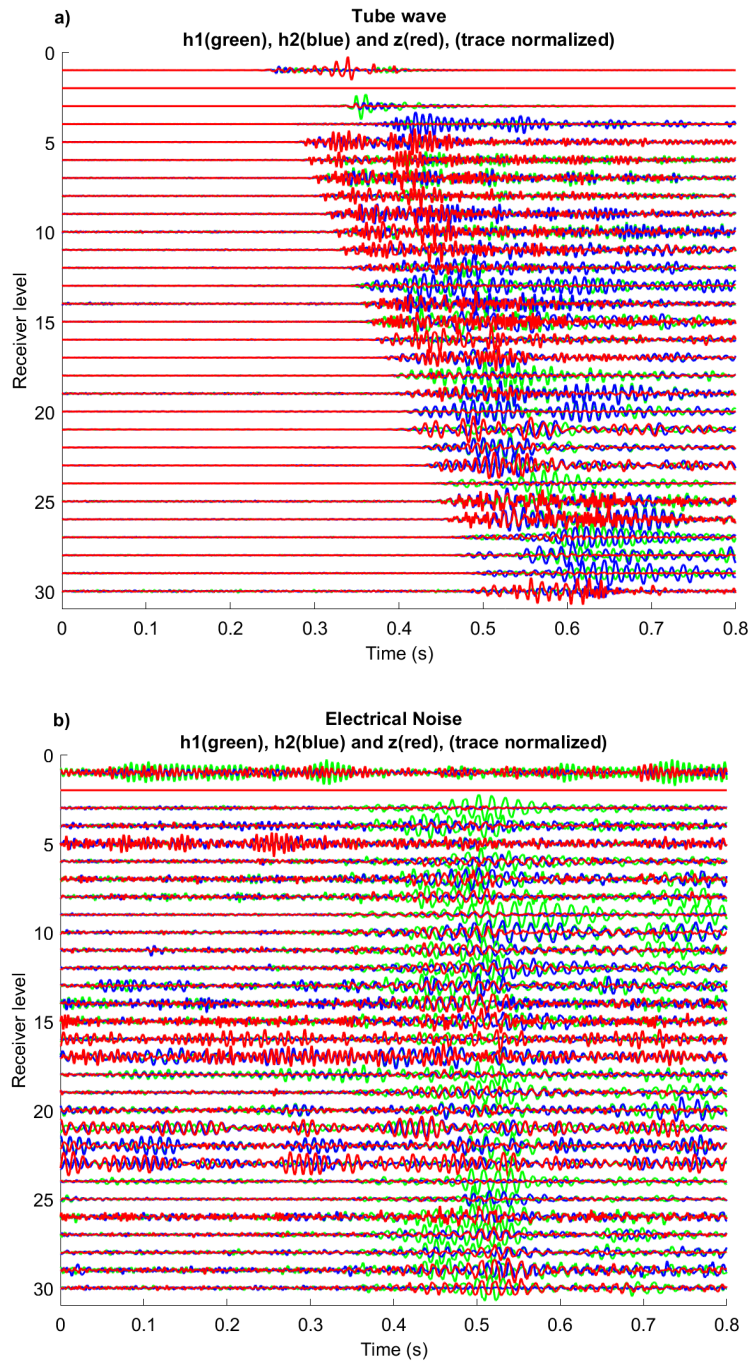


Figure 4.10: Examples of (a) a tube wave and (b) an electrical noise record incorrectly identified as true events by the STA/LTA. The data have 3 components, with 2 horizontal components indicated in green and blue and a vertical component indicated in red.

a comparable number of events as the STA/LTA in each stage.

For the vertical-array data (Figure 4.11a-d), most stages only have one template

event, indicating repetitive microseismic sources. There are only a few stages, such as stages 1 to 8 in well 1, that have two template events, but even in those stages, one template dominates with a higher number of events.

For the horizontal-array data (Figure 4.12a and 4.12b), the last treatment stages (such as stage 20 in well 2 and stages 16 to 20 in well 4) have 3 template events. Although the number of events from template 2 (indicated by the yellow color bar) in these stages is quite considerable, the dominant proportion of detected events from template 1 (indicated by the orange color bar) is still observed.

Overall, the fast MF and STA/LTA detectors show a comparable event distribution, with strong variations of microseismicity between treatment stages within each well. The majority of events are concentrated towards the last treatments near the heel of the wells, with hundreds of events recorded in each stage while others having a few events. For instance, in well 1, stages 13 to 15 have over 400 events each, while stages 1, 2, 7 to 12 have less than 100 events each. In well 3, stage 6 has almost 700 events, while stages 7, 8, 12, and 13 have around 50 events each. A similar trend is observed in wells 2 and 4 for both vertical- and horizontal-array data. The last treatment stages (17 to 20 in well 2 and 16 to 20 in well 4) have a large number of events, with over 400 events in each stage in well 2 and over 200 events in each stage in well 4, while other stages (such as stage 5 in well 2 or stages 1, 4, 7, 12, and 13 in well 4) have only 10 to 20 events. The two independent detection methods yield a similar pattern of event variation between stages, particularly with most events clustered in the later treatment stages close to the heel of the wells. This observation suggests an event anomaly in the event distribution in these treatment wells, which could be due to operational issues, changes in the treatment parameters, or geological/geomechanical changes in the medium rather than detection errors.

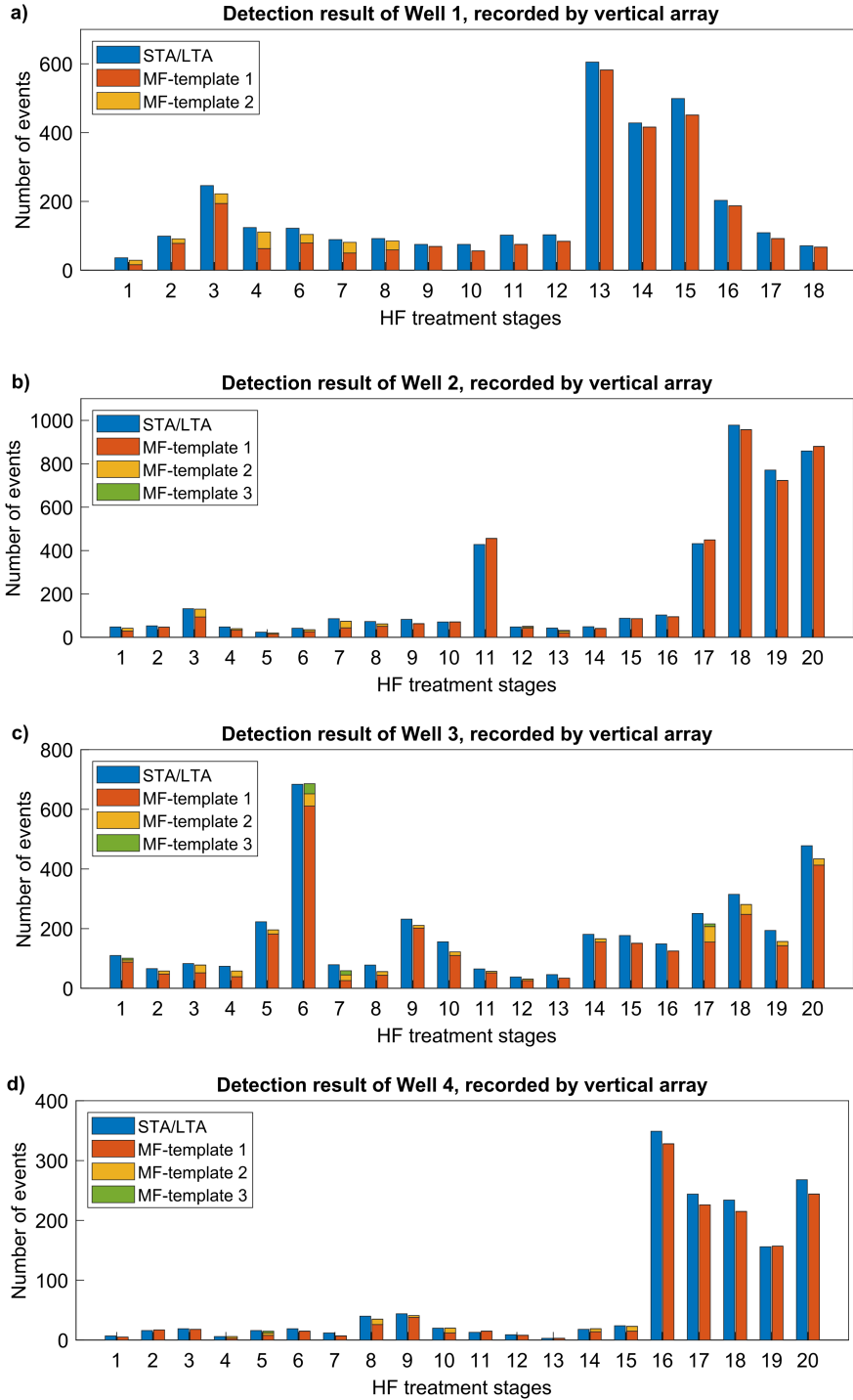


Figure 4.11: Detection results of the fast MF and the STA/LTA on the vertical-array data from 78 treatment stages in 4 treatment wells: (a) Well 1, (b) Well 2, (c) Well 3, and (d) Well 4. STA/LTA results are indicated in blue, while the fast MF results using different representative template events are displayed in other colors. Each treatment stage has its own representative template set, either 1, 2, or 3 templates, depending on the repetitiveness of the sources. MF detection results using templates numbered 1, 2, and 3 are shown in red, orange, and green, respectively.

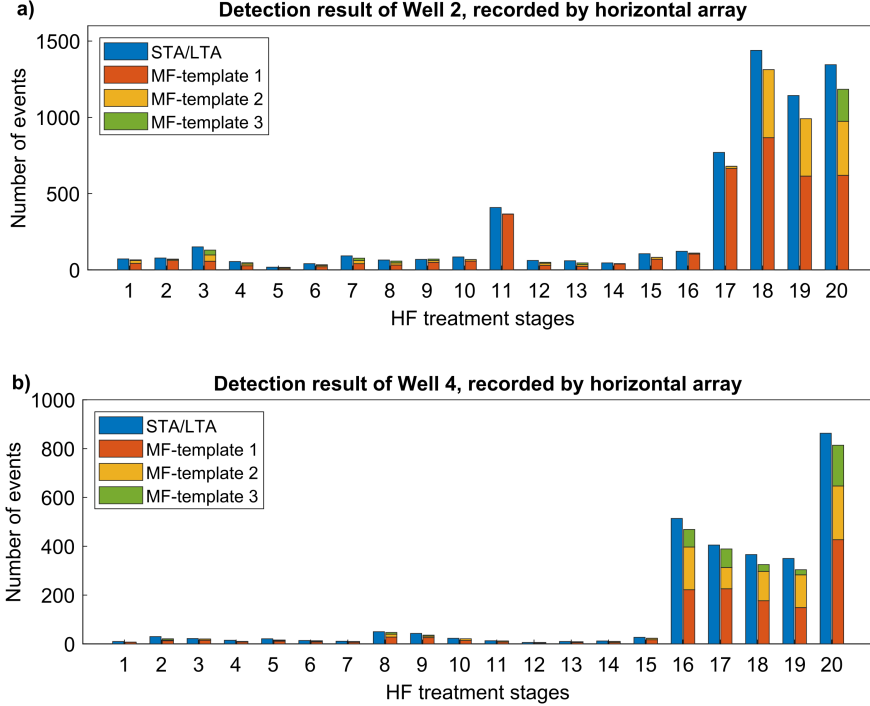


Figure 4.12: Detection results of the fast MF and the STA/LTA on the horizontal-array data from 40 treatment stages in 2 treatment wells: (a) Well 2 and (b) Well 4. STA/LTA results are indicated in blue, while the fast MF results using different representative template events are displayed in other colors. Each treatment stage has its own representative template set, either 1, 2, or 3 templates, depending on the repetitiveness of the sources. MF detection results using templates numbered 1, 2, and 3 are shown in red, orange, and green, respectively.

## 4.4 Discussions

### 4.4.1 Pros and cons of multiplexing

The multiplexing technique has some advantages and disadvantages. However, for this dataset the advantages outweigh the drawbacks, and multiplexing is incorporated into the fast MF detection.

A disadvantage for high-frequency data sets is that the technique may introduce sample-to-sample oscillations (that is, polarity reversals) and decreases cross-correlation coefficients. In cases where two waveforms are highly similar, a high cross-correlation coefficient and, thus, a high detection threshold, e.g., greater than 0.8, should be expected. However, if multiplexing is used before cross-correlation, the

detection threshold is significantly reduced for high-frequency waveforms. For this study, the fast MF is applied on the full data set with a quite low threshold of 0.2. Tests revealed that without multiplexing likely a higher threshold could have been used, but now with the need to handle potentially different detection thresholds for each component (Arrowsmith & Eisner, 2006).

Despite this drawback, the multiplexing technique is very useful in speeding up the MF detection process. It helps simplify the mathematical expression and accelerates the NCC coefficient calculation. When the 3C data are multiplexed, parallel computing can be utilized through the *par-for* command in the MATLAB environment in the NCC coefficient computation step. The *par-for* command in MATLAB executes for-loop iterations in parallel on workers in a parallel pool; thus, it speeds up the NCC coefficient calculation. Furthermore, multiplexing of low-frequency and time-aligned three-component waveforms is much less likely to introduce alternating polarity reversals in the resulting one-component signals, thus allowing to proceed as recommended.

#### **4.4.2 Pros and cons of the MF versus STA/LTA**

Both the fast MF and STA/LTA methods have some pros and cons. The STA/LTA is an incoherent energy detector with potential events detected based on high amplitude or energy compared to the background noise; thus, many uncorrelated noise records, such as tube waves, electrical noise, and high-amplitude noise, can be incorrectly identified as true events. Manual inspection and classification of the STA/LTA detection results of the STA/LTA method is time-consuming. Unlike the STA/LTA, the fast MF is a cross-correlation-based detection method that detects events based on their level of similarity with the template events. Uncorrelated noise records, thus, are not picked up by the fast MF. The application of the fast MF to the full data set shows that when using an appropriate detection threshold, the fast MF generates fewer false alarms than the STA/LTA while detecting a comparable number of true

events. Therefore, with an appropriate detection threshold, the fast MF has higher precision and accuracy rates than the STA/LTA.

The STA/LTA has an advantage that requires little to no information on the signals to be detected. This method can be applied to any waveform data without knowing any prior information about the true events. In contrast with the STA/LTA, the fast MF requires some knowledge of the signal to be detected (also known as a template event/master event/parent event). However, this can be done quickly using the STA/LTA to extract representative templates.

The fast MF is favored with microseismic data generated from repetitive sources for optimal detection performance. In this study, each treatment stage in the full data set has only a few selected representative template events (1, 2, or 3 templates). Applying MF detection to this data is suitable since it does not require running the MF multiple times for a single stage. Even for stages with the maximum number of templates, the fast MF only needs to be executed 3 times. However, for data sets with highly variable waveforms, multiple templates need to be considered, and the fast MF needs to be run multiple times, which might slow down the detection process. Otherwise, if all microseismic sources are not captured in the set of representative template events, the fast MF may have many missed events, reducing its recall and accuracy rates.

#### **4.4.3 Another cross-correlation-based detection alternative**

The subspace detection, introduced by Harris and Paik (2006), is another interesting alternative for microseismic event detection. The subspace detector extends the concept of the matched filter such that a signal subspace is built from a library of template events instead of relying on a single template event during the detection phase (Harris & Paik, 2006). While the matched filter is preferred for detecting events from repetitive microseismic sources, the subspace detector can enhance the ability to capture variations in seismic signals since it uses a library of different template events

during the detection step. Since the subspace detector is also a cross-correlation-based method, incorporating fast NCC coefficient computation into the subspace detection workflow is a promising approach as it can help accelerate the cross-correlation calculation and then the detection.

## 4.5 Conclusions

In conclusion, the fast MF outperforms the STA/LTA when considering the computation, inspection and classification times. The fast MF detects events based on their similarity to the representative template events, reducing many false triggers, such as tube waves and electrical noise, which are often misidentified as potential events by the traditional STA/LTA method. Most importantly, the proposed fast MF workflow works more efficiently for large microseismic data sets than the normal MF method and the STA/LTA. Combining the recursive STA/LTA for the extraction and selection of representative template events, the multiplexing technique for reformatting the data and utilizing parallel computation, and the fast NCC coefficient computation in the fast MF workflow accelerates the event detection process. The fast NCC coefficient computation technique employs summed-area tables to speed up the calculation of the NCC coefficients between the template events and the continuous data. Notably, I obtain results about 450 times faster when computing the NCC coefficients using the fast NCC technique on the test data than when using the normal NCC computation.

# Chapter 5

## Comparison of sparse Gabor-based methods for detection of microseismic events <sup>1</sup>

### Summary

Event detection and selection is a challenging and time-consuming step in microseismic data processing because signals are often embedded in noisy recordings. Automated triggering-based algorithms can detect many potential events in the data. However, their precision rates are often low, thus requiring substantial manual labor to select desired events of interest. This study investigates two time-frequency methods which combine signal enhancement with automated event detection and selection, namely: (1) the sparse Gabor transform and (2) the neighboring block thresholding. Both methods use thresholding in the time-frequency domain to increase signal enhancement, followed by an energy detection criterion, leading to improved event detection with higher precision rates. However, the neighboring block thresholding causes amplitude fidelity issues; I observe changes in the relative and maximum amplitudes of the waveforms reconstructed from the thresholded coefficients. Conversely, the sparse Gabor transform attenuates the noise significantly while preserving the signals. The sparse Gabor transform time-frequency method is thus more suitable for enhanced event detection and subsequent processing, including magnitude estimation

---

<sup>1</sup>This chapter has been published as an article in *Geophysics*.

and moment tensor inversion.

## 5.1 Introduction

Automated event detection is indispensable in microseismic data processing. Various automated methods are introduced to detect and select potential events. One traditional method is the short-term average over long-term average (STA/LTA) algorithm, which is susceptible to sudden increases in amplitude or energy (Allen, 1978; Trnkoczy, 2012). However, the STA/LTA method is an incoherent energy detector and is insensitive to weak events (Trnkoczy, 2012; Vaezi & van der Baan, 2015). It can falsely consider uncorrelated noise, such as electrical noise and tube waves with strong amplitudes, as potential events (Akram & Eaton, 2016; Vaezi & van der Baan, 2015). Another method is the cross-correlation-based detectors which detect events based on the similarities in waveforms with the template events (Gibbons & Ringdal, 2006). These methods often generate fewer false triggers and work better with noisy data; however, they are generally limited to events with similar rupture mechanisms and locations (Bui & van der Baan, 2020). Many recent alternatives based on machine learning approaches, such as Akram et al. (2017), Perol et al. (2018), Chen et al. (2019), Dokht et al. (2019), Mousavi et al. (2019), Qu et al. (2020), Othman et al. (2021), Zhang et al. (2021), Birnie and Hansteen (2022), are also used in event detection and selection. Deep-learning-based methods have promising detection performances, yet, they often require large training data sets, which in turn imply significant upfront efforts to ensure they perform well (Dokht et al., 2019; Mousavi et al., 2019; Perol et al., 2018; Qu et al., 2020). Also, generalization to other data sets is not guaranteed unless the training data are complete and fully representative of the task at hand for both the considered and any future data sets (Zhang & van der Baan, 2021, 2022). Because of its simplicity, I focus on STA/LTA in this paper but combine it with time-frequency methods to enhance detectability and signal quality.

Microseismic data sets can be large since the data are recorded continuously at a

high sample rate (i.e., 0.25 ms) over many hours during hydraulic fracturing treatments. Moreover, potential events are usually embedded in noise. Thus, choosing an appropriate method is crucial to obtain detection efficiency. For instance, Bui and van der Baan (2020) select over 20,000 events, after a short-term average over long-term average (STA/LTA) algorithm detected over 50,000 potential events, yielding a precision rate of 37.50% (precision rate is defined as the ratio of true events to the sum of true events and false triggers). The low precision rate of the STA/LTA algorithm (Bui & van der Baan, 2020) thus requires substantial manual quality control to verify and inspect each potential event. Bui and van der Baan (2020) also propose a fast-matched filter algorithm that was more efficient than the STA/LTA, producing a similar number of detected events with a higher precision rate of 74.12%. However, both detection methods require data preprocessing. Furthermore, not all detected events are of sufficient quality for event localization and subsequent moment tensor inversion (Bui & van der Baan, 2021). Considering that, I aim to (1) detect more useful events for the subsequent processing steps, those with noise attenuated and clear P- and S-phases, and (2) maintain relative amplitudes of P- and S-phases of the detected events. This study, therefore, evaluates two methods that combine signal enhancement with automated detection to increase precision rates, extract events with clear P- and S-phases, and maintain relative amplitudes of all phases to allow for a moment tensor inversion (Eyre & van der Baan, 2015).

I examine two algorithms (Mousavi & Langston, 2016; Sacchi et al., 2009) based on the Gabor transform, a specific implementation of the short-time Fourier transform to compute nonstationary time-frequency representations (Tary et al., 2014). Both algorithms rely on thresholding of the time-frequency coefficients, yet their implementations differ. Sacchi et al. (2009) invert an  $l_2 - l_1$  norm to obtain a sparse representation, whereas Mousavi and Langston (2016) use neighboring block thresholding. I analyze both methods in terms of precision and detection rates, amplitude fidelity, and their suitability for subsequent moment tensor inversion. The latter is

achieved by comparing the ratio of the S-wave/P-wave first arrival amplitudes of the original and denoised waveforms since this ratio reveals pertinent information on whether the event is likely shear- ( $S/P > 5$ ) or tensile- ( $S/P < 5$ ) dominated (Eaton et al., 2014; Pearson, 1981).

## 5.2 Methodology

### 5.2.1 Sparse Gabor transform

The Gabor pair of a time series  $s(t)$  with length  $L_s$  is defined as (Sacchi et al., 2009; Strohmer, 1998)

$$s(t) = \sum_{m=1}^M \sum_{n=1}^N C_{mn} g_{mn}(t - ma) e^{i(2\pi nb/L_s)t}, \quad (5.1)$$

$$C_{mn} = \sum_{t=1}^{L_s} s(t) g_{mn}^*(t - ma) e^{-i(2\pi nb/L_s)t}, \quad (5.2)$$

where  $m$  and  $n$  are the time and frequency samples;  $C_{mn}$  is the Gabor expansion coefficient corresponding to the amplitude of the elementary signal at the time  $ma$ ;  $a$  and  $b$  are the time and frequency shifts, respectively;  $g_{mn}$  and  $g_{mn}^*$  denote the set of synthesis and analysis windows, respectively. The Gabor transform in equation 5.2 is the short-time Fourier transform which uses a Gaussian as the window function. The window width can affect the joint time-frequency resolution of the spectrogram. Increasing the window width results in gaining some resolution in the frequency axis but losing some resolution in the time axis and vice versa.

I aim to obtain a better resolution of the time-frequency representation; thus, I compute a sparse solution for the Gabor coefficients via an inversion using an iterative solver - the fast iterative shrinkage-thresholding algorithm (FISTA) proposed by Beck and Teboulle (2009). The FISTA is designed to minimize the cost function  $J(\hat{\mathbf{C}})$  which is given as

$$J(\hat{\mathbf{C}}) = \|\mathbf{G}\hat{\mathbf{C}} - \mathbf{s}\|_2^2 + \mu\|\hat{\mathbf{C}}\|_1, \quad (5.3)$$

where  $\mathbf{G}$  is the Gabor transform synthesis operator (equation 5.1) represented as a

matrix. Similarly,  $\hat{\mathbf{C}}$  is the Gabor coefficient represented as a vector. Notice that the operation  $\mathbf{G}\hat{\mathbf{C}}$  is executed in an implicit form with no need to form the matrix  $\mathbf{G}$ . In equation 5.3, the first term stands for the  $l_2$  norm of the misfit between the data  $\mathbf{s}$  and the estimated data  $\mathbf{G}\hat{\mathbf{C}}$ . This term measures how well the Gabor expansion fits the data. The second term is the sparsity norm in the form of the  $l_1$  norm, which penalizes the non-sparse solution (Pérez et al., 2013; Sacchi et al., 2009). The sparsity constraint helps retrieve a unique and stable solution for the inversion (Sacchi et al., 2009). The trade-off parameter  $\mu$  controls the weight of two terms in the cost function. To choose  $\mu$ , I run the inversion using the FISTA algorithm with different trial values of  $\mu$  and plot the misfit normalized by the number of samples versus  $\mu$  values. An appropriate trade-off parameter  $\mu$  can be selected based on the resulting plot and the variance of the noise level.

For each FISTA iteration  $j^{th}$ , I compute the sparse solution using (Pérez et al., 2013)

$$\hat{\mathbf{C}}_j = T_{\beta}^{soft}\left(\mathbf{Z}_j - \frac{1}{\alpha}\mathbf{G}^T(\mathbf{G}\mathbf{Z}_j - \mathbf{s})\right), \quad (5.4)$$

where  $\hat{\mathbf{C}}_j$  is the sparse solution,  $T_{\beta}^{soft}(\cdot)$  is a soft-thresholding function,  $\beta$  is a thresholding value ( $\beta = \mu/2\alpha$ ,  $\alpha$  is a constant which is greater than or equal to the maximum eigenvalue of  $\mathbf{G}^T\mathbf{G}$ ),  $\mathbf{G}^T$  is the transpose of  $\mathbf{G}$ ,  $\mathbf{Z}_j$  is a temporary variable. The FISTA converges when the relative change of the cost function between two consecutive iterations is less than a user-defined criterion  $T_0$ ; otherwise, it updates the variable  $\mathbf{Z}_{j+1}$  using

$$\mathbf{Z}_{j+1} = \hat{\mathbf{C}}_j + \frac{t_j - 1}{\frac{1 + \sqrt{1 + 4t_j^2}}{2}}(\hat{\mathbf{C}}_j - \hat{\mathbf{C}}_{j-1}), \quad (5.5)$$

where  $t_j$  is the stepsize ( $t_1 = 1$ ).

## 5.2.2 Neighboring block thresholding

First, I transform the time-series data  $s(t)$  into the Gabor domain using equation 5.2. Then, I normalize the time-frequency coefficients  $C_{mn}$  using a noise level  $\sigma$

estimated by the recursive averaging estimator (Cohen, 2003; Cohen & Berdugo, 2001). After that, I apply a neighboring block thresholding technique proposed by Mousavi and Langston (2016), where the time-frequency plane is segmented into disjoint macroblocks with length  $L_a$  in time and width  $W_a$  in frequency (Mousavi & Langston, 2016). In each macroblock, the time-frequency coefficient is shrunk by an attenuation factor  $\Lambda_{mn}$  calculated from the neighboring coefficients in a square block  $B_s$  (Mousavi & Langston, 2016). The attenuation factor,  $\Lambda_{mn}$ , is given as (Mousavi & Langston, 2016)

$$\Lambda_{mn} = 1 - \frac{\lambda^2}{Y^2}, \quad (5.6)$$

where  $\lambda$  is the threshold level and the denominator  $Y^2$  is the energy of the neighboring coefficients in the square block  $B_s$ . Stein's unbiased risk estimate, an unbiased estimator of the mean-squared error of a nearly arbitrary estimate (Stein, 1981), is used to estimate the optimal block size  $\hat{L}_o$  and the optimal threshold  $\hat{\lambda}$ .

The thresholded time-frequency coefficient  $\hat{C}_{mn}$  is then computed as (Mousavi & Langston, 2016)

$$\hat{C}_{mn} = \Lambda_{mn} \bar{C}_{mn}, \quad (5.7)$$

where  $\Lambda_{mn}$  is the attenuation factor,  $\bar{C}_{mn}$  are the normalized coefficients in the neighboring square block.

### 5.2.3 Detecting events

I use a characteristic function built from the sum of all absolute values of the sparse time-frequency coefficients  $\hat{C}$  from both methods to detect the events. The characteristic function is given as

$$CF(m) = \sum_{n=1}^N |\hat{C}_{mn}|, \quad (5.8)$$

where  $CF(m)$  denotes the characteristic function,  $m$  is the time sample,  $n$  is the frequency sample in equation 5.2, and  $\hat{C}_{mn}$  are the sparse time-frequency coefficients. The characteristic function captures abrupt energy changes associated with potential

microseismic arrivals (Mousavi et al., 2016). A potential event is triggered when the characteristic function value is higher than a user-defined threshold level, similar to a generic STA/LTA approach (Bui & van der Baan, 2020). I reconstruct the detected waveforms from the thresholded coefficients using the inverse transform using equation 5.1 and classify these potential events into groups of true events (those having visible P- and S-phases) or false alarms (noise records), after manual inspection. Invisible weak events, including those with unclear P-/S-phases, are classified as noise records because they are not helpful for the subsequent location and moment tensor inversion steps.

### 5.3 Implementation and Detection Results

For illustration, I run the two discussed algorithms on synthetic and real data examples.

#### 5.3.1 Synthetic Data Example

I create a synthetic microseismic signal with 1024 time samples, a sampling rate of 1 ms, and P- and S-wave onsets at around 0.43 and 0.51 s, respectively (Figure 5.1a). To challenge the algorithms, I create and add bandpass-filtered noise, a colored noise and more complicated than pure white noise (having a flat power spectrum), to the synthetic signal. First, I add white Gaussian noise to the synthetic signal and use a bandpass filter with two corner frequencies [10 150] Hz to extract the colored noise. Then, I add the noise to the original synthetic signal and obtain a noisy synthetic signal (Figure 5.1b) for testing the two discussed algorithms.

#### *Sparse inversion*

I run the Gabor transform on the noisy synthetic signal (Figure 5.1b) using a number of frequency samples  $N = 1024$ , a time shift between Gabor atoms  $a = 2$  samples, and a number of time indices for the Gabor coefficients  $M = L_s/a = 256$  samples. Figure 5.1c shows the resulting spectrogram obtained from the Gabor

transform using equation 5.2 with a Gaussian window width of 5 ms. The window width can be easily chosen based on testing as I can anticipate its effect on the time-frequency resolution.

I then run the sparse inversion using the FISTA algorithm to obtain a better resolution spectrogram. Since the variance of the added noise is minimal, in the order of  $10^{-14}$ , a trade-off parameter of  $8 \times 10^{-8}$  is enough to denoise and retrieve the signal. The trade-off parameter is estimated by computing different trial trade-off values and comparing the variance of the misfit between the data and the estimated data and the noise variance. A right trade-off parameter is critical for an effective denoise and signal retrieval. I provide more details on how to estimate the trade-off parameter in the real data example. I set the initial solution  $\hat{\mathbf{C}}$  to be a matrix of zeros, and the constant  $\alpha$  is 1.05, estimated using the power method. The threshold value  $\beta = 3.8 \times 10^{-8}$  is computed using the estimated trade-off parameter  $\mu = 8 \times 10^{-8}$  and the constant  $\alpha = 1.05$ . For each FISTA iteration  $j$ , I compute the sparse solution  $\hat{\mathbf{C}}_j$  using equation 5.4 in which a soft-thresholding function using the threshold value  $\beta$  is applied. The cost function  $J_j$  for the sparse solution is then computed, and I set the convergence criterion  $T_0 = 0.001$ . With the input data in Figure 5.1b, the FISTA finds the sparse solution  $\hat{\mathbf{C}}_j$  after 16 iterations. The sparse Gabor coefficients are then used to reconstruct the waveforms using equation 5.1.

Figures 5.1d, e show the Gabor spectrogram plotted using the inverted coefficients and the reconstructed waveform, respectively. The Gabor transform produces a more noisy spectrogram (Figure 5.1c), whereas the sparse inversion attenuates the noisy coefficients and produces a better-resolution spectrogram with clear P- and S-phases (Figure 5.1d).

### ***Neighboring block thresholding***

For comparison with the sparse inversion, I use the same synthetic signal with bandpass-filtered noise (Figure 5.1b) and its Gabor transform (Figure 5.1c) with the same Gaussian window width of 5 ms. Next, I normalize the Gabor coefficients

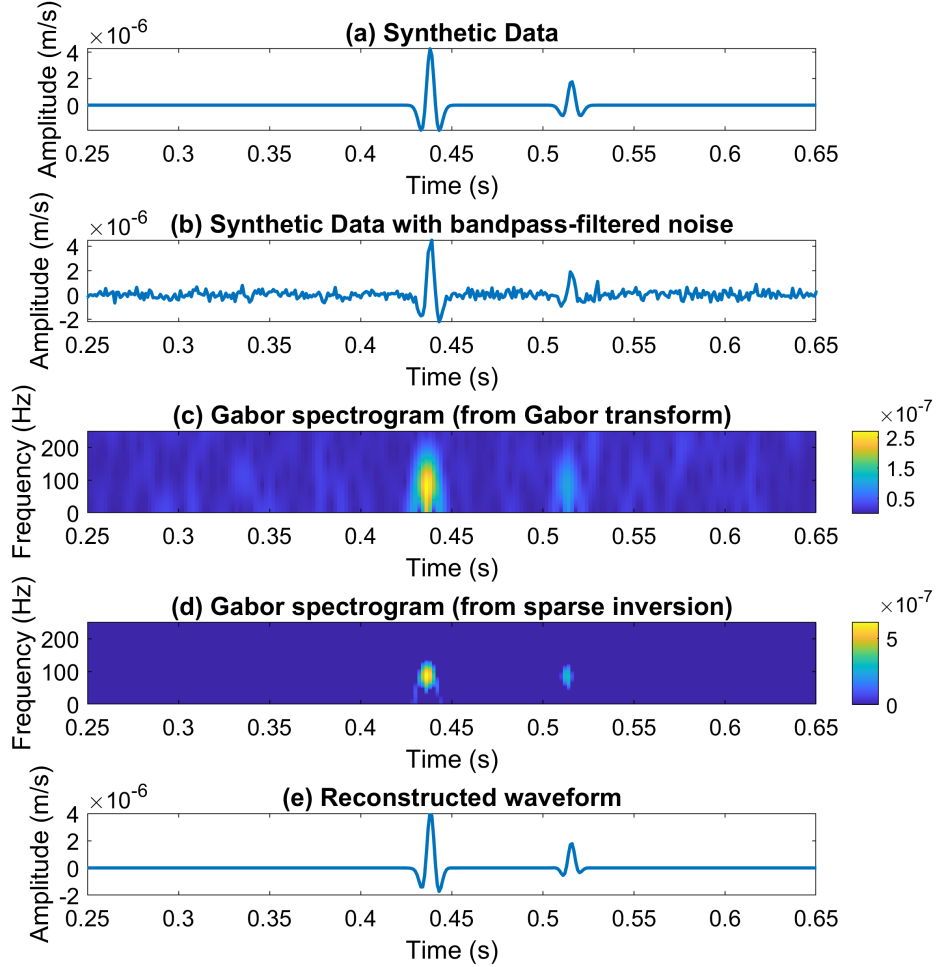


Figure 5.1: (a) Synthetic data, (b) Synthetic data with bandpass-filtered noise, (c) Gabor spectrogram obtained from the Gabor transform, (d) Gabor spectrogram obtained from the sparse inversion, (e) Waveform reconstructed from the inverted Gabor coefficients.

using a noise level  $\sigma$  with a mean of 0.0582 estimated by the minima controlled recursive averaging noise estimator. The time-frequency plane is then segmented into 51 disjoint macroblocks; each has a length of  $L_a = 8$  samples in time and width of  $W_a = 16$  samples in frequency. I use zero padding to ensure the segmentation into different blocks of the time-frequency coefficients. With the optimal block size  $\hat{L}_o$  and the optimal threshold level  $\hat{\lambda}$  (varying between blocks as it depends on the coefficients in each block), I sum the square of the normalized coefficients in the neighboring square block size of  $\hat{L}_o \times \hat{L}_o$  and use equation 5.6 to obtain the attenuation factor  $\Lambda_{mn}$ . After that, the normalized coefficient  $\tilde{C}_{mn}$  is shrunk by the attenuation factor

using equation 5.7. The resulting thresholded Gabor coefficients  $\hat{C}_{mn}$  are used to reconstruct the waveforms via the inverse short-time Gabor transform using equation 5.1.

Figures 5.2c, d show the resulting spectrograms after normalization by the noise level and block thresholding using the attenuation factor, respectively. The waveform reconstructed from the thresholded coefficients is shown in Figure 5.2e. Like the sparse Gabor transform, the neighboring block thresholding technique significantly attenuates the noise, and the reconstructed waveform has clearer P- and S-phases. A comparison of Figures 5.1e and 5.2e shows that the sparse inversion produces a better result with the bandpass-filter noise removed and the signal’s amplitudes remained the same order of magnitude as the original signal (Figure 5.1a). The normalization in the block-thresholding approach has, however, changed the amplitudes of the reconstructed signal considerably, in this case by  $10^6$  orders of magnitude, which raises difficulties in estimating the event magnitude unless this is done on the unfiltered instead of filtered data.

### 5.3.2 Real Data Example

I use a 50-min 3-component raw microseismic data set induced by hydraulic fracturing (Bui & van der Baan, 2020) to test both discussed algorithms. The data have a sampling rate of 0.25 ms. I select the vertical-component data recorded by one sensor to test the detection performance.

#### *Sparse inversion*

I use a 1.024 s raw data segment with a good signal-to-noise ratio, and the P- and S-wave onsets are at around 0.3 and 0.4 s, respectively. Figure 5.3a shows the signal between 0.25 and 0.6 s. I add some random noise (Figure 5.3b) to illustrate the sparse inversion using equation 5.4. The number of time samples is  $L_s = 4096$ , the number of frequency samples is  $N = 4096$ , the time shift between Gabor atoms is  $a = 4$  samples. The number of time indices for the Gabor coefficients is  $M = L_s/a =$

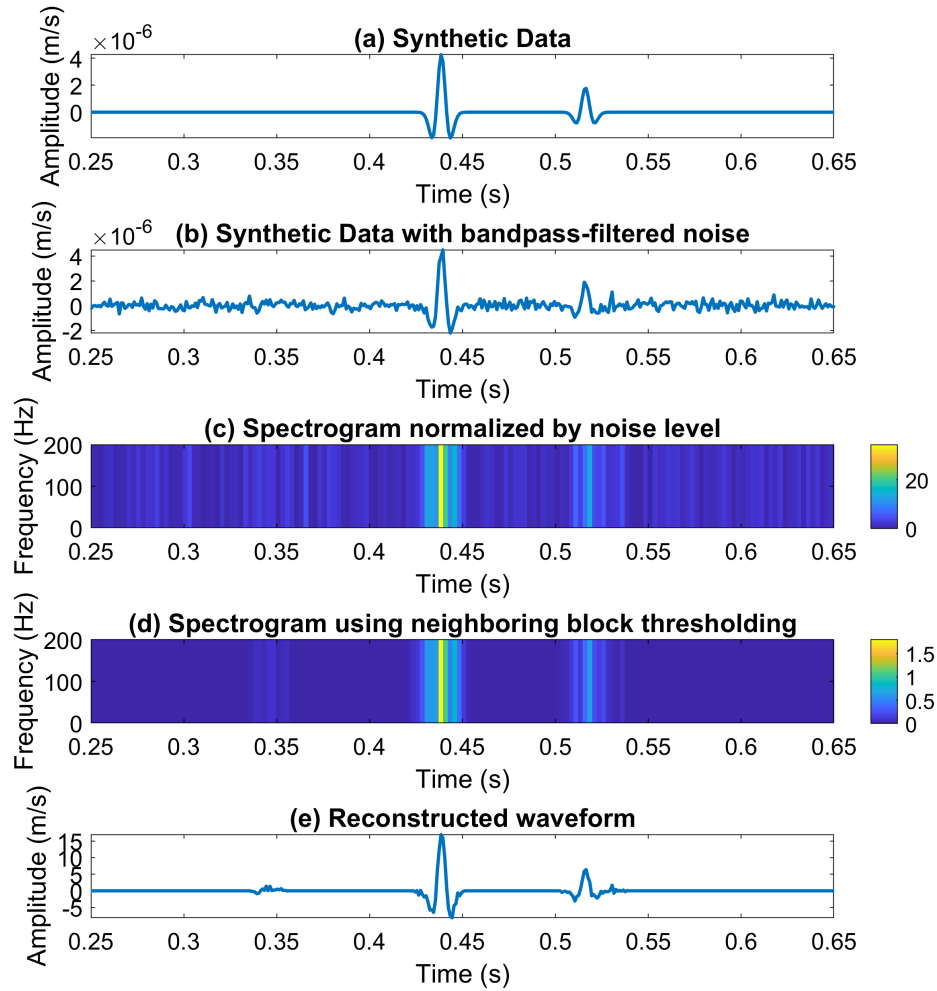


Figure 5.2: (a) Synthetic data, (b) Synthetic data with bandpass-filtered noise, (c) Spectrogram normalized by the noise level, (d) Spectrogram after neighboring block thresholding, and (e) Waveform reconstructed using thresholded coefficients.

1024 samples. I compute the Gabor transform (Figure 5.3c) using equation 5.2 with the Gaussian window having a width of 10 ms. The sparse solution of the Gabor coefficients depends on the trade-off parameter  $\mu$  (equation 5.3), so I first estimate a proper  $\mu$  value for the inversion. I compute the sparse solution using the FISTA for different trials of  $\mu$  ( $\mu = 0.0001, 0.001, 0.01, 0.1, 1, 10, 100$ ) and calculate the variance of the residuals between the original and reconstructed data from the inversion. The results are plotted in Figure 5.4. The noise variance in the first 0.2 s of the data is 0.48. Based on this value and the plot, I can find a suitable trade-off parameter of 0.0705, which is then used to obtain the sparse solution for the Gabor coefficients

using the FISTA.

The initial solution  $\hat{\mathbf{C}}$  is set to be a matrix of zeros, and the constant  $\alpha$  is 1.05. Using the trade-off parameter  $\mu = 0.0705$ , I obtain the threshold value  $\beta = 0.0336$ . I follow the same procedure as discussed in the synthetic example to compute the sparse solution  $\hat{\mathbf{C}}_j$  for each FISTA iteration  $j$ . Using a convergence criterion  $T_0 = 0.001$ , the FISTA finds the sparse solution  $\hat{\mathbf{C}}_j$  after 24 iterations for this 0.9 s input signal (Figure 5.3b). Then, I reconstruct the waveforms using the sparse Gabor coefficients through equation 5.1. Figures 5.3d, e show the Gabor spectrogram plotted using the inverted coefficients and the reconstructed waveform. The Gabor transform produces a more noisy spectrogram. In contrast, the sparse inversion attenuates the noisy coefficients and produces a better-resolution spectrogram with the P- and S-waves visible (highlighted in the black and red rectangles, Figure 5.3e), facilitating subsequent onset detection on the denoised waveforms.

### ***Neighboring block thresholding***

I use the same data segment (Figure 5.3b) and its Gabor transform (Figure 5.3c) with the same Gaussian window width of 10 ms. Next, I normalize the Gabor coefficients using a noise level  $\sigma$  with a mean of 0.227 estimated by the minima controlled recursive averaging noise estimator. The time-frequency plane is then segmented into 75 disjoint macroblocks; each has a length of  $L_a = 8$  samples in time and width of  $W_a = 16$  samples in frequency. With the optimal block size  $\hat{L}_o$  and the optimal threshold level  $\hat{\lambda}$ , I sum the square of the normalized coefficients in the adjacent time and frequency bins using equation 5.6 to obtain the attenuation factor  $\Lambda_{mn}$ . After that, the normalized coefficient  $\bar{C}_{mn}$  is shrunk by the attenuation factor using equation 5.7. The resulting thresholded Gabor coefficients  $\hat{C}_{mn}$  are used to reconstruct the waveforms via the inverse short-time Gabor transform using equation 5.1.

Figures 5.5c and d show the resulting spectrograms after normalization by the noise level and block thresholding using the attenuation factor, respectively. The waveform reconstructed from the thresholded coefficients is shown in Figure 5.5e. Like the

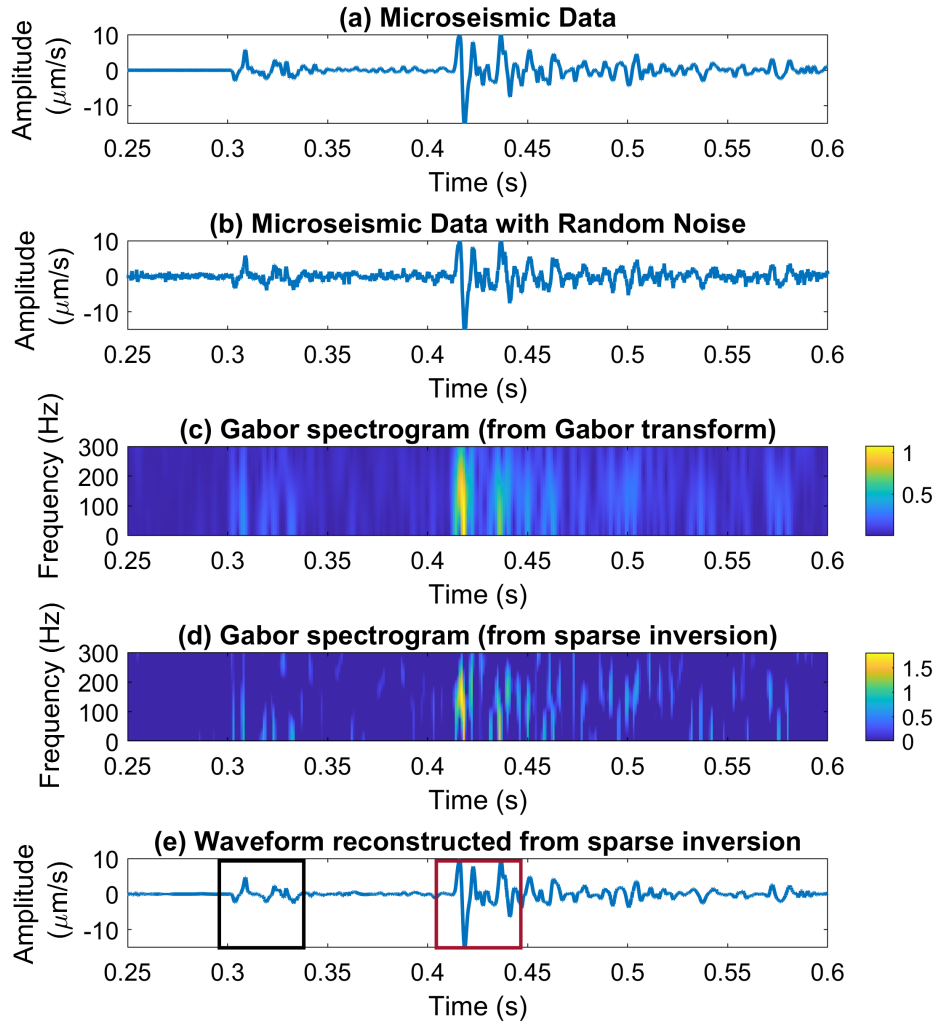


Figure 5.3: (a) Raw microseismic data with good signal-to-noise ratio, (b) Data with random noise added, (c) Gabor spectrogram from the Gabor transform, (d) Gabor spectrogram from the sparse inversion, (e) Waveform reconstructed from the inverted Gabor coefficients.

sparse Gabor transform, the neighboring block thresholding technique attenuates the noise, and the reconstructed waveform has clearer P- and S-phases (highlighted in the black and red rectangles, Figure 5.5e). A comparison of Figures 5.3e and 5.5e in terms of denoising effectiveness shows comparable waveforms with clear P- and S-phases after reconstruction, despite the different approaches to recognize and extract relevant features in the time-frequency plots (Figures 5.3c, d and Figures 5.5c, d). However, the neighboring block method changes the absolute amplitudes, in this case reducing them by a factor of 4.

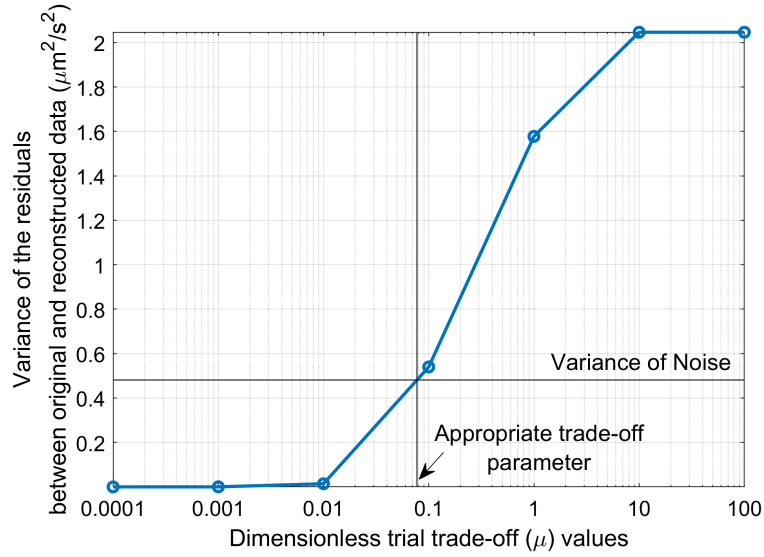


Figure 5.4: Estimating an appropriate trade-off parameter for the sparse inversion.

### 5.3.3 Event detection

To detect the potential microseismic events, I sum all absolute values of the resulting time-frequency coefficients over the frequencies and use the characteristic function (equation 5.8). Figures 5.6b, c and d show the characteristic function plots computed from the sparse inversion, the neighboring block thresholding, and the STA/LTA, respectively. The latter is applied to the original waveform directly (Figure 5.6a). I observe that the two time-frequency methods produce characteristic function plots with a better resolution than the STA/LTA result due to their denoising aspects. I can quickly recognize the onset of the P-wave at around 0.3 s with both methods (Figures 5.6b, c), contrary to the STA/LTA result. The time-frequency thresholding methods thus promise a higher detection capability than the STA/LTA.

### 5.3.4 Detection results

Table 5.1 shows the detection results of the 50-min microseismic data set obtained from the STA/LTA, the sparse Gabor transform, and the neighboring block thresholding methods. I classify the detected events into true events, false alarms, and missed events upon manual inspection. The time-frequency methods detect more true events

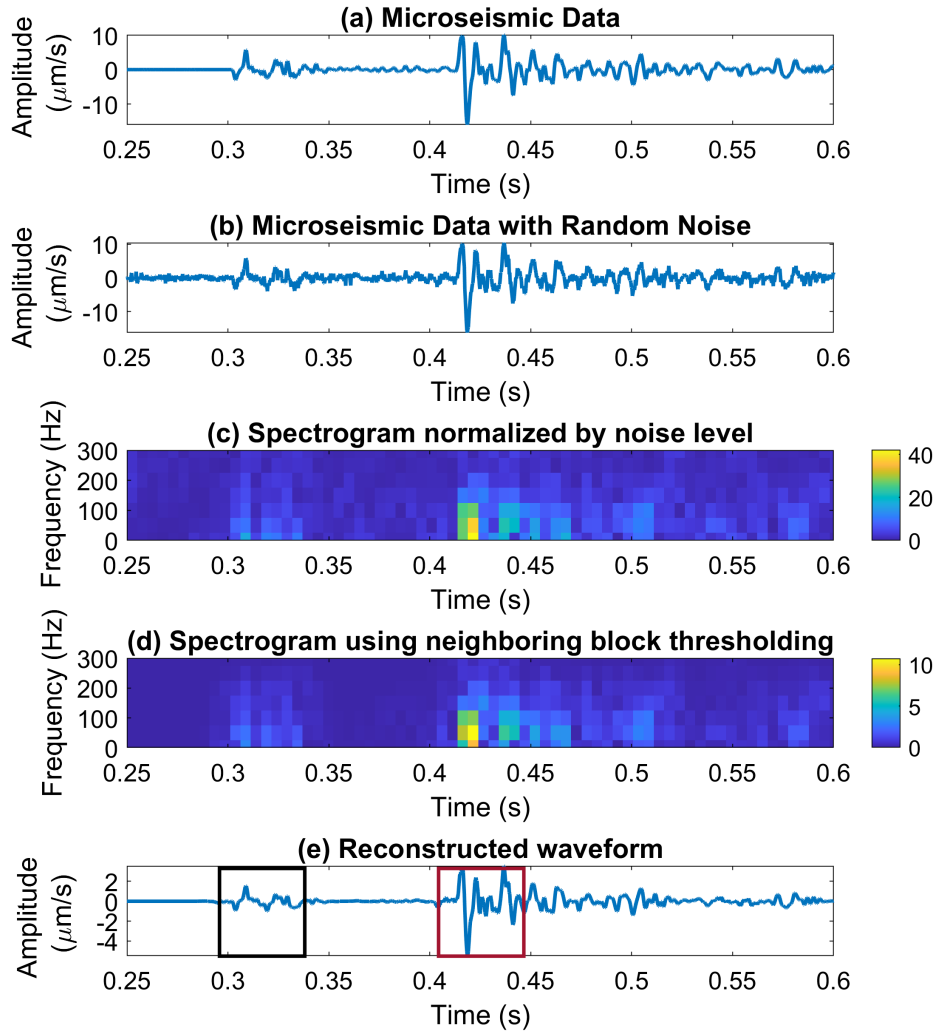


Figure 5.5: (a) Raw microseismic data, (b) Data with random noise, (c) Spectrogram normalized by the noise level, (d) Spectrogram after neighboring block thresholding, and (e) Waveform reconstructed using thresholded coefficients.

with fewer false alarms and missed events than the STA/LTA. The STA/LTA has the lowest precision rate of less than 50% with 96 true events and 105 false alarms, and the highest rate of missed events (defined as the ratio of missed events to true events) of about 19% with 23 missed events. In contrast, the time-frequency methods detect over 115 true events and produce less than 10 false alarms, yielding precision rates in excess of 92% and rates of missed events lower than 2%. These methods attenuate the noise significantly so they can capture more weak events in the detection process and require less manual inspection than the STA/LTA. The results indicate

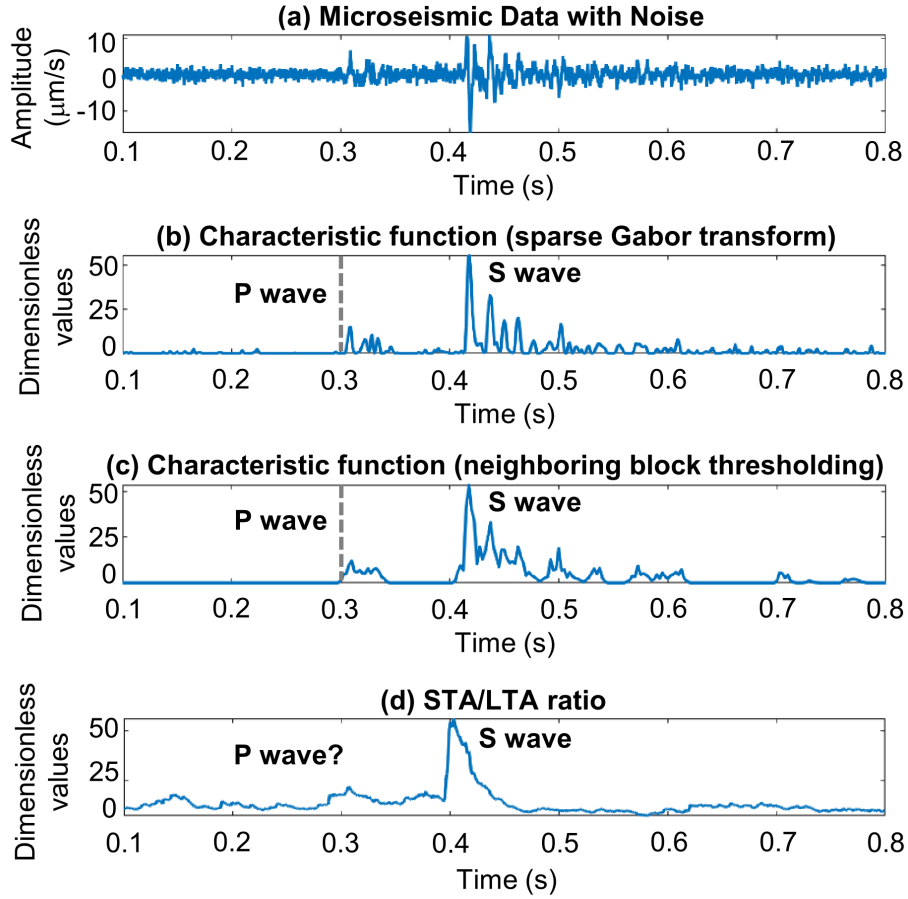


Figure 5.6: (a) Microseismic data with real noise and added random noise; (b), (c), and (d) Characteristic function computed from the sparse inversion, the neighboring block thresholding technique, and the STA/LTA method, respectively.

that both methods have superior event detection performance. Table 5.1 also shows a comparative computation time of each method. The time-frequency methods require longer computation time, particularly the sparse inversion. I thus should consider accelerating the inversion process when working with big data sets.

### 5.3.5 Amplitude fidelity

Since the amplitudes and phases of the reconstructed waveforms are essential for subsequent processing, I carefully inspect the reconstructed waveforms from both time-frequency methods. Figure 5.7 shows the results when detecting events of a 9 s noisy, raw data segment. The original recording (Figure 5.7a) has six potential

Table 5.1: Detection results of a 50-min microseismic data set. The computation time in the table only includes the time that the algorithms run and extract potential events and does not include the time for classifying events.

Methods	True events	False alarms	Missed events	Precision rate (%)	Rate of missed events (%)	(Relative) computation time (minutes)
STA/LTA	96	105	23	47.76	19.33	5
Sparse Gabor transform	119	6	0	95.20	0	60
Neighboring block thresholding	117	9	2	92.86	1.68	12

events numbered from 1 to 6. Figures 5.7b, c show the resulting characteristic function and the reconstructed waveforms from the inverted Gabor coefficients, and Figures 5.7d, e show the corresponding plots after neighboring block thresholding. With a threshold of 2.5, both methods detect all six events, including the two weak events at around 6.9 s (event 5) and 8.6 s (event 6). Events 5 and 6 have a low signal-to-noise ratio, 2.1 and 2.2, respectively, and are still detected by both methods, indicating the capability of the time-frequency methods to detect weak events. Again both methods produce cleaner waveforms (Figures 5.7c, e). However, I observe changes in the relative amplitudes between events in the neighboring block thresholding result regardless of the differences in the amplitude ranges. The most positive amplitude of event 1 is initially greater than that of event 2 (Figure 5.7a). Thus, the sparse Gabor transform attenuates the noise and still preserves the most positive and negative amplitudes between these events, whereas the neighboring block thresholding has event 2 greater than event 1. Such relative changes in event amplitudes may bias magnitude estimation, which is typically based on the absolute amplitudes (Eaton et al., 2014). Changes in relative event amplitudes were detected in multiple cases for the neighboring block transform throughout the full 50-minute data set.

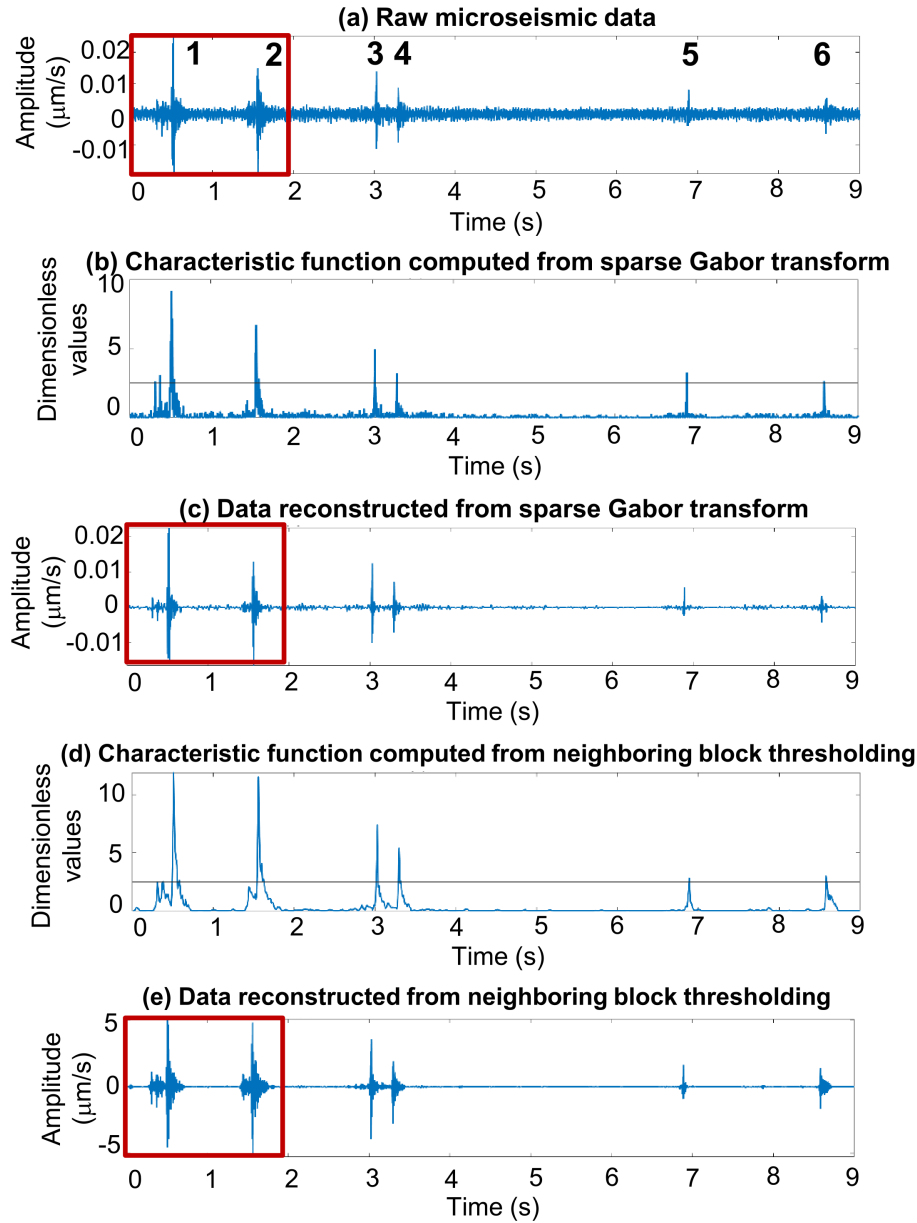


Figure 5.7: (a) Raw, noisy microseismic data with six events numbered from 1 to 6; (b), (c), (d), and (e) Characteristic function and data computed from the sparse Gabor transform and the neighboring block thresholding method, respectively. Note the changed amplitude range after the application of neighboring block thresholding.

Figure 5.8a shows a 0.6 s original microseismic data segment with the P- and S-phases at 0.356 and 0.468 s, respectively. The reconstructed waveform from the sparse inversion and the neighboring block thresholding methods are plotted in Figures 5.8b, c for comparison. The sparse inversion attenuates the noise while preserving the P-

and S-phases and the maximum absolute amplitude, whereas the neighboring block thresholding causes changes in both P- and S-waveforms and the maximum absolute amplitude.

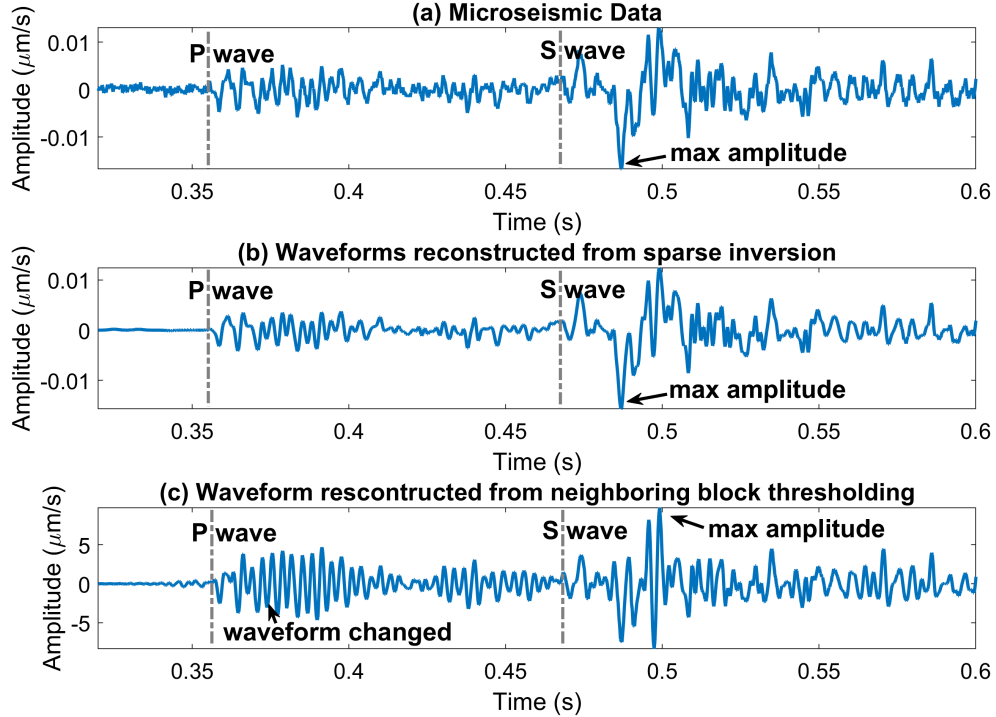


Figure 5.8: (a) Original microseismic data, (b) Waveform reconstructed from the sparse inversion, (c) Waveform reconstructed from the neighboring block thresholding. While the sparse inversion preserves the P- and S-waves and the maximum amplitude, changes in P- and S-waves and maximum amplitude are observed in the neighboring block thresholding result.

To quantify the changes in the waveforms reconstructed from the neighboring block thresholding, I use cross plots between the maximum absolute amplitudes of the original data and the reconstructed data from both methods. Figures 5.9a, b show the resulting cross plots. I observe a straight 1:1 grey line between the sparse inversion and the original data in Figure 5.9a, which indicates almost no changes in the maximum absolute amplitudes of the waveforms after the reconstruction. Figure 5.9c shows the percentage changes, and I observe minor changes in the maximum absolute amplitudes of the data reconstructed from the sparse Gabor transform, with over 95% of events having changes within 5%. These changes primarily are the noise removed

from the data. On the other hand, Figure 5.9b indicates that the neighboring block thresholding scales the amplitudes. The grey line indicates the best-fit trend, illustrating that the absolute amplitudes are perturbed and that large relative deviations occur in the maximum absolute amplitudes of the data reconstructed from the neighboring block thresholding method. In other words, a rescaling of the reconstructed amplitudes to those in the original waveforms is likely insufficient to obtain accurate magnitude estimates. Figure 5.9d shows the significant percent of changes, of the order of 10,000%, in the absolute maximum amplitudes. These changes could result in biases in the event magnitude estimation and subsequent moment-tensor inversion, including biased tensile/shear recognition, even if the reconstructed amplitudes are corrected using the trend line in Figure 5.9b.

Figures 5.10a, b show the cross plots of the S/P amplitude ratios (which are the ratios of the maximum absolute amplitudes of the P- and S-waves) of the original and the reconstructed waveforms from both methods. Likewise, I observe many deviations from a straight 1:1 grey line in the neighboring block thresholding result (Figure 5.10b) compared with the sparse inversion (Figure 5.10a). The number of tensile and shear events could be estimated based on a cutoff S/P ratio of 5 (Eaton et al., 2014; Pearson, 1981). Thus, the changes in the S/P amplitude ratios caused by the neighboring block thresholding (Figure 5.10b) could lead to events wrongly categorized into the likely tensile/shear events group. These relative amplitude changes between P- and S-phases also indicate that finding a simple correction procedure will be difficult. The relative amplitude changes are likely caused by temporal fluctuations in the noise levels, leading to rapid variations in attenuation factors and thresholded Gabor coefficients (equations 5.6 and 5.7).

## 5.4 Conclusions

This study examines two time-frequency thresholding techniques: (1) sparse Gabor transform and (2) neighboring block thresholding. Both methods have a superior

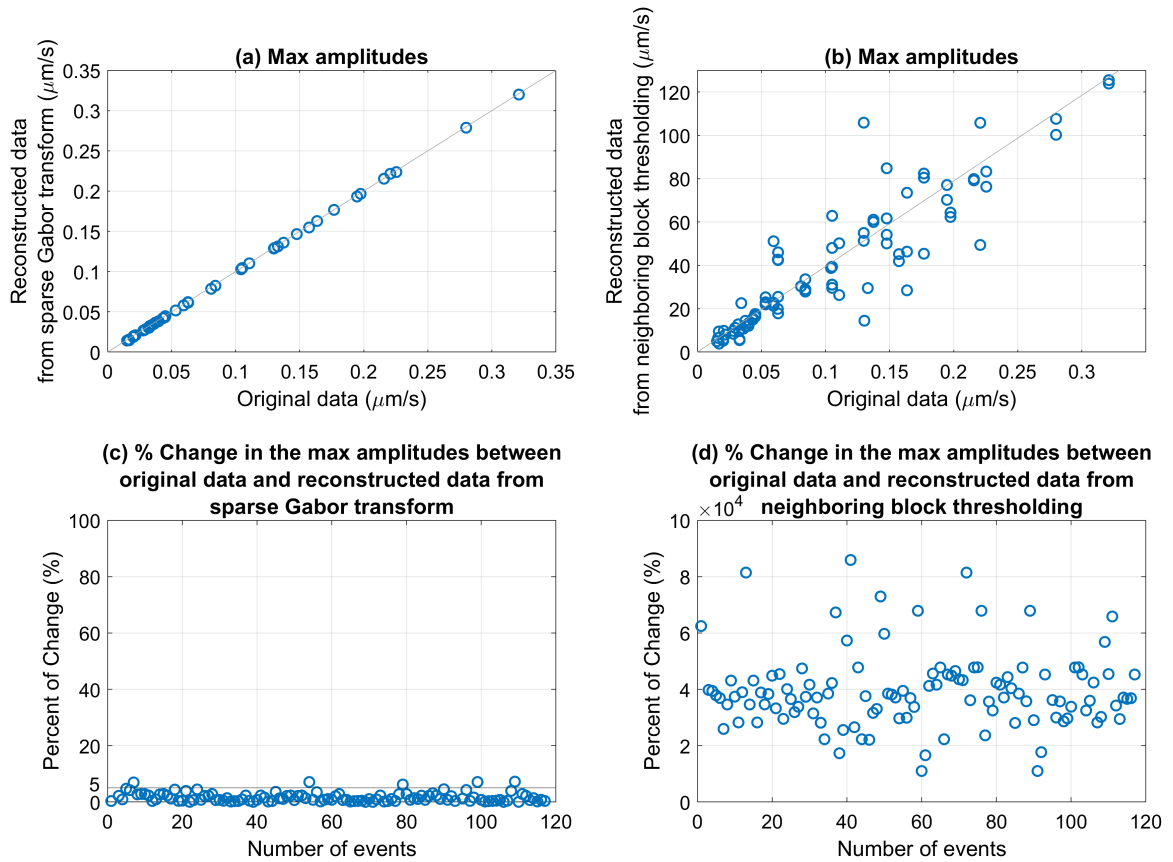


Figure 5.9: Cross plots show the maximum absolute amplitude of the original data and the reconstructed data from (a) the sparse Gabor transform and (b) the neighboring thresholding method. Percent of changes in the maximum absolute amplitudes between the original and reconstructed data from (c) the sparse Gabor transform and (d) the neighboring thresholding method. Note the very different amplitude ranges between the left and right columns.

detection capability with a precision rate of well above 90% compared with the STA/LTA method. These time-frequency detectors can attenuate the noise significantly and capture more weak events in the data. The sparse Gabor transform is more promising than the neighboring block threshold technique despite its longer computation time. Through an inversion using a sparsity constraint on the solution in the form of  $l_1$  norm, I obtain an efficient Gabor time-frequency representation of the signals, which enhances the detection capability, improves the signal-to-noise ratio of the events, and most importantly, preserves the absolute and relative amplitudes of P- and S-phases of the signals. Unlike the sparse Gabor transform, the neighboring

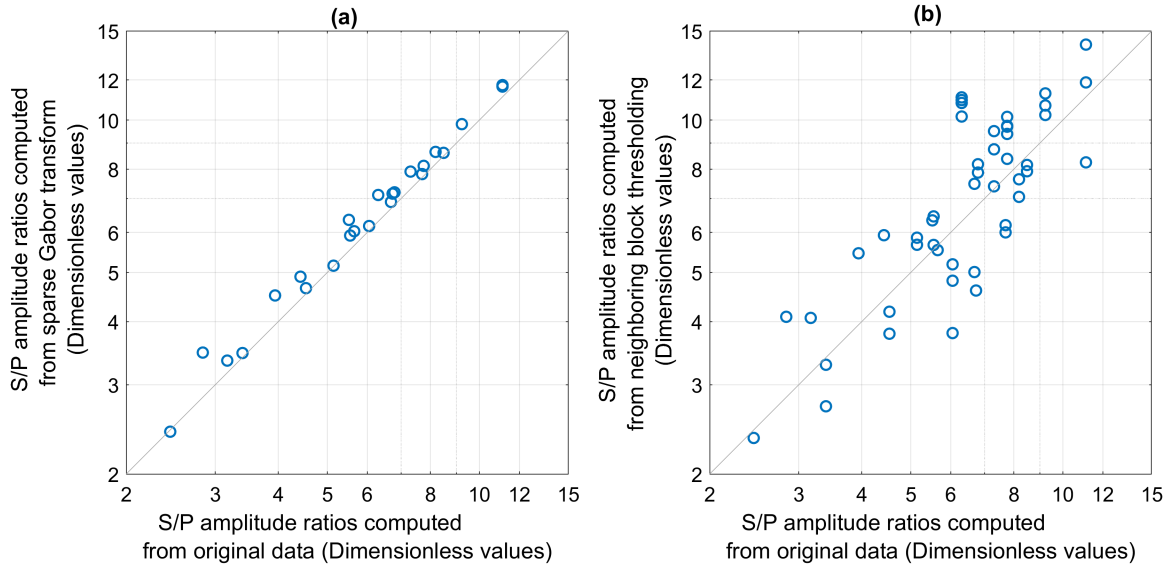


Figure 5.10: Cross plots show the S/P amplitude ratios of the original data and the reconstructed data from (a) the sparse Gabor transform and (b) the neighboring thresholding method.

block thresholding causes amplitude fidelity issues that hinder the interpretation of the detected events, resulting in artifacts such as biased tensile/shear recognition or under/overestimated magnitudes.

# Chapter 6

## Event locations: Speeding up grid searches using quadratic interpolation <sup>1</sup>

### Summary

The grid search method is a common approach to estimate the three spatial coordinates of event hypocenters. However, locating events in large search spaces with small grid spacings is computationally prohibitive. This study accelerates the grid searches over large search spaces using a quadratic interpolation technique. I start with the coarse-grid-estimated location, where I have the minimum value of the difference in the traveltimes between S- and P-waves summed over all receivers. Then, I select the neighboring grid points and build a 3D quadratic function. The unknown coefficients of the 3D quadratic function are computed by solving a system of linear equations. After that, I interpolate the location by solving partial derivatives of the quadratic function. The quadratic interpolation technique performs well on both synthetic and real microseismic data examples, typically leading to similar event locations as those obtained using 10 times smaller grid spacings in all three directions, at a minor additional computational expense, and without the need to generate traveltimes at new spatial positions.

---

<sup>1</sup>A manuscript including a version of this chapter has been submitted to *Geophysical Journal International*.

## 6.1 Introduction

Determination of the event location is one of the most crucial steps in microseismic processing. Accurate locations provide insights into the shapes and sizes of the induced hydraulic fractures and are used to estimate the dimensions of the stimulated rock (van der Baan et al., 2013). This step retrieves the three unknown spatial coordinates of the hypocenter and its origin time (defined as the occurrence time of the initial energy release of a seismic event (Lomax et al., 2009; Pavlis, 1986)). Event location methods can be generally divided into two categories: traveltimes-based and migration-based methods (Li & van der Baan, 2016). The traveltimes-based method utilizes P- and S-arrival times directly obtained from seismograms to estimate event locations by minimizing the residuals between observed and predicted traveltimes (Eisner et al., 2009; Geiger, 1912; Jones et al., 2014; Lomax et al., 2000; Oye & Roth, 2003; Tarantola & Valette, 1982; Wuestefeld et al., 2018; Zhou et al., 2015). The migration-based method does not require explicit phase identification and is possibly more suitable for noisy data than the traveltimes-based method since picking the arrival times is challenging in low-quality data (Artman et al., 2010; Chambers et al., 2010; Duncan et al., 2010; Gharti et al., 2010; Li & van der Baan, 2016).

The accuracy of the estimated locations depends on various factors, such as data quality, phase picking, velocity model, acquisition geometry, and location algorithms (Pavlis, 1986; Wuestefeld et al., 2018). Poor data quality often leads to errors in phase picking, negatively affecting the event location (Castellanos & van der Baan, 2015; Eisner et al., 2009, 2010; Maxwell, 2014). Limited sensor coverage also can cause potential biases in the estimated hypocenters (Eisner et al., 2009, 2010; Maxwell, 2014). Uncertainties in the velocity model can also introduce errors in the estimated hypocenters (Pavlis, 1986), in particular since the subsurface is often an anisotropic medium with significant differences in vertical and horizontal velocities due to deposition, layering, and rock fabric (Backus, 1962; Cipolla et al., 2011; Tsvankin et al.,

2010). How the ray-tracing is calculated or traveltimes are computed is also an issue. Location algorithms using different optimization methods can also result in differences in the resolved locations (Pavlis, 1986). Wuestefeld et al. (2018) test different location procedures on synthetic data, including the global full grid search and the directed grid search, and compare the results with the widely-used location NonLinLoc software package (Lomax et al., 2000). The study implies that the estimated locations include an additional inherent error associated with the chosen location algorithm.

Microseismic data sets are often large since waveforms are continuously recorded at a high sampling rate (e.g., 0.25 ms) over days or weeks using a dozen or more receivers (Bui et al., 2023). Desired location algorithms should generate event locations with high accuracy and minor computational expense. Different location algorithms have been introduced, from global grid searches to fine local inversion (Bai et al., 2009; Castellanos & van der Baan, 2013; Eisner et al., 2009; Li & van der Baan, 2016; Lomax et al., 2000; Waldhauser & Ellsworth, 2000; Zhang et al., 2019; Zhou et al., 2015). Previously, I use the direct search-based method in the form of a global search to estimate event locations in a microseismic data set acquired during a hydraulic fracturing treatment (Bui & van der Baan, 2021). I create a search space containing all possible hypocentral locations and search for the most likely hypocenter where I have the maximum value of the probability density functions of all possible locations. The differences in traveltimes between the S- and P-phases of the seismic waves are used in the calculation, which reduces the complexity of the location problem from four to three unknowns by omitting the unknown origin time in the objective function.

The grid search method is widely employed due to its simplicity; however, it is computationally prohibitive when locating events over a large search space with small grid spacing (Lomax et al., 2000). Different approaches are proposed for resolving this limitation. Lomax and Curtis (2001) and Lomax et al. (2000, 2009) use importance sampling methods, including the Metropolis-Gibbs and Oct-Tree, to resolve the inefficient, exhaustive grid searches. The Metropolis-Gibbs sampling, based on the

algorithm of Metropolis et al. (1953), performs a directed random walk within the solution space to obtain a set of samples that follow the location probability density function (PDF) (Lomax et al., 2000). Like the grid search, the Metropolis-Gibbs method does not require partial derivatives. Lomax et al. (2000) emphasize that this method performs well with moderately irregular (non-ellipsoidal) PDFs with a single optimum solution; however, it may yield inconsistent results when the PDFs are highly irregular (non-ellipsoidal) with multiple optimal solutions. The Oct-Tree importance sampling is another novel method presented by Lomax and Curtis (2001) and Lomax et al. (2009) for accelerating the grid searches and accurately determining the optimal location. This method involves an initial global sampling of the misfit function on a coarse grid, followed by a recursive bisection procedure of subdividing the grid cell with the highest location probability into 8 sub-cells and evaluating the misfit function in these sub-cells (Lomax & Curtis, 2001; Lomax et al., 2009). This procedure rapidly converges to a cascade of Oct-Tree structures specifying location PDF values, with a larger number of smaller cells in the regions of higher PDF (lower misfit) (Lomax & Curtis, 2001). The optimal hypocenter is the location of the minimum misfit point of the location PDF. Lomax and Curtis (2001) and Lomax et al. (2000) conclude that the Metropolis-Gibbs and Oct-Tree methods are about 100 times faster than a pure grid search, with the Oct-Tree being simpler, faster, more stable to implement and ultimately offering a more complete sampling of the solution space than the Metropolis-Gibbs approach. Bai et al. (2009) introduce another alternative that refines the location from coarse grid search using a fine local inversion with a minimum search routine and assessing the root mean squares residual distribution. Unlike the common global search, this method performs a matrix inversion-based local search. It simultaneously updates all potential initial source parameters around various local minima, including the global minimum, within the solution space and determines the most likely global solution (Bai et al., 2009). The hybrid global-local inversion produces similar location results with the Oct-Tree importance sampling of

Lomax and Curtis (2001) but has a two-order of magnitude faster computation.

This study aims to reduce the computational burden of the exhaustive grid search for event location by using a 3-dimensional (3D) quadratic interpolation algorithm to accelerate the search and refine the event location with higher accuracy. Since the S-P time difference has a quadratic form in a homogeneous space, I formulate it into a quadratic function and use interpolation to localize the event hypocenter. I start with a coarse-grid-estimated location and PDF from the grid search. Then, I select grid points neighboring this initial location and compute the unknown coefficients of the quadratic function by solving a system of linear equations. Next, I identify the minima and maxima of the resulting quadratic function to find the optimal hypocenter of the event. I implement the algorithm on synthetic data constructed using illustrative and field-based source-receiver configurations and compare the location results with the widely-used NonLinLoc software package developed by Lomax et al. (2000). The comparison shows that the combined coarse grid search and quadratic interpolation produce a better estimate of the hypocentral location, especially the event depth. I then employ the combined coarse grid search and quadratic interpolation on about 1000 real microseismic events from 20 hydraulic fracturing treatment stages in a hydrocarbon reservoir. The following section presents how I build the quadratic function and use the interpolation to speed up the grid search and obtain a better event location result.

## **6.2 Methodology**

### **6.2.1 The location problem**

The earthquake location is a nonlinear problem with four unknowns, including three spatial coordinates of the hypocenter and the event origin time, which is the occurrence time of the initial energy release of a seismic event (Lomax et al., 2009). Usually, the locations are determined using arrival times at recording stations. The

arrival time is the time needed for the seismic energy to reach the receiver. In a non-homogeneous medium, the observed arrival time,  $t_{obs}$ , of an event at a given station related to its hypocentral location through,

$$t_{obs} = t_0 + \int_{r_0(s)} u(r_0) ds, \quad (6.1)$$

where  $t_0$  is the event origin time,  $r_0(s)$  is a point at source-receiver distance  $s$  along ray path  $r_0$ , and  $u$  is the slowness ( $u = 1/v$  with  $v$  is the velocity of the seismic waves propagating in the medium) (Lomax et al., 2009). The integral term effectively represents the traveltimes.

In a homogeneous velocity field, the predicted traveltimes,  $t_{pred}$ , is a function of the receiver coordinates,  $(x_R, y_R, z_R)$ , coordinates of an assumed hypocenter,  $(x_a, y_a, z_a)$ , and velocity  $v$  and is given as

$$t_{pred} = \frac{\sqrt{(x_R - x_a)^2 + (y_R - y_a)^2 + (z_R - z_a)^2}}{v}. \quad (6.2)$$

In a non-homogeneous velocity field where  $v$  is no longer a constant, the predicted traveltimes (the integral term in equation 6.1) are typically obtained using ray-tracing. With four unknowns, estimating the event location can be formulated as a non-linear inverse problem. Usually, at least four arrival time observations are needed to determine the spatial coordinates of the hypocenter and the origin time (Havskov & Ottemoller, 2010). A solution is usually sought that minimizes the sum of the differences (residuals) between the observed and predicted arrival times, starting from an initial model for the hypocenter and can contain a significant trade-off between origin time and depth.

### 6.2.2 Grid search via lookup tables

The grid search method estimates the traveltimes and the origin times of seismic events in a given 3D gridded model from all possible locations (Lomax et al., 2009). Figure 6.1 depicts a 3D gridded space with each node representing a possible hypocenter location. The 3D grid is defined by an origin  $(x_0, y_0, z_0)$  and the grid spacings,

$dx$ ,  $dy$ ,  $dz$ , in the x, y, and z dimensions, respectively. The model is arranged in a lookup table format to avoid repeated computations and enable quick searches by the receiver number.

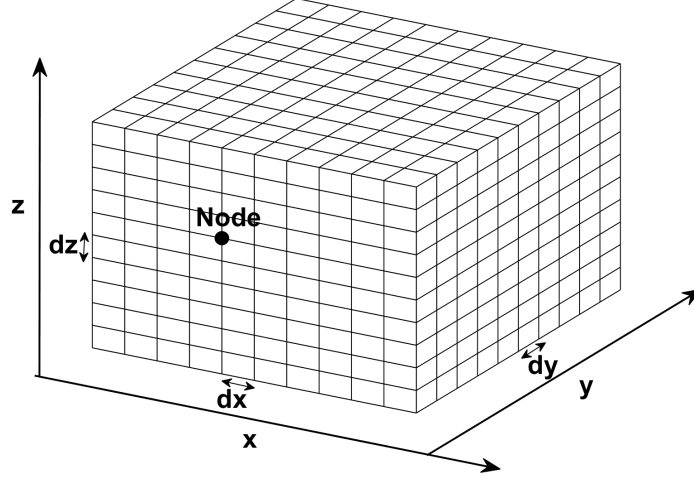


Figure 6.1: A 3D gridded model with each node representing a possible location;  $dx$ ,  $dy$ , and  $dz$  are the grid spacings in the x, y, and z dimensions, respectively.

I compute the PDFs for all possible hypocenters and search for the most likely hypocenter location, which gives the best agreement between the observed and predicted arrival times. Assuming that each receiver and the observed quantities are mutually independent, the PDFs can be computed as follows (Eisner et al., 2010)

$$\begin{aligned}
 PDF(t_{P_{obs}}, t_{S_{obs}}, \sin(Az)) = \\
 N e^{-\sum_R (t_{P_{obs}} - t_{P_{pred}} - t_0)^2 / 2\sigma_P^2} e^{-\sum_R (t_{S_{obs}} - t_{S_{pred}} - t_0)^2 / 2\sigma_S^2} \\
 e^{-\sum_R (\sin(Az_{obs}) - \sin(Az_{pred}))^2 / 2\sigma_{\sin(Az)}^2}, \quad (6.3)
 \end{aligned}$$

where  $t_{P_{obs}}$ ,  $t_{S_{obs}}$  and  $Az_{obs}$  are the observed P- and S-wave arrival times and azimuth angle, respectively;  $t_{P_{pred}}$ ,  $t_{S_{pred}}$  and  $Az_{pred}$  are the predicted P- and S-wave travel-times and azimuth angle;  $N$  is the normalization constant;  $t_0$  is the origin time;  $R$  is the number of receivers;  $\sigma_P$ ,  $\sigma_S$  and  $\sigma_{Az}$  are the uncertainties of the observed P- and S-wave arrival times and azimuth angle, respectively (Eisner et al., 2010). The  $(\sin(Az_{obs}) - \sin(Az_{pred}))^2 / 2\sigma_{\sin(Az)}^2$  term is added to account for the cyclic nature of angles.

Generally, it is impossible to have a priori information about the origin time independent of the data (Tarantola & Valette, 1982); thus, I construct PDFs that involve minimizing the difference between the observed S-P arrival time and predicted S-P traveltimes as follows

$$PDF(t_{SP}, \sin(Az)) = N e^{-\sum_R ((t_{Sobs} - t_{Pobs}) - (t_{SPred} - t_{PPred}))^2 / 2\sigma_{SP}^2} e^{-\sum_R (\sin(Az_{obs}) - \sin(Az_{pred}))^2 / 2\sigma_{\sin(Az)}^2}. \quad (6.4)$$

If only traveltimes are used, then equation 6.4 is simplified to

$$PDF(t_{SP}) = e^{-\sum_R ((t_{Sobs} - t_{Pobs}) - (t_{SPred} - t_{PPred}))^2 / 2\sigma_{SP}^2}. \quad (6.5)$$

After obtaining the spatial hypocenter coordinates (assuming the peak of the PDF), the origin time,  $t_0$ , can be derived using

$$\bar{t}_0 = \frac{\sum (t_{P(S)obs} - t_{P(S)pred})}{R}, \quad (6.6)$$

where  $\bar{t}_0$  is the mean origin time over all receivers,  $t_{P(S)obs}$  is the observed P- and S-wave arrival times,  $t_{P(S)pred}$  is the predicted P- and S-wave traveltimes, and  $R$  is the number of receivers.

### 6.2.3 Quadratic interpolation between grid points

The grid search method is computationally prohibitive for large search spaces with small grid spacings. I use a quadratic interpolation technique to accelerate the searches and resolve this well-known problem of the grid search method. The travel-time differences between the S- and P-waves summed over all receivers is proportional to equation 6.5 and given as

$$\sum_R ((t_{Sobs} - t_{Pobs}) - (t_{SPred} - t_{PPred}))^2. \quad (6.7)$$

Notice that the sum of all traveltime differences has a quadratic form; I build a quadratic function for the differences in the traveltimes between the S- and P-waves. I start with the location estimated from the grid search over a coarse grid, build the quadratic function, and then use quadratic interpolation to refine the event location. The quadratic form is also maintained, and the interpolation procedure is still applicable if I add the azimuths (equation 6.4); however, a normalization is needed (here the variances  $\sigma$ ) to give both terms similar weight as follows

$$\sum_R ((t_{Sobs} - t_{Pobs}) - (t_{Spred} - t_{Ppred}))^2 / 2\sigma_{SP}^2 + \sum_R (\sin(Az_{obs}) - \sin(Az_{pred}))^2 / 2\sigma_{\sin(Az)}^2. \quad (6.8)$$

In the following, I detail how I set up the 3D quadratic function, compute its unknown coefficients and use it to obtain the optimal hypocenter location from the initial coarse-grid-estimated location.

### 3D full quadratic function

In 3D, the full quadratic function,  $f(x, y, z)$ , can be given as

$$\begin{aligned} f(x, y, z) = & a_{000} + a_{100}x + a_{010}y + a_{001}z + a_{200}x^2 + a_{020}y^2 + a_{002}z^2 + a_{110}xy + a_{011}yz \\ & + a_{101}xz + a_{111}xyz + a_{210}x^2y + a_{201}x^2z + a_{120}xy^2 + a_{021}y^2z + a_{102}xz^2 + a_{012}yz^2 \\ & + a_{220}x^2y^2 + a_{022}y^2z^2 + a_{202}x^2z^2 + a_{211}x^2yz + a_{121}xy^2z + a_{112}xyz^2 + a_{221}x^2y^2z \\ & + a_{122}xy^2z^2 + a_{212}x^2yz^2 + a_{222}x^2y^2z^2, \quad (6.9) \end{aligned}$$

where  $a_{ijk}$ , with  $i, j, k = [0, 1, 2]$ , are the unknown coefficients; x, y, and z are the coordinates of the data points in the 3D search spaces.

### Solving the unknown coefficients of the quadratic function

#### *System of linear equations*

The full 3D quadratic function has 27 unknown coefficients. Each unknown can be considered as an available degree of freedom. To solve these unknowns, I build

a system of linear equations in which each equation can be viewed as a constraint that restricts one degree of freedom. The behavior of the linear system depends on the number of equations and the number of unknowns. In my case, I want to solve the 27 unknown coefficients of the full quadratic function in 3D; thus, a system of at least 27 linear equations is required to obtain an exact or approximate solution. The system of linear equations can be written in a matrix form as follows

$$\mathbf{AX} = \mathbf{B}, \quad (6.10)$$

where  $\mathbf{A}$  is a square 27x27 matrix with each row having 27 elements obtained from the quadratic function, equation 6.9, including 1,  $x_n, y_n, z_n, x_n^2, y_n^2, z_n^2, x_n y_n, y_n z_n, x_n z_n, x_n y_n z_n, x_n^2 y_n, x_n^2 z_n, x_n y_n^2, y_n^2 z_n, x_n z_n^2, y_n z_n^2, x_n^2 y_n^2, y_n^2 z_n^2, x_n^2 z_n^2, x_n^2 y_n z_n, x_n y_n^2 z_n, x_n y_n z_n^2, x_n^2 y_n^2 z_n, x_n y_n^2 z_n^2, x_n^2 y_n z_n^2, x_n^2 y_n^2 z_n^2$ ;  $n$  is the number of linear equations or number of rows of the matrix  $\mathbf{A}$  ( $n = 1:27$ );  $\mathbf{X}$  is a 27x1 column vector of unknown coefficients  $a_{ijk}$  with  $i, j, k = [0, 1, 2]$ ;  $\mathbf{B}$  is a 27x1 column vector of data values which are the traveltime differences between the S- and P-waves summed over all receivers, equation 6.7, or traveltimes and azimuths, equation 6.8. The equation 6.10 can be expanded as follows

$$\begin{bmatrix} 1 & x_1 & y_1 & z_1 & x_1^2 & \dots & x_1^2 y_1^2 z_1^2 \\ 1 & x_2 & y_2 & z_2 & x_2^2 & \dots & x_2^2 y_2^2 z_2^2 \\ \vdots & \vdots & \vdots & \vdots & \vdots & \ddots & \vdots \\ 1 & x_{27} & y_{27} & z_{27} & x_{27}^2 & \dots & x_{27}^2 y_{27}^2 z_{27}^2 \end{bmatrix} \begin{bmatrix} a_{000} \\ a_{100} \\ \vdots \\ a_{222} \end{bmatrix} = \begin{bmatrix} B_1 \\ B_2 \\ \vdots \\ B_{27} \end{bmatrix}, \quad (6.11)$$

### ***Selection of data points***

The selection of 27 data points for establishing the system of 27 linear equations in equation 6.11 is essential because they directly affect the coefficients of the quadratic function and the estimated location. The strategy is to start with the minimum value of the difference in traveltimes between S- and P-waves summed over all receivers  $R$ , equation 6.7, or equivalently the maximum in the probability density functions given by equations 6.3 and 6.4. In the usual implementation of the grid search method, the selected point becomes the most likely hypocenter location. If the maximum

likelihood occurs at the grid point  $(x_{max}, y_{max}, z_{max})$ , then I select the 26 neighboring grid points as  $(x_{max} \pm dx, y_{max} \pm dy, z_{max} \pm dz)$ , with  $dx$ ,  $dy$ , and  $dz$  respectively the grid spacing along each axis. Likewise, for misfit implementations, I select the 26 neighboring grid points as  $(x_{min} \pm dx, y_{min} \pm dy, z_{min} \pm dz)$ .

### ***Solving the linear equations***

I use the least squares method to find an approximate solution to the system. In the matrix form, the least squares formula is obtained from the problem

$$\min_{\mathbf{X}} \|\mathbf{AX} - \mathbf{B}\|, \quad (6.12)$$

where  $\mathbf{X}$  is a 27x1 column vector of desired coefficients,  $\mathbf{B}$  is a 27x1 column vector of data values, containing either the misfits, equation 6.7, or probabilities, equation 6.5, at each extracted grid position  $(x, y, z)$ . Matrix  $\mathbf{A}$  contains the corresponding grid positions, as in equations 6.10 and 6.11. Using the normal equation formulation, the solution can be given as (Menke, 2018)

$$\mathbf{X} = (\mathbf{A}^T \mathbf{A})^{-1} \mathbf{A}^T \mathbf{B}, \quad (6.13)$$

where  $\mathbf{T}$  indicates a matrix transpose, provided  $(\mathbf{A}^T \mathbf{A})^{-1}$  exists (that is, provided  $\mathbf{A}$  has full column rank). This formula finds an approximate solution when no exact solution exists and gives an exact solution when one does exist.

### **Ways to simplify the full quadratic function**

The complexity of the quadratic function can be reduced from the complete set of 27 unknown coefficients to a smaller set with 17 or 10 coefficients by excluding the high-order cross terms. The more cross terms are removed, the more the shape of the misfit (equation 6.7) or probability density function (equations 6.3, 6.4, and 6.5) is restricted. If all the cross terms with order greater or equal to 4 are excluded, the 3D

quadratic function has only 17 unknown coefficients and is given as

$$\begin{aligned}
 f(x, y, z) = & a_{000} + a_{100}x + a_{010}y + a_{001}z + a_{200}x^2 + a_{020}y^2 + a_{002}z^2 + a_{110}xy + a_{011}yz \\
 & + a_{101}xz + a_{111}xyz + a_{210}x^2y + a_{201}x^2z + a_{120}xy^2 + a_{021}y^2z + a_{102}xz^2 + a_{012}yz^2.
 \end{aligned}
 \tag{6.14}$$

If all the cross terms with order greater or equal to 3 are excluded, the quadratic function is simplified with only 10 unknown coefficients and becomes

$$\begin{aligned}
 f(x, y, z) = & a_{000} + a_{100}x + a_{010}y + a_{001}z + a_{200}x^2 + a_{020}y^2 + \\
 & a_{002}z^2 + a_{110}xy + a_{011}yz + a_{101}xz.
 \end{aligned}
 \tag{6.15}$$

Progressively reducing the number of coefficients increasingly restricts the shape of the interpolation function. For instance, in equation 6.15, the resulting hyperboloid can only have principal axes or planes of symmetries in the x-y, x-z, and y-z planes.

The unknown coefficients in equations 6.14 and 6.15 are also obtained by solving the system of linear equations, equation 6.13. With the reduced number of unknowns, a system of linear equations with fewer equations (at least 17 and 10 equations) can be built to obtain the 3D quadratic functions in equations 6.14 and 6.15, respectively. However, selecting a reduced subset of points around the grid point  $(x_{max}, y_{max}, z_{max})$ , or equivalently  $(x_{min}, y_{min}, z_{min})$ , would create ambiguity. Each set of data points will result in different solutions depending on the exact choice. Therefore, I use the same set of 27 points for solving the unknown coefficients of the full 3D quadratic function, equation 6.9, and then solve equation 6.13.

### **Computing the optimal grid point location**

Once the 3D quadratic function is obtained, the extreme value  $(x_{int}, y_{int}, z_{int})$  representing the optimal hypocenter of the event can be obtained by solving the partial

derivatives of the function  $f(x, y, z)$  which is given as

$$\begin{cases} \frac{\partial f(x, y, z)}{\partial x} = 0, \\ \frac{\partial f(x, y, z)}{\partial y} = 0, \\ \frac{\partial f(x, y, z)}{\partial z} = 0. \end{cases} \quad (6.16)$$

For the full 3D quadratic function (equation 6.9), equation 6.16 can be expanded as follows

$$\begin{cases} a_{100} + 2a_{200}x + a_{110}y + a_{101}z + a_{111}yz + 2a_{210}yx + 2a_{201}zx + a_{120}y^2 \\ \quad + a_{102}z^2 + 2a_{220}xy^2 + 2a_{202}xz^2 + 2a_{211}xyz + a_{121}y^2z + a_{112}yz^2 \\ \quad + 2a_{221}xy^2z + a_{122}y^2z^2 + 2a_{212}xyz^2 + 2a_{222}xy^2z^2 = 0, \\ a_{010} + 2a_{020}y + a_{110}x + a_{011}z + a_{111}xz + 2a_{120}xy + 2a_{021}yz + a_{210}x^2 \\ \quad + a_{012}z^2 + 2a_{220}x^2y + 2a_{022}yz^2 + a_{211}x^2z + 2a_{121}xyz + a_{112}xz^2 \\ \quad + 2a_{221}x^2yz + 2a_{122}xyz^2 + a_{212}x^2z^2 + 2a_{222}x^2yz^2 = 0, \\ a_{001} + 2a_{002}z + a_{011}y + a_{101}x + a_{111}xy + 2a_{102}xz + 2a_{012}yz + a_{201}x^2 \\ \quad + a_{021}y^2 + 2a_{022}y^2z + 2a_{202}x^2z + a_{211}x^2y + a_{121}xy^2 + 2a_{112}xyz \\ \quad + a_{221}x^2y^2 + 2a_{122}xy^2z + 2a_{212}x^2yz + 2a_{222}x^2y^2z = 0. \end{cases} \quad (6.17)$$

With the simplified functions (equations 6.14 and 6.15), equation 6.16 becomes 6.18 and 6.19, respectively.

$$\begin{cases} a_{100} + 2a_{200}x + a_{110}y + a_{101}z + a_{111}yz + 2a_{210}yx + \\ \quad 2a_{201}zx + a_{120}y^2 + a_{102}z^2 = 0, \\ a_{010} + 2a_{020}y + a_{110}x + a_{011}z + a_{111}xz + 2a_{120}xy + \\ \quad 2a_{021}yz + a_{210}x^2 + a_{012}z^2 = 0, \\ a_{001} + 2a_{002}z + a_{011}y + a_{101}x + a_{111}xy + 2a_{102}xz + \\ \quad 2a_{012}yz + a_{201}x^2 + a_{021}y^2 = 0. \end{cases} \quad (6.18)$$

$$\begin{cases} a_{100} + 2a_{200}x + a_{110}y + a_{101}z = 0, \\ a_{010} + 2a_{020}y + a_{110}x + a_{011}z = 0, \\ a_{001} + 2a_{002}z + a_{011}y + a_{101}x = 0. \end{cases} \quad (6.19)$$

The three unknown coordinates of the optimal hypocenter  $(x_{int}, y_{int}, z_{int})$  are obtained by analytically solving either equation 6.17, or 6.18, or 6.19 through substitution.

For real data, the location estimates are negatively affected by poor data quality, errors in arrival time picking, and inaccurate velocity models (Pavlis, 1986; Wuestefeld et al., 2018). I thus evaluate the location uncertainties using the error ellipsoids obtained from the 3D misfit functions by considering the area where the misfit value is less than or equal to 5% of the minimum misfit (Goertz-Allmann et al., 2022). The error ellipsoids have the shape determined by the receiver configuration and the size determined by the differences between the observed P- and S-wave arrival times and the predicted arrival times for the obtained localization (Havskov et al., 2012).

#### **6.2.4 NonLinLoc**

The NonLinLoc developed by Lomax et al. (2000) is an earthquake location software package that uses a probabilistic, non-linear, global-search algorithm. The software has different options depending on the event types (local or teleseismic), wave types, search space, velocity model, predicted traveltimes calculation, search type, and location method. This study focuses on microseismic events; I thus use the NonLinLoc Non-Global mode for event localization. The NonLinLoc has a VPVS ratio option to be set either positive or negative, allowing the use of either one seismic phase (e.g., P-waves) or both P- and S-waves in the calculation. For a fair comparison with the combined coarse grid search and quadratic interpolation, I set the VPVS ratio to be negative to include both P- and S-waves in calculating the misfit function. For the search space, the program defines a 3D grid using coordinates of an origin, the number of nodes in x, y, and z directions, and grid spacing that includes the receiver locations. The velocity model in the NonLinLoc could be a 1D layered model or a 3D velocity model. This study uses 1D velocity models for comparison with the proposed method. The NonLinLoc has 3 different search types: grid search, Metropolis,

and Oct-Tree. This study uses the NonLinLoc with the Oct-Tree search for comparison with the proposed method. For location methods, the NonLinLoc has two options, including the inversion approach of Tarantola and Valette (1982) with the L2-RMS likelihood function and the equal differential time likelihood function with several modifications. I use the NonLinLoc with the inversion approach of Tarantola and Valette (1982) with the L2-RMS likelihood function for comparison with the proposed method (equations 6.7 and 6.8). The method uses an original coarse grid, followed by a bisection approach to subdivide the cell with the highest PDF into 8 sub-cells, which are then evaluated to determine which new cell should be divided again, leading to an improvement of the location accuracy by a factor of 2 in each grid dimension, with each iteration. New P- and/or S-wave traveltimes are computed for each sub-cell to obtain the relevant PDFs (misfits), contrary to the quadratic interpolation that requires only the PDFs on the coarse grid locations. For full details see Lomax and Curtis (2001) and Lomax et al. (2000, 2009).

## 6.3 Implementation and Results

### 6.3.1 Synthetic Data Examples

#### Illustrative source-receiver configuration

##### *Test setup*

I first test the quadratic interpolation on an illustrative source-receiver configuration. I create three vertical monitoring arrays; each array has 30 receivers with a spacing of 10 m. The true source location is at  $x_S = 763$  m,  $y_S = 402$  m, and  $z_S = 2464$  m. Figure 6.2 shows the source and receiver locations.

For the synthetic case, I use homogeneous velocity models  $V_p = 5000 \text{ ms}^{-1}$  and  $V_s = 3500 \text{ ms}^{-1}$  and compute the theoretical traveltimes of the P- and S-waves using equation 6.2. Then, I create a coarse 3D grid of 1000 m in the x and y dimensions and 600 m in the z dimension with a grid spacing  $dx = dy = dz = 200$  m. The search space has a size of 6x6x4 ( $N_x = N_y = 6$ ,  $N_z = 4$ , where  $N_x$ ,  $N_y$ , and  $N_z$  are the number of

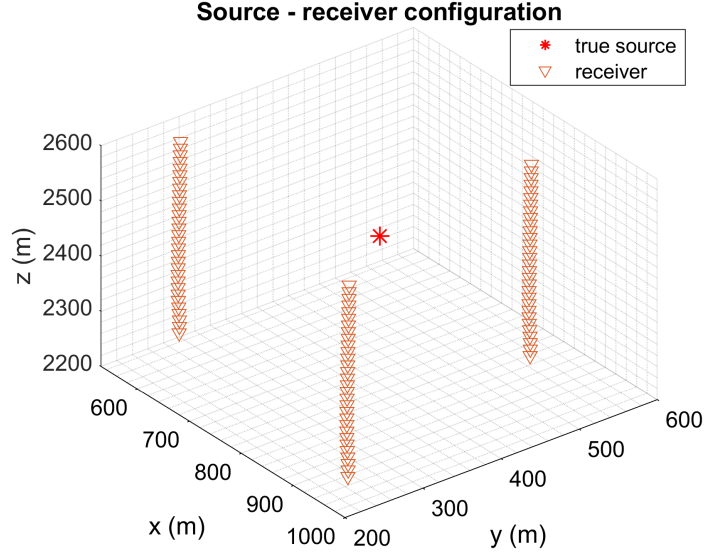


Figure 6.2: Illustrative source-receiver configuration with 3 vertical monitoring arrays depicted by open triangles and a true source indicated by the red star.

grid points in  $x, y, z$ ) with 144 nodes equivalent to 144 possible hypocenter locations. I repeat this using a fine grid spacing of 10 m in each dimension; the search space has  $N_x = N_y = 101, N_z = 61$  grid points with 622,261 nodes equivalent to 622,261 possible hypocenter locations.

I calculate the predicted P- and S-wave traveltimes of all possible hypocenter locations using equation 6.2. Next, I compute the differences in the traveltimes between these seismic phases for all possible hypocenter locations and sum over all receivers using equation 6.7. Figure 6.3 shows the resulting data points - the traveltime differences between the S- and P-waves summed over all receivers for all grid point locations.

The location errors in each dimension relative to the grid spacing can be computed using

$$\begin{cases} e_x = \frac{\Delta x}{dx} \times 100, \\ e_y = \frac{\Delta y}{dy} \times 100, \\ e_z = \frac{\Delta z}{dz} \times 100, \end{cases} \quad (6.20)$$

where  $e_x, e_y,$  and  $e_z$  are the errors (in percentage) in  $x, y,$  and  $z$  dimensions;  $x_{int}, y_{int},$

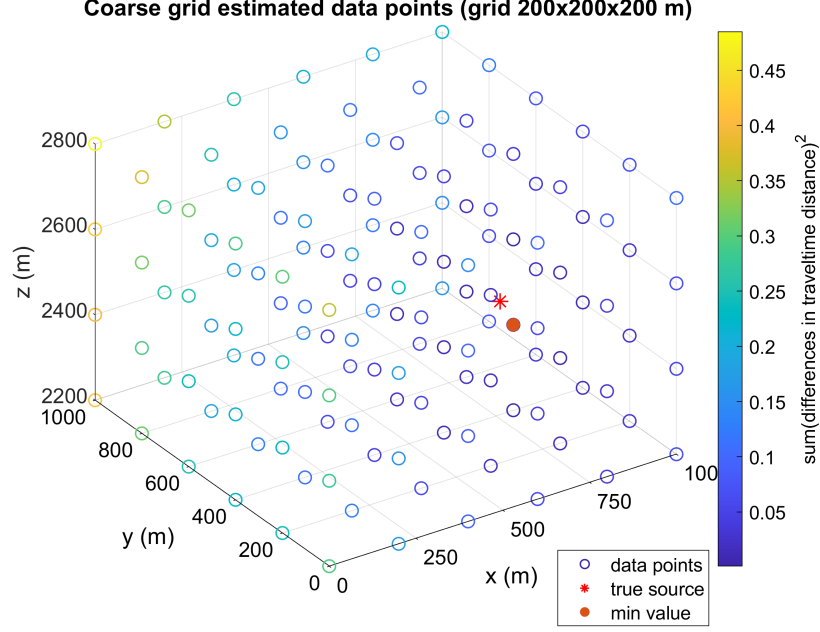


Figure 6.3: Open circles indicate data points computed using a coarse grid spacing of 200 m in each dimension. The filled red circle is where I have the minimum value, and the red star represents the actual source location.

and  $z_{int}$  are the resulting optimal location obtained from the root of equations 6.16, 6.17, 6.18, and 6.19;  $x_S$ ,  $y_S$ , and  $z_S$  are the actual source location;  $\Delta x = |x_{int} - x_S|$ ,  $\Delta y = |y_{int} - y_S|$ ,  $\Delta z = |z_{int} - z_S|$ ;  $dx$ ,  $dy$ , and  $dz$  are the grid spacings in x, y, z dimensions, respectively.

### ***Implementation of quadratic interpolation***

I search for the minimum value in the misfit function equation 6.7. The location of the minimum value using the coarse grid is at  $x_{min} = 800$  m,  $y_{min} = 400$  m, and  $z_{min} = 2400$  m (the filled red circle in Figure 6.3) which compares well with the true source location at (763 m, 402 m, 2464 m) (the red star in Figure 6.3) and the equal grid spacing of 200 m in each dimension. With this initial location, I select the 26 neighboring grid points as  $(800 \pm 200$  m,  $400 \pm 200$  m,  $2400 \pm 200$  m). Figure 6.4 shows the selected data points (filled, blue circles). I then establish the system of 27 linear equations from these data points and solve the unknown coefficients using equation 6.13. Table 6.1 shows the resulting coefficients. I insert these coefficients

into the quadratic function, equation 6.9, and compute the partial derivatives using equations 6.16 and 6.17 to find the optimal hypocenter location.

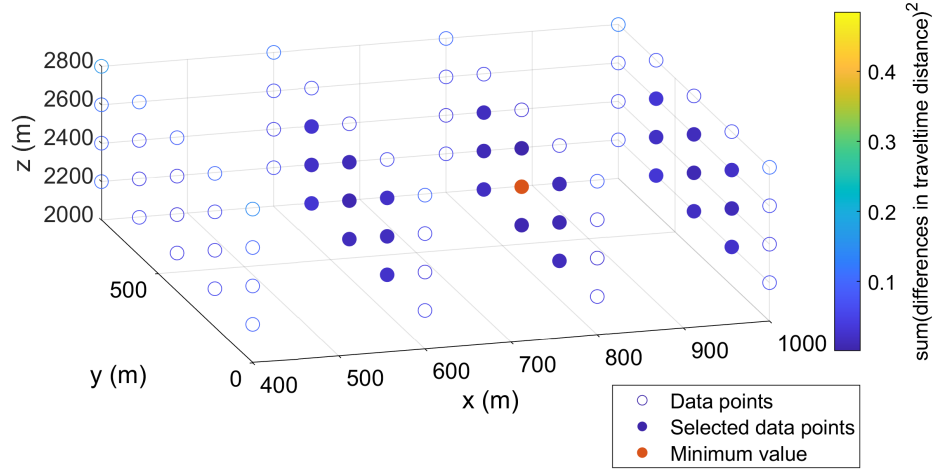


Figure 6.4: Filled, blue circles represent the 26 data points neighboring the minimum value (filled, red circle). These 27 grid points are used to solve the unknown coefficients of the quadratic function.

Table 6.1: Resulting coefficients of the full 3D quadratic function (equation 6.9).

Coefs	Value	Coefs	Value	Coefs	Value
$a_{000}$	7.5648	$a_{101}$	$7.0514 \times 10^{-6}$	$a_{022}$	$2.4551 \times 10^{-12}$
$a_{100}$	$-8.7504 \times 10^{-3}$	$a_{111}$	$-2.2415 \times 10^{-8}$	$a_{202}$	$3.8299 \times 10^{-13}$
$a_{010}$	$-1.8857 \times 10^{-2}$	$a_{210}$	$-1.0904 \times 10^{-8}$	$a_{211}$	$8.5246 \times 10^{-12}$
$a_{001}$	$-6.2211 \times 10^{-3}$	$a_{201}$	$-1.8556 \times 10^{-9}$	$a_{121}$	$2.2133 \times 10^{-11}$
$a_{200}$	$2.8621 \times 10^{-6}$	$a_{120}$	$-2.6246 \times 10^{-8}$	$a_{112}$	$4.7071 \times 10^{-12}$
$a_{020}$	$1.3966 \times 10^{-5}$	$a_{021}$	$-1.1651 \times 10^{-8}$	$a_{221}$	$-1.5287 \times 10^{-14}$
$a_{002}$	$1.3075 \times 10^{-6}$	$a_{102}$	$-1.4791 \times 10^{-9}$	$a_{122}$	$-4.6604 \times 10^{-15}$
$a_{110}$	$2.6872 \times 10^{-5}$	$a_{012}$	$-3.2975 \times 10^{-9}$	$a_{212}$	$-1.7787 \times 10^{-15}$
$a_{011}$	$1.5654 \times 10^{-5}$	$a_{220}$	$1.8408 \times 10^{-11}$	$a_{222}$	$3.2186 \times 10^{-18}$

### *Interpolated results*

Table 6.2 shows the interpolated source location and the corresponding errors in each dimension computed for different grid spacings using equation 6.20, from a coarse grid spacing of 200 m to finer grid spacings of 30 and 10 m. I observe that the errors

in each dimension are within the grid spacing. The errors are relatively small, e.g., for a coarse grid spacing of 200 m, the errors are less than 15% of the grid spacing; for finer grids, the errors are about 10% or less than 10% of the grid spacing in all three dimensions. Notably, the errors in the resulting location of the quadratic interpolation on a grid with a grid spacing of 200 m are less than 30 m, equivalent to using a grid with a 30 m spacing, which would typically be  $(200/30)^3 = 296$  times larger. Likewise, the interpolation on a grid with a 10 m grid spacing has can achieve in x, y, and z dimensions of about 1 m, equivalent to the grid search on a grid  $10^3 = 1000$  times smaller.

Ideally, when using a grid search, the maximum error would be half of the grid spacing in each direction. However, this only occurs for very well-resolved misfit functions. In the case of limited acquisition geometries, the resulting misfit functions can have flat portions, leading to spatially extensive global minima, spanning multiple grid points. In our comparisons of grid spacing here, all calculations use the same traveltimes recorded at the various receivers (same acquisition geometry). None of the tested location methods therefore change the theoretical misfit function. Variations in source locations and calculated misfit function are therefore restricted both by the grid spacing and limitations imposed by the acquisition geometry. The source of the location biases will become clear in the figures displaying the calculated misfit curves.

Figures 6.5 and 6.6 show the interpolated and true data surfaces for a coarse grid (size of 200 m in each dimension) and a fine grid (size of 10 m in each dimension) in the x-y, y-z, and x-z planes. The interpolated data surface is plotted using the resulting 3D full quadratic function. The true data surface is plotted using the selected data points used to find the coefficients of the quadratic function. Locations of the true source, interpolated source, and initial grid estimated source are plotted for comparison. I obtain a good fit between the interpolated and true data surfaces for coarse and fine grids.

Figures 6.5 and 6.6 also reveal an important aspect in that the accuracy of the re-

Table 6.2: Interpolated locations and corresponding errors in each dimension when using a coarse grid spacing of 200 m and finer grid spacings of 30 and 10 m when using the full 3D quadratic function with 27 unknown coefficients.  $x_{min}$ ,  $y_{min}$ , and  $z_{min}$  are the coordinates of the initial location where I have the minimum value of the sum of all traveltime differences (estimated from the coarse grid search).  $x_{int}$ ,  $y_{int}$ , and  $z_{int}$  are the coordinates of the optimal location obtained from interpolation.  $\Delta x$ ,  $\Delta y$ , and  $\Delta z$  are the absolute differences between the interpolated and actual source location.  $e_x$ ,  $e_y$ , and  $e_z$  are the errors in percentage between the interpolated and actual source locations. The actual source location is at  $x_S = 763$  m,  $y_S = 402$  m, and  $z_S = 2464$  m.

Grid spacing (m)	$x_{min}$ (m)	$y_{min}$ (m)	$z_{min}$ (m)	$x_{int}$ (m)	$y_{int}$ (m)	$z_{int}$ (m)	$\Delta x$ (m)	$\Delta y$ (m)	$\Delta z$ (m)	$e_x$ (%)	$e_y$ (%)	$e_z$ (%)
200	800	400	2400	789.01	386.64	2435.48	26.01	15.36	28.52	13	8	14
30	750	390	2470	761.88	403.19	2462.99	1.12	1.19	1.01	4	4	3
10	760	400	2460	761.94	403.07	2463.94	1.06	1.07	0.06	11	11	1

solved hypocenter using the interpolation algorithm is mostly limited by the flatness of the misfit function in certain directions instead of by how well the interpolation function resembles the true misfit/probability density function. The flatness of the misfit function (indicating any null spaces in the hypocenter solutions) is, in return, determined by the acquisition geometry (receiver locations) with respect to the source position. A more limited acquisition geometry creates a flatter misfit function, resulting in hypocenter estimates with large potential biases regardless of location method used (i.e., linearized, grid search, Bayesian, etc).

I observe that the higher-order cross terms shown in Table 6.1 have typically small coefficients; I obtain similar interpolation results when I exclude these terms to simplify the quadratic function, leaving 17 and 10 coefficients (equations 6.14 and 6.15). Table 6.3 shows the resulting 10 coefficients of the simplified equation 6.15 when using the initial location from a coarse grid spacing of 200 m. Table 6.4 shows the interpolated location and corresponding errors in each dimension computed for a coarse grid spacing of 200 m and finer grid spacings of 30 and 10 m using only the 10 coefficients. The apparent location biases in the  $x$  and  $y$  dimensions in the case of 10 m grid spac-

ing are larger than in the case of 30 m grid spacing. This is because of the limitation in the acquisition geometry, leading to the misfit function with a spatially extensive global minimum, and many grid points may fall within the location uncertainty. The full 3D quadratic function, equation 6.9, and the simplified function, equation 6.15, produce similar interpolated results and errors. Thus, I use the simplified function with 10 coefficients, equation 6.15, when applying the algorithm to the field-based source-receiver configuration in the next test.

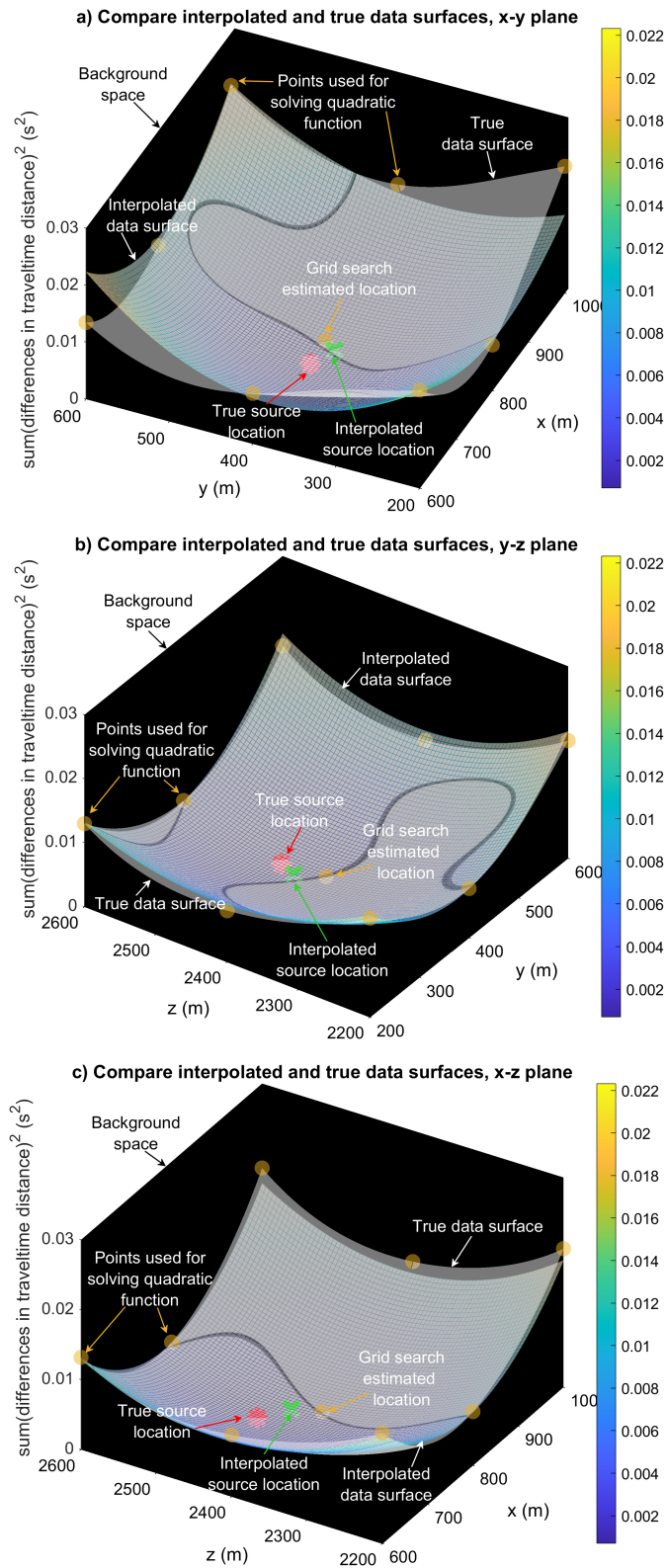


Figure 6.5: Interpolation results when using the full 3D quadratic function (equation 6.9) with the illustrative source-receiver configuration on a coarse grid spacing of 200 m in each dimension. a) Interpolated and true data surfaces in the x-y plane. b) Interpolated and true data surfaces in the y-z plane. c) Interpolated and true data surfaces in the x-z plane.

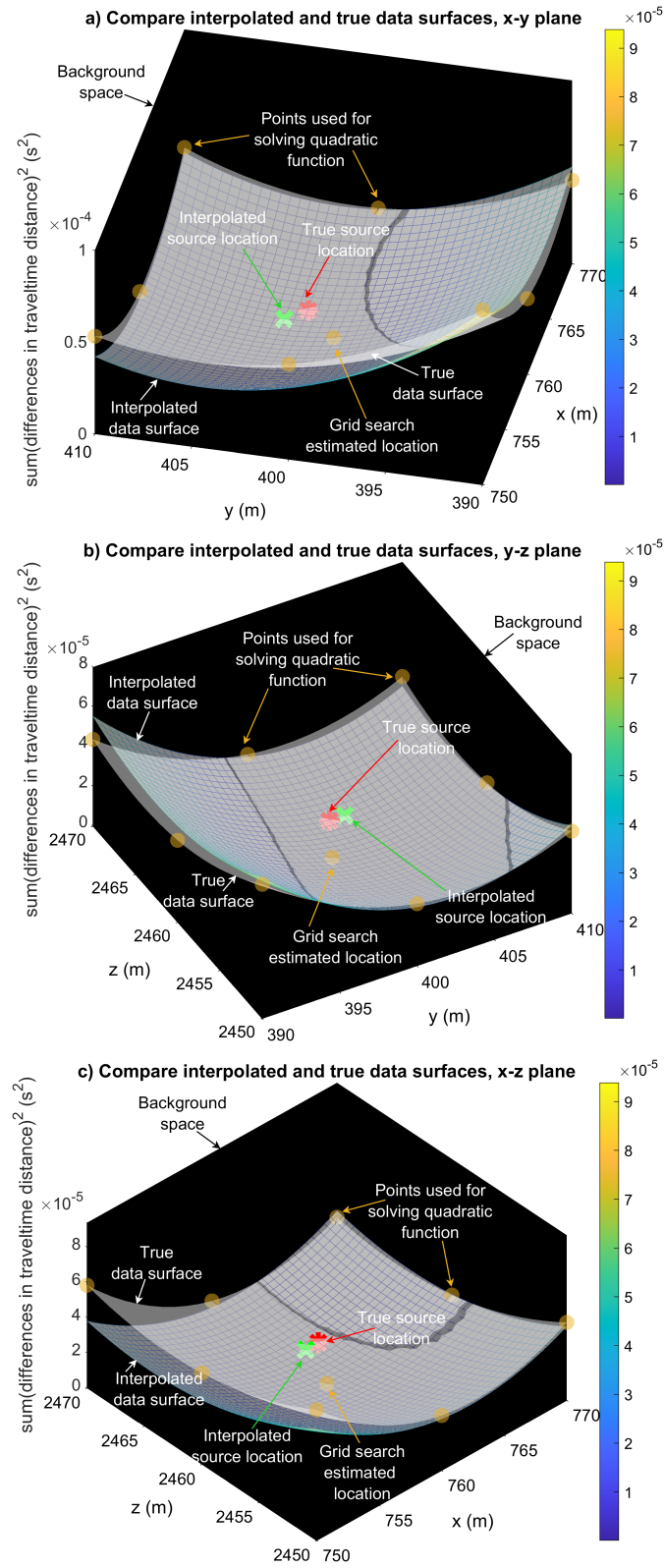


Figure 6.6: Interpolation results when using the full 3D quadratic function (equation 6.9) with the illustrative source-receiver configuration on a fine grid spacing of 10 m in each dimension. a) Interpolated and true data surfaces in the x-y plane. b) Interpolated and true data surfaces in the y-z plane. c) Interpolated and true data surfaces in the x-z plane.

Table 6.3: Resulting coefficients of the simplified quadratic function (equation 6.15).

Coef	Value	Coef	Value
$a_{000}$	1.2810	$a_{200}$	$2.6428 \times 10^{-7}$
$a_{100}$	$-2.1257 \times 10^{-4}$	$a_{020}$	$2.3852 \times 10^{-7}$
$a_{010}$	$-4.0191 \times 10^{-4}$	$a_{002}$	$1.8454 \times 10^{-7}$
$a_{001}$	$-8.9684 \times 10^{-4}$	$a_{110}$	$1.3273 \times 10^{-8}$
$a_{011}$	$6.8393 \times 10^{-9}$	$a_{101}$	$1.9275 \times 10^{-9}$

Table 6.4: Interpolated locations and corresponding errors in each dimension when using a coarse grid spacing of 200 m and finer grid spacings of 30 and 10 m when using the simplified quadratic function with 10 unknown coefficients.  $x_{min}$ ,  $y_{min}$ , and  $z_{min}$  are the coordinates of the initial location where I have the minimum value of the sum of all traveltime differences (estimated from the coarse grid search).  $x_{int}$ ,  $y_{int}$ , and  $z_{int}$  are the coordinates of the optimal location obtained from interpolation.  $\Delta x$ ,  $\Delta y$ , and  $\Delta z$  are the absolute differences between the interpolated and actual source locations.  $e_x$ ,  $e_y$ , and  $e_z$  are the errors in percentage between the interpolated and actual source locations. The actual source location is at  $x_S = 763$  m,  $y_S = 402$  m, and  $z_S = 2464$  m.

Grid spacing (m)	$x_{min}$ (m)	$y_{min}$ (m)	$z_{min}$ (m)	$x_{int}$ (m)	$y_{int}$ (m)	$z_{int}$ (m)	$\Delta x$ (m)	$\Delta y$ (m)	$\Delta z$ (m)	$e_x$ (%)	$e_y$ (%)	$e_z$ (%)
200	800	400	2400	797.52	373.34	2413.25	34.52	28.66	50.75	17	14	25
30	750	390	2470	763.27	402.03	2462.41	0.27	0.03	1.59	1	0	5
10	760	400	2460	762.10	402.93	2463.87	0.90	0.93	0.13	9	9	1

### ***Computation time***

Table 6.5 compares the computation time of the grid search method and the combination between grid search and quadratic interpolation in estimating the optimal hypocenter location for a coarse grid spacing of 200 m and finer grid spacings of 30 and 10 m. The total computation time of the combination method is broken down into three components, including (1) time used for grid search (generating initial location), (2) time for solving the system of linear equations and obtaining coefficients of the quadratic function, and (3) time spent solving the partial derivatives of the quadratic function to retrieve the optimal hypocenter location.

The efficiency of the grid search algorithm is inversely proportional to the number of grid points, with the computation time increasing significantly for finer grid spacings. Table 6.5 shows that a grid search over a space of 1000 m x 1000 m x 600 m with a grid spacing of 10 m is about  $3.5930/0.0145 = 250$  times slower than the search with a coarse grid spacing of 200 m. Refining locations using the grid search requires exhaustive searches over all possible locations in the search space, and it becomes computationally prohibitive when using a fine grid spacing (e.g., 1 m). This limitation can be resolved by employing the proposed quadratic interpolation algorithm (equation 6.15) on coarse-grid-estimated results from the grid search with 10 m grid spacing. The optimal location is obtained with errors within  $\pm 1$  m (Table 6.2 and 6.4), and the interpolation time is relatively small (within less than 0.1 s) regardless of the grid spacings (about 0.015 s for obtaining the coefficients of the quadratic function and about 0.06 s for solving the partial derivatives (Table 6.5)). For most cases, the coarse grid search combined with interpolation will be faster than a fine grid search to obtain similar location results. Total computation times are determined by both the forward modeling costs for the grid searches and, for each event, either the lookup (database) search to identify the grid location with the minimum misfit or time required to solve the interpolation step. Forward modeling costs (e.g., to compute traveltimes) are linearly proportional to the number of grid points and can thus be significantly different for coarse versus fine grids. Forward modeling is a fixed cost as it is done only once and does not depend on the number of events. The cost to search the database is also proportional to the grid size and has to be repeated for each individual event. The interpolation cost does not depend on the grid size but only on the number of grid points involved, but it is repeated for each event. The additional cost of a coarse grid search plus interpolation is small compared to solely performing a coarse grid search (Table 6.5), thus a coarse grid search plus interpolation can be orders of magnitude faster than a fine grid search to obtain comparable event locations irrespective if small or large numbers of events are

involved.

Table 6.5: Computation time of the grid search and the combination of grid search and quadratic interpolation (equation 6.15) when using a 3D search space 1000 m x 1000 m x 600 m with a coarse grid spacing of 200 m and finer grid spacings of 30 and 10 m. The actual source location is at  $x_S = 763$  m,  $y_S = 402$  m, and  $z_S = 2464$  m.

Methods	Number of grid points	Total computation time (s)	Time breakdown (s)		
			Grid search	Obtain coef	Solve derivatives
Grid search (grid spacing 200 m)	144	0.0145			
Grid search (grid spacing 200 m) + Quadratic interpolation (equation 6.15)	144	0.0931	0.0155	0.0154	0.0622
Grid search (grid spacing 30 m)	80,631	0.2226			
Grid search (grid spacing 30 m) + Quadratic interpolation (equation 6.15)	80,631	0.2963	0.2251	0.0148	0.0564
Grid search (grid spacing 10 m)	622,261	3.5930			
Grid search (grid spacing 10 m) + Quadratic interpolation (equation 6.15)	622,261	3.5823	3.5170	0.0143	0.0510

### ***Compare with location results from NonLinLoc***

I run the NonLinLoc software using the same synthetic data, including sensor geometry, actual source location, 1D velocity model, 3D search space, theoretical traveltimes of P- and S-waves, and L2 misfit function. The program first generates a 3D grid file containing P- and S-wave velocities and computes the predicted traveltimes of P- and S-waves. Then, it calculates the PDFs and locates the event using the Oct-Tree importance sampling. I test different sets of the initial grid cells for the Oct-Tree search. These cells define an initial Oct-Tree gridding over the full grid, not the fraction of the full grid (Lomax et al., 2000). The maximum number of grid cells should be 25,000 to 50,000; otherwise, it slows down the searches (Lomax et al., 2000). I use the Oct-Tree search with an initial number of grid cells of 10x10x6. Table 6.6 shows the NonLinLoc location results from coarse (200 m) and finer grid spacings (30 and 10 m). Compared with the results from combined coarse grid search and quadratic interpolation in Table 6.2 and Table 6.4, the NonLinLoc produces similar hypocenter estimates, indicating the validity of the proposed method. Both location methods are fast and complete within seconds (Tables 6.2, 6.4, and 6.5). The

quadratic interpolation produces the optimal hypocenter solution faster since the solution is generated analytically in 0.1 s, without any subdivision into new cells or additional traveltimes computations.

Table 6.6: NonLinLoc (NLL) locations and corresponding errors in each dimension when using a coarse grid spacing of 200 m and finer grid spacings of 30 and 10 m.  $x_{NLL}$ ,  $y_{NLL}$ , and  $z_{NLL}$  are the coordinates of the estimated location.  $\Delta x$ ,  $\Delta y$ , and  $\Delta z$  are the absolute differences between the NonLinLoc results and actual source locations. The actual source location is at  $x_S = 763$  m,  $y_S = 402$  m, and  $z_S = 2464$  m.

Grid spacing (m)	$x_{NLL}$ (m)	$y_{NLL}$ (m)	$z_{NLL}$ (m)	$\Delta x$ (m)	$\Delta y$ (m)	$\Delta z$ (m)	Computation time (s)
200	765	410	2476.17	2	8	12.17	2.96
30	763	400	2464.45	0	2	0.45	3.01
10	763	400	2463.67	0	2	0.33	3.23

## Field-based source-receiver configuration

### *Test setup*

I test the quadratic interpolation algorithm on a field-based source-receiver configuration with vertical and horizontal monitoring arrays. The vertical array has 30 receivers spacing of 10 m, and the horizontal array has 16 receivers spacing of 30 m (Bui & van der Baan, 2020). The true source location is at  $x_S = 563$  m,  $y_S = 352$  m, and  $z_S = 2464$  m. Figure 6.7 shows the source and receiver locations.

The test setup, including the velocity model and search space, is the same as in the illustrative source-receiver case. I repeat the calculation for a coarse grid spacing of 200 m and a finer size of 10 m. The predicted traveltimes of the P- and S-waves of all possible hypocenter locations in the search space are computed using equation 6.2. Then, the misfit is calculated using equation 6.7.

### *Implementation of quadratic interpolation*

The algorithm first searches for the minimum value in the misfit function equation 6.7. The location of the minimum value using the coarse grid is at  $x_{min} = 600$  m,

$y_{min} = 400$  m, and  $z_{min} = 2400$  m which compares well with the true source location at (563 m, 352 m, 2464 m) and the equal grid spacing of 200 m in each dimension. With this initial location, I select the 26 neighboring grid points as  $(600 \pm 200$  m,  $400 \pm 200$  m,  $2400 \pm 200$  m). I then build the system of 27 linear equations from these grid points and solve the unknown coefficients using equation 6.13. Since the simplified quadratic function can produce similar results as the full function, I use the function with 10 coefficients, equation 6.15, in this test. Table 6.7 shows the resulting coefficients. I then compute the partial derivatives, equation 6.19, to find the optimal hypocenter location.

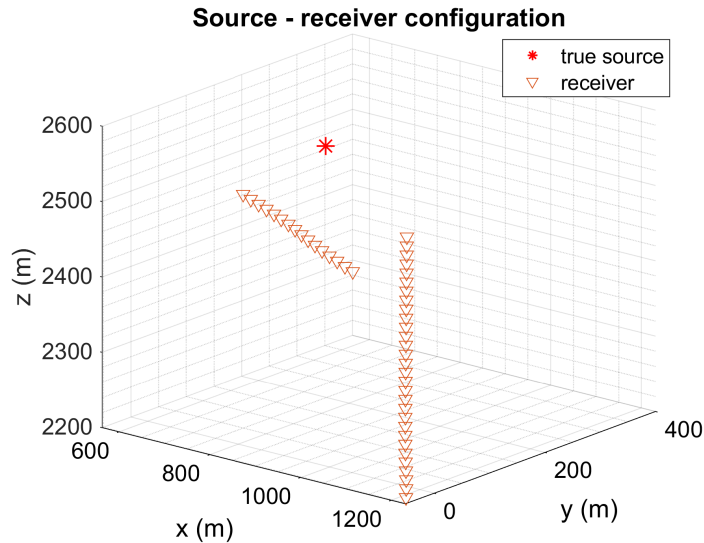


Figure 6.7: Field-based source-receiver configuration with vertical and horizontal monitoring arrays depicted by open triangles and a true source indicated by the red star.

### ***Interpolated results***

Table 6.8 shows the interpolated source location and the errors in each dimension computed using equation 6.20 for a coarse grid spacing of 200 m and finer grid spacings of 30 and 10 m. With a reduced set of 10 coefficients, I still obtain the optimal location with relatively small errors compared with the grid spacing. More importantly, I observe that the interpolation on a grid with a grid spacing 10 m has errors in x, y, and z dimensions of about 1 m, equivalent to the grid search on a grid  $10^3 = 1000$

Table 6.7: Resulting coefficients of the simplified quadratic function (equation 6.15).

Coef	Value	Coef	Value
$a_{000}$	$9.9816 \times 10^{-2}$	$a_{200}$	$1.8942 \times 10^{-7}$
$a_{100}$	$-2.4535 \times 10^{-5}$	$a_{020}$	$1.4645 \times 10^{-7}$
$a_{010}$	$-3.3860 \times 10^{-5}$	$a_{002}$	$1.4960 \times 10^{-8}$
$a_{001}$	$-6.9593 \times 10^{-5}$	$a_{110}$	$-2.4797 \times 10^{-7}$
$a_{011}$	$-1.1111 \times 10^{-8}$	$a_{101}$	$3.8979 \times 10^{-9}$

times smaller.

Table 6.8: Interpolated locations and corresponding errors in each dimension when using a coarse grid spacing of 200 m and finer grid spacings of 30 and 10 m when using the simplified quadratic function with 10 unknown coefficients.  $x_{min}$ ,  $y_{min}$ , and  $z_{min}$  are the coordinates of the initial location where I have the minimum value of the sum of all traveltime differences (estimated from the coarse grid search).  $x_{int}$ ,  $y_{int}$ , and  $z_{int}$  are the coordinates of the optimal location obtained from interpolation.  $\Delta x$ ,  $\Delta y$ , and  $\Delta z$  are the absolute differences between the interpolated and actual source locations.  $e_x$ ,  $e_y$ , and  $e_z$  are the errors in percentage between the interpolated and actual source locations. The actual source location is at  $x_S = 563$  m,  $y_S = 352$  m, and  $z_S = 2464$  m.

Grid spacing (m)	$x_{min}$ (m)	$y_{min}$ (m)	$z_{min}$ (m)	$x_{int}$ (m)	$y_{int}$ (m)	$z_{int}$ (m)	$\Delta x$ (m)	$\Delta y$ (m)	$\Delta z$ (m)	$e_x$ (%)	$e_y$ (%)	$e_z$ (%)
200	600	400	2400	544.59	396.75	2476.63	18.41	43.75	12.63	9	22	6
30	570	360	2470	561.37	353.66	2467.23	1.63	1.66	3.23	5	6	11
10	560	350	2460	561.77	352.89	2463.80	1.23	0.89	0.20	12	9	2

Figures 6.8 and 6.9 show the interpolated and true data surfaces for the coarse grid spacing of 200 m and the fine grid spacing of 10 m in the x-y, y-z, and x-z planes. The interpolated data surface is plotted using the simplified quadratic function (equation 6.15). The true data surface is plotted using the selected data points used to find the coefficients of the quadratic function. Locations of the true source, interpolated source, and initial grid estimated source are plotted for comparison. I obtain a good fit between the interpolated and true data surfaces for coarse and fine grids.

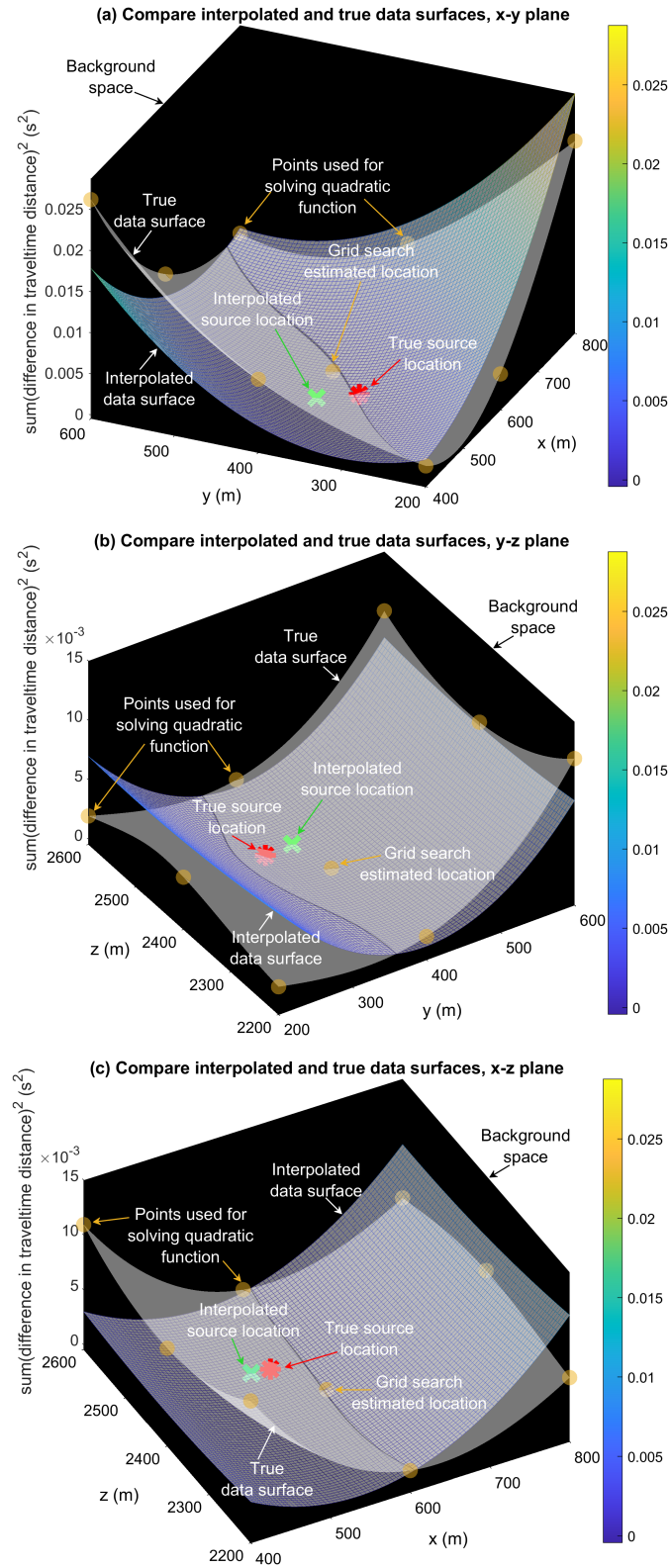


Figure 6.8: Interpolation results when using the simplified quadratic function (equation 6.15) with the field-based source-receiver configuration on a coarse grid spacing of 200 m in each dimension. a) Interpolated and true data surfaces in the x-y plane. b) Interpolated and true data surfaces in the y-z plane. c) Interpolated and true data surfaces in the x-z plane.

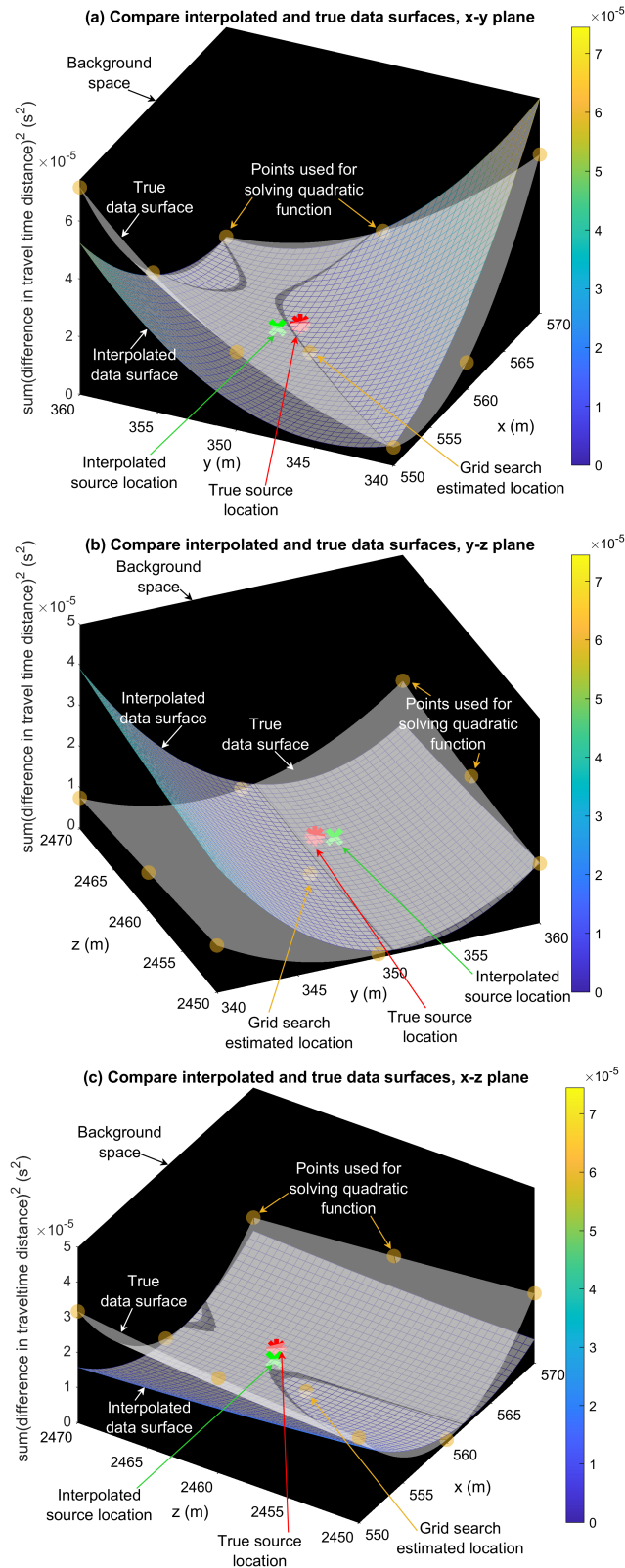


Figure 6.9: Interpolation results when using the simplified quadratic function (equation 6.15) with the field-based source-receiver configuration on a fine grid spacing of 10 m in each dimension. a) Interpolated and true data surfaces in the x-y plane. b) Interpolated and true data surfaces in the y-z plane. c) Interpolated and true data surfaces in the x-z plane.

### *Compare with location results from NonLinLoc*

I also estimate the event location for this synthetic data set using the NonLinLoc and compare it with the results from the combined coarse grid search and quadratic interpolation. Table 6.9 shows the NonLinLoc location results and errors in  $x$ ,  $y$ , and  $z$  dimensions from coarse and fine grid spacings when using the Oct-Tree with an initial number of grid cells of  $10 \times 10 \times 6$ . Compared with the quadratic interpolation results in Table 6.8, the NonLinLoc produces similar hypocenter estimates with relatively small errors in all three dimensions. Both the proposed method and the NonLinLoc have fast calculations, resolving the inefficiency of the exhaustive grid search. For this case, data are generated from the field-based source-receiver configuration with 46 receivers (fewer than in the previous case), so the NonLinLoc computation time is about 1 s.

Table 6.9: NonLinLoc (NLL) locations and corresponding errors in each dimension when using a coarse grid spacing of 200 m and finer grid spacings of 30 and 10 m.  $x_{NLL}$ ,  $y_{NLL}$ , and  $z_{NLL}$  are the coordinates of the estimated location.  $\Delta x$ ,  $\Delta y$ , and  $\Delta z$  are the absolute differences between the NonLinLoc results and actual source locations. The actual source location is at  $x_S = 563$  m,  $y_S = 352$  m, and  $z_S = 2464$  m.

Grid spacing (m)	$x_{NLL}$ (m)	$y_{NLL}$ (m)	$z_{NLL}$ (m)	$\Delta x$ (m)	$\Delta y$ (m)	$\Delta z$ (m)	Computation time (s)
200	541	300	2465.63	22	52	1.63	0.88
30	561	350	2464.06	2	2	0.06	0.89
10	564	350	2464.06	1	2	0.06	1.07

## 6.3.2 Real Data Example

### Data overview and preprocessing

I use the microseismic data induced by a hydraulic fracturing treatment in a hydrocarbon reservoir. All treatment wells used the sliding sleeve completion technique. The microseismicity was recorded at a high sampling rate of 0.25 ms by 3-component (3C) receivers in two monitoring arrays, a vertical array with 30 receivers equally

spacing of 10 m and a horizontal array with 16 receivers equally spacing of 30 m. Figure 6.10 shows the locations of the treatment wells (wells 1, 2, 3, and 4) and the two monitoring arrays. The horizontal array was deployed on a tool string moving every five treatment stages.

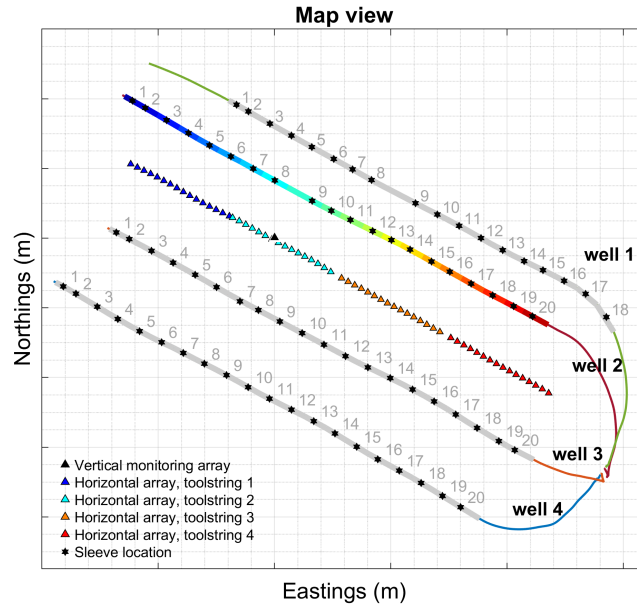


Figure 6.10: Locations of treatment wells and monitoring arrays. The black star symbol indicates the sleeve locations. The black triangle indicates the vertical monitoring array. The horizontal array was on a moving tool string with four positions indicated by blue, cyan, orange, and red triangles corresponding to tool strings 1, 2, 3, and 4, respectively.

The microseismic data emitted from treatment stages in wells 1 and 3 were recorded only by the vertical array, while the data from wells 2 and 4 were recorded by both arrays. I first preprocess this raw 3C data of 1.2 terabytes by estimating the sensor orientation and rotating the data into the geographical frame (North, East, and Z (Up)) to correct the amplitude and polarity of the waveforms. Then, I apply a bandpass filter with two cutoff frequencies of 60 and 300 Hz to reduce the unwanted noise and improve the data quality. Next, I detect and extract potential events from the data using a fast matched filter algorithm (Bui & van der Baan, 2020). Nearly 20,000 excellent microseismic events (those with clear P- and S-phases) are detected in both vertical and horizontal monitoring wells. After that, I build a 1D velocity

model using compressional and shear sonic logs data and available well tops and estimate the hypocenters of about 1000 events (those having a signal-to-noise ratio (SNR) larger than 6) using a grid search with a grid spacing of 20 m and the PDFs constructed using the difference between the observed and predicted S-P time and azimuth angle. Figure 6.12a-c shows the map view and profile views of the initial location obtained from the grid search with a grid spacing of 20 m. Since I use the grid search with a quite coarse grid spacing, I observe the grid imprint effect on the location results, which can adversely affect the interpretation of the shape and size of microseismic events. I thus use the quadratic interpolation algorithm to refine these coarse-grid-estimated locations.

### **Implementation of quadratic interpolation and Results**

I employ quadratic interpolation to refine the locations obtained from the grid search with a 20 m grid spacing of about 1000 microseismic events. First, the predicted traveltimes of P- and S-waves of all possible locations are computed using raytracing (Cerveny, 2001) and a 1D layered velocity model. The 1D ray-tracing algorithm guesses an initial ray path and perturbs iteratively to optimize the ray parameter to be constant along the ray and be the same in all layers such that the Snell's law is satisfied (Cerveny, 2001). The resulting traveltimes are stored in a lookup table format. I compute the misfit function, equation 6.7, using the predicted traveltimes and the observed arrival times of P- and S-waves from picking. The initial location obtained from the grid search with a grid spacing of 20 m is the most likely hypocenter where I have the minimum value in the misfit function. Figure 6.11 shows the histogram of residuals between the predicted and observed S-P traveltimes. Relatively small residuals are obtained because all events used for grid searches have a good SNR with visible P- and S-phases. Moreover, I also manually inspect the P- and S-wave time picks to ensure that the time picks used for event locations have small uncertainties. Stages towards the well's heel exhibit a shear wave splitting phenomenon (more details

are discussed in Chapter 8); I made sure to be consistent with the S-wave time picks, which are the first arriving horizontal S waves.

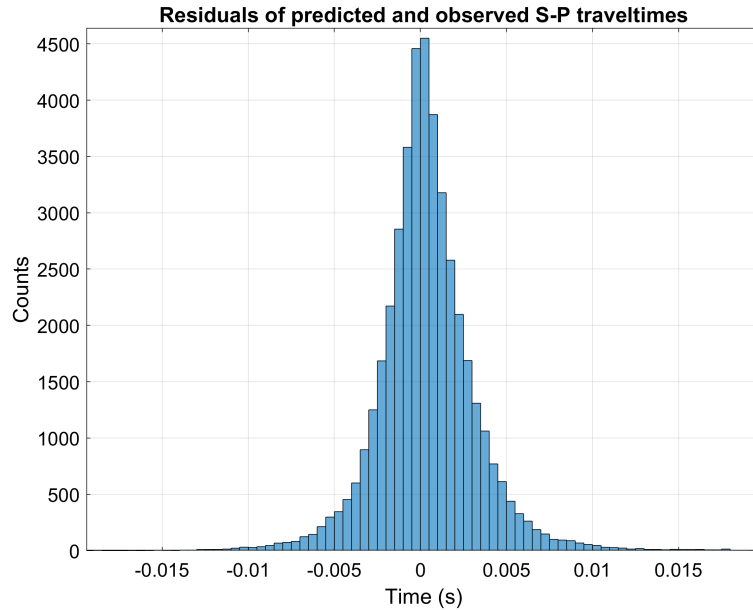


Figure 6.11: Residuals of the predicted and observed S-P traveltimes.

With the initial location  $(x_{min}, y_{min}, z_{min})$ , I can get its indexes in the table lookup and select the 26 neighboring grid points as  $(x_{min} \pm 20 \text{ m}, y_{min} \pm 20 \text{ m}, z_{min} \pm 20 \text{ m})$ . This set of grid points is then used to solve the coefficients of the quadratic function, equation 6.15. After that, I calculate the partial derivatives of the quadratic function using equation 6.19 to retrieve the optimal hypocenter location. Figure 6.13a-c shows the map view and profile views of the interpolation results on the grid (grid spacing = 20 m) estimated locations. The grid imprint effect is reduced as the event locations are refined. However, I still observe the imprint effect in the North direction in Figure 6.13c, which might be due to the flatness of the misfit function (caused by the source-receiver configuration), and the interpolation can not help much with the refinement in this direction.

To improve the location results, I implement the quadratic interpolation on a finer grid estimated results. Figure 6.14a-c shows the map view and profile views of the initial locations obtained from the grid search with a grid spacing of 10 m. Figs

6.15a-c shows the map view and profile views of the interpolation results with the grid imprint effect reduced significantly. The combination of quadratic interpolation and a grid search (grid spacing = 10 m) produces better results than the grid search (Figure 6.14a-c). The event locations are refined as the interpolation accelerates the searches and helps to retrieve the optimal location as if using the grid search with a finer grid spacing which can not be obtained due to the computational limitations of the grid search method. Figure 6.16a-c shows the error ellipsoids obtained from the misfit functions by considering the area where the misfit value is less than or equal to 5% of the minimum misfit. The location errors are larger, especially in the depth direction, for events in the last treatment stages. These errors could be attributed to uncertainties in polarization analysis (as these stages are at the furthest distance from the vertical monitoring array), pickings or velocity models due to the complexities caused by anisotropy as I observe strong evidence of anisotropy with the S-waves arriving at different times on the seismograms of the last treatment data.

## **6.4 Discussions**

### **6.4.1 Pros and cons of quadratic interpolation**

The quadratic interpolation helps refine the event location from coarse-grid-estimated results. The interpolated surfaces closely resemble the true surfaces around the optimal hypocenter locations, as seen in Figures 6.5, 6.6, 6.8, and 6.9. The combined coarse grid search and interpolation produces the optimal grid point location equivalent to a finer grid search and reduces the grid imprint effect of the grid search method, which is often seen in the coarse-grid-estimated results. Through synthetic examples in which I know the actual source location, I observe that the accuracy of the estimated locations is improved with quadratic interpolation; I can obtain the locations with errors within  $\pm 1$  m when applying the interpolation on the grid search with 10 m grid spacing. The accuracy of the interpolated hypocenter location is typi-

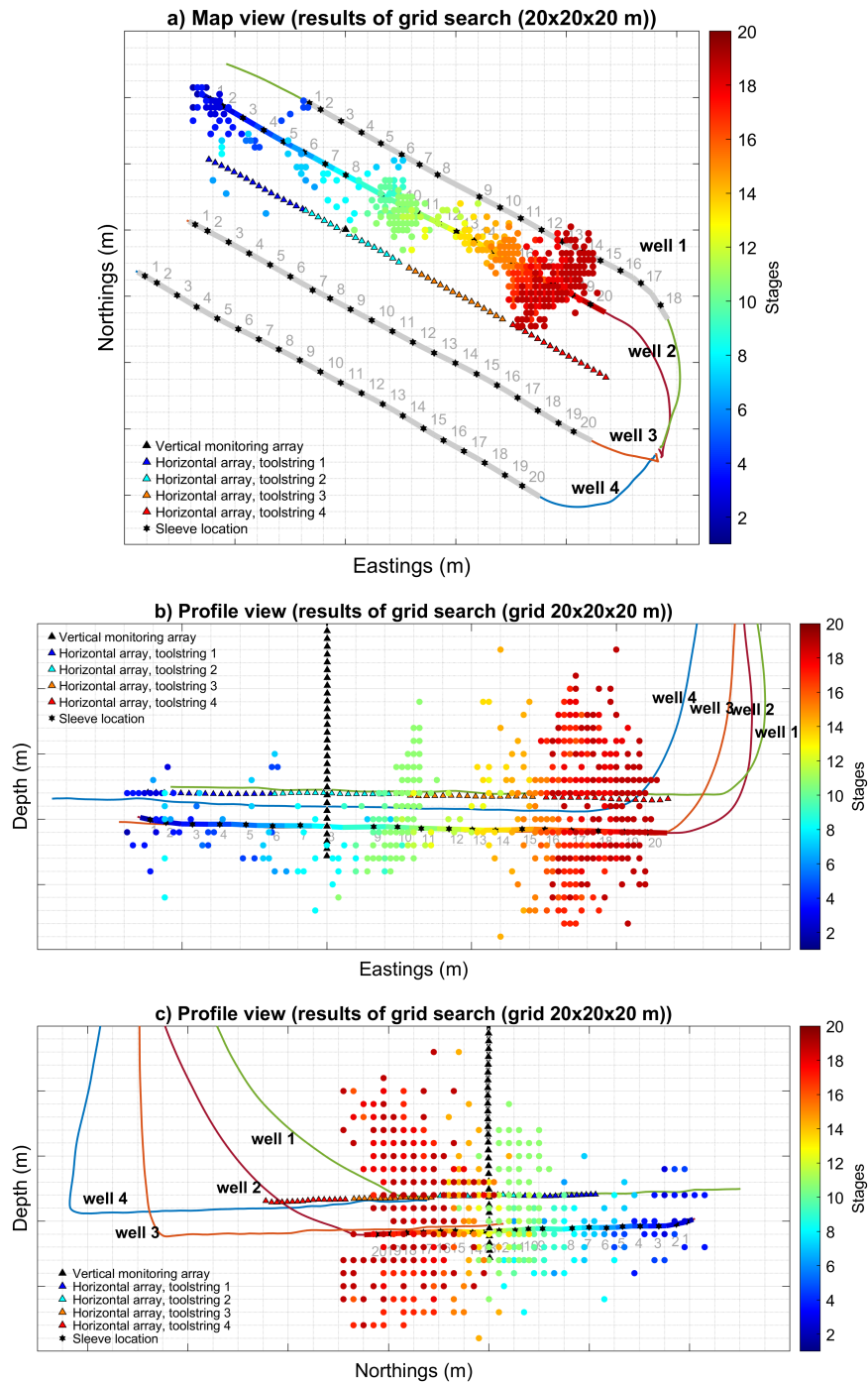


Figure 6.12: Initial event locations obtained from the grid search method with a grid spacing of 20 m. a) Map view. b) and c) Profile views.

cally more influenced by limitations in the acquisition geometry instead of the choice of interpolation function, equations 6.9, 6.14, 6.15, because misfit functions have to first order a quadratic shape, equation 6.7.

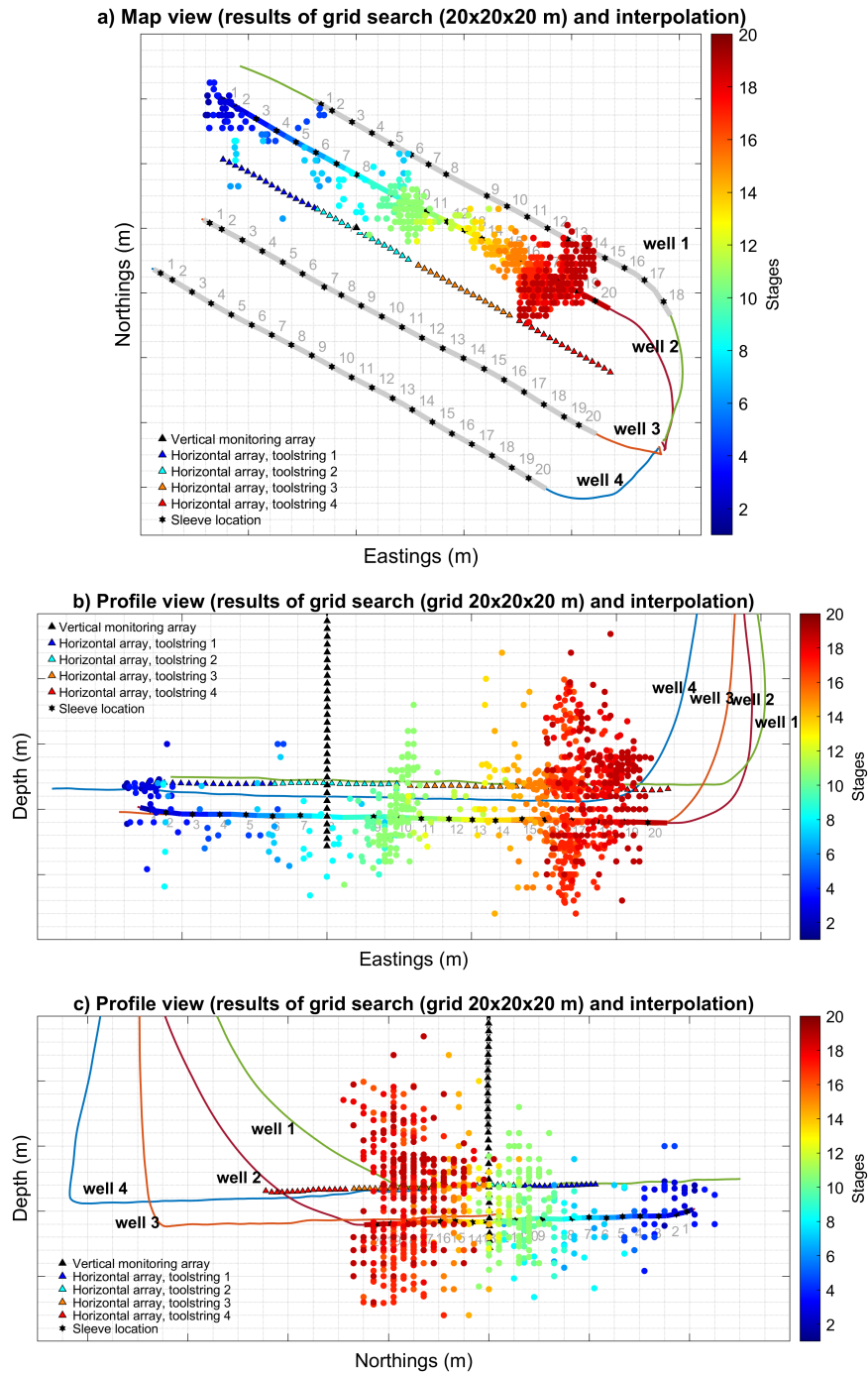


Figure 6.13: Interpolated results when applying the interpolation on the grid (grid spacing = 20 m) estimated locations. a) Map view. b) and c) Profile views.

The combination of coarse-grid-estimated location and interpolation accelerates the grid searches in the case of large search spaces with small grid spacings. Localizing the events in such a search space is computationally prohibitive for the grid search since

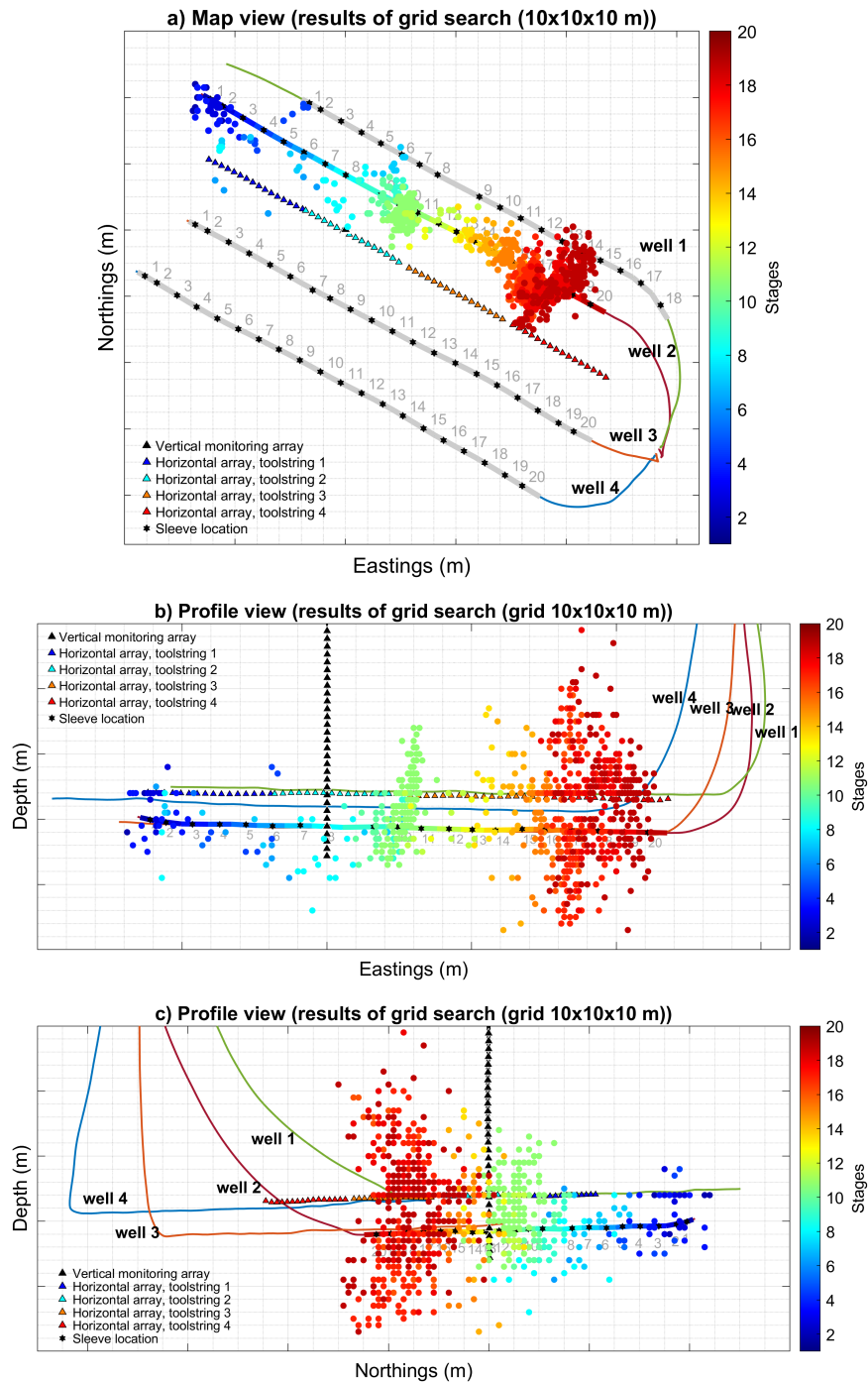


Figure 6.14: Initial locations obtained from the grid search method with a grid spacing of 10 m. a) Map view. b) and c) Profile views.

the number of gridded data points increases with a power of three of the grid spacing difference. Although the grids of P- and S-wave traveltimes need to be computed only once, it can take hours to complete the computation over large search spaces

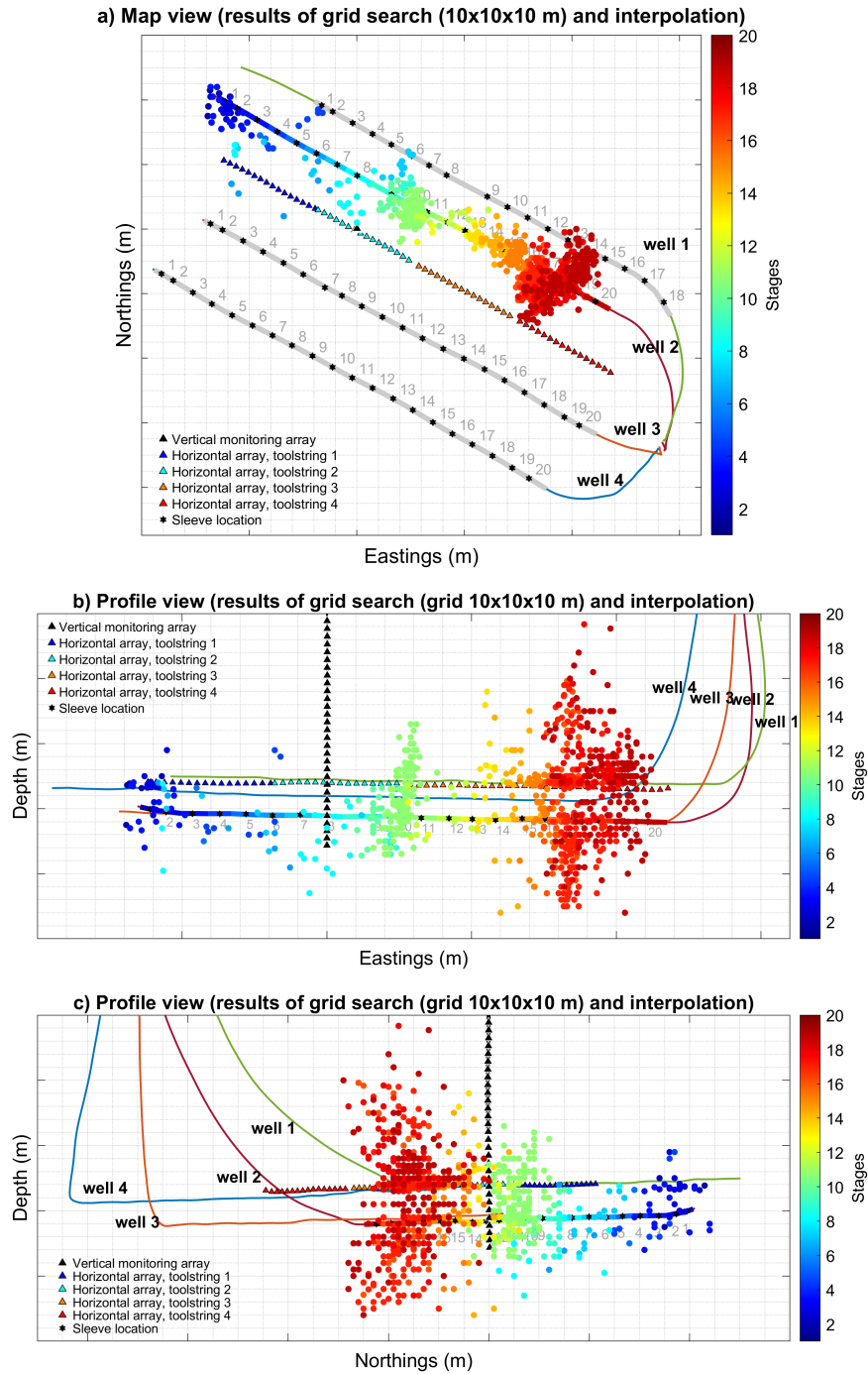


Figure 6.15: Interpolated results when applying the interpolation on the grid (grid spacing = 10 m) estimated locations. a) Map view. b) and c) Profile views.

with a fine grid spacing (e.g., 1 m) and also requires a significant amount of memory (up to gigabytes) to store tables of grids and traveltimes. When I perform the grid search, it also takes several minutes to execute the lookup search to determine the grid

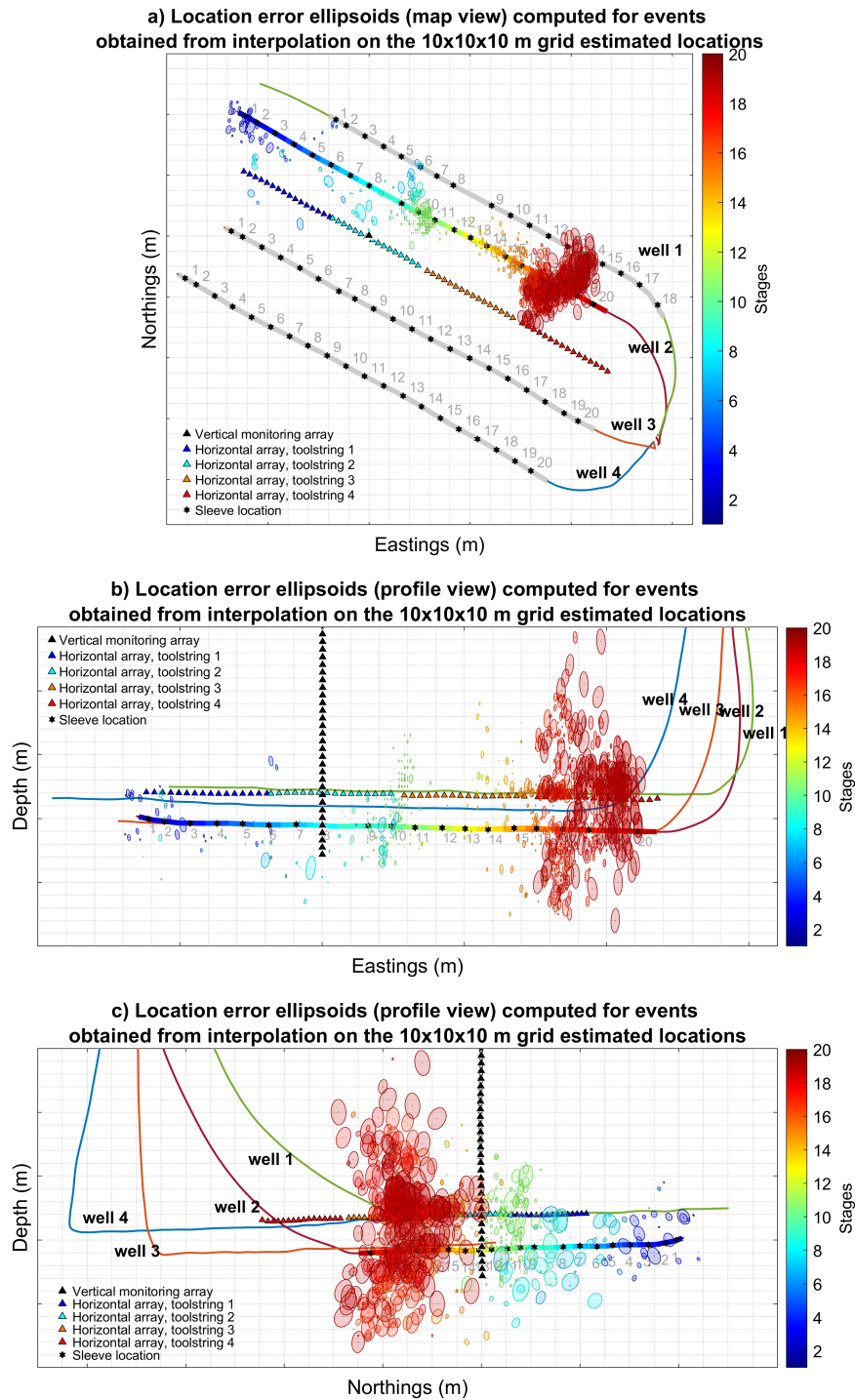


Figure 6.16: Location error ellipsoids computed for events obtained from interpolation on the grid (grid spacing = 10 m) estimated locations. a) Map view. b) and c) Profile views.

location with the minimum misfit. In contrast, when using the quadratic interpolation technique, I only need to acquire the initial locations estimated from a coarse grid

and then can quickly refine the locations by solving a system of linear equations and partial derivatives of the quadratic function. Although I need to perform the interpolation for each event, the interpolation time is relatively small (less than 1 s per event) regardless of the grid spacings (Table 6.5). When applying to 1000 events and using 10-m-grid-estimated locations, the interpolation for all events can be completed within several minutes to refine the locations, which is much faster than only using a grid search with finer grid spacing (up to several hours).

I can reduce the complexity of the full 3D quadratic function by excluding the high-order cross terms. The number of degrees of freedom (number of unknown coefficients) can be reduced from a full set of 27 to only 10. In that way, the full quadratic function in 3D becomes a quadratic polynomial, and computing the partial derivatives is more straightforward, equation 6.18. More importantly, I still obtain similar interpolation results with the simplified function as when using the full function because of the shape of the full misfit functions for hypocenter locations, which typically have principal axes in the x-y, x-z and y-z planes (Figures 6.5, 6.6, 6.8, and 6.9). Using a reduced set of coefficients has a negligible impact on the computation times, which are mostly influenced by computing the traveltimes at all grid positions. Thus, the full set of coefficients could also be used if preferred.

## 6.4.2 Alternative acceleration methods

### Bisection

Bisection is one of the alternatives for estimating the location (Bachrathy & Stépán, 2012; Lomax & Curtis, 2001; Lomax et al., 2000, 2009; Press et al., 1992). This method is also known as the half-interval method, which finds the solutions of the given equation by repeatedly dividing the interval (Press et al., 1992). The bisection method, therefore, does not require solving the partial derivatives as the quadratic interpolation technique. However, bisection requires to compute new traveltimes for each additional bisection point, contrary to the quadratic interpolation method since

the inversion is determined by the misfits at the existing grid locations (Lomax & Curtis, 2001; Lomax et al., 2000, 2009). Computing new traveltimes may add noticeably to the total computation times depending on the complexity of the velocity field. Nonetheless, bisection on a coarse grid is faster than solely performing a grid search using a finer grid. In 3D spaces, the bisection method also requires a cube of initial data points (nodes), which can be divided into multiple smaller cubes (Bachrathy & Stépán, 2012; Lomax & Curtis, 2001; Lomax et al., 2000, 2009). The method iteratively refines the bracketing cubes and evaluates the function with new nodes of the new sub-cubes until obtaining the roots of the function (Bachrathy & Stépán, 2012). The convergence of the bisection method is guaranteed linearly; however, the convergence rate is often slow, which is a disadvantage of the bisection compared with quadratic interpolation (Bachrathy & Stépán, 2012; Press et al., 1992).

Because the interpolation is applied to the values of the misfit function on the grid points surrounding the minimum (Figure 6.4), the interpolation approach will converge to the same answer as obtained by a continuously refined grid search, for instance as implemented by bisection, as long as the misfit function varies smoothly between the interpolation points. Both the bisection and interpolation techniques honor the shape of the misfit function in the grid search, and are influenced to the same extent as a brute force fine grid search by noisy picks or limited acquisition geometries.

### **Coarse grid search and fine local inversion**

Another alternative for refining the event location is the combined coarse grid search and fine local inversion (Bai et al., 2009). This method is more computationally efficient than the corresponding fine grid search, similar to our implementation of coarse grid search plus quadratic interpolation. I anticipate that both acceleration methods will produce highly similar results for well-behaved misfit functions with single extremal values within the search domain around the grid point  $(x_{min}, y_{min}, z_{min})$  since the misfit function is determined predominantly by the acquisition geometry,

and both approaches employ the difference between predicted and observed travel-times. However, a local inversion requires the calculation of additional traveltimes and their derivatives if multiple iterations are used. Depending on the complexity of the medium and the algorithm used to compute the traveltimes and/or gradients this can augment computation times substantially compared with the quadratic interpolation technique. Also, it is likely that for more complex misfit functions, a local search will be influenced strongly by the type of solver used and the exact settings for any regularization parameters. Furthermore, the local inversion starts from a single point, contrary to the quadratic interpolation, which uses 26 grid points surrounding the minimum. This may provide some smoothing of the misfit function, thereby reducing any local fluctuations, for instance, due to picking uncertainties.

## **6.5 Conclusions**

This study employs the quadratic interpolation technique to refine the coarse-grid-estimated locations, resolving the computational challenge of the grid search method. Synthetic and real data examples show that this technique enables event location refinement. The combination of coarse grid search and quadratic interpolation produces optimal hypocenter locations equivalent to finer grid searches. Using quadratic interpolation speeds up the grid search method over large search spaces. Moreover, this technique reduces the grid imprint effect often seen in the coarse-grid-estimated results.

# Chapter 7

## Moment-tensor inversion of hydraulic-fracturing-induced events in a Montney reservoir, northeastern British Columbia

### Summary

Source mechanisms help understand the fracturing behavior and the evolving stress field in microseismic monitoring. This chapter studies the source mechanisms of hydraulic-fracturing-induced events recorded by vertical and horizontal monitoring arrays from 20 stages in a treatment well in a Montney reservoir, northeastern British Columbia, using amplitude-based data methods to continue investigating the causes of the event anomaly between stages. First, I apply the inversion on synthetic amplitudes to examine the acquisition geometry effects on the inversion and test different input parameters to find the best inversion scheme for the real data. The forward modeling results show that the horizontal monitoring array better samples the focal sphere than the vertical monitoring array. Moment-tensor inversion produces more reliable results when using P- and S-wave amplitudes in all three data components from both monitoring arrays. Then, I analyze the source mechanisms of over 1000 excellent microseismic events using a screening test based on the S/P amplitude ratios and a full inversion. The screening test quickly provides a rough estimate of the source

mechanisms, indicating a similar characteristic between the vertical-array data and horizontal-array data, with tensile mechanisms being dominant, particularly in stages toward the heel of the well. This first classification into the number of shear and tensile events per stage is then compared with the full moment-tensor inversion results. The comparison shows that both tensile and shear faultings exist in the data. The first 15 stages have a similar characteristic in the inversion results, with 3 clusters of events distributed at the center (shearing), top-left (opening tensile cracks), and bottom-right (closing tensile cracks) of Hudson’s source-type plot. The last 5 stages (toward the well’s heel) have the solutions plotted in many places on Hudson’s source-type plot, likely due to an anisotropic velocity field since strong shear-wave splitting evidence is observed in these stages. Thus, different moment tensor characteristics are observed between stages, indicating that the event anomaly is likely related to a geological/geomechanical role.

## 7.1 Introduction

Microseismic monitoring is a valuable tool for remotely monitoring the performance of hydraulic fracturing treatments in unconventional resources (e.g., shale gas) (Eaton, 2018; van der Baan et al., 2013). An advanced understanding of the fracturing behavior and how the stress field evolves within a reservoir and the surrounding rocks can be obtained through microseismic data processing (Baig & Urbancic, 2010; Eaton et al., 2014; Eyre & van der Baan, 2015; Van der Baan et al., 2016). Essential source parameters of microseismic events, including fracture types (e.g., shearing (double-couple) or tensile), orientations, and magnitudes, can be retrieved and used to assess the induced fracture growth.

I have been provided with a microseismic data set induced by hydraulic fracturing stages in 4 horizontal treatment wells (wells 1, 2, 3, and 4) in a Montney reservoir in northeastern British Columbia (BC). The microseismic data in these wells (especially wells 2 and 4) exhibit a similar characteristic in the number of events, with substantial

variations in microseismicity between stages (the majority concentrated toward the heel of the wells). This chapter thus focuses on the analysis of the microseismic data from one of the treatment wells: well 2. The anomalous microseismic behavior could be caused by various reasons: operational issues, changes in treatment parameters, errors in data processing, geological/geomechanical changes in the medium, or pre-existing faults. The detection results shown in Chapter 4 reveal that the strong variations in microseismicity between stages at well 2 are not linked to data processing. It is still unresolved why there is a big difference in the number of microseismic events between treatment stages. Here, I investigate the leading causes of this abnormal microseismic behavior by analyzing the source mechanisms of these events to have a more comprehensive understanding of fracture types.

In the following, I present how to retrieve the source information of microseismic events using moment-tensor inversions on the amplitude data. The seismic amplitudes recorded at stations are the convolution between the source mechanism, the propagation effects in the medium, and the instrument response (Eyre & Van der Baan, 2017). These amplitudes thus inherently contain valuable source information of microseismic events. Many studies have utilized seismic wave amplitudes to determine the moment tensors (Eyre & Van der Baan, 2017; Hardebeck & Shearer, 2003; Julian & Foulger, 1996; Kisslinger, 1980). Using amplitude data and/or in addition to first-arrival polarities helps constrain the inversion as the number of observations in the inversion is increased, and amplitudes have a range of values, not just the simple binary inputs (up or down) as in the first-arrival polarity method.

The results of moment-tensor inversion could be affected by the acquisition geometry (Eyre & Van der Baan, 2017). For example, moment-tensor inversions on the amplitude data from a star-shaped surface array can give reliable results with less bias and variance compared to results from a two-borehole case (Eyre & Van der Baan, 2017). Thus, I first examine the effects of the monitoring array geometry on the moment-tensor inversion by running the inversion on synthetic amplitude data. I

also test different input parameters, either P-wave amplitudes or both P- and S-wave amplitudes in one (vertical) or all three data components, to seek the most reliable solutions. Then, I implement the inversion scheme on over 1000 induced microseismic events in 20 treatment stages of the studied well. The full moment-tensor inversion results are also compared with the results obtained from a screening test based on S/P amplitude ratios.

In the following sections, I describe the methodology of the moment-tensor inversion using the amplitude-based approach. Then, I explain the model setup and present forward modeling results. After that, I show the implementation and results of the source mechanism screening test and the full inversion of the microseismic data with some additional discussions on the source mechanisms of the events.

## **7.2 Methodology**

### **7.2.1 Source mechanisms of microseismic events**

In earthquake seismology, it is generally assumed that all events are double-couple (DC, shear) events. However, in microseismic monitoring, this is not the case. The injection of fracturing fluids into the reservoir causes pressure changes and creates/re-activates hydraulic fractures. Since microseismic data are recorded during the treatments, there might be a large volumetric change in the source mechanisms due to the influence of the injected fluids (Eyre & van der Baan, 2015). Microseismicity, thus, might have both tensile faulting or combined tensile and shear faulting in the source mechanisms. When performing moment-tensor inversion for microseismic events, it is necessary to invert for both DC and non-DC components. In this study, I use Vavryčuk’s tensile source model to explain this type of source (Vavryčuk, 2011). Figure 7.1 shows the model of the tensile earthquakes developed by Vavryčuk (2011). The tensile earthquake model can be described using a dislocation vector,  $[\mathbf{u}]$ , that is not restricted to the fault plane (Vavryčuk, 2011). The dislocation vector deviates

from the fault and causes its opening or closing. The slope,  $\alpha$ , represents the tensility of the source and is defined as the deviation of the dislocation vector from the fault:  $\alpha = 90^\circ$  corresponds to pure extensive sources,  $\alpha = 0^\circ$  corresponds to pure shear sources, and  $\alpha = -90^\circ$  corresponds to pure compressive sources (Vavryčuk, 2011).

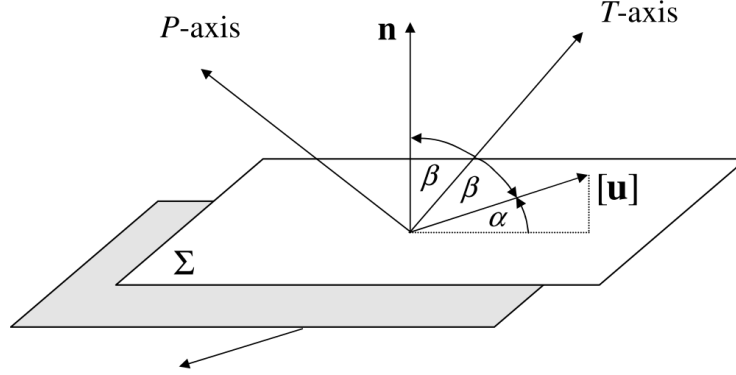


Figure 7.1: Tensile earthquake model,  $\Sigma$  is the fault plane,  $[\mathbf{u}]$  is the dislocation vector,  $\mathbf{n}$  is the fault normal, and  $\alpha$  is the slope. Angle  $\beta$  is defined as  $\beta = (90^\circ - \alpha)/2$  (Vavryčuk, 2011).

The seismic moment tensor,  $M$ , can be given as

$$M = u \begin{bmatrix} \lambda \sin \alpha & 0 & \mu \cos \alpha \\ 0 & \lambda \sin \alpha & 0 \\ \mu \cos \alpha & 0 & (\lambda + 2\mu) \sin \alpha \end{bmatrix}, \quad (7.1)$$

where  $\lambda$  and  $\mu$  are Lamé's constants,  $\alpha$  is the inclination of the slip  $[\mathbf{u}]$  from the fault,  $\alpha$  ranging from  $-90^\circ$  to  $90^\circ$  with  $-90^\circ$  for pure compressive,  $0^\circ$  for pure shear source and  $90^\circ$  for pure tensile (Vavryčuk, 2011).

## 7.2.2 Moment-tensor inversion using amplitude methods

### A rough estimate from amplitude ratios

The S/P amplitude ratios can provide useful information about the source mechanisms of microseismic events (Eaton et al., 2014; Pearson, 1981; Walter & Brune, 1993). Pearson (1981) examined the S/P amplitude ratios for both shear and tensile faulting as a function of inclination from the fracture plane and concluded that the

ratios for tensile fractures are smaller than 4 while the ratios for shear events can be considerably higher. Walter and Brune (1993) modeled and compared the far-field source spectra for tensile and shear-slip events. The study showed that low S/P spectral amplitude ratios often indicate tensile ruptures. Eaton et al. (2014) investigated the P- and S-wave radiation patterns for uniform sampling of the focal sphere and estimated the probability density functions for the S/P amplitude ratio for both shear and tensile failure (Figure 7.2). The study suggested that microseismic events with S/P amplitude ratios of less than 5 are most likely tensile events, and larger than 5 could be shear events. Therefore, the S/P amplitude ratios estimated directly from the recordings could be used as an approximate measure to distinguish between the shear and tensile events. The S/P amplitude ratios will provide a quick screening of source mechanisms without any prior knowledge of the sources.

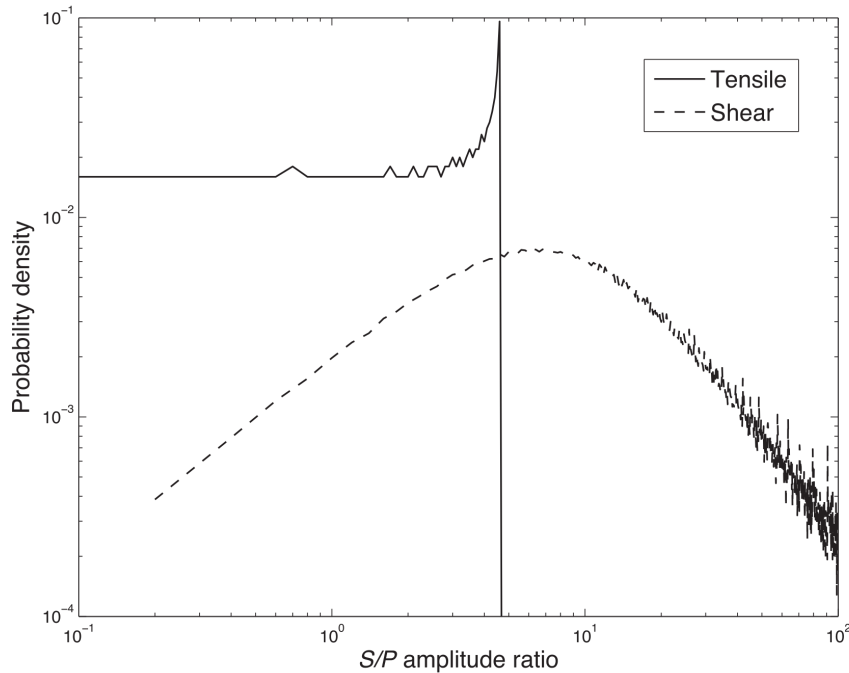


Figure 7.2: The normalized probability density for S/P amplitude ratios for shear and tensile events based on a uniform sampling of the focal sphere. For a random direction of propagation from the source, a 100% probability of  $S/P < 4.617$  are tensile events while only 9.1% probability of  $S/P < 4.617$  are shear events (Eaton et al., 2014).

## Moment-tensor inversion using amplitude-based methods

Moment-tensor inversion is the principal method for calculating seismic-source mechanisms (Baig & Urbancic, 2010; Eyre & van der Baan, 2015). The method adopted herein uses the seismic radiation pattern to invert for the seismic moment tensor of the seismic source. There are three main techniques for moment-tensor inversion: the first-arrival polarity method, amplitude methods (including amplitude-based and S/P amplitude-ratio methods), and the full-waveform method.

The amplitude methods better constrain the inversion than the first-arrival polarity method and are relatively simple compared to the full-waveform method (Eyre & van der Baan, 2015; Hardebeck & Shearer, 2003). When using the amplitude methods, the number of observations used in the inversion is increased compared to the first motion P-wave methods. The amplitude data have a range of values, not just binary values (up or down), as in the first-arrival polarity method; thus, amplitude methods can result in a better-constrained orientation of the P- and S-wave radiation (Hardebeck & Shearer, 2003). Therefore, I run the moment-tensor inversion using an amplitude-based method, which uses both P- and S-wave amplitudes to compute the moment tensors of microseismic events.

The seismic-wave amplitudes recorded at the receivers are the results of the source mechanism (approximated by the moment tensor) convolved with the propagation effects (e.g., Green's functions) and with instrument response (Eyre & Van der Baan, 2017). The moment-tensor inversion algorithm calculates Green's functions using the equations for particle motion generated by the P- and S-wave radiations from a point source in a homogeneous elastic medium (Aki & Richards, 2002). The P- and S-wave amplitudes for the  $i^{th}$  component recorded on a given receiver at position  $x$  and time  $t$  are given as,

$$a_i^P(x, t) = \frac{1}{4\pi r \rho \alpha^3} \{\gamma_i \gamma_j \gamma_k M_{jk}\}, \quad (7.2)$$

and

$$a_i^S(x, t) = \frac{1}{4\pi r \rho \beta^3} \{(\delta_{ij} - \gamma_i \gamma_j) \gamma_k M_{jk}\}, \quad (7.3)$$

where  $i$  is the component,  $r$  is the source-receiver distance,  $\rho$  is the density,  $\alpha$  is the P-wave velocity,  $\beta$  is the S-wave velocity,  $\gamma_i$  is the direction cosine from the source to the receiver,  $M$  is the moment tensor (with  $j, k = [1, 2, 3]$ ) and  $\delta_{ij}$  is the Kronecker delta.

For a non-homogeneous velocity model (e.g., 1D layered velocity model), I use the 1D ray bending algorithm to calculate the average P-wave velocity,  $\alpha$ , and S-wave velocity,  $\beta$ , along the ray path. The source (S) and receiver (R) must be located at a layer boundary; the source may be above or below the receiver. The algorithm guesses an initial ray path (the initial trajectory need not correspond to any actual ray; it may just be an auxiliary reference curve connecting points S and R). The initial guess is perturbed iteratively until a final ray path that best fits the boundary conditions is obtained. I input the receiver and source locations into the 1D ray bending algorithm, calculate the distance and the travel time along the ray, and then compute the average velocities to use in Green's function computation.

The amplitudes in equations (7.2) and (7.3) can be rewritten in matrix form:

$$\mathbf{d} = \mathbf{G}\mathbf{m}, \quad (7.4)$$

where  $\mathbf{d}$  contains the observed ground displacement amplitudes of both P- and S-waves on 3 data components at receivers,  $\mathbf{m}$  is the moment tensor, and  $\mathbf{G}$  represents Green's functions. Equation (7.4) can be expanded as follows (Eyre & Van der Baan, 2017; Forouhideh & Eaton, 2009)

$$\begin{bmatrix} \mathbf{d}_1 \\ \mathbf{d}_2 \\ \vdots \\ \mathbf{d}_n \end{bmatrix} = \begin{bmatrix} G_{11} & G_{12} & G_{13} & G_{14} & G_{15} & G_{16} \\ \vdots & \vdots & \vdots & \vdots & \vdots & \vdots \\ \vdots & \vdots & \vdots & \vdots & \vdots & \vdots \\ G_{n1} & G_{n2} & G_{n3} & G_{n4} & G_{n5} & G_{n6} \end{bmatrix} \begin{bmatrix} m_1 \\ m_2 \\ \vdots \\ m_6 \end{bmatrix}, \quad (7.5)$$

where  $\mathbf{d}_i$  is a vector containing the observed ground displacement amplitudes of P- and S-waves on 3 data components at receiver  $i$  ( $i = 1 : n$ ,  $n$  is the number of receivers);  $\mathbf{G}$  is a  $n \times 6$  matrix, mathematically analogous to the Green's function, with each element  $\mathbf{G}_{jk}$  ( $j, k = [1, 2, 3]$ ) represents the response of the  $j^{\text{th}}$  component of the displacement field to a unit impulse in the  $k^{\text{th}}$  component of the source field.

Equation (7.5) indicates an overdetermined system of linear equations with  $n$  equations and only 6 unknowns, which is solved by a least-squares solution (Menke, 2018; Sipkin, 1982),

$$\mathbf{m} = (\mathbf{G}^T \mathbf{G})^{-1} \mathbf{G}^T \mathbf{d}. \quad (7.6)$$

The inversion results obtained from equation (7.6) can be visualized using source-type plots, including the Hudson's source-type and stereonet plots (Aki & Richards, 2002; Hudson et al., 1989). Fault-plane orientations, including strike, dip, rake, and the angle between the fracture plane and the slope,  $\alpha$ , can be computed from the eigenvalues and eigenvectors of the inverted moment tensor  $\mathbf{m}$  (Vavryčuk, 2011).

The angle,  $\alpha$ , can be computed using

$$\sin \alpha = \frac{M_1 + M_3 + 2M_2}{M_1 - M_3}, \quad (7.7)$$

where  $M_1$ ,  $M_2$ , and  $M_3$  are the eigenvalues of the moment tensor  $\mathbf{m}$  ( $M_1 \geq M_2 \geq M_3$ ) (Vavryčuk, 2011).

The fracture normal vector,  $n$ , and the dislocation direction,  $\nu$ , are given as

$$n = \frac{M_1 - M_2}{M_1 - M_3} e_1 + \frac{M_3 - M_2}{M_3 - M_1} e_3, \quad (7.8)$$

$$\nu = \frac{M_1 - M_2}{M_1 - M_3} e_1 - \frac{M_3 - M_2}{M_3 - M_1} e_3, \quad (7.9)$$

where  $e_1$ ,  $e_2$ ,  $e_3$  are the corresponding eigenvectors of the moment-tensor  $m$ ,  $e_1$  and  $e_3$  should have a negative vertical component for the equations to work correctly (Vavryčuk, 2011).

The strike  $\phi$ , dip  $\delta$ , and rake  $\lambda$  of the fracture plane can be calculated from (Gasperini & Vannucci, 2003)

$$\left. \begin{aligned} \delta &= \arccos(-n_z), \\ \phi &= \arctan\left(\frac{-n_x}{n_y}\right), \\ \lambda &= \arctan\left(\frac{(\nu_z - \cos\delta \sin\alpha) / \sin\delta \cos\alpha}{\nu_x \cos\phi + \nu_y \sin\phi / \cos\alpha}\right), \end{aligned} \right\} \hat{n}_z \neq -1, \quad (7.10)$$

$$\left. \begin{aligned} \delta &= 0, \\ \phi &= 0, \\ \lambda &= \arctan\left(\frac{\nu_x}{\nu_y}\right), \end{aligned} \right\} \hat{n}_z = -1. \quad (7.11)$$

## 7.3 Forward modeling

### 7.3.1 Model setup

Eyre and Van der Baan (2017) demonstrated that the acquisition geometry could influence the moment-tensor inversion results with examples of surface and borehole monitoring arrays. The study showed that all inversions can constrain reliable results for the surface array, while the two-borehole arrays give reliable results only when using P- and S-wave amplitudes in all three data components. The three-borehole geometry produces lower biases than the two-borehole case. Being inspired by the study of Eyre and Van der Baan (2017), I generate synthetic amplitude data, study the effect of the acquisition geometry on the moment-tensor inversion and examine different inputs for the inversion before performing the inversion on the field data.

The microseismic data used for moment tensor inversion analysis in this study are recorded by sensors in two monitoring arrays: a vertical array with 30 sensors (10 m equally spaced) and a horizontal array with 16 sensors (30 m equally spaced). The horizontal array moves every 5 treatment stages, and it has 4 different locations. To simplify the forward modeling problem, I use the horizontal array at its first location (close to treatment stages 1 and 5). Figure 7.3 shows a three-dimensional (3D) view of the acquisition geometry. A synthetic microseismic source is located between two

monitoring arrays with 1650 m East, 2050 m North, and 2550 m depth. I compute P- and S-wave synthetic amplitudes for this acquisition geometry using equations (7.2) and (7.3) and run the inversion algorithm on the synthetic data.

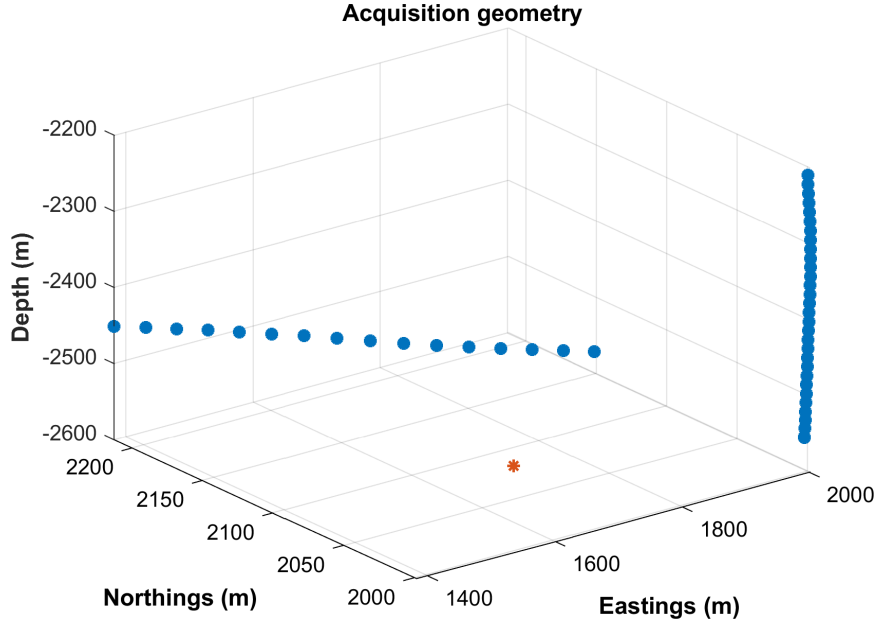


Figure 7.3: A 3D view of the acquisition geometry shows two monitoring arrays: vertical and horizontal arrays and a microseismic source. Blue circles represent the sensors in each array, and the orange star indicates the source.

I set up an ideal medium, which is a homogeneous, elastic, non-attenuated medium with P- and S-wave velocities of 5000 and 3100  $m/s$ , respectively, a density of 2650  $kg/m^3$ , and set a fracture orientation to be a southwest-northeast-striking vertical strike-slip surface (same as in the study of Eyre and Van der Baan (2017)). Both shear and tensile mechanisms can be present in hydraulic fracturing due to the impact of the injected fluids (Eyre & Van der Baan, 2017; Eyre & van der Baan, 2015); thus, I examine different source types from pure tensile, a combined tensile-shear to pure shear mechanisms. These types of sources are represented by different values of  $\alpha$ , the angle between the slip vector and the fracture plane, with  $\alpha = 0^\circ$  - pure shear source,  $\alpha = 90^\circ$  - pure tensile source and  $\alpha \in (0, 90)$  - a combined shear - tensile source. In the forward model, I test  $\alpha = 0^\circ, 30^\circ, 45^\circ$ , and  $90^\circ$ .

### 7.3.2 Effects of acquisition geometry

The sensor distribution is a crucial factor in moment-tensor inversion, especially when performing the inversion for microseismic events in which the source mechanisms are not assumed to be DC (Eyre & Van der Baan, 2017; Eyre & van der Baan, 2015). If the monitoring arrays allow for a good sampling of the focal sphere, the inversion results will be more reliable and vice versa (Eyre & Van der Baan, 2017; Eyre & van der Baan, 2015). Ideally, deploying as many sensors in the region surrounding the events is desirable. However, this does not happen in practice for many reasons (e.g., cost and equipment availability). If the monitoring array poorly samples the focal sphere, we have limited constraints on the inversion and have poorly defined mechanisms (Eyre & Van der Baan, 2017; Eyre & van der Baan, 2015). Thus, in this section, I examine how the two monitoring arrays sample the focal sphere.

I use different values of  $\alpha$  ( $\alpha = 0^\circ, 30^\circ, 45^\circ$ , and  $90^\circ$ ) to calculate the moment tensor  $\mathbf{m}$  using equation (7.1). The resulting moment tensor is then used to compute the synthetic amplitudes (Green's function) for a southwest-northeast strike-slip fracture plane using equations (7.2) and (7.3). Figure 7.4 shows the synthetic amplitudes plotted on the upper hemisphere projection of the focal sphere. The left figures show the normalized P-wave amplitudes and the right figures indicate the S/P amplitude ratios. I normalize the synthetic P-wave amplitudes using the maximum amplitude of the P-waves; thus, the normalized P-wave amplitudes are dimensionless, ranging from -1 to 1. The S/P amplitude ratios are also dimensionless, as the units cancel out. When  $\alpha = 0^\circ$  and  $\alpha = 30^\circ$ , the S-waves have very large amplitudes compared with the P-wave amplitudes as shear faulting is prominent and the S/P amplitude ratios are considerable. Thus, I set the color scale from -10 to 10 for these two cases for visualization purposes.

The relative locations of the sensors are also plotted in Figure 7.4 to examine how the monitoring arrays sample the focal sphere. The vertical array poorly samples

the focal sphere, while the horizontal array better samples the focal sphere than the vertical array, with both positive and negative amplitudes on the upper hemisphere projection of the focal sphere. Moment-tensor inversions using only the vertical-array data will have higher uncertainties. Horizontal-array data and the combined use of both horizontal-array and vertical-array data in moment-tensor inversion generate more reliable results. Thus, the following subsection focuses on testing the inversion of the horizontal-array data and both-array data.

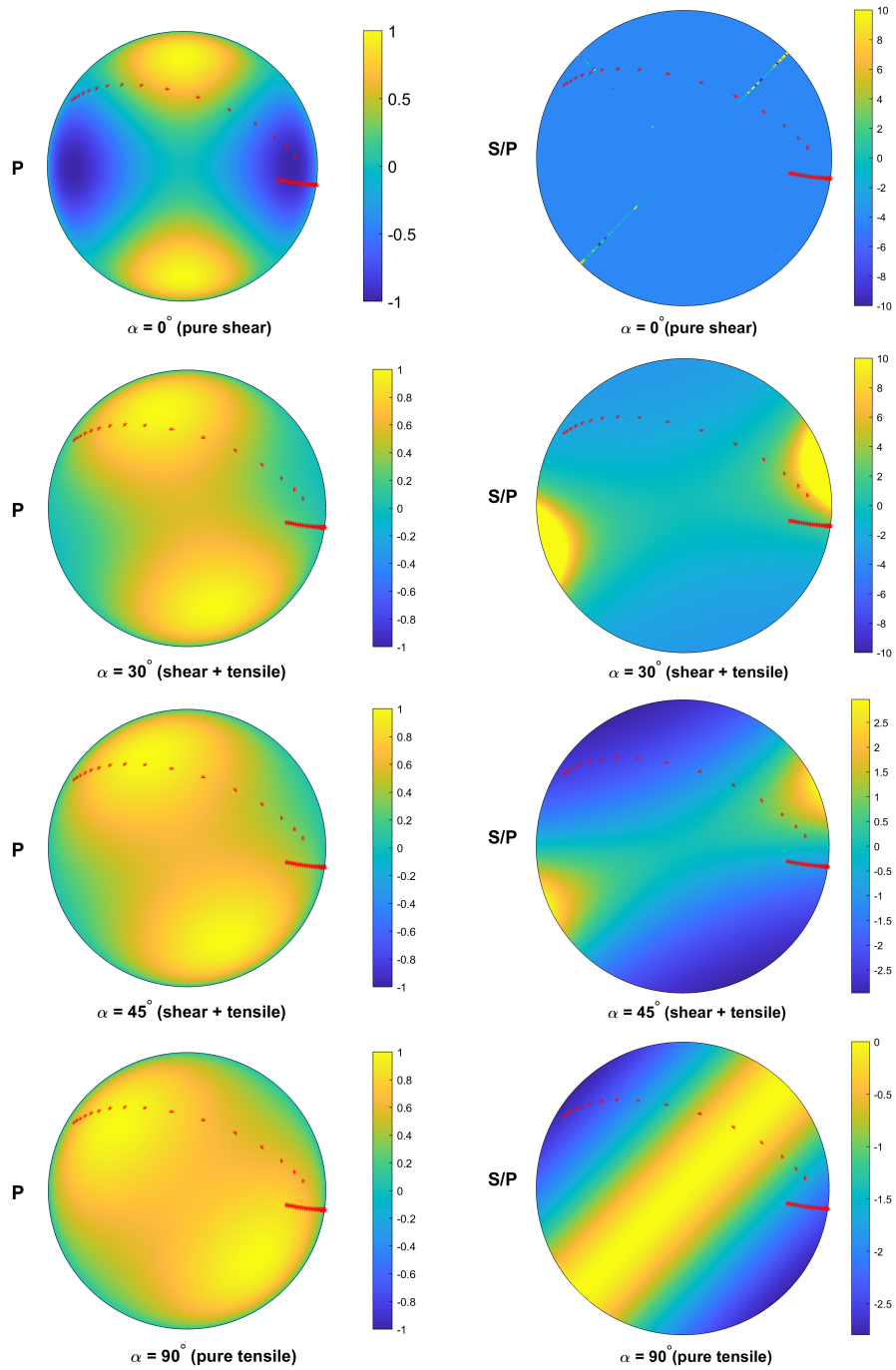


Figure 7.4: Upper hemisphere projection of the focal sphere showing the dimensionless normalized P-wave amplitudes and S/P amplitude ratios for a southwest-northeast strike-slip fracture plane for 4 different source mechanisms:  $\alpha = 0^\circ$  - pure shear,  $\alpha = 30^\circ$  and  $45^\circ$  - a combined tensile and shear, and  $\alpha = 90^\circ$  - pure tensile. The red stars indicate the sensor locations.

### 7.3.3 Moment-tensor inversion results of synthetic amplitude data

This subsection shows the moment-tensor inversion results of the synthetic amplitude data computed using both monitoring arrays and only the horizontal monitoring array. To investigate the stability of the results, I add some random noise with a standard deviation of 10% (the added noise was inspired by the study of Eyre and Van der Baan (2017)) of the maximum amplitude on each array to the computed amplitudes and generate 50 synthetic data sets for each inversion test. The moment-tensor inversion results are then displayed on the Hudson's source-type plots. The Hudson's source-type plots help visualize the retrieved moment tensors graphically with the DC mechanisms plotting in the center, explosive and implosive events at the top and bottom of the diagram, opening and closing tensile crack mechanisms on the top-left and bottom-right edges, respectively (Hudson et al., 1989).

Figure 7.5 shows the moment-tensor inversion results for three different cases,  $\alpha = 0^\circ$  (pure shear),  $30^\circ$  (combined tensile and shear), and  $90^\circ$  (pure tensile). Figure 7.5a, b, c uses the synthetic amplitudes computed using both vertical and horizontal monitoring arrays. Figure 7.5d, e, f displays the results computed using only the horizontal array. The big red cross indicates the actual source location. Dots with different colors represent the inversion results from different inputs. Black dots represent the results using only P-wave data in the vertical (Z) component, green dots indicate the results using only P-wave data in all 3 components (3C), magenta dots represent the results using both P- and S-wave data in the vertical component, and blue dots show the results using both P- and S-wave data in all 3 components.

For the synthetic amplitudes computed using the two monitoring arrays, Figure 7.5a, b, c show that inversions using both P- and S-wave amplitudes in all three data components (shown by blue dots) or the Z component (indicated by magenta dots) yield reliable results. The cluster of moment-tensor solutions has a small size and is close to the actual source location (shown by the big red cross). Other inversion

strategies: using only P-wave data in the Z component (indicated by black dots) or all 3 components (displayed by green dots) produce unreliable solutions, with the solutions plotting in completely incorrect regions of Hudson's source-type plots.

For synthetic amplitudes calculated using only the horizontal array, Figure 7.5d, e, f reveal that the inversion using both P- and S-wave amplitudes in the Z component gives more reliable results compared with other inputs (P-wave data in the Z component or 3C P-wave data, and P- and S-wave data in all 3 components). The inversion using both P- and S-wave in all 3 components gives the solutions in a completely incorrect region, indicating that inversions using only horizontal-array data are less stable than using both-array data. Moreover, the solution obtained from both P- and S-wave amplitudes in the Z component in this case are not as close to the actual source as the results obtained from the case using the two monitoring arrays (Figure 7.5a, b, c).

Overall, based on these tests, using both P- and S-wave amplitudes in all three components or the Z-component that are computed using both monitoring arrays yields the most reliable inversion results.

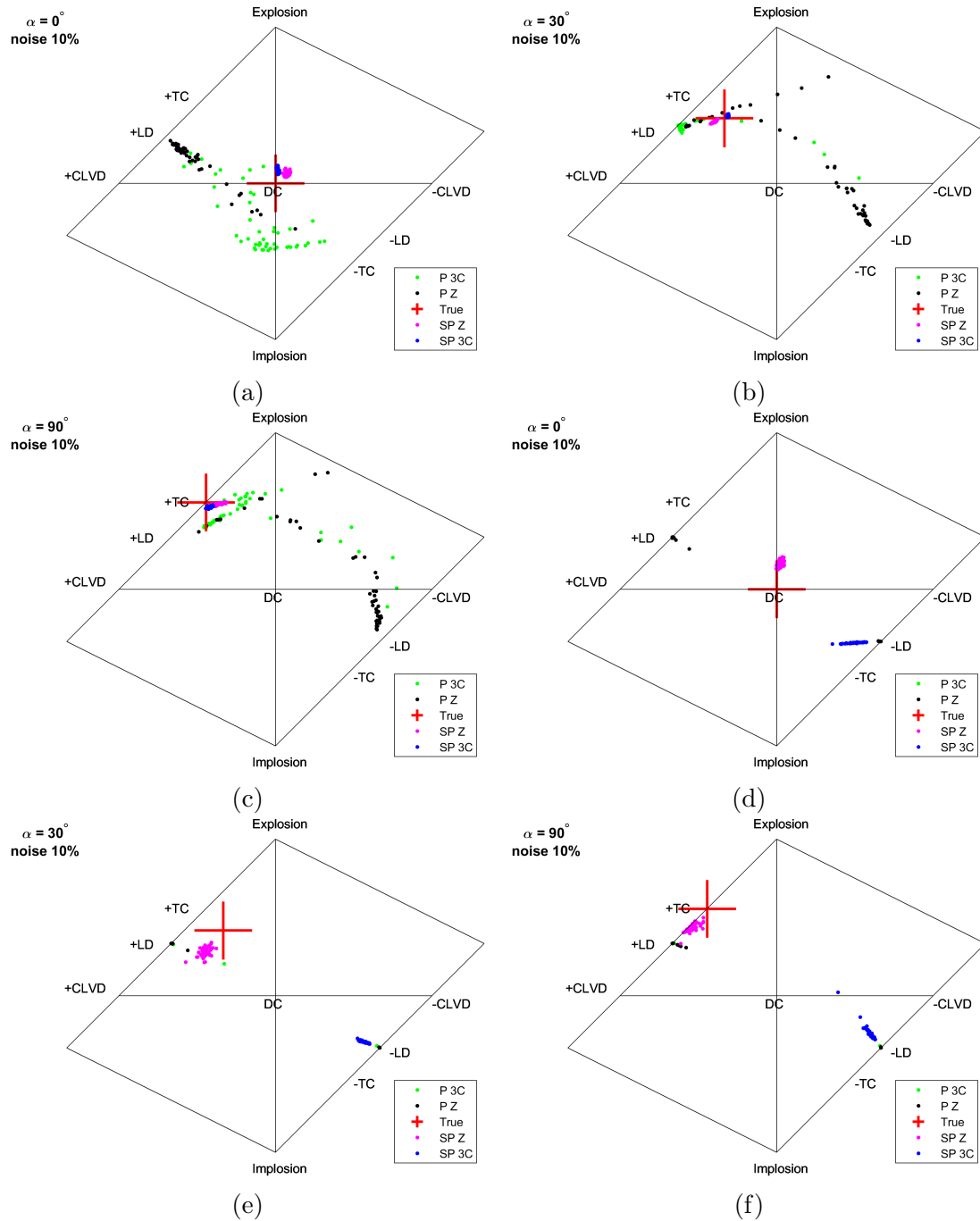


Figure 7.5: Hudson's source-type plots showing the inversion results from 50 synthetic amplitude data sets for different mechanisms, from pure shear (a and d), a combined tensile and shear (b and e) to pure tensile (c and f) using different inputs: only P-wave amplitudes in the 3C (green dots), only P-wave amplitudes in the Z component (black dots), both P- and S-wave amplitudes in the Z component (magenta dots), and both P- and S-wave amplitudes in the 3C (blue dots). The big red cross indicates the actual source location. Figure 7.5a, b, c shows the results for data computed using **two monitoring arrays**. Figure 7.5d, e, f display the results for data calculated using **only the horizontal array**. (The green points on Figure 7.5d, e, f are not observed as they are in the same places as the black points.)

The Hudson’s source-type plots do not distinguish between the type of pure DC mechanisms (e.g., strike-slip, normal, or reverse faulting) (Eyre & Van der Baan, 2017; Hudson et al., 1989). Therefore, I use stereonet plots to visualize the moment-tensor inversion results. Stereonet plots are lower hemisphere projections that portray the fault planes’ strike, dip, and rake (Eyre & Van der Baan, 2017; Stein & Wysession, 2009).

Figure 7.6 displays stereonet plots showing the inversion results of the synthetic amplitude data computed from both monitoring arrays. I plot for two types of mechanisms: pure shear  $\alpha = 0^\circ$  (Figure 7.6a-d) and pure tensile  $\alpha = 90^\circ$  (Figure 7.6e-h) using different inputs: only P-wave amplitude in the Z component (Figure 7.6 a, e), only P-wave amplitudes in 3C (Figure 7.6b, f), both P- and S-wave amplitudes in the Z component (Figure 7.6c, g), and both P- and S-wave amplitudes in 3C (Figure 7.6d, h). The orientation of possible nodal planes is also plotted along with the true fracture plane for comparison. The fracture-plane orientations are best resolved for the two-array case when including both P- and S-wave amplitudes in the Z component or all 3C.

Figure 7.7 shows stereonet plots for the inversion results of the synthetic amplitude data calculated using the horizontal array only. I plot for two types of mechanisms: pure shear  $\alpha = 0^\circ$  (Figure 7.7a-d) and pure tensile  $\alpha = 90^\circ$  (Figure 7.7e-h) using different inputs (the annotations are similar to Figure 7.6). In this case, the fracture-plane orientations are best resolved when using both P- and S-wave amplitudes in the Z component only. Other inversions, even when using both P- and S-wave amplitudes in all 3C, generate incorrect solutions. These results indicate that inversions using only horizontal-array data will be less stable than using both-array data.

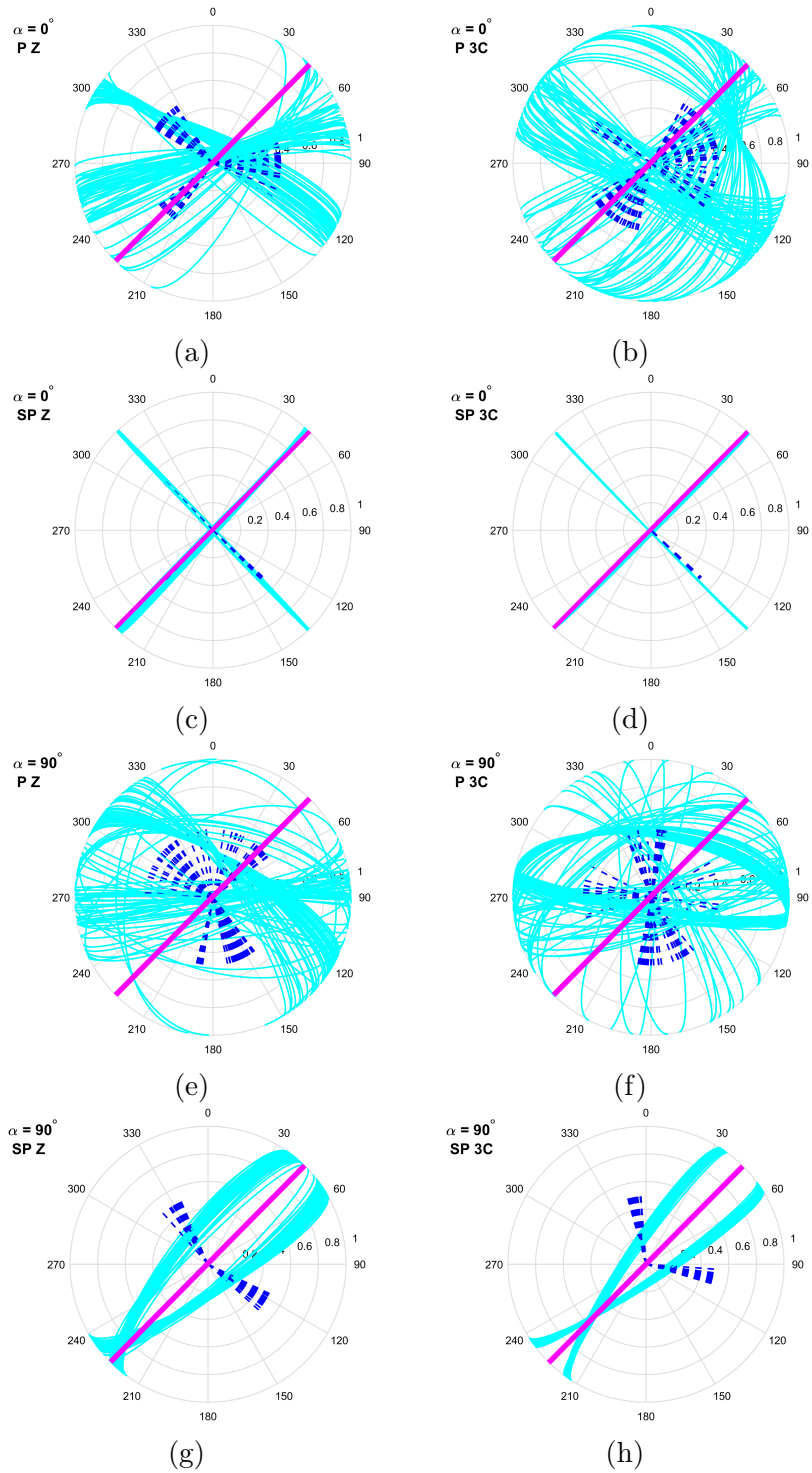


Figure 7.6: Stereonet plots showing nodal-plane orientation results from moment-tensor inversion of 50 synthetic data sets computed using **both vertical and horizontal monitoring arrays** for two mechanisms: (a-d) pure shear  $\alpha = 0^\circ$  and (e-h) pure tensile  $\alpha = 90^\circ$  using different inputs: (a and e) only P-wave amplitudes in the Z component, (b and f) only P-wave amplitudes in 3 data components, (c and g) using both P- and S-wave in the Z component, (d and h) using both P- and S-wave in 3 data components. The great circles correspond to the nodal planes and the shorter dashed lines correspond to rakes. The solid magenta line indicates the true fracture-plane orientation for comparison.

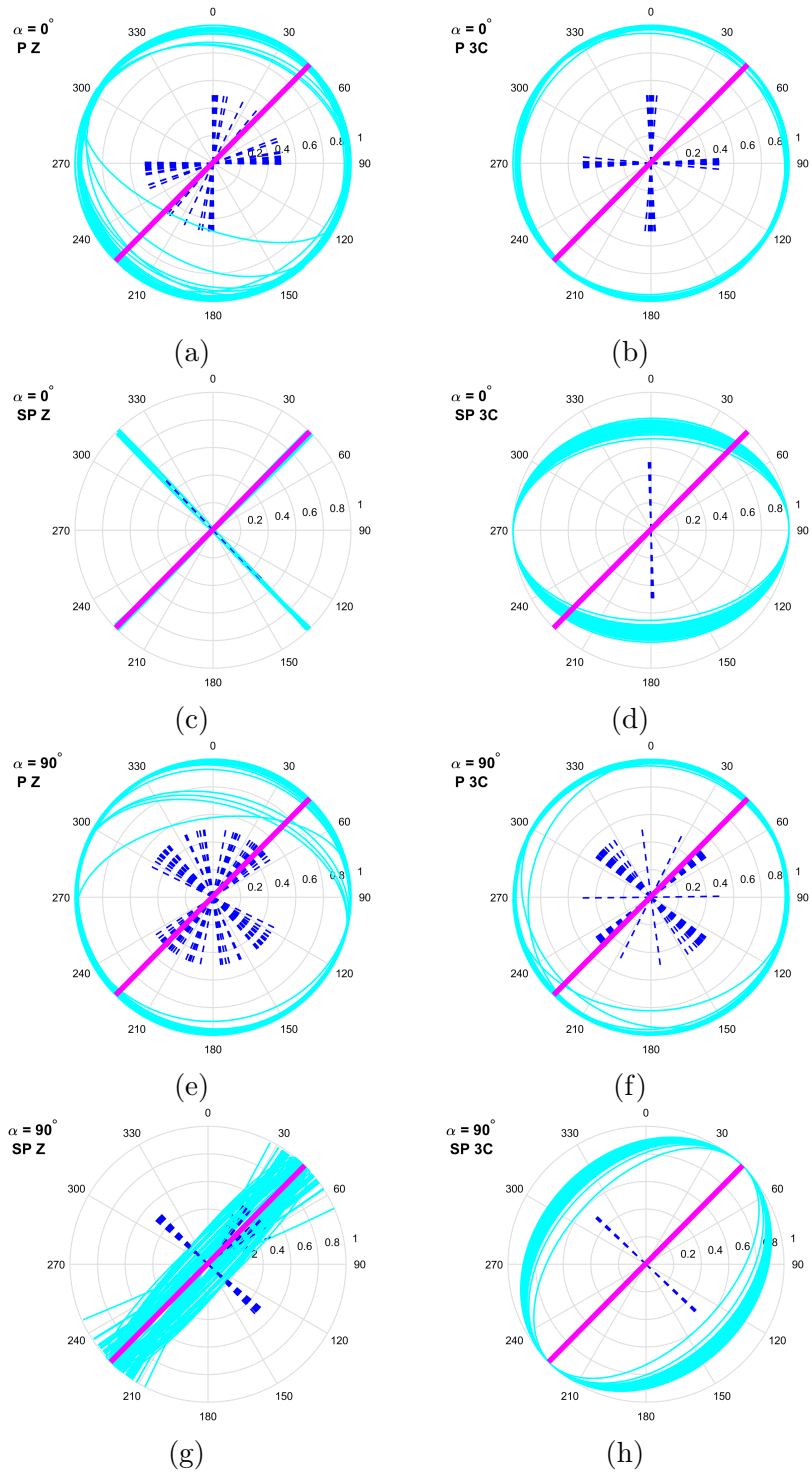


Figure 7.7: Stereonet plots showing nodal-plane orientation results from moment-tensor inversion of 50 synthetic data sets computed using **only the horizontal array** for two mechanisms: (a-d) pure shear  $\alpha = 0^\circ$  and (e-h) pure tensile  $\alpha = 90^\circ$  using different inputs: (a and e) only P-wave amplitudes in the Z component, (b and f) only P-wave amplitudes in 3 data components, (c and g) using both P- and S-wave in the Z component, (d and h) using both P- and S-wave in 3 data components. The great circles correspond to the nodal planes and the shorter dashed lines correspond to rakes. The solid magenta line indicates the true fracture-plane orientation for comparison.

## 7.4 A Case Study

### 7.4.1 Data overview

I focus on the microseismic data seen by both vertical and horizontal monitoring arrays in well 2 to perform moment tensor analysis. Chapter 6 presents the locations of over 1000 excellent microseismic events in 20 treatment stages in well 2 using a combined grid search and quadratic interpolation (Figure 6.15). In this chapter, I use these event locations and study their source mechanisms using (1) a screening test based on S/P amplitude ratios and (2) a full moment-tensor inversion using amplitude-based method (Eyre & Van der Baan, 2017). This step aims to gain more insights into the distribution of the number of tensile and shear events between treatment stages and see if there are any links between moment tensor characteristics and the event anomaly. I use both P- and S-wave amplitudes in all 3 data components from both vertical and horizontal monitoring arrays to run the full moment-tensor inversion of the microseismic events since this inversion scheme is demonstrated to generate the most reliable inversion results based on the forward modeling tests.

### 7.4.2 A rough estimate from amplitude ratios

The S/P amplitude ratio can quickly provide useful information about the source types: tensile or shear failure. Thus, I calculate the S/P ray amplitude ratios for over 1000 microseismic events seen by both vertical and horizontal monitoring arrays in 20 treatment stages in well 2. I first carefully select P- and S-wave windows long enough to contain the P- and S-wave peak (maximum) amplitudes. The starts of the windows are determined based on the P- and S-wave time picks. I use a fixed S-wave window length of 0.125 s for all computations and a dynamic P-window length depending on the S-P arrival time differences. I use a P-window of length 0.05 s for the events with S-P arrival time differences larger than 0.05 s. For the events with P- and S-phases close to each other (often near the monitoring wells, e.g., stage 11),

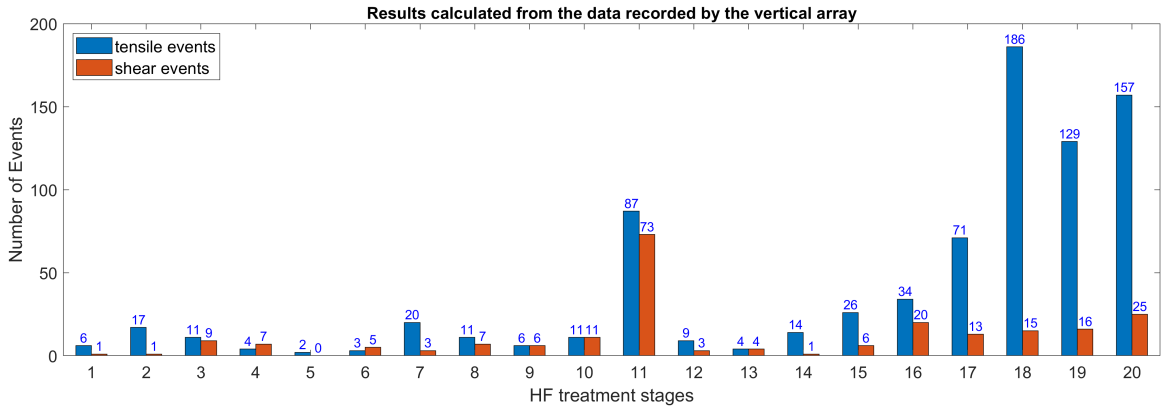
the P-window starts from P picks and ends 0.0005 s before the S picks to ensure only P-wave amplitudes are selected.

Since using all 3 (preprocessed, see Chapter 3 for more details) data components for the calculation, I then compute the root-mean-square (RMS) of the maximum absolute amplitudes of the 3 data components for each receiver to reduce the effect of noise and obtain consistent peak amplitude values. I perform the calculations for the vertical and horizontal monitoring arrays separately. The final S/P amplitude ratio for each microseismic event is the median value between different receivers in the monitoring array used for calculation.

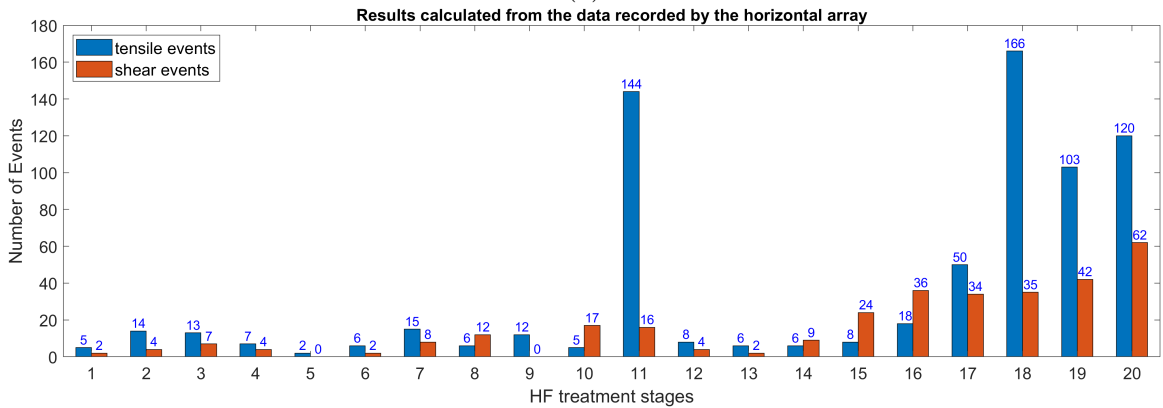
After obtaining the final S/P ray amplitude ratios for each monitoring array, I classify the data into tensile events if the ratio is smaller than 5, and if the ratio is larger than 5, I consider the events as shear events. This step permits the first classification into the number of shear and tensile events per stage, which can then be compared with the subsequent moment-tensor inversion results.

In the first instance, treating the horizontal and vertical monitoring wells separately possibly leads to two contradicting solutions. This step is done to simplify the computations but also to get some ideas about uncertainty. Figure 7.8 shows the results calculated from the vertical-array data (Figure 7.8a) and horizontal-array data (Figure 7.8b). The classification results show a similar characteristic, with tensile mechanisms being prominent in well 2, particularly in stages toward the heel of the well. Hundreds of events are likely to be tensile faulting in the stages from 18 to 20. For stages with a few events (e.g., 1, 2, 7, 8, 14-16), a similar feature with more tensile than shear failure is also observed.

The source screening test is an approximate measure based on the ratios and is not applicable in all cases, such as the treatment stage 11 in well 2. There is a difference in the number of tensile and shear events between the results from the two monitoring arrays in stage 11. The S/P amplitude ratios computed from the horizontal-array data generate many tensile events and only a few shear events, while



(a)



(b)

Figure 7.8: Source mechanism screening test results using S/P amplitude ratios calculated using data recorded by the (a) vertical and (b) horizontal monitoring q arrays. Tensile events are indicated by blue, and shear events are indicated by orange. The number on top of each bar displays tensile/shear events in each stage.

the vertical-array data show a comparable number of tensile and shear events. The treatment stage 11 is located in between the vertical and horizontal arrays; seismic waves could travel in different directions to reach the sensors in each monitoring array. This difference in ray paths might cause the discrepancy in the number of tensile and shear events of the microseismic events in this stage 11.

I carefully inspect the S/P amplitude ratio values of the events in stage 11 for each monitoring array. Figure 7.9 shows the histograms of the S/P amplitude ratios computed from the vertical-array data (Figure 7.9a) and horizontal-array data (Figure 7.9b). Most values fall between 3.5 and 6.5 for the vertical-array data and between 2.5 and 4.5 for the horizontal-array data. Most of the shear events in the vertical array

have S/P amplitude ratios quite close to the classification threshold of 5. Therefore, these events could be tensile events, which are in line with the characteristics of many tensile events and few shear events from the horizontal-array data.

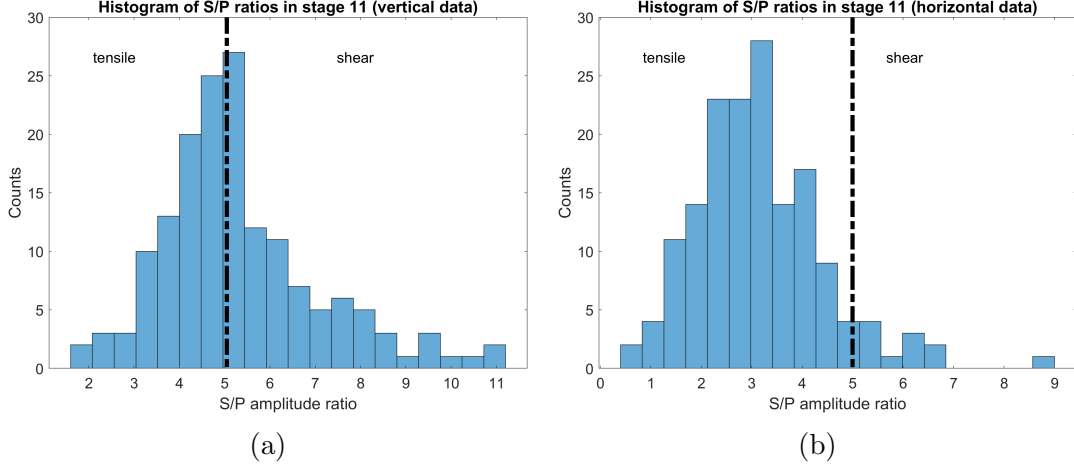


Figure 7.9: Histogram of S/P amplitude ratios computed from the (a) vertical-array and (b) horizontal-array data in stage 11.

### 7.4.3 Moment-tensor inversion results using amplitude-based method

The original microseismic data are in millivolts (mV); thus, I first convert to m/s units using,

$$u = \frac{V_{out}}{10^{\frac{gain}{20}} * 1000 * sensitivity} \quad (7.12)$$

where  $u$  is the particle velocity in m/s,  $V_{out}$  is the sensor output in mV,  $gain$  is the recording system gain given in dB (the acquisition notes show that  $gain = 42$ ), 1000 is a factor that converts from millivolts to volts (V) and  $sensitivity$  is a factor given in V/m/s (Albert, 1993). Then, I integrate the data (ground motion velocity, unit m/s) to obtain the displacement amplitudes (unit m) since the required inputs for the moment-tensor inversion are the ground displacement amplitudes.

The inversion algorithm inverts for the moment tensors using the P- and S-wave amplitudes taken from the data segments that have the start based on P- and S-wave time picks and are long enough to contain the maximum amplitudes. I use a

fixed S-wave window length of 0.125 s (corresponding to 500 data samples since the sampling rate of data is 0.25 ms) and a dynamic P-window length depending on the differences in S-P arrival times. A P-window of length 0.05 s (corresponding to 200 data samples) is used for the events with S-P arrival time differences larger than 0.05 s. For the events with P- and S-phases close to each other, the P-window ends 0.0005 s before the start of the S picks to ensure only P-wave amplitudes are selected.

The amplitude data from a total of 44 receivers in two monitoring arrays are selected to run the inversion as two receivers (receivers 2 and 32) did not record the data properly in some stages. For each receiver, the algorithm searches and extracts the first of either the minimum or maximum amplitude (considering the sign information) within the specified P- and S-wave windows for all 3 data components. Thus, for each receiver, there are 6 amplitude values of P- and S-wave extracted from 3 data components and used for the inversion. The amplitude values extracted from 44 receivers are appended to each other along the row dimension and form the ground displacement amplitude vector,  $\mathbf{d}$ , with a size of (44\*6) rows x 1 column (corresponding to 264 rows x 1 column).

The synthetic amplitudes (Green's function,  $\mathbf{G}$ ) are computed using equations (7.2) and (7.3). A 1D layered velocity model (described in section 3.3.3 in Chapter 3) built from sonic logs and available well tops using the blocking technique is used in the calculation. With information on event locations (Chapter 6), receivers, the 1D velocity model, and the density of the medium, a 1D ray bending algorithm is first used to calculate the travel time and the distances along the ray for P- and S-waves. Then, the algorithm calculates the average velocity along the ray for P- and S-waves and uses these velocities in Green's function computation. For each receiver, the resulting  $\mathbf{G}$  matrix has a size of 6 rows x 6 columns. I append the values of  $\mathbf{G}$  to each other along the row dimension; thus, with 44 receivers, the Green's function  $\mathbf{G}$  has a size of (44\*6) rows x 6 columns (corresponding to 264 rows x 6 columns). The moment tensor  $\mathbf{m}$  (with a size of 6 rows x 1 column) is then obtained through a

least-squares solution using equation (7.6).

Figure 7.10 shows Hudson’s source-type plots for visualizing the inversion results of over 1000 excellent microseismic events in 20 treatment stages in well 2. Since the horizontal monitoring array moves every 5 stages, I plot the inversion results of every five stages: stages 1-5, 6-10, 11-15, and 16-20. Figure 7.10a displays the results of events in stages 1-5, showing 3 main clusters of events in the center, top-left, and bottom-right of Hudson’s source-type plots. Thus, stages 1-5 have both tensile (opening/closing cracks) and DC (shear) faultings. Figure 7.10b, c shows the results of events in stages 6-10 and 11-15. These stages also show similar features as stages 1-5, with 3 main clusters on Hudson’s source-type plots indicating both types of tensile and shear faultings, although the solutions of a few events are not in the DC and tensile cracks (TC) regions. Compared with the screening test results, inversion results of events in stages 1-15 show a similar characteristic with both types of faultings. However, the prominent feature of tensile events is less obvious than the screening test results.

For stages 16-20, the solutions are spread out in many places on Hudson’s source-type plot (Figure 7.10d) and do not show any similar features as stages 1-15. This effect might be because of an anisotropic velocity field since evidence of anisotropy is observed in the stages toward the heel of the well, with more details shown in the following section. Most importantly, different moment tensor characteristics are observed between treatment stages, suggesting that the substantial variations in the number of events are likely associated with a geological/geomechanical role.

## 7.5 Discussions

Moment-tensor inversion is an intricate processing step in microseismic monitoring as it may reveal non-DC source mechanisms (Baig & Urbancic, 2010; Eyre & Van der Baan, 2017). Yet caution is advisable when interpreting the results as the inversion solutions can be nonunique (Baig & Urbancic, 2010; Eyre & Van der Baan, 2017;

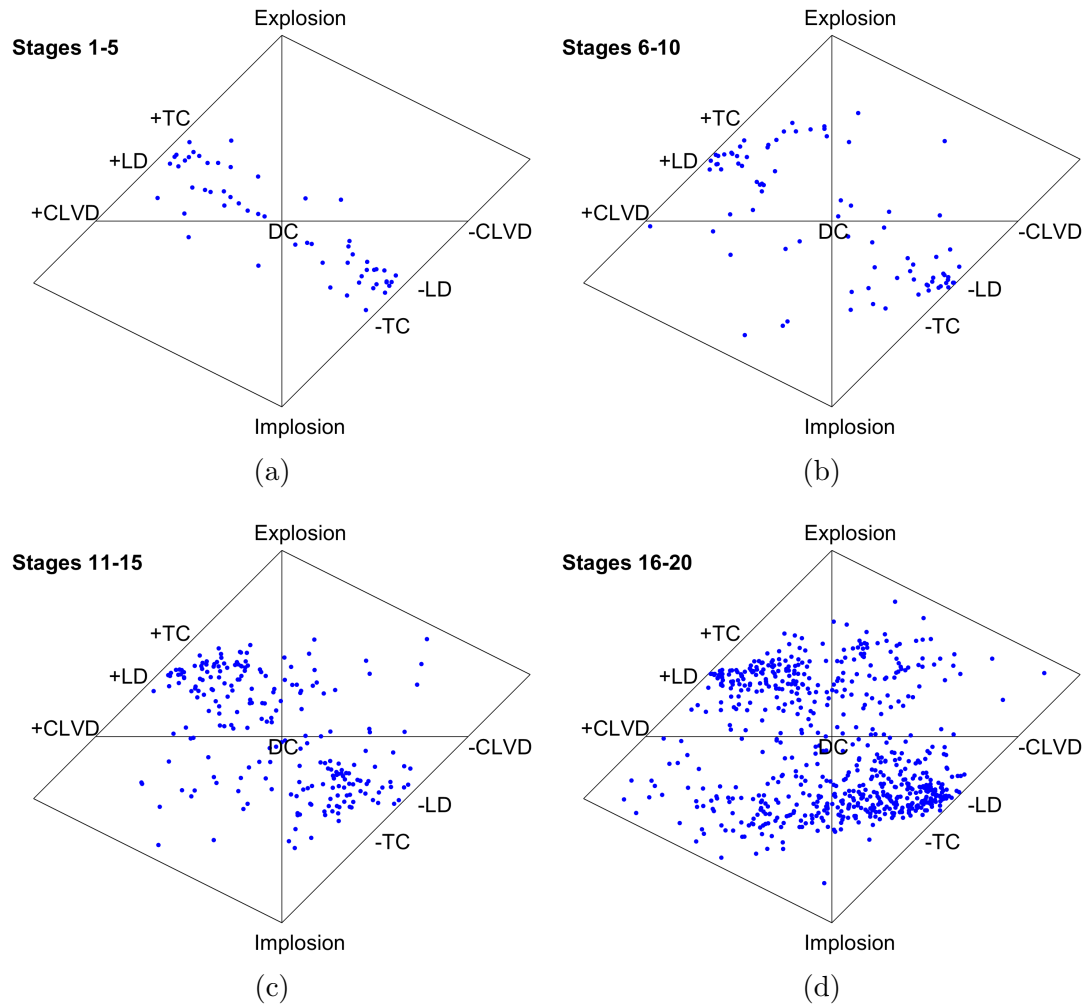


Figure 7.10: Hudson's source-type plots for visualizing the moment-tensor inversion results of microseismic events in well 2. The inversion results are plotted for every 5 treatment stages: (a) stages 1-5, (b) stages 6-10, (c) stages 11-15, and (d) stages 16-20.

Vavryčuk, 2007). For this reason, I strongly advocate performing synthetic tests as described in section 1.3 and by Eyre and Van der Baan (2017) to look into possible systematic biases and variances in the inversion results given the acquisition geometry and source locations. Ideally, deploying an extensive number of sensors in the surrounding region of events is optimal since it can provide a good sampling of the focal sphere and produce more reliable inversion results. However, this is often not feasible in practice. In this study, the acquisition geometry has two monitoring arrays: vertical and horizontal. Testing the inversion using different synthetic amplitude inputs

helps reveal that the best inversion scheme (that generates reliable inversion results) for the recorded microseismic data is to use both P- and S-wave amplitudes in all 3 data components from both monitoring arrays.

This study first uses the S/P amplitude ratios as a source mechanism screening test before performing the full inversion. Although it is not an absolute test, it quickly provides a useful estimate of the number of tensile and shear events without any prior knowledge of the sources. The test is performed separately on the vertical- and horizontal-array data, revealing an overall trend of tensile mechanisms being dominant. This first classification of tensile and shear can support the full inversion results, generating a more reasonable interpretation of the event's source mechanisms.

Many factors can influence the inversion solutions, such as errors in the hypocenter locations (Castellanos & van der Baan, 2015) or the presence of anisotropy (Vavryčuk, 2005). We usually estimate the location from the observations at stations (e.g., arrival times, azimuths), which has inherent errors in time picking, velocity model, and polarization analysis. Improving the locations will better constrain the moment-tensor inversion results (Castellanos & van der Baan, 2015). Anisotropy is another critical and complicated aspect. Vavryčuk (2005) demonstrated that if the focal area is anisotropic, the inversion procedure may yield distorted results. However, this study calculates the moment-tensor inversion under the assumption of an isotropic focal area. While this assumption simplifies the inversion procedure, it is important to note that anisotropy is evident in the data, and it may lead to distorted results and limitations in the interpretation of the event's source mechanism. Stages toward the well's heel (e.g., stages 16-20) have clear evidence of anisotropy, with the shear waves arriving at different times (also known as the shear-wave splitting phenomenon, (Teauby et al., 2004a)) on the seismogram. Figure 7.11 shows example waveforms with the shear-wave splitting phenomenon observed in events from stages toward the well's heel, with the S waves being faster in the horizontal components than in the vertical component. This phenomenon is highly likely to be the reason why the

inversion results of events in stages 16-20 are plotted in many places on Hudson's source-type plot (Figure 7.10d).

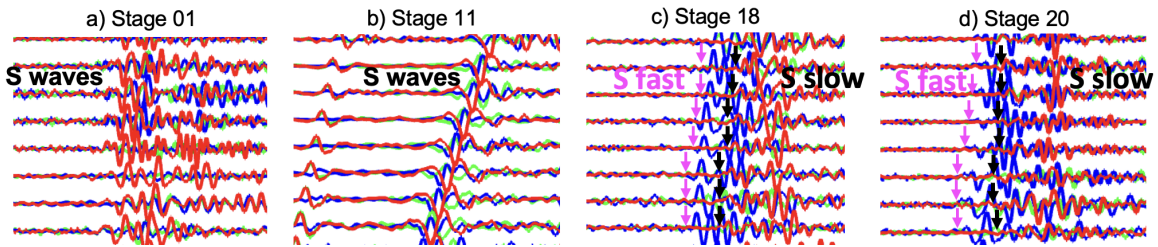


Figure 7.11: Examples of three-component waveforms (2 horizontal components shown in green and blue, and one vertical component displayed in red) showing the S-wave segment from treatment stages 1, 11, 18, and 20. For the events in stages 18 and 20, the onsets of the fast S-waves are indicated by pink, and the onsets of the slow S-wave are denoted by black. The S-waves are faster in the horizontal components of the events in stages toward the heel of the well.

## 7.6 Conclusions

The synthetic tests show that moment-tensor inversions give more accurate results when using the amplitudes of P- and S-phases in all 3 data components from both monitoring arrays. The inverted solutions are well-constrained and adjacent to the actual source location. Therefore, both P- and S-wave amplitudes in all 3C are used to run the moment-tensor inversion of the microseismic events seen by two monitoring arrays in the case study. The source mechanism screening test using S/P amplitude ratios of vertical- and horizontal-array data shows both tensile and shear faultings are present, with tensile events being highly likely prominent. The full inversion results of the microseismic events, especially in stages 1-15, also show similar characteristics with both types of faultings. Hudson's source-type plots of the inverted moment tensors for stages 1-15 reveal 3 main clusters: center (shear faulting), top-left (opening tensile cracks) and bottom-right (closing tensile cracks). However, the prominent feature of tensile events is less evident compared with the results of the screening test. For stages 16-20, the solutions are plotted in many places on Hudson's source-type plot. This feature might be due to the effect of the anisotropic velocity

field since the shear-wave splitting phenomenon is evident in the stages toward the well's heel. Overall, both the screening test and full moment-tensor inversion reveal that there are different moment tensor characteristics depending on the stages. This characteristic indicates that the event anomaly between stages is likely linked to a geological/geomechanical role.

## Chapter 8

# Integrated analysis of anomalous microseismic behavior in a Montney treatment: Engineering parameters, locations, moment tensors, and geomechanics

### Summary

This chapter presents an integrated analysis of an extensive raw microseismic dataset induced by hydraulic fracturing activities in a Montney reservoir. The microseismicity behaves anomalously, exhibiting significant variations between treatment stages, with many events concentrated near the heel of the treatment wells and only a few events in other areas. The underlying causes of this unusual behavior remain unclear. I first investigate all operational issues and their links with the number of events between stages. Then, I examine changes in treatment parameters, including surface pressure, injection rate, and treatment duration, and their effects on the microseismicity. The event anomaly might also result from errors in data processing, such as event detection. I thus investigate different detection methods and compare the detection results. Event localization, r-t plots, moment tensor inversion, variations in lithology, and shear wave splitting phenomenon are also performed to investigate the effects of geological and geomechanical changes on the number of events between treatment

stages. The analyses show that operational issues, changes in treatment parameters, and data processing are not the leading causes of the event anomaly. Geological and geomechanical changes are, therefore, most likely linked with anomalous microseismic behavior.

## 8.1 Introduction

I examine an extensive, raw microseismic data set induced from 78 hydraulic fracturing treatment stages in four horizontal wells in a Montney reservoir in northeastern British Columbia (NE BC), Canada. The microseismic data set was recorded by 3-component sensors deployed in vertical and horizontal monitoring arrays. Figure 8.1 shows map and depth views of 4 horizontal treatment wells (wells 1, 2, 3, and 4), two monitoring arrays, and sleeve locations where the hydraulic fracturing stimulation is performed. Each horizontal well has 18-20 treatment stages. The microseismic activity in these wells behaves anomalously, with a substantial variation between treatment stages: many events are concentrated towards the heel of the treatment wells and hardly any in the other areas. The underlying causes of this unusual behavior are unclear and require investigation. Figure 8.2 shows the number of detected events in 20 treatment stages in the treatment well 2. For comparison, I plot the detection results obtained from 2 methods: (1) the short-time average over the long-time average (STA/LTA), a traditional, incoherent energy detector and (2) the matched filter (MF), a cross-correlation-based detector based on a fast normalized cross-correlation (Bui & van der Baan, 2020; Lewis, 1995). Both detection methods identify approximately 20,000 events from 4 treatment wells and have a similar event distribution (especially wells 2 and 4), with stages near the heel of the well observing many events (e.g., up to 1,000 events in stages 18, 19, 20) and stages near the toe of the well having a few events (e.g., fewer than 50 events in stages 5, 6). Since these treatment wells have similar characteristics of microseismicity between stages, this chapter focuses on analyzing the microseismic data from one of the treatment wells: well 2. Figure

8.3 shows a typical 3-component (3C) microseismic event recorded by sensors in the vertical monitoring array during treatment stage 18 in the horizontal well 2. Two horizontal data components are shown in green and blue; the vertical data component is shown in red. Two seismic phases are observed, including a P-phase at about 0.21 s and an S-phase at around 0.34 s.

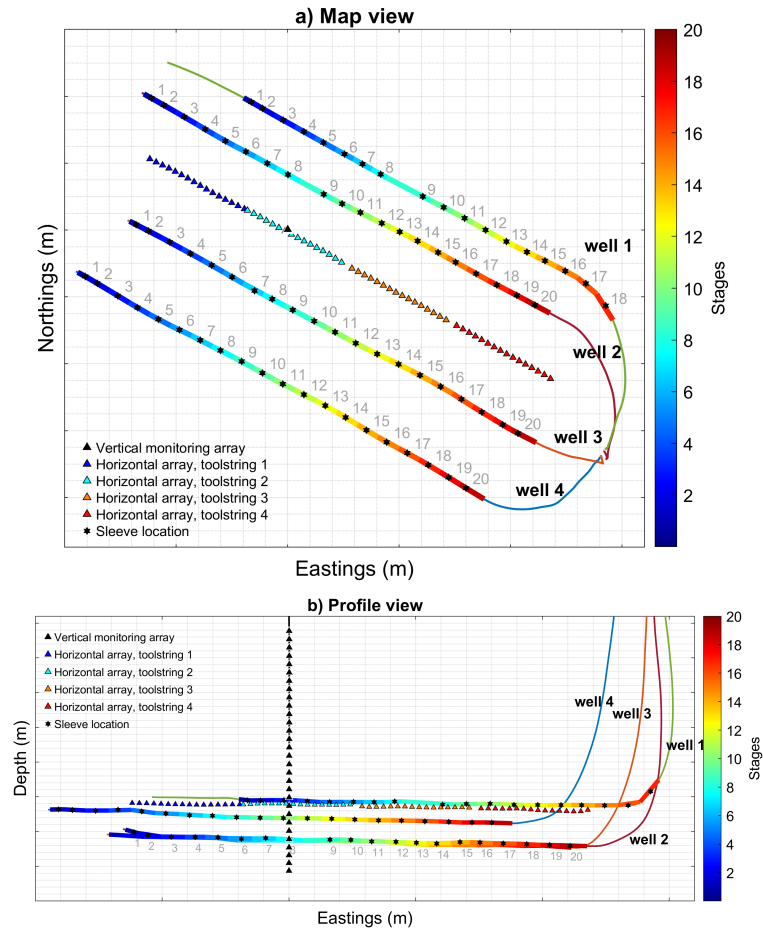


Figure 8.1: (a) Map view and (b) profile view showing 4 horizontal treatment wells (namely, wells 1, 2, 3, and 4) with stages shown in different colors, vertical and horizontal monitoring arrays denoted by triangles, and treatment locations denoted by hexagrams.

Different hypotheses have been proposed for the leading cause of anomalous microseismic behavior. The event anomaly could be attributed to operational issues, changes in treatment parameters, errors in microseismic data processing, or changes in the geomechanical properties of the medium and the existence of natural frac-

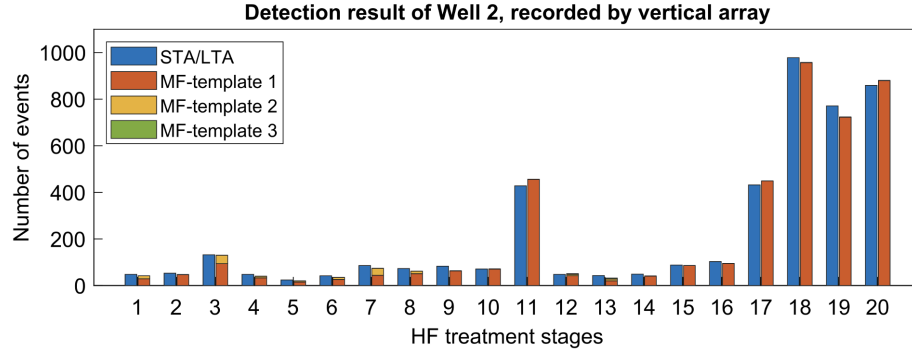


Figure 8.2: Number of detected events from data recorded by the vertical monitoring array in 20 treatment stages in treatment well 2. The STA/LTA detection results are shown in blue, and results from the MF method are indicated in other colors, representing the different template events.

tures/faults. First, I investigate if any operational issues require the cessation of the fracturing treatments that link to the unusual microseismic behavior between stages. Second, I investigate if the event anomaly relates to changes in any treatment parameters, such as breakdown pressure (the pressure at which the rock formation breaks and creates fractures (Tariq et al., 2021; Warpinski et al., 2004)), injection (slurry) rate, and treatment duration. I investigate the completion data to see if a poor injectivity rate could lead to fewer events and if stages having a lower treating pressure make it easier for the rocks to be fractured and induce more events. Third, I investigate whether the abnormal microseismic behavior originated from errors in data processing (e.g., inefficient detection algorithms with many false alarms (when noise is incorrectly detected as a potential event) and missed events (when the event occurs, but the detector does not capture it) (Bui & van der Baan, 2020)). Fourth, I investigate whether the event anomaly is associated with changes in the geological and geomechanical properties or existing fractures/faults.

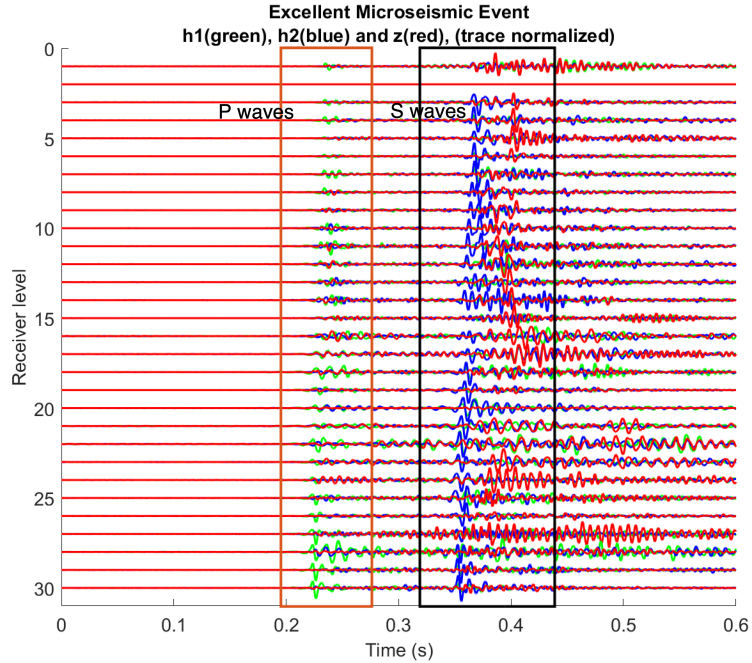


Figure 8.3: A typical microseismic event recorded by sensors in the vertical monitoring array during treatment stage 18 in the horizontal well 2. There are 3 data components: 2 horizontal components shown in green and blue and one vertical component shown in red.

## 8.2 Methods

### 8.2.1 Investigate operational issues

In hydraulic fracturing, the brittle failures induced by the stimulation are recorded as microseismicity by sensitive sensors in nearby monitoring arrays (Eaton, 2018). A typical fracturing treatment is aimed to create hydraulic fractures in the rocks and thus is expected to observe many microseismic events. Treatments with operational issues where fractures cannot be formed and monitoring arrays are shut down might correlate to less active microseismicity in some stages. I first examine the treatment records of every fracturing stage from available fracturing observer notes and completion reports to identify any issues during fracturing operations and their impacts on microseismic activity.

All treatment wells used an open-hole sliding sleeve completion technique. Operational problems might be sleeve malfunction, fluid loss, frac hits, poor stage isolation,

poor injectivity rate, screen-out conditions, and no/weak ball seats. For example, sliding sleeves may fail to open or close as intended, leading to the incorrect placement of fractures or an inability to isolate sections of the wellbore. If sliding sleeves do not close properly, there can be interference between fractures created in different stages, leading to fractures communicating with each other, reducing the effectiveness of individual fracturing treatments, and affecting the microseismic behavior. Fluid loss during fracturing operations can cause reduced hydraulic pressure within the wellbore, resulting in poor fracture propagation, lowering fracture conductivity and reducing microseismicity. Frac hits (the interference between fractures created during hydraulic fracturing between neighboring zones due to poor isolation) can lead to unwanted communication between fractures, negatively impacting fracturing performance and microseismicity. Poor stage isolation can result in fractures communicating with each other, reducing the effectiveness of individual fracturing treatments. Poor injectivity rate can limit fracture propagation and make it challenging to deliver proppants deep into the fractures, reducing the treatment effectiveness and affecting the microseismicity.

Screen-out conditions can happen during the treatment and cause a rapid rise in the pump pressure, which exceeds the safe-operating parameters of the wellbore and wellhead equipment (Maxwell, 2014). When the screen-out condition occurs, the fracturing operation needs to be ceased, and monitoring arrays are shut down to have time for flow back to clean any obstructions. Screen-out conditions will affect hydraulic fracturing creation/reactivation and microseismic recording. In sliding sleeve completion, the ball and seat have two functions, including (1) isolating the lower zone from the fracturing fluid and pressure and (2) shifting the fracturing sleeve into the open position. No/weak ball seats can result in losing control over downhole tools, making it difficult to selectively open or close sliding sleeves, leading to uncontrolled fracturing fluid flow and proppant placement. Without reliable ball seats, there is a risk of unintended fracture placement, and fractures may open in the wrong zones or

intervals. Weak ball seats may allow fracturing fluid to flow into unintended zones, leading to interference between fractures created in different stages and reducing the treatment effectiveness, potentially affecting the extent of fracture propagation and microseismic behavior.

### 8.2.2 Investigate treatment parameters

Second, I investigate if the anomalous behavior of microseismicity relates to changes in any treatment parameters, including breakdown pressure, injection rate, and treatment duration. Breakdown pressure indicates the minimum pressure needed to overcome the tensile strength of the rock. The injection rate is the rate at which the fracturing fluid and proppants are pumped into the wellbore to create fractures. Higher injection rates can create wider and longer fractures. Treatment duration is the total time over which the fracturing treatment is performed. Treatment duration is closely linked to the injection rate and the desired fracture geometry. Longer treatment durations can be used to create more extensive fractures.

To understand the effects of changes in treatment parameters on microseismicity, I calculate the injection energy for every treatment stage and correlate it with the number of events detected in each stage. The injection energy is the total energy put into the fracturing system. It is the product of the treatment duration, the average surface pressure, and the injection rate (Boroumand & Eaton, 2012). If the pumping data at the surface is readily available, the total input energy can be calculated using (Boroumand & Eaton, 2012; Goodfellow et al., 2015)

$$E_1 = \int_{t_1}^{t_2} PQdt, \quad (8.1)$$

where  $t_1$  and  $t_2$  are the start and end times of the treatment,  $P(t)$  is the surface treatment pressure and  $Q(t)$  is the injection rate. The injection energy can also be approximated by (Boroumand & Eaton, 2012)

$$E_1 \approx \langle P(t) \rangle \langle Q(t) \rangle \Delta t, \quad (8.2)$$

where  $\langle x \rangle$  denotes the average value of  $x$  and  $\Delta t$  is the total duration of the fracture stage. The injection energy is crucial in initiating and propagating fractures within the reservoir rock. The greater the injection energy, the more extensive the fractures can potentially become. Injection energy will reflect if a low injection rate, a high surface pressure, or a longer treatment duration is associated with the event anomaly.

### **8.2.3 Investigate event detection**

Third, the event anomaly might be related to inefficient detection algorithms that produce many false alarms (when noise is incorrectly detected as a potential event). Traditional automated triggering-based detectors such as the STA/LTA method have detection performance depending strongly on the setup parameters, including lengths of the short and long windows used for calculating the STA/LTA ratio and the detection threshold. The STA/LTA with a very low detection threshold can trigger many false alarms. Using only one detection algorithm may lead to biased results; for instance, careless event classification can result in wrongly classified potential events. I thus investigate if different automated detection methods, such as the STA/LTA and the cross-correlation-based matched filter, result in similar event distribution with many events towards the well's heel and few events in other stages. Chapter 4 provides a comprehensive description of this investigation, including the methodology, implementation, and results. In this chapter, I incorporate the detection results with other analyses to find out the underlying cause of the event anomaly.

### **8.2.4 Investigate locations, moment tensors, geomechanics**

Fourth, I investigate whether the event anomaly is associated with changes in the geological and geomechanical properties of the medium or the presence of existing fractures/faults. The horizontal treatment wells could travel in and out of zones with lateral variation in lithology, which can influence the behavior of microseismicity. Also, suppose the rocks have natural fractures/faults or zones of weaknesses.

In that case, hydraulic fractures can intersect with these pre-existing fractures, and fluid entry can alter effective stress and mechanical properties, leading to microseismicity (Cipolla et al., 2011; Maxwell, 2014). To address this question, I integrate the event location results obtained from the combined quadratic interpolation and grid searches (shown in Chapter 6) and source mechanisms estimated using moment tensor inversion (described in Chapter 7) with known geological and geomechanical information such as Montney depth trend and variation in lithology observed from available well logs. See Chapters 6 and 7 for details about the methodology and implementation of event location and moment tensor inversion steps. In this section, I focus on obtaining the r-t plots from the estimated event locations and studying the shear wave splitting phenomenon since it is arguably the most robust indication of seismic anisotropy (Teauby et al., 2004a) and thus is useful for understanding the source mechanism results shown in Chapter 7 and the integrated analysis.

### **Studying r-t plots**

After obtaining event locations and their origin time, I examine r-t plots, which show the distance “r” of the event from the injection point in each stage over time “t” to understand the evolution of the microseismic cloud distance over time and it might help uncover the underlying physical mechanisms that cause the events (Ortega Perez, 2022; Shapiro et al., 2006). The r-t plots are useful; they often show growth patterns of the microseismic cloud. Four development patterns can be found in the r-t plots, including the “normal”, “reactivation”, “halted growth”, and “stress transfer” patterns. The “normal” pattern is characterized by microseismic events following a parabolic trend, driven by the pore pressure diffusion. Figure 8.4a is an example of the “normal” pattern, which has the events move away monotonically from the treated well following a parabolic trend. The “reactivation” pattern is distinguished by a linear trend in the distribution of microseismicity, which is related to the reactivation of a pre-existing fracture. Figure 8.4b is an example of the “reactivation” pattern,

which has the microseismicity develop in a linear fashion (highlighted by an orange circle), indicating that the fluids are moving into pre-existing fractures or faults and reactivating them. The “halted growth” pattern is defined by microseismic events concentrating within a specific interval, indicating that the fracture stops growing. The “stress transfer” pattern is when microseismic events occur within a short period of time at different distances from an injection point, indicating that these events are triggered by stress transfer because they take place instantaneously, whereas the transfer of pore pressure perturbations from the injection point to the reactivated fault requires time (Ortega Perez, 2022; Shapiro & Dinske, 2009). Figure 8.4c is an example of an r-t plot with “halted growth” and “stress transfer” patterns. In the beginning, microseismicity occurs instantaneously at different distances, which is characteristic of the “stress transfer” pattern (Ortega Perez, 2022).

### **Studying shear wave splitting phenomenon**

Additionally, I study the shear-wave splitting phenomenon. This phenomenon occurs when a shear wave propagates through an anisotropic medium, such as a fractured medium, leading to the partitioning of energy into orthogonally polarized fast and slow shear waves (De Meersman et al., 2009a; Hardage et al., 2011; Teanby et al., 2004a; Wuestefeld et al., 2010). The shear wave splitting parameter, which is simply the fractional difference between the fast and slow vertical shear wave velocities, is an excellent tool for fracture characterization, as its magnitude correlates directly with fracture density (Tsvankin & Grechka, 2011). MacFarlane and Davis (2015) used amplitude variation with angle inversion to obtain proxy measurements of the fast and slow shear wave velocities and observed lateral and vertical fracture heterogeneity within the Montney formation. The study found an excellent correlation between regions with shear velocity anisotropy and microseismic events when plotting the time slices of the shear wave splitting parameter through the well and superimposing the microseismic event locations (Figure 8.5). I thus investigate if there is any evidence

of the shear-wave splitting phenomenon in the data.

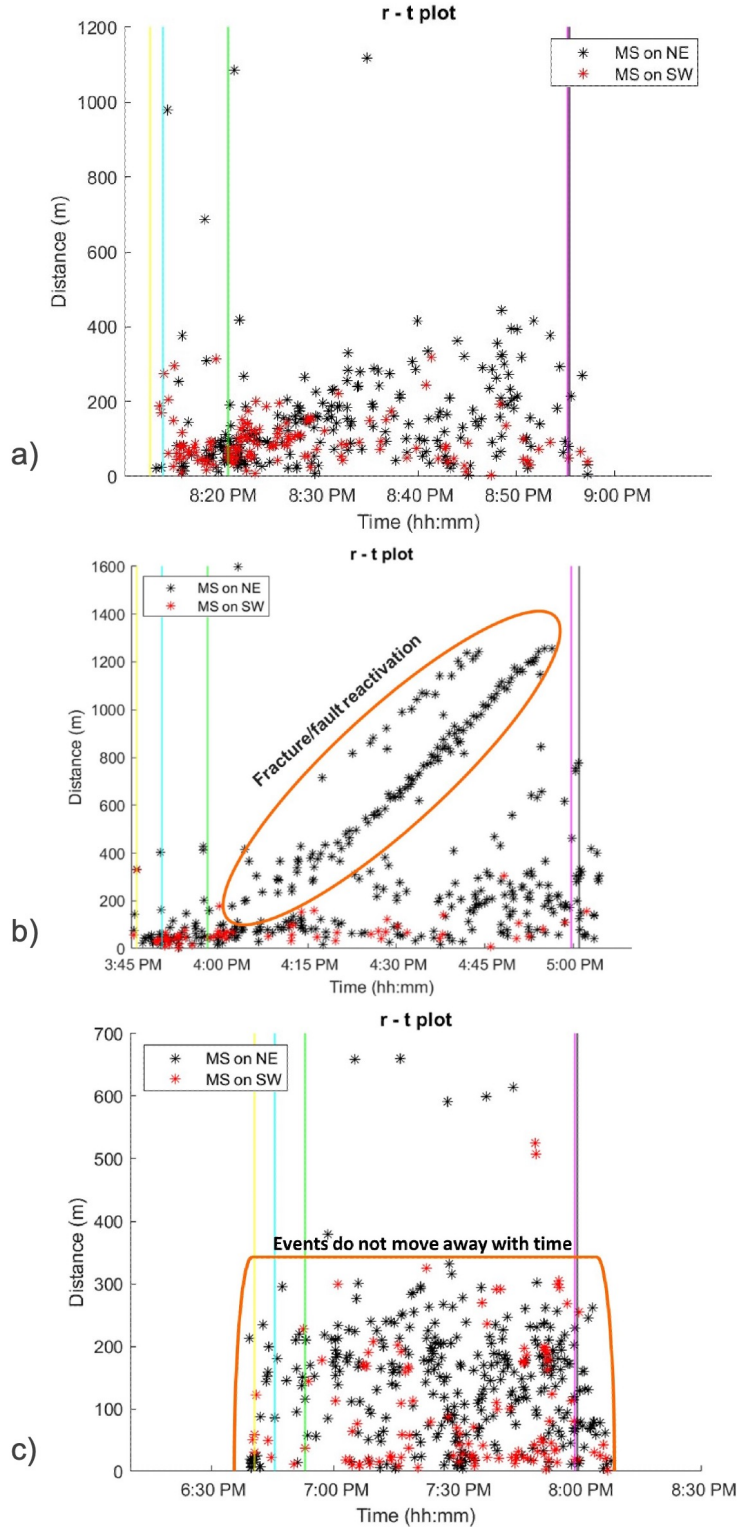


Figure 8.4: Examples of r-t plots with (a) “normal”, (b) “fault reactivation”, and (c) “halted growth” patterns. Black stars denote microseismic events propagating towards the northeast (NE) and red towards the northwest (SW). Yellow, blue, and green lines indicate the start of injection, formation breakdown pressure, and frac hit time (Ortega Perez, 2022).

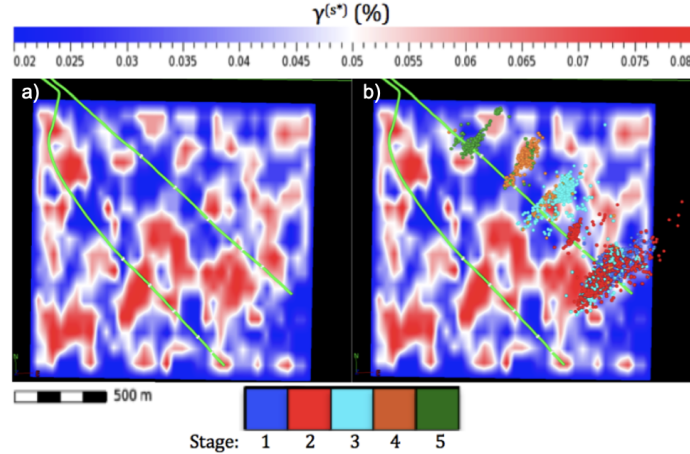


Figure 8.5: Time slices of shear wave splitting parameter through the well (a) without and (b) with microseismic events. There is a strong correlation between microseismic events (filled circles with colors representing the treatment stages) and regions with high shear velocity anisotropy (indicated by red) (MacFarlane & Davis, 2015).

## 8.3 Results

### 8.3.1 Investigate operational issues

I study the fracturing notes and completion reports to check for any operational problems during the treatment in each stage and to determine if they correlate with the number of events.

Several stages in well 2 had issues during operations. For example, stage 1 had mechanical problems with the blender, the fracturing operations were ceased, and the vertical and horizontal monitoring arrays were shut down temporarily and then resumed normal functioning. Stages 3 and 4 experienced screen-out problems, especially stage 3, where screen-outs occurred multiple times, which required time for frac flow back, multiple shutdowns of the monitoring arrays, and then the fracturing operation and recording could be continued. These two stages also had a poor injectivity rate, failing to achieve the target injection rate of  $2 \text{ m}^3/\text{min}$  at the beginning of the operation. In stage 7, a screen-out occurred; the fractures could not be created, and the monitoring arrays were shut down for about 2 hours. Stages 11 and 12 experienced a weak ball seat, while stage 13 had no ball seat.

Different operational problems, from blender issues, screen-out conditions, and poor injection rate to no/weak ball seats, occurred during the treatments. These operational issues can negatively affect hydraulic fracturing performance, hindering fracture activation/reactivation. They can also influence the recording of induced microseismicity due to multiple temporary shutdowns of the monitoring arrays. I observe that most treatment stages with operational issues (stages 1, 3, 4, 7, 12, 13) had few microseismic events (Figure 8.6). Only stage 11 has many events despite having a weak ball seat. However, many stages with normal treatment (2, 5, 6, 8, 9, 10, 14-16) also had a few events. The stages with normal treatments are expected to result in many events because a typical fracturing treatment aims to create hydraulic fractures. Therefore, while operational issues could influence microseismicity, they were not the primary cause of the event anomaly in the well.

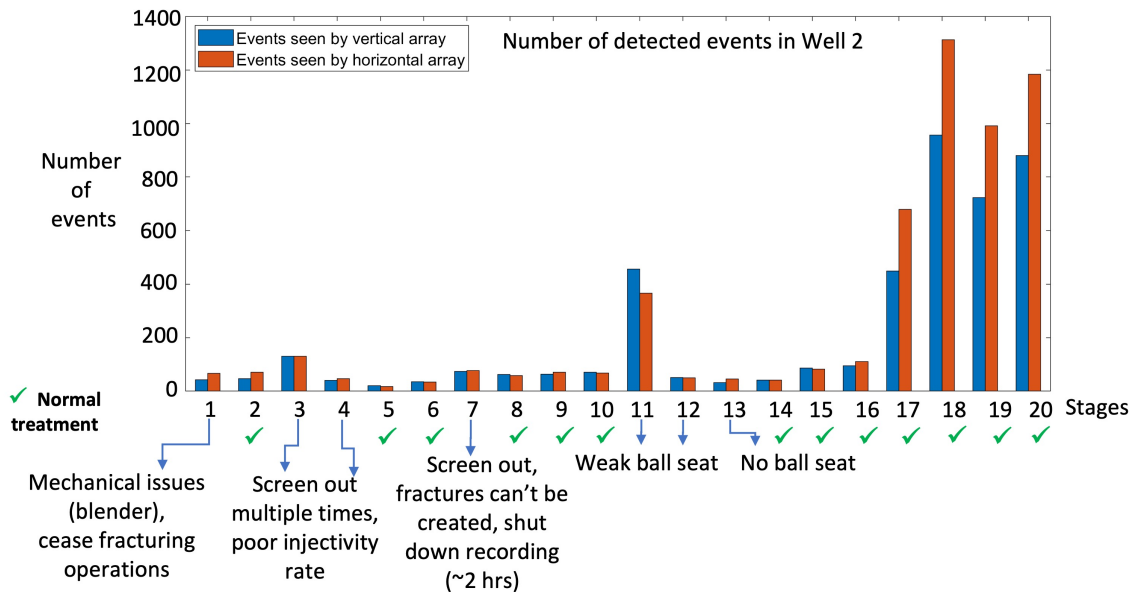


Figure 8.6: Number of events detected in each treatment stage in well 2 and information on operational problems. The green check mark indicates stages with normal treatment.

### 8.3.2 Investigate treatment parameters

I compute the total injection energy for each of the 20 treatment stages in well 2 using equation 8.2. The total energy input into the operation is the product of the treatment duration, the average surface pressure and the average injection (slurry) rate. Figures 8.7a, b, and c show the histograms of treatment duration, the average surface pressure and the average injection rate of 20 stages in well 2, respectively.

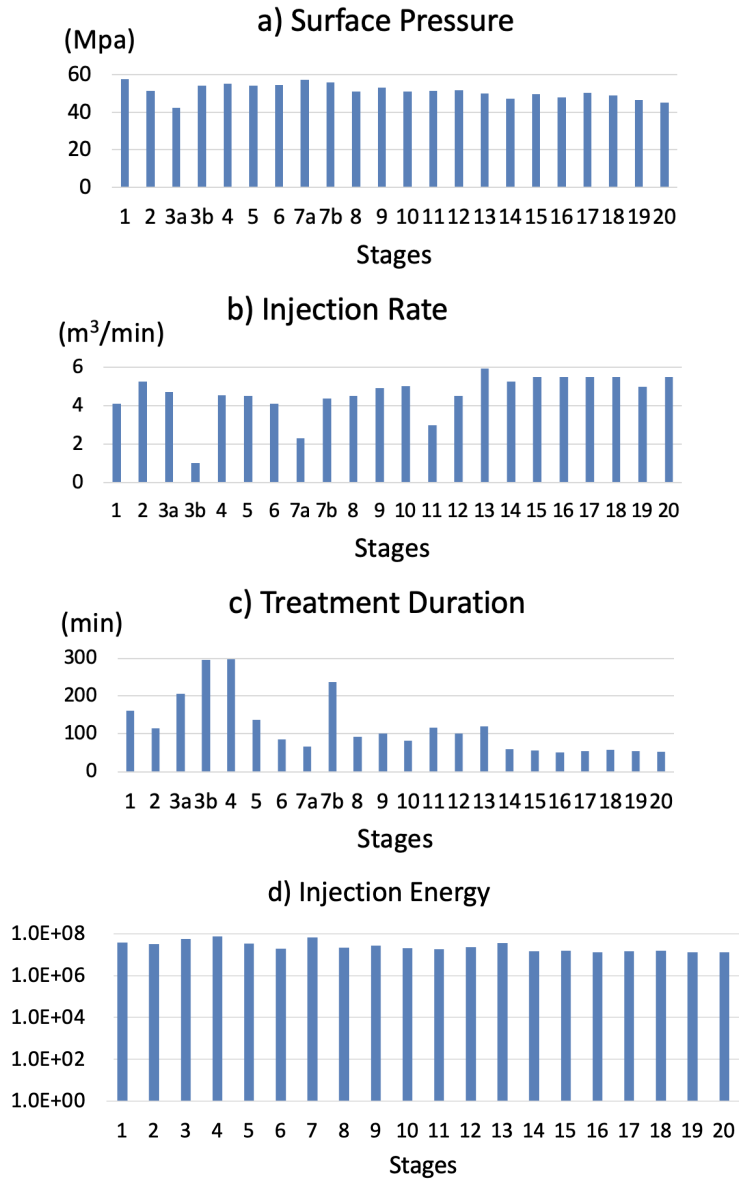


Figure 8.7: (a) Surface pressure (MPa), (b) Injection rate ( $m^3/min$ ), (c) Treatment duration (min), and (d) Injection energy (KJ) calculated for each treatment stage in well 2.

The average surface pressure varies between 45 and 55 MPa, the injection rate ranges from 1 to 6  $m^3/min$ , and the duration of the treatment is between 50 and 300 min. Figure 8.7d shows the resulting injection energy for all treatment stages in well 2. While there are variations in the treatment parameters, with some stages (e.g., stages 3, 4, 7) having longer treatment durations and poorer injectivity rates (e.g., stages 3, 4, 7, 11), the resulting injection energy is almost the same for all treatment stages,  $\approx 10^7$  KJ. Thus, the total energy input into each stage's operation is similar and is unlikely linked with the event anomaly between stages in this well. The changes in the treatment parameters are not the causes of abnormal microseismic behavior.

### 8.3.3 Investigate event detection

Potential microseismic events in each treatment stage of well 2 are detected using the MF and STA/LTA methods (see Chapter 4 for details about the detection workflow and implementation). After the manual inspection and classification step, I obtain 21,766 excellent events from the STA/LTA method. The fast MF method performs more efficiently than the STA/LTA; it detects almost the same number of excellent events, with 19,913 events, and generates fewer false alarms, which helps to avoid the time-consuming classification of detection results as in the STA/LTA. Figures 8.8a and b show the MF and STA/LTA detection results for each treatment stage in well 2 using vertical-array and horizontal-array data. Both MF and STA/LTA methods exhibit similar event patterns. They have strong variations in microseismicity between stages, with the majority of events concentrated towards the heel of the well. For example, stages 16-20 have a large number of events (over 400 and can be up to 1000 in stage 18). In contrast, other stages (e.g., stages 1, 2, 4, 5, 6, 12, 13, and 14) have only a few events (fewer than 50). The similar, substantial variations between the MF and STA/LTA detection results indicate that the event anomaly is unlikely to be attributed to errors in data processing.

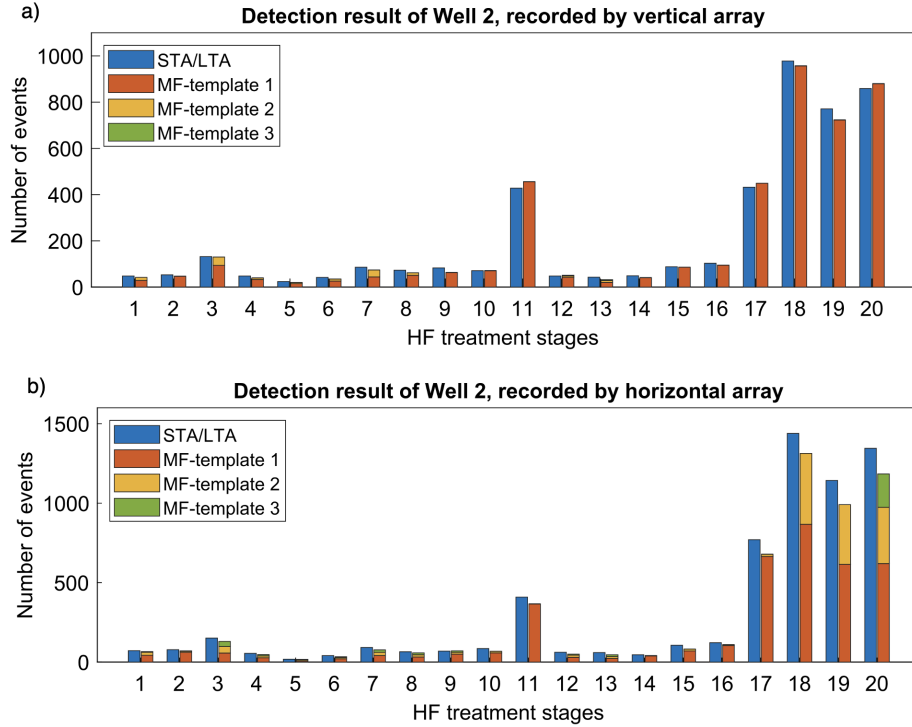


Figure 8.8: Event detection results of (a) vertical-array and (b) horizontal-array data in well 2. STA/LTA results are indicated in blue, while the fast MF results using different representative template events are displayed in other colors.

### 8.3.4 Investigate location, moment tensors, geomechanics

#### Estimating event locations

Figure 8.9 shows the map and depth views of the event locations obtained from quadratic interpolation on 10-m-grid-estimated locations. I also plot the error ellipsoids obtained from the misfit functions by considering the area where the misfit value is less than or equal to 5% of the minimum misfit. The map view shows that the events are parallel and develop in the northeast-southwest direction, which parallels the direction of the maximum horizontal stress northeast-southwest (NE-SW) in the study area (Figure 8.10). Due to the limitation in the acquisition geometry (receiver locations with respect to the source positions), I could not get a better interpretation of event locations. This is because the accuracy of the interpolated locations is mainly limited by the flatness of the misfit function in certain directions instead of by how well the interpolation function resembles the true misfit (see Chapter 6 for

more details).

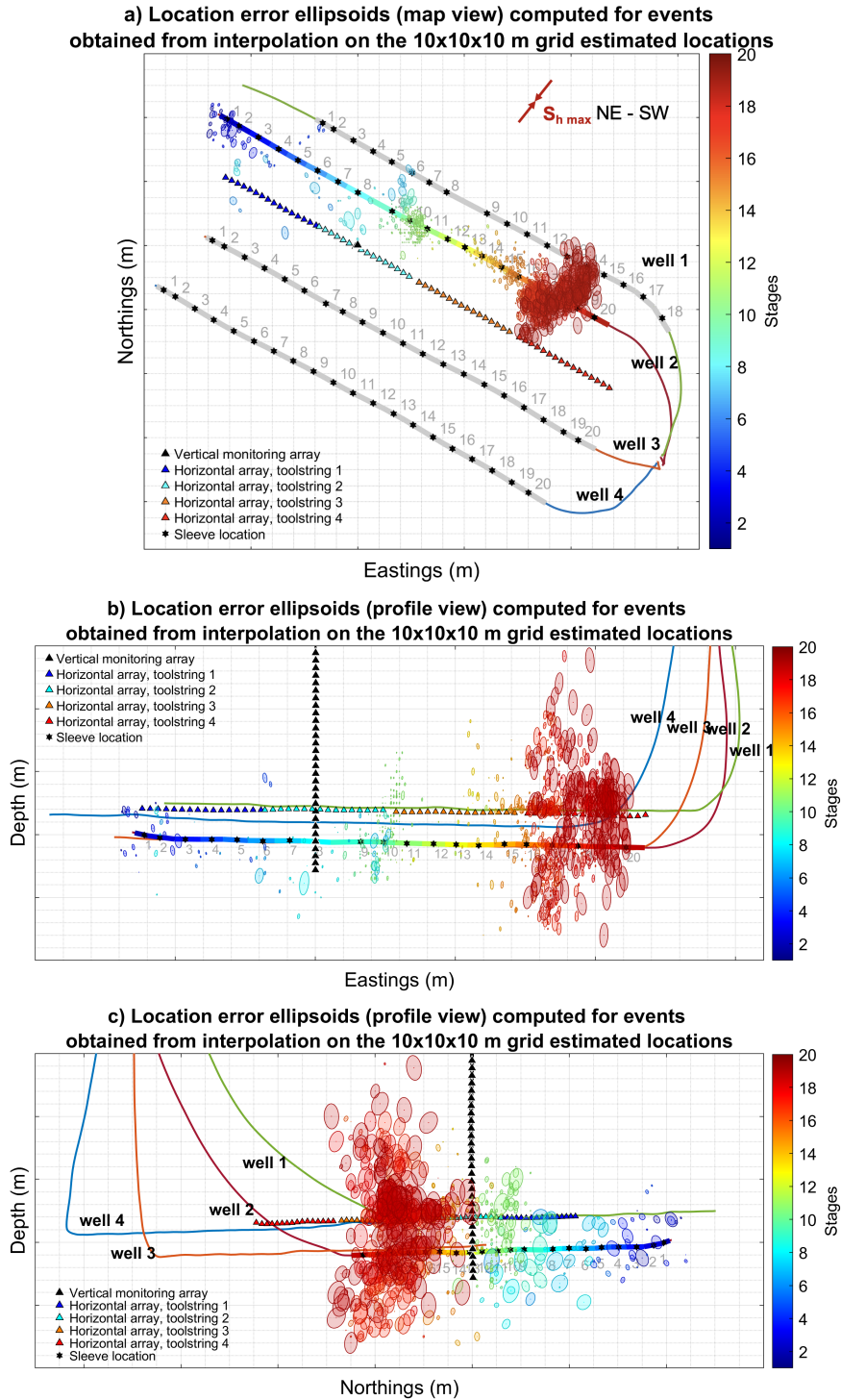


Figure 8.9: Event locations with error ellipsoids computed for events obtained from interpolation on the grid (grid spacing = 10 m) estimated locations. (a) Map view. (b) and (c) Profile views.

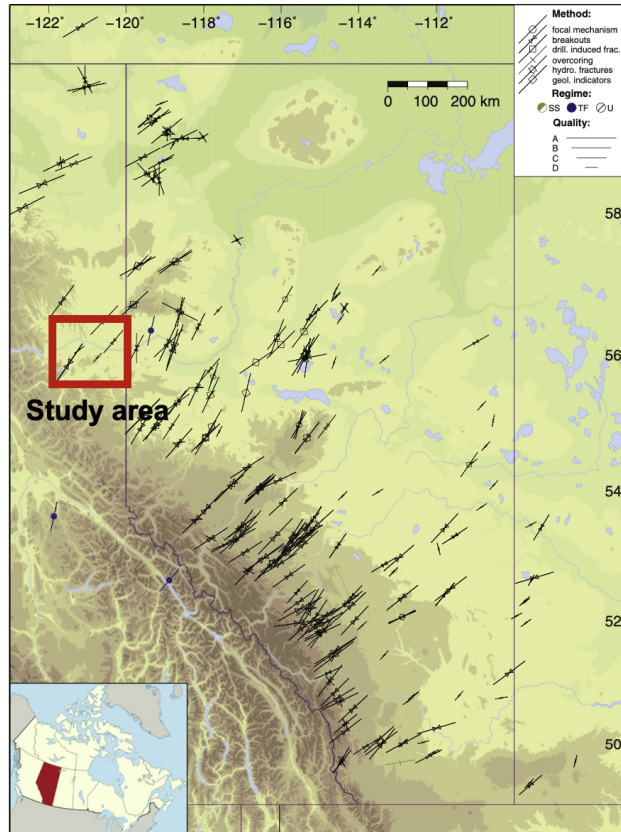


Figure 8.10: Stress map of the study area. The orientations of the maximum horizontal stress are indicated by black lines with line length proportional to quality (Modified from (Reiter et al., 2014)).

### Studying r-t plots

I calculate the distance between the events and treatment locations for each stage using the resulting event locations. Figure 8.11 presents the r-t plot showing the distance of events from the treatment locations over time in 20 treatment stages. Figure 8.11a shows that the microseismicity behaves differently from stage to stage, with a substantial concentration observed in the later treatment stages. A zoom section on stages 17-20, in which there are many microseismic events (Figure 8.11b), shows that the microseismic events move away monotonically from the treatment location, indicating a “normal” r-t development pattern of microseismicity. The “normal” r-t pattern means no fault reactivation (pre-existing faults) is related, supporting the hypothesis that the event anomaly is linked with the geological/geomechanical changes

in the medium.

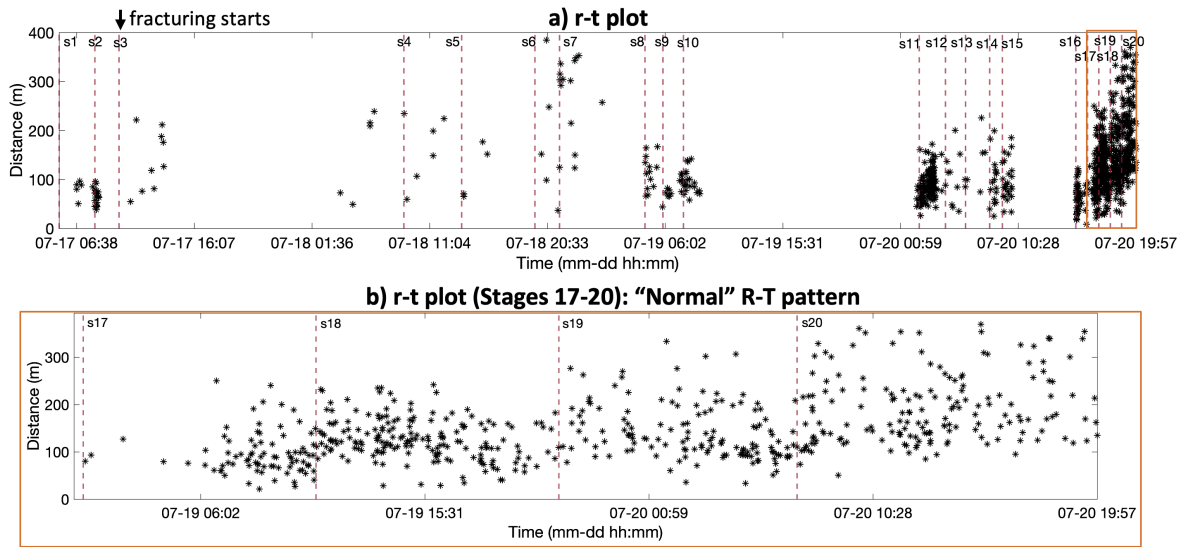


Figure 8.11: (a) r-t plot showing the distance of events from the treatment location versus the origin time of the events. (b) A zoom section displaying the r-t plot of events during treatment stages 17-20.

## Understanding source mechanisms

Chapter 7 provides a thorough analysis of the source mechanisms of microseismic events using two different methods: a quick screening test based on S/P ray amplitude ratios and a full moment tensor inversion using P- and S-wave amplitudes in all 3 data components.

The source mechanism screening test allows the first classification into the number of shear and tensile events per stage, which is then used to compare with the moment tensor inversion results, supporting a more reasonable interpretation of the event's source mechanisms. Figures 8.12a and b display the results calculated from the vertical-array and horizontal-array data. A similar characteristic is observed, with both tensile and shear faulting present in each stage and tensile mechanisms likely being prominent in well 2, particularly in stages towards the heel of the well.

Figure 8.13 shows Hudson's source-type plots for visualizing the moment tensor inversion results of microseismic events in well 2 with the solutions plotted for every five stages (stages 1-5, 6-10, 11-15, and 16-20) since the horizontal monitoring array moves

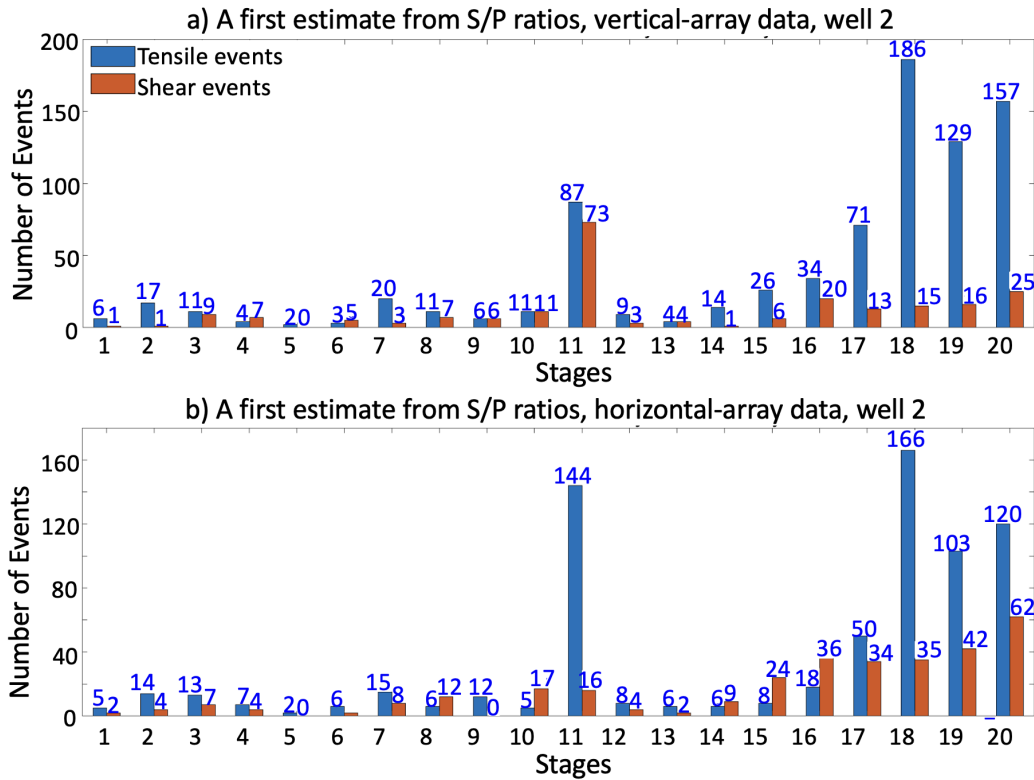


Figure 8.12: S/P amplitude ratios result from the vertical-array and horizontal-array data. Tensile events are indicated by blue color; shear events are indicated by orange color. The numbers in the figures show the number of tensile/shear events in each stage.

every 5 stages. The first 15 stages show similar features, with the solutions plotted in the center (shear faulting), top-left and bottom-right (opening/closing cracks or tensile faulting) of Hudson’s diagrams. Both types of faultings are evident; however, the prominent feature of tensile faulting is less obvious than the screening test results. The solutions of events in the stages toward the well’s heel (stages 16-20) are plotted in many places on Hudson’s diagram, possibly caused by the anisotropic velocity field since the shear wave splitting phenomenon is evident in these stages.

Thus, different moment tensor characteristics are observed between treatment stages, suggesting that the substantial variations in the number of microseismic events between stages are likely related to a geological/geomechanical role.

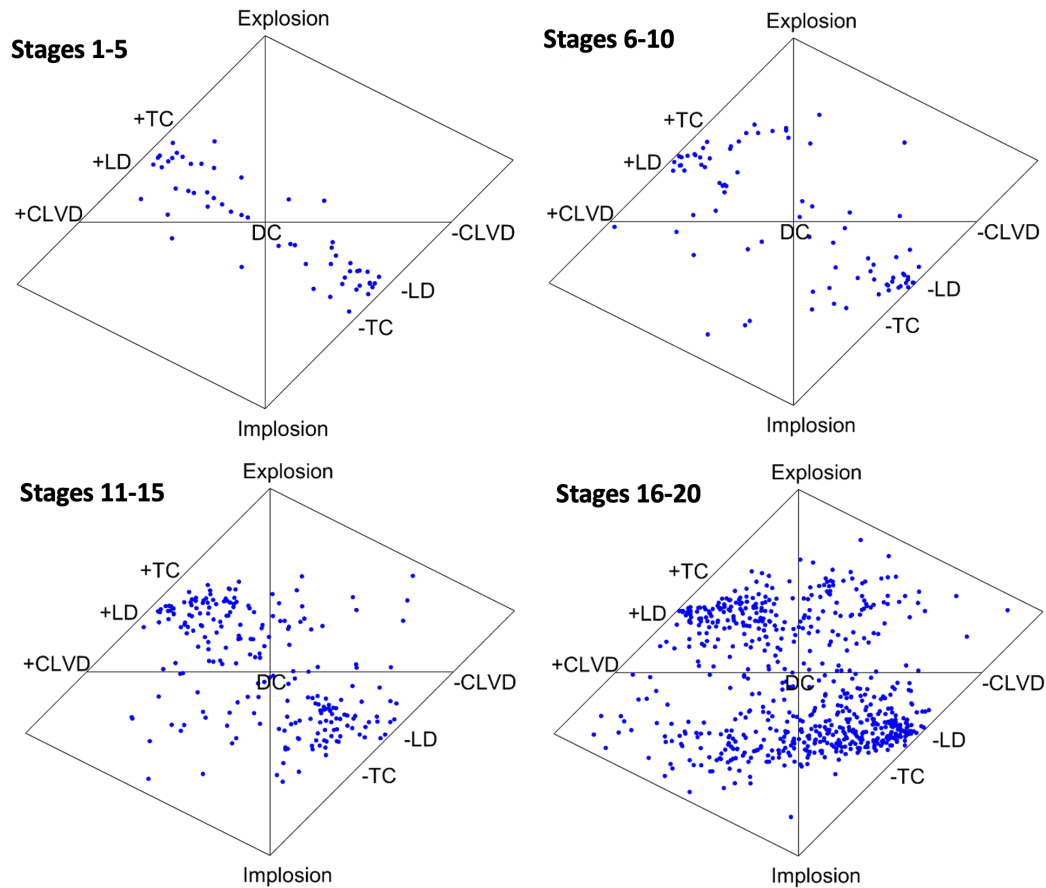


Figure 8.13: Hudson's source-type plot for visualizing the moment-tensor inversion results of microseismic events in well 2.

### Investigating Montney local depth trend and variation in lithology

Figure 8.14 shows the Montney local depth trend obtained using available well tops and the regional depth trend of the Montney using well tops from nearby wells. Among the available well tops provided by the anonymous company, the Upper Montney layer is between Tops F and Mid B, the Middle Montney layer is between Tops Mid B and Lower B, and the Lower Montney layer is between Tops Lower B and Montney Base. All the dashed lines in the plot represent the depth trend predicted using regional tops obtained through the available geoSCOUT software. All the dotted lines show the depth trend obtained using available well tops in treatment well 2 and the vertical monitoring well. The event locations in 20 treatment stages in well 2 are superimposed using filled circles with colors indicating different treatment stages.

Clearly, the treatment well 2 first penetrates the Lower Montney and then intersects the Middle Montney. Different landing heights might link to the event anomaly at the well heel because of the variability in geological heterogeneities of the Lower and Middle Montney. According to González et al. (2022), the lithostratigraphy of the Montney in the NE BC area has many complexities associated with the subtle grain-size variation, diminutive biogenic structures, lateral facies variability, and distribution of local discontinuities. González et al. (2022) also emphasizes that these rocks exhibit small-to-large-scale heterogeneities and, in some intervals, are characterized by thin interbeds of rheologically anisotropic properties.

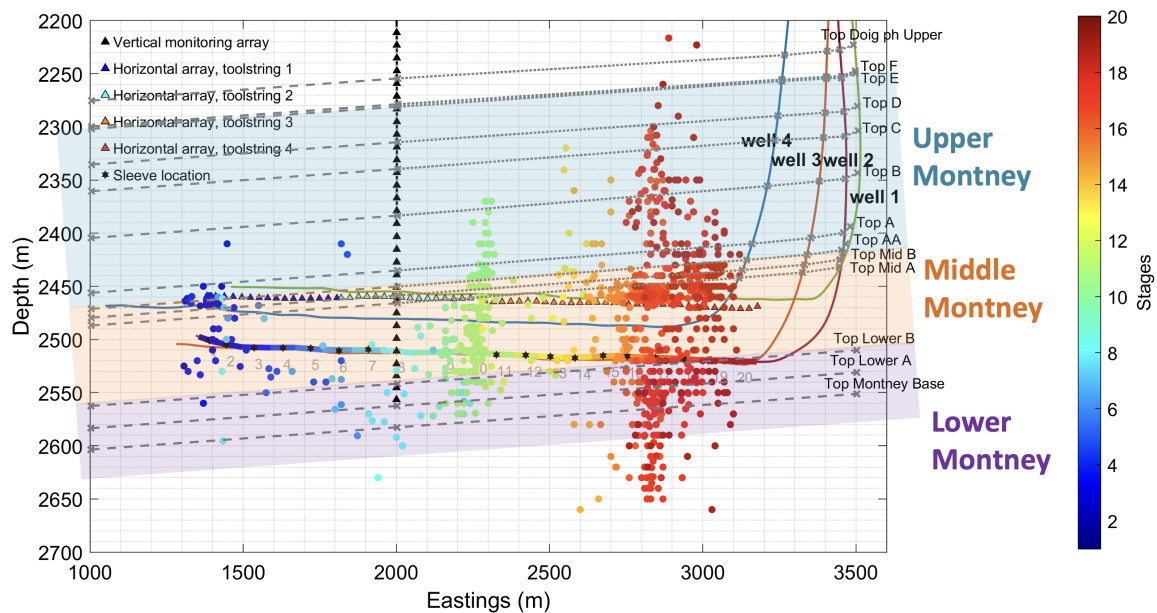


Figure 8.14: Montney depth trend using available well tops and regional depth trend from tops in nearby wells. All the dashed lines indicate the predicted depth trend obtained from the regional tops using geoSCOUT. All the dotted lines show the depth trend obtained using available well tops in treatment well 2 and the vertical monitoring well. Event locations are superimposed using filled circles with colors indicating different treatment stages. Black triangles indicate the vertical monitoring array and triangles with other colors indicate the horizontal array.

I continue investigating to see if there is any correlation between the event anomaly with the variation in lithology using the only available well log: the gammay ray (GR) log acquired in 4 treatment wells. The density log is only available on the

vertical monitoring well; thus, it is not incorporated here to interpret the variation in lithology. The GR log is useful; it can be a good indication of shaly (high GR values) and clean (low GR values) intervals. However, it should be noted that unlike other unconventional plays (e.g., the Duvernay and the Marcellus, (Becerra et al., 2021; Lili et al., 2015; Venieri et al., 2020)) where the GR log is primarily due to organic matter and clay contents, in the Montney formation, the presence of potassium feldspars significantly influences the GR log (Becerra et al., 2021; Krause et al., 2011).

Figure 8.15a, b displays the GR log plotted along with the trajectory of well 2 and the number of detected events in each treatment stage. The GR log shows that the well penetrates layers with high GR values (above 90 AAPI units), which are highly likely due to the presence of potassium feldspars. Notably, the variations in the GR log between treatment stages are observed clearly, which are highlighted using different colors in Figure 8.15a. For example, stages 7-10 and 12-16 have similar characteristics (indicated by light orange), with higher GR values than others, thick interbeds, and only a few events. Stages 17-20 (indicated by green) also have thick interbeds but lower GR values than the GR of stages 7-10 and 12-16, and many events (up to 1000 events in stage 18) are observed. Stages 1-6 also have lower GR than the GR of stages 7-10 and 12-16; however, these stages are very thin interbeds with many streaks (strong variations) observed on the GR log and have only a few events. Stage 11 has comparable GR values but does not have similar streaks as stages 1-6, and the microseismic behavior in stage 11 is similar to stages 17-20, with many events. The observations on the GR log acquired in well 2 indicate that there are variations in lithology between stages in this well. These variations likely correlate with the anomalous microseismic behavior.

Figures 8.16, 8.17, and 8.18 display the GR logs acquired in wells 1, 3, and 4 and the microseismic events detected in each treatment stage in these wells. The patterns of the GR logs reveal that these treatment wells penetrate complicated lithological intervals consisting of interbeds with varying GR values and thicknesses. Similarly, I

observe some degree of correlation between the GR logs and the number of microseismic events between stages (particularly in well 4 (Figure 8.18), which has a similar event anomaly towards the well’s heel as in well 2 (Figure 8.15). While wells 1 and 3 exhibit less evident variations in microseismicity; however, the variations in GR logs (indicated by different colors) also indicate some correlation with the number of microseismic events between stages.

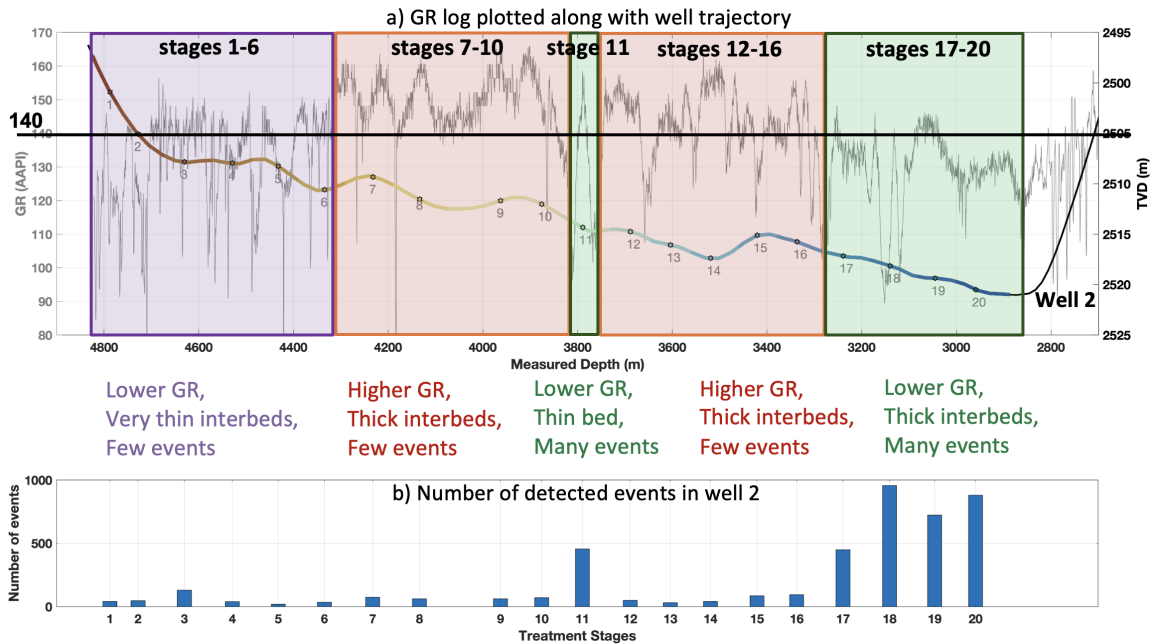


Figure 8.15: (a) Gamma ray log plotted along with the trajectory of well 2. The variations in the GR log between treatment stages are highlighted using different colors. (b) Number of detected events in well 2.

### Studying shear-wave splitting phenomenon

In the stages toward the well heel, I observe strong evidence of an anisotropic velocity field. Figure 8.19a, b, c, d shows the S-wave data segment of 3 components (vertical and two horizontal, indicated by red, green, and blue, respectively) of microseismic events detected from treatment stages 1 (near the toe of the well), 11, 18, and 20 (near the heel of the well). For the events in stages 1 and 11 (Figure 8.19a, b), there is not much difference in the arrival times of the S-waves between the vertical component and the horizontal components. In contrast, the S waves clearly arrive faster on the

horizontal component than on the vertical component for the events in stages 18 and 20 (Figure 8.19c, d). Thus, when moving from stages near the toe to the heel of the well, the shear wave splitting phenomenon is more visible, with S-waves arriving at different times on the seismograms.

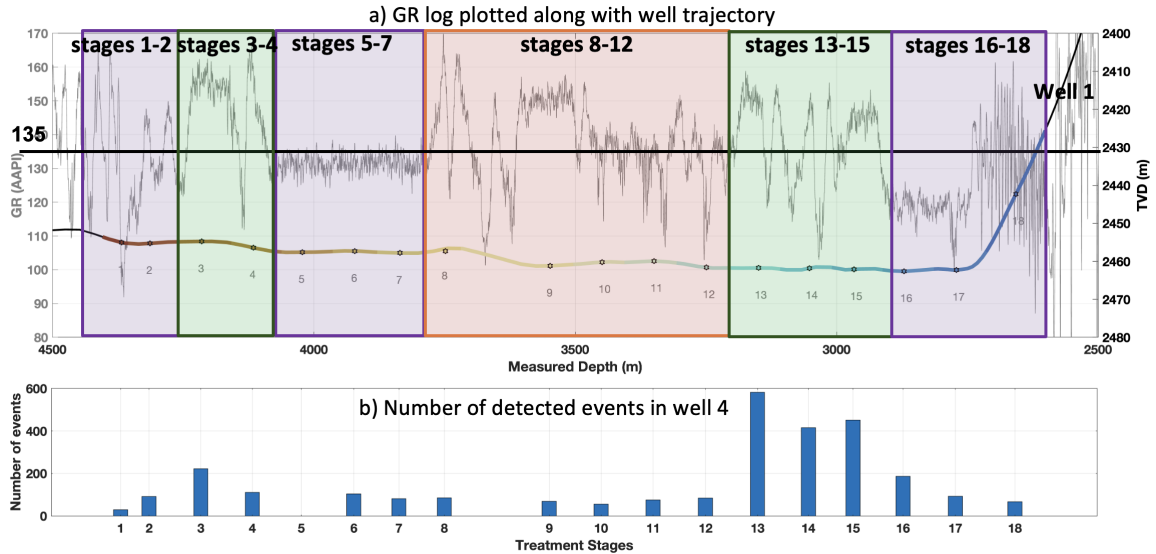


Figure 8.16: (a) Gamma ray log plotted along with the trajectory of well 1. The variations in the GR log between treatment stages are highlighted using different colors. (b) Number of detected events in well 1.

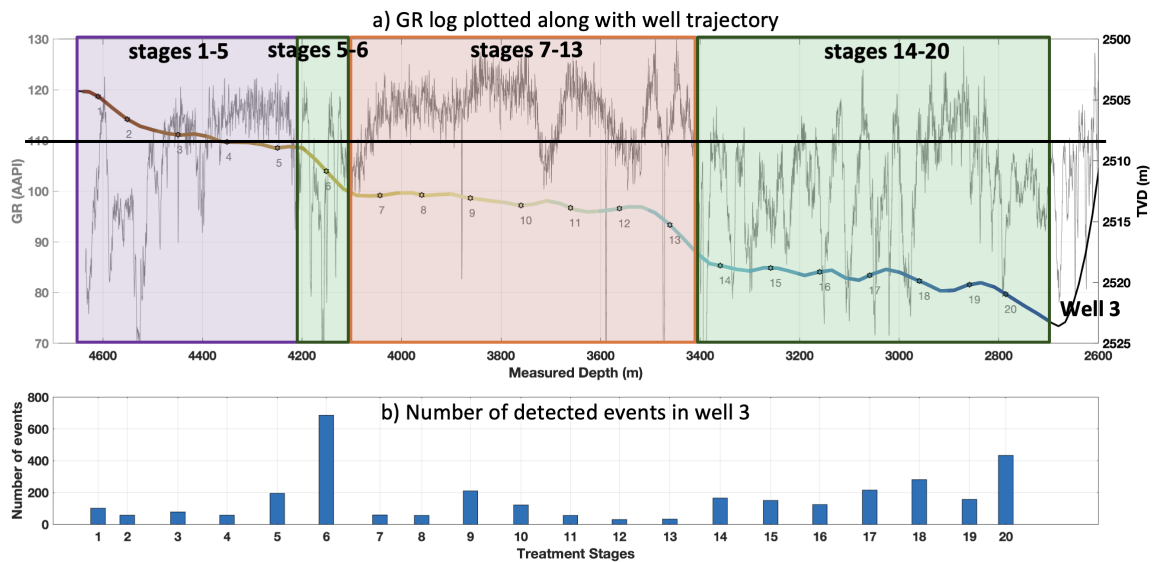


Figure 8.17: (a) Gamma ray log plotted along with the trajectory of well 3. The variations in the GR log between treatment stages are highlighted using different colors. (b) Number of detected events in well 3.

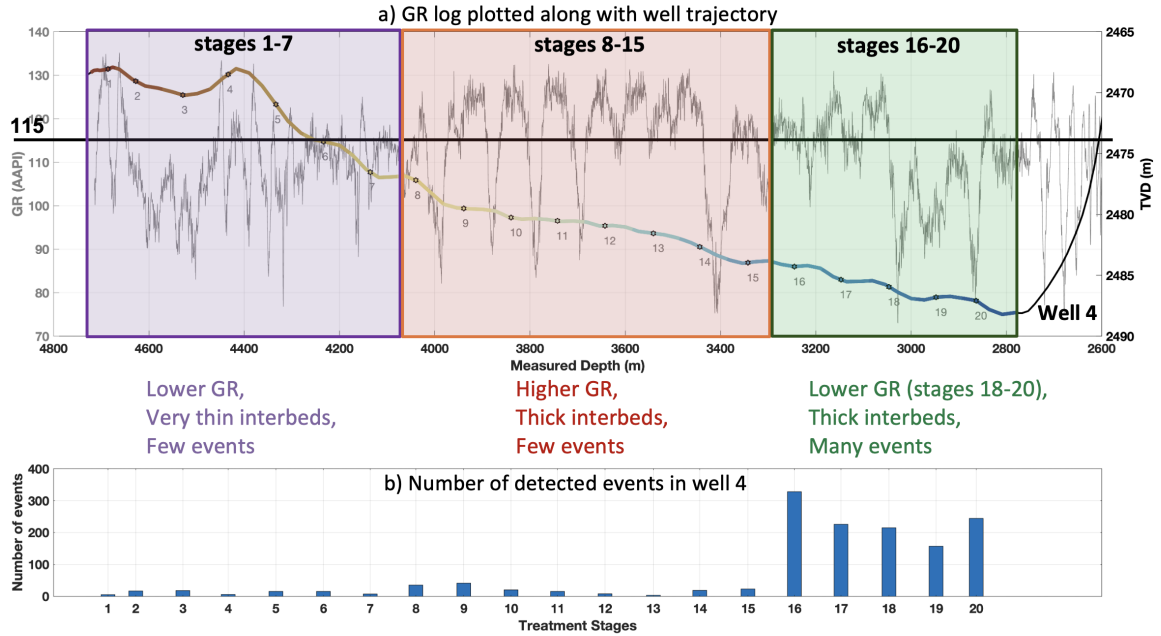


Figure 8.18: (a) Gamma ray log plotted along with the trajectory of well 4. The variations in the GR log between treatment stages are highlighted using different colors. (b) Number of detected events in well 4.

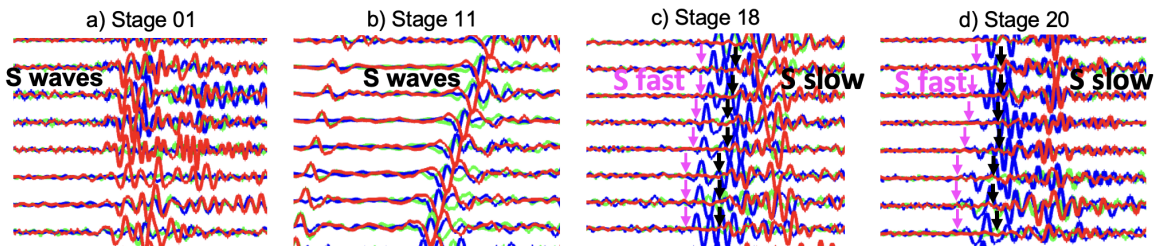


Figure 8.19: Three-component waveforms of the S-wave of microseismic events from treatment stages 1, 11, 18, and 20. For the events in stages 18 and 20, the onsets of the fast S-waves are indicated by pink and the onsets of the slow S-wave are denoted by black.

The study of Tsvankin and Grechka (2011) showed that the magnitude of the shear wave splitting parameter (the fractional difference between the fast and slow vertical shear wave velocities) correlates directly with fracture density. MacFarlane and Davis (2015) demonstrated that regions with large shear wave splitting values are expected to be associated with high fracture densities. Figure 8.20 shows a cross-section of the shear wave splitting parameter through 2 wells in the Montney, with well 00/07-07 having a strong production volume (high fracture densities) and penetrating regions

with large persistent shear wave splitting values (indicated by red) and well 02/07-07 having a poor production volume (low fracture densities) and penetrating regions with low shear wave splitting values (indicated by grey) (MacFarlane & Davis, 2015). Since microseismic events are local small brittle failures caused by changes in local pressure and the in-situ stress in the reservoir rocks through the hydraulic fracturing process (van der Baan et al., 2013), regions with high fracture densities suggest that there are many microseismic events. Thus, the majority of events concentrated toward the heel of well 2 in this study are likely linked to increased fracture density and, consequently, high shear wave velocity anisotropy.

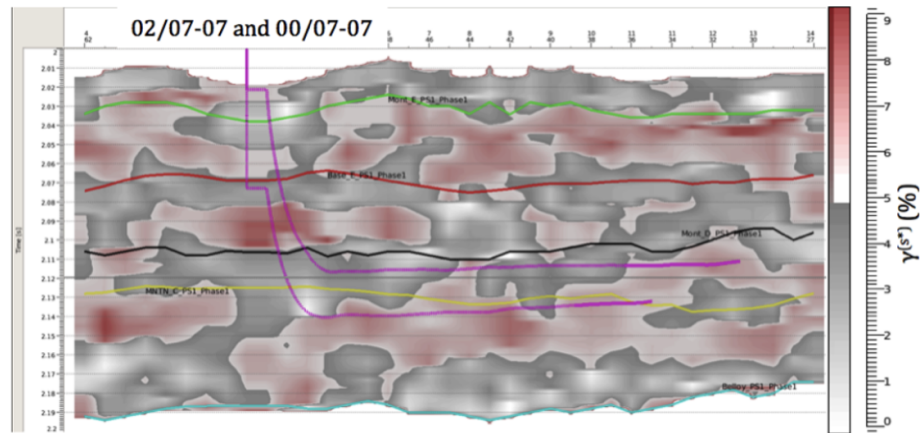


Figure 8.20: A cross-section of the shear wave splitting parameter through 2 wells (02/07-07 and 00/07-07) in the Montney (MacFarlane & Davis, 2015).

## 8.4 Discussions

Various factors, including reservoir fluids, the existing stress regime, natural fractures, matrix permeability, and rock properties, can greatly affect the patterns of microseismic events (Cipolla et al., 2011). Understanding the geomechanical context in which microseismic events occur and the underlying physical processes is crucial for properly interpreting microseismic behavior. In this study, I conduct an integrated analysis of engineering parameters, event locations, moment tensors, and geomechanics to comprehend the primary causes of the strong variations in microseismicity between

treatment stages, with an event anomaly located near the heel of the well in NE BC. The lithostratigraphy of the Montney in the study area is complicated, consisting of interbedded successions of fine- and coarse-grained siltstone, very fine-grained sandstone, and bioclastic siltstone intervals (González et al., 2022). According to González et al. (2022), these rocks exhibit small-to-large-scale heterogeneities and, in some intervals, are characterized by thin interbeds of rheologically anisotropic properties. By incorporating all available data, from fracturing reports, completion data, well data, and known geological information from previous studies to more advanced processing results of microseismic data, I investigate all possible hypotheses of the underlying causes of abnormal microseismic behavior. The comprehensive analysis reveals that operational issues, changes in treatment parameters, errors in data processing, and pre-existing faults are not the primary causes. Based on evidence from r-t plots, moment tensor characteristics, landing heights, lithological variations, and anisotropic velocity field, I find that geological and geomechanical changes in the medium are highly likely associated with unusual microseismic behavior.

Microseismic monitoring is important in understanding microseismic activity induced by hydraulic fracturing treatments and improving the treatment performance (Eaton, 2018). Other integrated case studies, such as Rafiq et al. (2016), Ma and Zoback (2017), MacKay et al. (2018), and Feroz and van der Baan (2024), also tried to understand the microseismic behavior in the subsurface by incorporating different types of data and analyses.

Rafiq et al. (2016) observed significant differences in microseismicity between the two hydraulic fracturing treatment wells in a tight sand reservoir in central Alberta, although identical treatment parameters were applied. One well exhibits a greater persistence of post-pumping activity and an inferred higher density of event clusters with a complex spatial distribution. Approximately 50% of the events oriented in the direction of the maximum horizontal stress (northeast-southwest), and the remaining events exhibited oblique orientations to the maximum horizontal stress, indicating

the reactivation of preexisting fractures. Rafiq et al. (2016) combined microseismic facies analysis with surface seismic attributes to characterize reservoir heterogeneity, rock fabric, and compartments in the reservoir and understand the differences in microseismic behavior of the two wells. Rafiq et al. (2016) found that the reservoir is compartmentalized: two treatment wells intersect distinct facies with varying rock fabric, possibly indicative of different depositional environments (e.g., porous sandbars or silty interbar facies) that caused the differences in the microseismic response for the two wells.

Ma and Zoback (2017) investigated the petrophysical and geomechanical factors that control the effectiveness of hydraulic fracturing in the Mississippi Limestone-Woodford Shale play in Oklahoma. The study of Ma and Zoback (2017) found that the heterogeneity of the reservoir primarily affected the hydraulic fracturing performance and the variations in microseismicity. Small variations in the well trajectories caused the wells to penetrate three thin but compositionally distinct lithofacies (Ma & Zoback, 2017). Subsequently, some stages occurred in a zone with high clay and kerogen content, decreasing the microseismicity. The study also found that the normal and strike-slip faults cutting across the wells also influenced the microseismic event distribution. These pre-existing, pad-scale faults frequently redirected fracturing fluids, limited the ability of fracturing operations and consequently affected induced microseismicity (Ma & Zoback, 2017).

MacKay et al. (2018) used a rock-mass characterization approach, integrating outcrop observations, core and well-log analysis, and microseismic interpretation to gain a comprehensive understanding of natural fracture networks. They performed a numerical simulation of the microseismic response of artificial rock mass to hydraulic fracturing and compared it with the observed microseismicity in a Duverney reservoir in western Canada. The findings of MacKay et al. (2018) suggest that lithology significantly impacts intact rock properties, subsequently affecting the fracture network distribution, which controls the stress distribution (and microseismicity) and

fluid flow within the subsurface during injection. The comparison between simulated microseismic response and observed microseismicity provides insights into stress redistribution and partition within the rock mass. MacKay et al. (2018) found that the concentration of deformation within the upper and lower Duvernay members in their case study indicates that stresses are shed into the surrounding carbonate units, potentially increasing the likelihood of induced seismicity because large shear stresses cannot be sustained within the Duvernay due to increased fluid pressures and weak bedding planes.

Feroz and van der Baan (2024) investigated the unusual pattern of microseismicity from an Alberta heavy oil field. Feroz and van der Baan (2024) observed that 95% of recorded microseismicity occurred during injection and in the overburden; 70% of the events triggered during the first cycle. By incorporating microseismicity and engineering data, the study found that the high brittleness likely caused the concentration of microseismicity in the overburden. Additionally, the occurrence of microseismic events in the overburden is caused by a low well landing height, causing injection points to be very close to the top of the reservoir and triggering microseismicity due to the volumetric expansion of the reservoir (Feroz & van der Baan, 2024). Moreover, the microseismicity is influenced by the Kaiser effect, where event rates remain low in subsequent cycles until the current injection pressure exceeds the previous maximum. This explains why 70% of the events occurred during the first cycle and possibly why microseismicity during production accounted for only 5% (Feroz & van der Baan, 2024).

Overall, the subsurface is complicated and unknown; these case studies, including the integrated analysis presented in this study, provide insightful information on understanding the subsurface and enhancing hydraulic fracturing operations.

## 8.5 Conclusions

In conclusion, I perform an integrated analysis of an extensive, raw microseismic dataset induced by hydraulic fracturing in a Montney reservoir in northeastern BC. The investigation aims to understand the primary causes of the anomalous behavior of microseismicity between treatment stages, with many events concentrated toward the well's heel and only a few events in other areas.

I find that operational issues (e.g., screen-outs, poor injectivity rate, weak/no ball seats, and multiple shutdowns of monitoring arrays), changes in treatment parameters (e.g., breakdown pressure, injection rate, and treatment duration), data processing (e.g., inefficient event detectors), and pre-existing faults in the medium are not the primary causes of the substantial variations in microseismicity between treatment stages, with the majority concentrated toward the well's heel. While operational problems might affect microseismicity, they are not the leading causes since I observe a few microseismic events in both stages experiencing operational issues and stages with normal treatments. Variations in treatment parameters between stages are also observed; however, the resulting total energy input into each stage is similar so these changes are unlikely linked with the anomalous microseismic behavior. Detection results obtained from the STA/LTA and MF methods show similar event distribution between stages, with many events concentrated toward the heel and hardly any in other stages; thus, data processing is also not the leading cause of the strong variations in microseismicity between stages.

Evidence from different r-t plots, source mechanism characteristics, landing heights, variations in lithology observed from the GR log, and high shear-wave velocity anisotropy strongly suggest that geological and geomechanical changes are most likely linked with the event anomaly. The r-t (distance between events and treatment locations plotted over time) plot shows that the microseismicity behaves differently from stage to stage, with a substantial concentration toward the well heel. Additionally, I observe a

“normal” r-t pattern, indicating that no fault reactivation is related to the abnormal microseismic behavior. Moment tensor analyses using a screening test based on S/P amplitude ratios and a full moment tensor inversion show that there are different moment tensor characteristics between stages, supporting the geological/geomechanical role in the strong variations in microseismicity. Moreover, investigating the Montney depth trend indicates that well 2 has different landing heights; it first penetrates the Lower Montney and then intersects the Middle Montney. This might link to the event anomaly at the well heel due to the variability in geological heterogeneities of the Lower and Middle Montney. Observations on the GR logs reveal that there are variations in lithology between stages, and they are likely to correlate with the number of events. Furthermore, evidence of a highly anisotropic velocity field is observed in the stages toward the well heel, with slow and fast S waves evident on seismograms. Larger shear wave splitting is expected to be associated with high fracture densities and many microseismic events; therefore, high shear-wave velocity anisotropy is highly likely linked with the event anomaly near the well heel.

# Chapter 9

## Conclusions and suggested directions for future research

### 9.1 Conclusions

Microseismic monitoring provides an insightful understanding of the subsurface and the performance of hydraulic fracturing operations. However, the large volume of recorded data and the variability in microseismic signals present significant challenges in the efficient and accurate processing and analysis of microseismic data. This thesis performs an integrated analysis of engineering parameters, event locations, moment tensors, and geomechanics using an extensive microseismic data set from a Montney reservoir in northeastern BC to investigate the anomalous behavior of microseismicity between treatment stages, with many events concentrated toward the well's heel and only a few events in other areas.

The integrated analysis reveals that operational issues (e.g., screen-outs, poor injectivity rate, and weak/no ball seats), changes in treatment parameters (e.g., breakdown pressure, injection rate, and treatment duration), data processing (e.g., inefficient event detectors), and pre-existing faults in the medium are not the leading causes of the event anomaly. Geological and geomechanical changes are most likely linked with the event anomaly, supported by evidence from various analyses, including r-t plots, moment tensor characteristics, landing heights, variations in lithology, and high shear-wave velocity anisotropy.

This thesis also focuses on improving automated processing algorithms and workflows for large microseismic data sets. The fast and efficient MF algorithm detected nearly 20,000 events from over 300 hours of microseismic data. The fast MF outperforms the STA/LTA method with fewer false triggers (high precision) and higher detection probability (high recall). Combining a recursive STA/LTA method, a multiplexing technique, and the fast NCC computation in the fast MF workflow accelerates the event detection process. The fast NCC employs summed-area tables to speed up the calculation of the NCC coefficients between the template events and the continuous data.

The thesis also examines two time-frequency methods, the sparse Gabor transform and neighboring block thresholding, which combine signal enhancement with automated event detection and selection. The sparse Gabor transform proves more promising, with enhanced detection capability, improved data quality, and preserved absolute and relative amplitudes of the P- and S-phases of the signals. Unlike the sparse Gabor transform, the neighboring block thresholding causes amplitude fidelity issues that can hinder the interpretation of the detected events.

Furthermore, this thesis introduces a quadratic interpolation technique to address the computational challenges associated with grid searches over large search spaces. The quadratic interpolation technique performs well on both synthetic and real microseismic data examples, typically leading to similar event locations as those obtained from the grid search using 10 times smaller grid spacings in all three directions, at a minor additional computational expense, and without the need to generate traveltimes at new spatial positions. Combining coarse grid search and quadratic interpolation produces optimal hypocenter locations equivalent to finer grid searches while reducing the grid imprint effect often observed in coarse-grid-estimated results.

In conclusion, this thesis unravels the underlying causes of abnormal microseismic behavior in a Montney treatment. The enhancements in automated processing algorithms and workflows contribute to overcoming challenges posed by the large volume

and variability of microseismic signals, providing valuable tools for future research and practical applications in microseismic monitoring.

## 9.2 Suggested directions for future research

1. The subspace detection, as proposed by (Harris & Paik, 2006), is another interesting cross-correlation-based detection alternative. The matched filter implemented in Chapter 4 works effectively for repetitive seismic sources, which require a few template events for detection purposes. The subspace detection approach, on the other hand, detects events using a design set of earthquakes instead of relying on a single template during detection and can overcome the disadvantage of the matched filter and become applicable to highly variable waveforms. This method uses cross-correlation to build a design set of waveforms. Events are cross-correlated, pairwise, and grouped; the largest groups with NCC coefficients are included in the design set. Employing the fast NCC coefficient computation technique (Lewis, 1995) into the construction of the design set can accelerate the subspace detector.

2. Relative relocation methods using the double-difference algorithm (Castellanos & van der Baan, 2013; Waldhauser & Ellsworth, 2000) or GrowClust (Trugman & Shearer, 2017) may help refine the event locations obtained from the grid search and quadratic interpolation in Chapter 6. This method assumes that ray paths between two events will be very similar if their hypocentral separation is small compared to the source-receiver distances. Consequently, the relative travel-time difference at a common station is attributed to the spatial offset between both events, and the effects of most velocity heterogeneities will cancel out. Thus, only knowledge of the velocities in the source region is required. A more refined event location might provide greater insights into the interpretation of microseismic behavior.

3. Integrating microseismic event locations with seismic reflection data can provide more insightful information for interpreting abnormal microseismic behavior. For example, event hypocenters can be overlaid on seismic sections, time slices of 3-

dimensional seismic data and seismic attributes, supporting the understanding of pre-existing faults (Rodriguez-Pradilla & Eaton, 2020; Weir et al., 2022). The r-t plots (Chapter 8) indicate a “normal” development pattern of microseismicity, highly suggesting no fault reactivation related to the substantial variations in microseismicity between stages. The integration with seismic reflection data can further strengthen this conclusion.

4. The shear wave splitting phenomenon is observed in the later treatment stages near the heel of the well, with S waves arriving at different times on the seismograms (faster on the horizontal component and slower on the vertical components) (Chapter 8). This phenomenon can be further analyzed quantitatively. The splitting can be measured using two parameters: the polarization of the fast shear wave and the lag time between fast and slow components (De Meersman et al., 2009a; Teanby et al., 2004b). These parameters provide constraints on the mechanism causing the anisotropy and an advanced understanding of high shear wave velocity anisotropy.

5. The brittleness index (BI) is useful for characterizing rocks under stress (Zhang et al., 2016). The brittle index can be calculated using the dynamic elastic moduli logs that are derived from available compressional and shear sonic logs and density log (Feroz & van der Baan, 2024; Mavko et al., 2020). The BI analysis can indicate reservoir intervals that are more brittle, with a higher potential to sustain brittle failure (microseismicity) (Feroz & van der Baan, 2024). Utilizing the BI log along with the GR log can provide more insightful information for interpreting anomalous microseismic behavior, strengthening the geological/geomechanical role in the strong variations of microseismicity between stages.

# Bibliography

- Abdulaziz, A. M. (2013). Microseismic imaging of hydraulically induced-fractures in gas reservoirs: A case study in Barnett shale gas reservoir, Texas, USA. *Open Journal of Geology*, 2013.
- Aki, K., & Richards, P. G. (2002). *Quantitative seismology*.
- Akram, J., & Eaton, D. W. (2012). Adaptive microseismic event detection and automatic time picking. *2012 CSEG Annual Convention*.
- Akram, J., & Eaton, D. W. (2016). A review and appraisal of arrival-time picking methods for downhole microseismic data. *Geophysics*, 81(2), KS71–KS91.
- Akram, J., Ovcharenko, O., & Peter, D. (2017). A robust neural network-based approach for microseismic event detection. *87th Annual International Meeting, SEG, Expanded Abstracts*, 2929–2933.
- Albert, D. G. (1993). *Attenuation of outdoor sound propagation levels by a snow cover* (tech. rep.). Cold Regions Research and Engineering Lab Hanover NH.
- Allen, R. V. (1978). Automatic earthquake recognition and timing from single traces. *Bulletin of the Seismological Society of America*, 68(5), 1521–1532.
- Arrowsmith, S. J., & Eisner, L. (2006). A technique for identifying microseismic multiplets and application to the Valhall field, North sea identifying microseismic multiplets. *Geophysics*, 71(2), V31–V40.
- Artman, B., Podladtchikov, I., & Witten, B. (2010). Source location using time-reverse imaging. *Geophysical Prospecting*, 58(5), 861–873.
- Bachrathy, D., & Stépán, G. (2012). Bisection method in higher dimensions and the efficiency number. *Periodica Polytechnica Mechanical Engineering*, 56(2), 81–86.
- Backus, G. E. (1962). Long-wave elastic anisotropy produced by horizontal layering. *Journal of Geophysical Research*, 67(11), 4427–4440.
- Bai, C., Zhao, R., & Greenhalgh, S. (2009). Fast and accurate earthquake location within complex medium using a hybrid global-local inversion approach. *Earthquake Science*, 22(5), 435–448.
- Baig, A., & Urbancic, T. (2010). Microseismic moment tensors: A path to understanding frac growth. *The Leading Edge*, 29(3), 320–324.
- Barrett, S. A., & Beroza, G. C. (2014). An empirical approach to subspace detection. *Seismological Research Letters*, 85(3), 594–600.
- BC Oil and Gas Commission. (2012). Montney Formation Play Atlas NEBC [<https://www.bcogc.ca/files/reports/Technical-Reports/montney-format-play-atlas-nebc.pdf>], 1–36.

- BC Oil and Gas Commission. (2021). BC OIL AND GAS COMMISSION MONTNEY DATA RESOURCES For Researchers and Others [https://www.bcogc.ca/files/resources/BCOGC-Webinar-for-Montney-Researchers-Jan-2021.pptx. Accessed: 2022-03-09].
- Becerra, D., Clarkson, C. R., Ghanizadeh, A., Pires de Lima, R., Tabasinejad, F., Zhang, Z., Trivedi, A., & Shor, R. (2021). Evaluation of reservoir quality and forecasted production variability along a multi-fractured horizontal well. Part 1: Reservoir characterization. *Energies*, *14*(19), 6154.
- Beck, A., & Teboulle, M. (2009). A fast iterative shrinkage-thresholding algorithm for linear inverse problems. *SIAM Journal on Imaging Sciences*, *2*(1), 183–202.
- Berger, Z., Boast, M., & Mushayandebvu, M. (2008). The contribution of integrated HRAM studies to exploration and exploitation of unconventional plays in North America, Part 1: The Peach River Arch. *Reservoir*, *35*(10), 42–47.
- Berger, Z., Boast, M., & Mushayandebvu, M. (2009). The contribution of integrated HRAM studies to exploration and exploitation of unconventional plays in North America, Part 2: Basement structures control on the development of the Peace River Arch's Montney/Doig resource plays. *Reservoir*, *36*(2), 40–44.
- Bird, T., Barclay, J., Campbell, R., & Lee, P. (1994). Triassic Gas Resources of Western Canada Sedimentary Basin, Interior Plains-Geological Play Analysis and Resource Assessment.
- Birnie, C., & Hansteen, F. (2022). Bidirectional recurrent neural networks for seismic event detection. *Geophysics*, *87*(3), KS97–KS111.
- Boroumand, N., & Eaton, D. (2012). Comparing energy calculations - Hydraulic fracturing and microseismic monitoring. *74th EAGE Conference and Exhibition incorporating EUROPEC 2012*, cp–293.
- Briechele, K., & Hanebeck, U. D. (2001). Template matching using fast normalized cross correlation. *Optical Pattern Recognition XII*, *4387*, 95–102.
- Bui, H., & van der Baan, M. (2020). Event detection using a fast matched filter algorithm - An efficient way to deal with big microseismic data sets. *90th Annual International Meeting, SEG, Expanded Abstracts*, 1325–1329.
- Bui, H., & van der Baan, M. (2021). Moment-tensor inversion of hydraulic fracturing-induced events in a Montney reservoir, northeastern British Columbia. *First International Meeting for Applied Geoscience & Energy, SEG/AAPG, Expanded Abstracts*, 2076–2080.
- Bui, H., & van der Baan, M. (2023). Event locations: Speeding up grid searches using quadratic interpolation (submitted). *Geophysical Journal International*.
- Bui, H., van der Baan, M., & Sacchi, M. D. (2023). Comparison of sparse Gabor-based methods for detection of microseismic events. *Geophysics*, *88*(2), L27–L35.
- Castellanos, F., & van der Baan, M. (2013). Microseismic event locations using the double-difference algorithm. *CSEG Recorder*, *38*(3), 26–37.
- Castellanos, F., & van der Baan, M. (2015). Waveform similarity for quality control of event locations, time picking, and moment tensor solutions. *Geophysics*, *80*(6), WC99–WC106.

- Cerveny, V. (2001). *Seismic ray theory* (Vol. 110). Cambridge university press Cambridge.
- Chalmers, G. R., & Bustin, R. M. (2012). Geological evaluation of Halfway-Doig-Montney hybrid gas shale-tight gas reservoir, northeastern British Columbia. *Marine and Petroleum Geology*, *38*(1), 53–72.
- Chalmers, G., Bustin, R., & Bustin, A. (2011). Geological controls on matrix permeability of the Doig-Montney hybrid shale-gas-tight-gas reservoir, northeastern British Columbia (NTS 093P). *Geoscience BC Summary of Activities*, 2012–1.
- Chambers, K., Kendall, J.-M., Brandsberg-Dahl, S., & Rueda, J. (2010). Testing the ability of surface arrays to monitor microseismic activity. *Geophysical Prospecting*, *58*(5), 821–830.
- Chen, Y., Zhang, G., Bai, M., Zu, S., Guan, Z., & Zhang, M. (2019). Automatic waveform classification and arrival picking based on convolutional neural network. *Earth and Space Science*, *6*(7), 1244–1261.
- Cipolla, C., Maxwell, S., Mack, M., & Downie, R. (2011). A practical guide to interpreting microseismic measurements. *North American Unconventional Gas Conference and Exhibition*.
- Cohen, I. (2003). Noise spectrum estimation in adverse environments: Improved minima controlled recursive averaging. *IEEE Transactions on Speech and Audio Processing*, *11*(5), 466–475.
- Cohen, I., & Berdugo, B. (2001). Speech enhancement for non-stationary noise environments. *Signal Processing*, *81*(11), 2403–2418.
- Crombez, V., Rohais, S., Baudin, F., & Euzen, T. (2016). Facies, well-log patterns, geometries and sequence stratigraphy of a wave-dominated margin: Insight from the Montney Formation (Alberta, British Columbia, Canada). *Bulletin of Canadian Petroleum Geology*, *64*(4), 516–537.
- Crow, F. C. (1984). Summed-area tables for texture mapping. *Proceedings of the 11th annual conference on computer graphics and interactive techniques*, 207–212.
- Davies, G. R., Moslow, T. F., & Sherwin, M. D. (1997). The lower Triassic Montney formation, west-central Alberta. *Bulletin of Canadian Petroleum Geology*, *45*(4), 474–505.
- Davies, G. R., Watson, N., Moslow, T. F., & MacEachern, J. A. (2018). Regional subdivisions, sequences, correlations and facies relationships of the Lower Triassic Montney Formation, west-central Alberta to northeastern British Columbia, Canada - with emphasis on role of paleostructure. *Bulletin of Canadian Petroleum Geology*, *66*(1), 23–92.
- De Meersman, K., Kendall, J.-M., & Van der Baan, M. (2009a). The 1998 Valhall microseismic data set: An integrated study of relocated sources, seismic multiplets, and S-wave splitting. *Geophysics*, *74*(5), B183–B195.
- De Meersman, K., Kendall, J.-M., & Van der Baan, M. (2009b). The 1998 Valhall microseismic data set: An integrated study of relocated sources, seismic multiplets, and S-wave splitting. *Geophysics*, *74*(5), B183–B195.
- Dokht, R. M., Kao, H., Visser, R., & Smith, B. (2019). Seismic event and phase detection using time-frequency representation and convolutional neural networks. *Seismological Research Letters*, *90*(2A), 481–490.

- Duhault, J. L. (2012). Cardium microseismic west central Alberta: A case history. *CSEG Recorder*, 37(8).
- Duncan, P. M., Lakings, J. D., & Flores, R. A. (2010). Method for passive seismic emission tomography [US Patent 7,663,970].
- Eaton, D. W. (2018). *Passive seismic monitoring of induced seismicity: Fundamental principles and application to energy technologies*. Cambridge University Press.
- Eaton, D. W., & Eyre, T. S. (2018). Induced seismicity in Western Canada: Causes and consequences. *Geohazards 7, Canmore, Alberta, Canada*.
- Eaton, D. W., van der Baan, M., Birkelo, B., & Tary, J.-B. (2014). Scaling relations and spectral characteristics of tensile microseisms: Evidence for opening/closing cracks during hydraulic fracturing. *Geophysical Journal International*, 196(3), 1844–1857.
- Edwards, D., Barclay, J., Gibson, D., Kvill, G., Halton, E., Mossop, G., & Shetsen, I. (1994). Geological atlas of the Western Canada sedimentary basin. *Canadian Society of Petroleum Geologists & Alberta Research Council*, 257–275.
- Eisner, L., De La Pena, A., Wessels, S., Barker, W., & Heigl, W. (2011a). Why surface monitoring of microseismic events works. *Third EAGE Passive Seismic Workshop-Actively Passive 2011*.
- Eisner, L., Duncan, P. M., Heigl, W. M., & Keller, W. R. (2009). Uncertainties in passive seismic monitoring. *The Leading Edge*, 28(6), 648–655.
- Eisner, L., Hulsey, B., Duncan, P., Jurick, D., Werner, H., & Keller, W. (2010). Comparison of surface and borehole locations of induced seismicity. *Geophysical Prospecting*, 58(5), 809–820.
- Eisner, L., Thornton, M., & Griffin, J. (2011b). Challenges for microseismic monitoring. *2011 SEG Annual Meeting*.
- Emoto, Y., Funasaka, S., Tokura, H., Honda, T., Nakano, K., & Ito, Y. (2018). An optimal parallel algorithm for computing the summed area table on the GPU. *2018 IEEE International Parallel and Distributed Processing Symposium Workshops (IPDPSW)*, 763–772.
- Everitt, B. S., Landau, S., Leese, M., & Stahl, D. (2011). *Cluster analysis* (5th ed.). Wiley West Sussex.
- Eyre, T. S., & Van der Baan, M. (2017). The reliability of microseismic moment-tensor solutions: Surface versus borehole monitoring. *Geophysics*, 82(6), KS113–KS125.
- Eyre, T. S., & van der Baan, M. (2015). Overview of moment-tensor inversion of microseismic events. *The Leading Edge*, 34(8), 882–888.
- Feroz, A., & van der Baan, M. (2024). Integrated analysis of cyclic steam stimulation in a heavy oil reservoir: Microseismicity, brittleness and landing height. *Geophysics*, 89(2), 1–46.
- Forouhideh, F., & Eaton, D. W. (2009). Microseismic monitoring: Insights from moment tensor inversion. *CREWES Research Report*.
- Furlong, C. M., Gegolick, A., Gingras, M. K., González, P., Moslow, T. F., Prenoslo, D., Playter, T., & Zonneveld, J.-P. (2018a). Sedimentology and ichnology of the Middle Triassic (Anisian) Sunset Prairie Formation of the Western Canada Sedimentary Basin. *Bulletin of Canadian Petroleum Geology*, 66(1), 215–236.

- Furlong, C. M., Gingras, M. K., Moslow, T. F., & Zonneveld, J.-P. (2018b). The Sunset Prairie Formation: Designation of a new middle Triassic formation between the lower Triassic Montney formation and middle Triassic Doig formation in the Western Canada Sedimentary Basin, northeast British Columbia. *Bulletin of Canadian Petroleum Geology*, *66*(1), 193–214.
- Furlong, C. M., Gingras, M. K., & Zonneveld, J.-P. (2020). High-resolution sequence stratigraphy of the Middle Triassic Sunset Prairie Formation, Western Canada Sedimentary Basin, north-eastern British Columbia. *The Depositional Record*, *6*(2), 383–408.
- Gadallah, M. R., & Fisher, R. (2008). *Exploration geophysics*. Springer Science & Business Media.
- Gasperini, P., & Vannucci, G. (2003). FPSPACK: A package of Fortran subroutines to manage earthquake focal mechanism data. *Computers & Geosciences*, *29*(7), 893–901.
- Gegolick, A. E. (2017). Sedimentology, ichnology and biogenic permeability of the upper Montney Formation, northeast British Columbia.
- Geiger, L. (1912). Probability method for the determination of earthquake epicentres from the arrival time only. *Bull. St. Louis Univ.*, *8*, 60.
- Ghanizadeh, A., Clarkson, C. R., Vahedian, A., Ardakani, O. H., Wood, J. M., & Sanei, H. (2018). Laboratory-based characterization of pore network and matrix permeability in the Montney Formation: Insights from methodology comparisons. *Bulletin of Canadian Petroleum Geology*, *66*(2), 472–498.
- Gharti, H. N., Oye, V., Roth, M., & Kühn, D. (2010). Automated microearthquake location using envelope stacking and robust global optimization. *Geophysics*, *75*(4), MA27–MA46.
- Gibbons, S. J., & Ringdal, F. (2006). The detection of low magnitude seismic events using array-based waveform correlation. *Geophysical Journal International*, *165*(1), 149–166.
- Gibbons, S. J. (2022). The optimal correlation detector? *Geophysical Journal International*, *228*(1), 355–365.
- Goertz-Allmann, B., Langet, N., Kühn, D., Baird, A., Oates, S., Rowe, C., Harvey, S., Oye, V., & Nakstad, H. (2022). Effective microseismic monitoring of the Quest CCS site, Alberta, Canada. *Alberta, Canada (November 22, 2022)*.
- Golding, M., Orchard, M., Zonneveld, J.-P., Henderson, C., Dunn, L., & Russell-Houston, J. (2014). An exceptional record of the sedimentology and biostratigraphy of the Montney and Doig formations in British Columbia. *Bulletin of Canadian Petroleum Geology*, *62*(3), 157–176.
- González, P. D., Furlong, C. M., Gingras, M. K., Playter, T., & Zonneveld, J.-P. (2022). Depositional framework and trace fossil assemblages of the lower Triassic Montney formation, northeastern British Columbia, Western Canada Sedimentary Basin. *Marine and Petroleum Geology*, *143*, 105822.
- Goodfellow, S., Nasser, M., Maxwell, S., & Young, R. (2015). Hydraulic fracture energy budget: Insights from the laboratory. *Geophysical Research Letters*, *42*(9), 3179–3187.

- Grechka, V., & Heigl, W. M. (2017). *Microseismic monitoring*. Society of Exploration Geophysicists.
- Grechka, V., Li, Z., Howell, B., & Vavryčuk, V. (2016). Single-well moment tensor inversion of tensile microseismic events. *Geophysics*, *81*(6), KS219–KS229.
- Grigoli, F., Cesca, S., Krieger, L., Kriegerowski, M., Gammaldi, S., Horalek, J., Priolo, E., & Dahm, T. (2016). Automated microseismic event location using master-event waveform stacking. *Scientific reports*, *6*(1), 1–13.
- Hardage, B. A., DeAngelo, M. V., Murray, P. E., & Sava, D. (2011). *Multicomponent seismic technology*. Society of Exploration Geophysicists.
- Hardebeck, J. L., & Shearer, P. M. (2003). Using S/P amplitude ratios to constrain the focal mechanisms of small earthquakes. *Bulletin of the Seismological Society of America*, *93*(6), 2434–2444.
- Harris, D. B., & Paik, T. (2006). *Subspace detectors: Efficient implementation* (tech. rep.). Lawrence Livermore National Lab (LLNL), Livermore, CA (United States).
- Havskov, J., Bormann, P., & Schweitzer, J. (2009). Earthquake location. In *New manual of seismological observatory practice (nmsop)* (pp. 1–28). Deutsches GeoForschungsZentrum GFZ.
- Havskov, J., Bormann, P., & Schweitzer, J. (2012). Seismic source location. In *New manual of seismological observatory practice 2 (nmsop-2)* (pp. 1–36). Deutsches GeoForschungsZentrum GFZ.
- Havskov, J., & Ottemoller, L. (2010). *Routine data processing in earthquake seismology: With sample data, exercises and software*. Springer Science & Business Media.
- Henderson, C. M. (1997). Uppermost Permian conodonts and the Permian-Triassic boundary in the western Canada sedimentary basin. *Bulletin of Canadian Petroleum Geology*, *45*(4), 693–707.
- Holditch, S. A. (2003). The increasing role of unconventional reservoirs in the future of the oil and gas business. *Journal of petroleum technology*, *55*(11), 34–79.
- Hudson, J., Pearce, R., & Rogers, R. (1989). Source type plot for inversion of the moment tensor. *Journal of Geophysical Research: Solid Earth*, *94*(B1), 765–774.
- Jones, G., Kendall, J., Bastow, I., & Raymer, D. (2013). Locating microseismic events using borehole data. *Geophysical Prospecting*, *62*(1), 34–49.
- Jones, G., Kendall, J.-M., Bastow, I., & Raymer, D. (2014). Locating microseismic events using borehole data. *Geophysical Prospecting*, *62*(1), 34–49.
- Julian, B. R., & Foulger, G. (1996). Earthquake mechanisms from linear-programming inversion of seismic-wave amplitude ratios. *Bulletin of the Seismological Society of America*, *86*(4), 972–980.
- Julian, B. R., Miller, A. D., & Foulger, G. (1998). Non-double-couple earthquakes: Theory. *Reviews of Geophysics*, *36*(4), 525–549.
- Kisslinger, C. (1980). Evaluation of S to P amplitude ratios for determining focal mechanisms from regional network observations. *Bulletin of the Seismological Society of America*, *70*(4), 999–1014.
- Krause, F., Wiseman, A., Williscroft, K., Solano, N., Morris, N., Meyer, R., & Marr, R. (2011). The Montney Formation: Mineralogy, What Shall It Be? *Canadian*

- Society of Petroleum Geologists, Canadian Society of Exploration Geophysicists, Canadian Well Log Society, Joint Annual Convention.*
- Lay, T., & Wallace, T. C. (1995). *Modern global seismology*. Vol. 58, Elsevier.
- Lewis, J. P. (1995). Fast normalized cross-correlation. *Industrial Light & Magic*.
- Li, Z., & van der Baan, M. (2016). Microseismic event localization by acoustic time reversal extrapolation. *Geophysics*, *81*(3), KS123–KS134.
- Lili, X., Yates, M., Anifowoshe, O., Uschner-Arroyo, N., Yang, Y., & MacPhail, K. (2015). Comparing strategies for optimizing horizontal shale completions by projecting pilot well measurements across laterals. *SPE Eastern Regional Meeting*, SPE–177297.
- Lomax, A., & Curtis, A. (2001). Fast, probabilistic earthquake location in 3D models using oct-tree importance sampling. *Geophys. Res. Abstr*, *3*(955), 10–1007.
- Lomax, A., Michelini, A., & Curtis, A. (2009). Earthquake location, direct, global-search methods. *Encyclopedia of Complexity and Systems Science*, *5*, 2449–2473.
- Lomax, A., Virieux, J., Volant, P., & Berge-Thierry, C. (2000). Probabilistic earthquake location in 3D and layered models: Introduction of a Metropolis-Gibbs method and comparison with linear locations. *Advances in seismic event location*, 101–134.
- Ma, X., & Zoback, M. D. (2017). Lithology-controlled stress variations and pad-scale faults: A case study of hydraulic fracturing in the Woodford Shale, Oklahoma. *Geophysics*, *82*(6), ID35–ID44.
- Ma, Y. Z., & Holditch, S. (2015). *Unconventional oil and gas resources handbook: Evaluation and development*. Gulf professional publishing.
- MacFarlane, T., & Davis, T. (2015). Fracture characterization of the Montney Formation using amplitude inversion of converted wave seismic. *SPE/AAPG/SEG Unconventional Resources Technology Conference*, URTEC–2154222.
- MacKay, M. K., Eaton, D. W., Pedersen, P. K., & Clarkson, C. R. (2018). Integration of outcrop, subsurface, and microseismic interpretation for rock-mass characterization: An example from the Duvernay Formation, Western Canada. *Interpretation*, *6*(4), T919–T936.
- Mahani, A. B., Schultz, R., Kao, H., Walker, D., Johnson, J., & Salas, C. (2017). Fluid injection and seismic activity in the northern Montney play, British Columbia, Canada, with special reference to the 17 August 2015 Mw 4.6 induced earthquake. *Bulletin of the Seismological Society of America*, *107*(2), 542–552.
- Mavko, G., Mukerji, T., & Dvorkin, J. (2020). *The rock physics handbook*. Cambridge university press.
- Maxwell, S. C. (2014). *Microseismic imaging of hydraulic fracturing: Improved engineering of unconventional shale reservoirs*. Society of Exploration Geophysicists.
- Maxwell, S. C., Shemeta, J. E., Campbell, E., & Quirk, D. J. (2008). Microseismic deformation rate monitoring. *SPE Annual Technical Conference and Exhibition*, 439–466.
- Maxwell, S., Bennett, L., Jones, M., & Walsh, J. (2010). Anisotropic velocity modeling for microseismic processing: Part 1-Impact of velocity model uncertainty.

- In *SEG Technical Program Expanded Abstracts* (pp. 2130–2134). Society of Exploration Geophysicists.
- Maxwell, S. C., & Le Calvez, J. H. (2010). Horizontal versus vertical borehole-based microseismic monitoring: Which is better? *SPE Unconventional Gas Conference, Society of Petroleum Engineers*.
- McKean, S. H. (2017). *Geomechanical properties of the Montney and Sulphur Mountain Formations* [Master's thesis, Graduate Studies].
- Menke, W. (2018). *Geophysical data analysis: Discrete inverse theory*. Academic Press.
- Metropolis, N., Rosenbluth, A. W., Rosenbluth, M. N., Teller, A. H., & Teller, E. (1953). Equation of state calculations by fast computing machines. *The journal of chemical physics*, *21*(6), 1087–1092.
- Moslow, T. F. (2000). Reservoir architecture of a fine-grained turbidite system: Lower Triassic Montney Formation, western Canada sedimentary basin.
- Moslow, T. F., Haverslew, B., & Henderson, C. M. (2018). Sedimentary facies, petrology, reservoir characteristics, conodont biostratigraphy and sequence stratigraphic framework of a continuous (395m) full diameter core of the Lower Triassic Montney Fm, northeastern British Columbia. *Bulletin of Canadian Petroleum Geology*, *66*(1), 259–287.
- Mousavi, S. M., & Langston, C. A. (2016). Adaptive noise estimation and suppression for improving microseismic event detection. *Journal of Applied Geophysics*, *132*, 116–124.
- Mousavi, S. M., Langston, C. A., & Horton, S. P. (2016). Automatic microseismic denoising and onset detection using the synchrosqueezed continuous wavelet transform. *Geophysics*, *81*(4), V341–V355.
- Mousavi, S. M., Zhu, W., Sheng, Y., & Beroza, G. C. (2019). CRED: A deep residual network of convolutional and recurrent units for earthquake signal detection. *Scientific reports*, *9*(1), 1–14.
- National Energy Board, BC Oil and Gas Commission, Alberta Energy Regulator and BC Ministry of Natural Gas development. (2013). The Ultimate Potential for Unconventional Petroleum from the Montney Formation of British Columbia and Alberta - Energy Briefing Note [<https://www.cer-rec.gc.ca/en/data-analysis/energy-commodities/natural-gas/report/archive/ultimate-potential-montney-formation/the-ultimate-potential-unconventional-petroleum-from-montney-formation-british-columbia-alberta-energy-briefing-note.pdf>], 1–23.
- Ortega Perez, A. K. (2022). Hydraulic fracture monitoring: Integrated analysis of DAS, pumping information, microseismicity and PKN modelling.
- Othman, A., Iqbal, N., Hanafy, S. M., & Waheed, U. B. (2021). Automated event detection and denoising method for passive seismic data using residual deep convolutional neural networks. *IEEE Transactions on Geoscience and Remote Sensing*, *60*, 1–11.
- Oye, V., & Roth, M. (2003). Automated seismic event location for hydrocarbon reservoirs. *Computers & Geosciences*, *29*(7), 851–863.

- Pavlis, G. L. (1986). Appraising earthquake hypocenter location errors: A complete, practical approach for single-event locations. *Bulletin of the Seismological Society of America*, 76(6), 1699–1717.
- Pearson, C. (1981). The relationship between microseismicity and high pore pressures during hydraulic stimulation experiments in low permeability granitic rocks. *Journal of Geophysical Research: Solid Earth*, 86(B9), 7855–7864.
- Pérez, D. O., Velis, D. R., & Sacchi, M. D. (2013). High-resolution prestack seismic inversion using a hybrid FISTA least-squares strategy. *Geophysics*, 78(5), R185–R195.
- Perol, T., Gharbi, M., & Denolle, M. (2018). Convolutional neural network for earthquake detection and location. *Science Advances*, 4(2), e1700578.
- Pike, K. A. (2014). *Microseismic data processing, modeling and interpretation in the presence of coals: A Falher member case study* [Doctoral dissertation, University of Calgary].
- Playter, T., Corlett, H., Konhauser, K., Robbins, L., Rohais, S., Crombez, V., MacCormack, K., Rokosh, D., Prenoslo, D., Furlong, C. M., et al. (2018). Clinof orm identification and correlation in fine-grained sediments: A case study using the Triassic Montney Formation. *Sedimentology*, 65(1), 263–302.
- Press, W. H. (1992). *Numerical recipes in Fortran 77: The art of scientific computing*. Cambridge university press.
- Press, W. H., Saul, A. T., William, T. V., & Brian, P. F. (1992). *Numerical recipes in Fortran 77: The art of scientific computing*. Cambridge University Press.
- Qu, S., Guan, Z., Verschuur, E., & Chen, Y. (2020). Automatic high-resolution microseismic event detection via supervised machine learning. *Geophysical Journal International*, 222(3), 1881–1895.
- Rafiq, A., Eaton, D. W., McDougall, A., & Pedersen, P. K. (2016). Reservoir characterization using microseismic facies analysis integrated with surface seismic attributes. *Interpretation*, 4(2), T167–T181.
- Reiter, K., Heidbach, O., Schmitt, D., Haug, K., Ziegler, M., & Moeck, I. (2014). A revised crustal stress orientation database for Canada. *Tectonophysics*, 636, 111–124.
- Rodriguez-Pradilla, G., & Eaton, D. W. (2020). Automated microseismic processing and integrated interpretation of induced seismicity during a multistage hydraulic-fracturing stimulation, Alberta, Canada. *Bulletin of the Seismological Society of America*, 110(5), 2018–2030.
- Sacchi, M., Kaplan, S., & Naghizadeh, M. (2009). FX Gabor seismic data reconstruction. *71st EAGE Conference and Exhibition Incorporating SPE EUROPEC*, cp-127.
- Shapiro, S., Dinske, C., & Rothert, E. (2006). Hydraulic-fracturing controlled dynamics of microseismic clouds. *Geophysical Research Letters*, 33(14).
- Shapiro, S. A., & Dinske, C. (2009). Fluid-induced seismicity: Pressure diffusion and hydraulic fracturing. *Geophysical Prospecting*, 57(2), 301–310.
- Sipkin, S. A. (1982). Estimation of earthquake source parameters by the inversion of waveform data: Synthetic waveforms. *Physics of the Earth and Planetary interiors*, 30(2-3), 242–259.

- Smith, M. B., & Montgomery, C. (2015). *Hydraulic fracturing*. CRC press.
- Song, F., Warpinski, N. R., Toksöz, M. N., & Kuleli, H. S. (2014). Full-waveform based microseismic event detection and signal enhancement: An application of the subspace approach. *Geophysical Prospecting*, *62*(6), 1406–1431.
- Stein, C. M. (1981). Estimation of the mean of a multivariate normal distribution. *The annals of Statistics*, *9*(6), 1135–1151.
- Stein, S., & Wysession, M. (2009). *An introduction to seismology, earthquakes, and earth structure*. John Wiley & Sons.
- St-Onge, A., & Eaton, D. (2011). Noise examples from two microseismic datasets. *CSEG Recorder*, *36*(10), 46–49.
- Strohmer, T. (1998). Numerical algorithms for discrete Gabor expansions. In *Gabor analysis and algorithms* (pp. 267–294). Springer.
- Tarantola, A., & Valette, B. (1982). Inverse Problems = Quest for Information. *Journal of Geophysics*, *50*(1), 159–170.
- Tariq, Z., Aljawad, M. S., Murtaza, M., Mahmoud, M., Al-Shehri, D., & Abdulaheem, A. (2021). A data-driven approach to predict the breakdown pressure of the tight and unconventional formation. *SPE Annual Technical Conference and Exhibition*.
- Tary, J. B., Herrera, R. H., Han, J., & van der Baan, M. (2014). Spectral estimation - What is new? What is next? *Reviews of Geophysics*, *52*(4), 723–749.
- Teanby, N., Kendall, J.-M., Jones, R., & Barkved, O. (2004a). Stress-induced temporal variations in seismic anisotropy observed in microseismic data. *Geophysical Journal International*, *156*(3), 459–466.
- Teanby, N. A., Kendall, J.-M., & Van der Baan, M. (2004b). Automation of shear-wave splitting measurements using cluster analysis. *Bulletin of the Seismological Society of America*, *94*(2), 453–463.
- Trnkoczy, A. (2012). Understanding and parameter setting of STA/LTA trigger algorithm. In *Bormann, p. (ed.), new manual of seismological observatory practice 2 (nmsop-2), potsdam* (pp. 1–20). Deutsches GeoForschungsZentrum GFZ.
- Trugman, D. T., & Shearer, P. M. (2017). GrowClust: A hierarchical clustering algorithm for relative earthquake relocation, with application to the Spanish Springs and Sheldon, Nevada, earthquake sequences. *Seismological Research Letters*, *88*(2A), 379–391.
- Tsvankin, I., Gaiser, J., Grechka, V., Van Der Baan, M., & Thomsen, L. (2010). Seismic anisotropy in exploration and reservoir characterization: An overview. *Geophysics*, *75*(5), 75A15–75A29.
- Tsvankin, I., & Grechka, V. (2011). *Seismology of azimuthally anisotropic media and seismic fracture characterization*. Society of Exploration Geophysicists.
- Vaezi, Y., & van der Baan, M. (2015). Comparison of the STA/LTA and power spectral density methods for microseismic event detection. *Geophysical Supplements to the Monthly Notices of the Royal Astronomical Society*, *203*(3), 1896–1908.
- Van der Baan, M., Eaton, D. W., & Preisig, G. (2016). Stick-split mechanism for anthropogenic fluid-induced tensile rock failure. *Geology*, *44*(7), 503–506.

- van der Baan, M., Eaton, D. W., & Dusseault, M. (2013). Microseismic monitoring developments in hydraulic fracture stimulation. *ISRM International Conference for Effective and Sustainable Hydraulic Fracturing*.
- Van Dok, R., Fuller, B., Engelbrecht, L., & Sterling, M. (2011). Seismic anisotropy in microseismic event location analysis. *The Leading Edge*, *30*(7), 766–770.
- Vavryčuk, V. (2005). Focal mechanisms in anisotropic media. *Geophysical Journal International*, *161*(2), 334–346.
- Vavryčuk, V. (2007). On the retrieval of moment tensors from borehole data. *Geophysical Prospecting*, *55*(3), 381–391.
- Vavryčuk, V. (2011). Tensile earthquakes: Theory, modeling, and inversion. *Journal of Geophysical Research: Solid Earth*, *116*(B12).
- Venieri, M., Weir, R., McKean, S. H., Pedersen, P. K., & Eaton, D. W. (2020). Determining elastic properties of organic-rich shales from core, wireline logs and 3-d seismic: A comparative study from the Duvernay play, Alberta, Canada. *Journal of Natural Gas Science and Engineering*, *84*, 103637.
- Vermilyen, J. P., & Zoback, M. D. (2011). Hydraulic fracturing, microseismic magnitudes, and stress evolution in the Barnett Shale, Texas, USA. *SPE Hydraulic Fracturing Technology Conference*.
- Waldhauser, F. (2001). Hypodd-A program to compute double-difference hypocenter locations.
- Waldhauser, F., & Ellsworth, W. L. (2000). A double-difference earthquake location algorithm: Method and application to the northern Hayward fault, California. *Bulletin of the Seismological Society of America*, *90*(6), 1353–1368.
- Walter, W. R., & Brune, J. N. (1993). Spectra of seismic radiation from a tensile crack. *Journal of Geophysical Research: Solid Earth*, *98*(B3), 4449–4459.
- Warpinski, N. R. (2009). Microseismic monitoring: Inside and out. *Journal of Petroleum Technology*, *61*(11), 80–85.
- Warpinski, N. R., Sullivan, R. B., Uhl, J., Waltman, C., & Machovoie, S. (2005). Improved microseismic fracture mapping using perforation timing measurements for velocity calibration. *10*(1), 14–23.
- Warpinski, N., Wolhart, S., & Wright, C. (2004). Analysis and prediction of microseismicity induced by hydraulic fracturing. *Spe Journal*, *9*(01), 24–33.
- Weir, R. M., Eaton, D. W., Eyre, T. S., & Lawton, D. C. (2022). Integrated interpretation: Defining risk corridors by combining 3-D seismic interpretation with induced seismicity hypocenters. *Tectonophysics*, *827*, 229263.
- Withers, M., Aster, R., Young, C., Beiriger, J., Harris, M., Moore, S., & Trujillo, J. (1998). A comparison of select trigger algorithms for automated global seismic phase and event detection. *Bulletin of the Seismological Society of America*, *88*(1), 95–106.
- Wuestefeld, A., Al-Harrasi, O., Verdon, J. P., Wookey, J., & Kendall, J. M. (2010). A strategy for automated analysis of passive microseismic data to image seismic anisotropy and fracture characteristics. *Geophysical Prospecting*, *58*(5), 755–773.

- Wuestefeld, A., Greve, S. M., Näsholm, S. P., & Oye, V. (2018). Benchmarking earthquake location algorithms: A synthetic comparison. *Geophysics*, *83*(4), KS35–KS47.
- Zhang, C., & van der Baan, M. (2021). Complete and representative training of neural networks: A generalization study using double noise injection and natural images. *Geophysics*, *86*(3), V197–V206.
- Zhang, C., & van der Baan, M. (2022). Signal Processing Using Dictionaries, Atoms, and Deep Learning: A Common Analysis-Synthesis Framework. *Proceedings of the IEEE*, *110*(4), 454–475.
- Zhang, C., Qiao, W., Che, X., Lu, J., & Men, B. (2019). Automated microseismic event location by amplitude stacking and semblance microseismic location method. *Geophysics*, *84*(6), KS191–KS210.
- Zhang, D., Ranjith, P., & Perera, M. (2016). The brittleness indices used in rock mechanics and their application in shale hydraulic fracturing: A review. *Journal of petroleum science and Engineering*, *143*, 158–170.
- Zhang, X., Chen, H., Zhang, W., Tian, X., & Chu, F. (2021). Generalized neural network trained with a small amount of base samples: Application to event detection and phase picking in downhole microseismic monitoring. *Geophysics*, *86*(5), KS95–KS108.
- Zhou, W., Wang, L., Guan, L., Guo, Q., Cui, S., & Yu, B. (2015). Microseismic event location using an inverse method of joint P-S phase arrival difference and P-wave arrival difference in a borehole system. *Journal of Geophysics and Engineering*, *12*(2), 220–226.
- Zonneveld, J.-P., Beatty, T. W., MacNaughton, R. B., Pemberton, S. G., Utting, J., & Henderson, C. M. (2010a). Sedimentology and ichnology of the Lower Triassic Montney Formation in the Pedigree-Ring/Border-Kahntah River area, northwestern Alberta and northeastern British Columbia. *Bulletin of Canadian Petroleum Geology*, *58*(2), 115–140.
- Zonneveld, J.-P., Gingras, M. K., & Beatty, T. W. (2010b). Diverse ichnofossil assemblages following the PT mass extinction, Lower Triassic, Alberta and British Columbia, Canada: Evidence for shallow marine refugia on the northwestern coast of Pangaea. *Palaios*, *25*(6), 368–392.
- Zonneveld, J.-P., Golding, M., Moslow, T. F., Orchard, M. J., Playter, T., & Wilson, N. (2011). Depositional framework of the lower Triassic Montney formation, west-central Alberta and northeastern British Columbia. *CSPG CSEG CWLS Convention*, 1–4.
- Zonneveld, J.-P., & Moslow, T. F. (2018). Palaeogeographic setting, lithostratigraphy, and sedimentary framework of the Lower Triassic Montney Formation of western Alberta and northeastern British Columbia. *Bulletin of Canadian Petroleum Geology*, *66*(1), 93–127.
- Zonneveld, J.-P., Furlong, C., Gegolick, A., Gingras, M., Golding, M., Moslow, T., Orchard, M., Playter, T., Prenoslo, D., & Sanders, S. (2015). Stratigraphic Architecture of the Montney Formation, Peace District, Alberta and British Columbia. *William C. Gussow Geoscience Conference*.